



Etude expérimentale des cinétiques de diffusion et de la ségrégation induite sous irradiation d'alliages modèles et industriel austénitiques.

Solène Rouland

► To cite this version:

Solène Rouland. Etude expérimentale des cinétiques de diffusion et de la ségrégation induite sous irradiation d'alliages modèles et industriel austénitiques.. Matériaux. Normandie Université, 2020. Français. NNT : 2020NORMR050 . tel-03128646

HAL Id: tel-03128646

<https://theses.hal.science/tel-03128646>

Submitted on 2 Feb 2021

HAL is a multi-disciplinary open access archive for the deposit and dissemination of scientific research documents, whether they are published or not. The documents may come from teaching and research institutions in France or abroad, or from public or private research centers.

L'archive ouverte pluridisciplinaire **HAL**, est destinée au dépôt et à la diffusion de documents scientifiques de niveau recherche, publiés ou non, émanant des établissements d'enseignement et de recherche français ou étrangers, des laboratoires publics ou privés.



Normandie Université

THÈSE

Pour obtenir le diplôme de doctorat

Spécialité Physique – Science des Matériaux

Préparée au sein de l'Université de Rouen Normandie

Etude expérimentale des cinétiques de diffusion et de la ségrégation induite sous irradiation d'alliages modèles et industriels austénitiques

**Présentée et soutenue par
Solène ROULAND**

**Thèse soutenue publiquement le 10 décembre 2020
devant le jury composé de**

Mme Grace BURKE	Professeur – University of Manchester	Rapporteur
M. Pascal BELLON	Professeur – University of Illinois	Rapporteur
M. Éric ANDRIEU	Professeur – INP Toulouse	Président
M. Bertrand RADIGUET	Maître de conférences – GPM Rouen	Co-encadrant de thèse
M. Philippe PAREIGE	Professeur – GPM Rouen	Directeur de thèse
Mme Maylise NASTAR	Chercheur – CEA Saclay	Invité
Mme Martine BLAT-YRIEIX	Ingénieur Chercheur – EDF Lab Les Renardières	Invité

**Thèse dirigée par Pr. Philippe PAREIGE, co-encadrée par Dr. Bertrand RADIGUET
Groupe de Physique des Matériaux
UMR CNRS 6634 – Université de Rouen Normandie**



ACKNOWLEDGEMENTS-REMERCIEMENTS

I first want to express my sincere gratitude to my thesis committee. Prof. M. Grace Burke and Prof. Pascal Bellon, thank you for investing time in the thesis review, for your helpful suggestions and your wishes. Prof. Eric Andrieu, I am gratified that you preside at this unconventional virtual defense. Dr. Maylise Nastar, thank you very much for your availability and your advice during these three years, from its beginning to its end. Dr. Martine Blat-Yrieux, it was a great pleasure that you answered positively to this invitation, thank you very much for your involvement, your help and your kindness. I felt honoured and proud that you all accepted to offer your expert view on my work. I am looking forward collaboration opportunities in the future.

As I feel more comfortable to express my feelings in French, I'm switching language for these following part to thank all the people who supported me all along this enriching experience.

Bertrand Radiguet, Philippe Pareige, en vous choisissant j'ai tiré le duo gagnant. Vous avez largement contribué à mon épanouissement durant ces trois ans, autant sur le plan scientifique qu'humain. Vous savez joindre l'utile à l'agréable, toujours avec beaucoup d'humour. Merci pour votre soutien indéfectible et vos conseils avisés mais également d'avoir encouragé et dosé ma curiosité.

Bertrand, ça y est, tu vas pouvoir savourer ta liberté retrouvée, enfin débarrassé du pot de colle. Je ne veux pas t'envoyer trop de fleurs pour que tes chapeaux restent à ta taille mais je dois avouer que j'admire chez toi (entre autres) ta capacité d'écoute, ton investissement et ta pédagogie.

Philippe, ta capacité à valoriser la science ainsi que ceux qui la font me surprendra toujours. Un n^{ième} merci pour ton accompagnement et ton appui.

J'adresse à chacun mon profond respect et mon amitié.

J'aimerais profiter de l'occasion qui m'est offerte pour remercier Philippe Le-Bec et Laurent Legras d'avoir cru en mes chances et de m'avoir construit scientifiquement. Plus largement, j'ai une pensée pour mes anciens collègues d'EDF Lab Les Renardières.

Merci donc à mes encadrants de m'avoir transmis le goût de la recherche, ainsi qu'à mes étudiants et stagiaires qui m'ont donné le goût de transmettre.

Un grand merci à Marie Loyer-Prost pour sa disponibilité et ses nombreux conseils lors de ces trois années ainsi qu'à Alain Billard pour l'élaboration des matériaux modèles et leur optimisation.

Merci à Constantinos Hatzoglou, Liangzhao Huang, Andrey Medvedev et Brice Njakou Nguendo pour leur précieuse contribution à ces travaux permettant de confronter expérience et modélisation.

Merci à l'ensemble des membres du laboratoire du GPM pour votre accueil chaleureux et pour tous ces moments d'échange conviviaux, de m'avoir rapidement intégré et confié des responsabilités. Je

souhaite remercier en particulier Béatrice, Cristelle, Charly, Fred, Helena, Raphaëlle, Célia, Simona, Manu, Fabien, Laurence, Xavier, Williams, Fabienne, Linda, Christine, Leslie, Caroline et Marie-Ange pour votre bonne humeur, votre aide, vos conseils et votre soutien.

J'adresse une mention spéciale à Auriane et Constantinos, merci d'avoir toujours répondu présent à mes si nombreuses sollicitations avec entrain et un éternel sourire.

Merci à Ivan (le français), Romain, Aidar, Maria, Bence, Gilles, Linda, Souhaila, Alfiia, Sasha, Felix, Inna, Amandine, le Père Noël, Mekola, Damien et Senda, Ivan (le russe), Leifang, Andrey, Sid, Casey, Elie, Florian... pour tous ces bons moments partagés et arrosés.

Bego, Olha et Sana, toujours présentes dans les moments de joies, de plaintes et de peine. Vous avez pimenté ces trois ans, maintenant que je vous tiens, je ne vous lâche plus !

Guy, Jacqueline et Geoffrey, merci de nous avoir ouvert le portillon de votre jardin avec confiance et générosité et pour ces sessions de sport intense (quoi, le jardinage c'est pas du sport ?).

Alix(e), Lolo, JL, Mélanie, Maéva, Marine, François, Romain, Benja, Ju : loin des yeux, proche du cœur !

Tony, Simon, Thibaut, Alex, Théo, Alison et Romain, compagnons d'école, de fête, de voyage et plus et plus et plus.

Merci à mes anciens colloques : Babas le baroudeur, Jerem le champion du monde de la connerie, Max le cuisinier (le tablier te va si bien), Ludo le papa et Hélène l'artiste d'avoir vu en mes comptes-rendus de TP un réel avenir dans la recherche.

Un Big Up aux Beach Youth. Ce manuscrit va très certainement cumuler des millions de lecteurs, super vitrine pour un coup de pub, écoutez-les → <https://www.youtube.com/watch?v=hwAYs4EUigA>

Merci à Aveline, l'inconditionnelle, d'une fidélité et d'un soutien sans faille, que j'admire et je chéris.

Merci à Gautier, patient, attentionné et aimant, trop souvent loin mais toujours à mes côtés, je t'aime.

A ma mère, mon père et mon frère : mer(sisi) la famille pour vos encouragements, votre suivi et votre tendresse. Merci à ma large et belle famille, qui ont vécu pour certains des moments heureux, d'autres douloureux durant ces trois ans à qui j'adresse toutes mes pensées.

TABLE OF CONTENTS

GENERAL INTRODUCTION	1
----------------------------	---

CHAPTER 1

BIBLIOGRAPHIC REVIEW.....	5
---------------------------	---

I. Understanding and mitigating performance issues of austenitic stainless steels components in nuclear reactors.....	6
---	---

II. Microstructure evolution after thermal ageing.....	9
--	---

1. Austenite stability.....	9
-----------------------------	---

2. Vacancy mediated substitutional diffusion.....	10
---	----

3. Precipitation	22
------------------------	----

III. Microstructure evolution after ageing under irradiation	26
--	----

1. Neutron production and transmutations in nuclear reactors	26
--	----

2. Collision event and radiation damage.....	27
--	----

3. Radiation enhanced and modified diffusion: 4 regimes	29
---	----

4. Emulate neutrons with ions	30
-------------------------------------	----

5. Effect of radiation damage on resulting microstructure and microchemistry.....	32
---	----

IV. Prediction of microstructural evolution up to 60 years of irradiation: focus on RIS.....	52
--	----

1. By the experimental determination of interdiffusion kinetics to improve diffusion of point defect models under irradiation in austenitic Fe-Ni-Cr system	53
---	----

2. Quantifying segregation levels on biased sinks by implementing recent development in terms of nanoscale characterisations on a 316L(N) austenitic stainless steel.	53
--	----

CHAPTER 2

EXPERIMENTAL TECHNIQUES	55
-------------------------------	----

I. Analytical Electron Microscopy.....	56
--	----

1. Basic principle.....	56
-------------------------	----

2. Real space to reciprocal space: imaging with diffraction.....	62
--	----

TABLE OF CONTENTS

3. Other types of contrast	71
4. Defect characterization	72
II. Atom Probe Tomography	90
1. Basic principle.....	90
2. Data acquisition and data treatment	100

CHAPTER 3

IRRADIATION EFFECT ON DIFFUSION KINETICS.....	113
I. Introduction.....	114
II. Theoretical approach of the nanolayers method	114
1. In the binary system	114
2. In the ternary system.....	117
III. Experimental implementation	118
1. Ageing conditions: annealing and irradiations	118
2. Nanolayers elaboration and optimizations	122
3. Specimen preparation.....	126
IV. Interdiffusion kinetics in Ni/Ni-20Cr system after thermal ageing and under irradiation.....	128
1. Microstructure evolution.....	128
2. Concentration amplitude evolution.....	135
3. Interdiffusion coefficients	142
4. Discussion	144
V. Interdiffusion kinetics in Ni-40Fe-25Cr/Ni-35Fe-20Cr system after thermal ageing and under irradiation	149
1. Microstructure evolution.....	149
2. Concentration amplitude evolution.....	152
3. Interdiffusion coefficients	155
4. Discussion	157
VI. General discussion.....	161
VII. Conclusion.....	164

CHAPTER 4

INVESTIGATION OF RADIATION INDUCED SEGREGATION ON INTRAGRANULAR DEFECTS IN 316L(N)167

I. Introduction.....168

II. As-received material: 316L(N)168

1. At the microscale168

2. At the nanoscale171

III. Irradiation conditions.....177

1. JANNuS Orsay177

2. JANNuS Saclay.....179

IV. Nanoscale characterizations strategy180

1. Correlative microscopy on an APT tip180

2. Correlative microscopy on a tip extracted from a lamella181

V. Post-irradiations characterizations.....184

1. 1 dpa 450°C184

2. 2.5 dpa 440°C.....198

VI. General discussion.....205

VII. Conclusion.....209

GENERAL CONCLUSION211

REFERENCES217

APPENDIX i

GENERAL INTRODUCTION

Production of low carbon energy is a global ambition and nuclear electricity is part of this energetic mix strategy. Because the world nuclear power plant (NPP) fleet is ageing, to achieve this objective in accordance to the imposed deadlines, the following approach is adopted: at short term, extend existing reactors lifetime and at longer term, develop a new generation of reactors which guarantee safety, sustainability and competitiveness. In both existing and later generations of NPP, it is a necessity to ensure reliable mechanical resistance under harsh operating conditions of austenitic stainless steels components. To prevent their degradation, mechanisms involved need to be better understood in order to predict any risk of service failure. A better knowledge of degradation mechanisms will also help to optimize materials.

Irradiation-assisted stress corrosion cracking (IASCC) appears to be one of the major concerns for components integrity made of austenitic stainless steels because it causes unexpected failure. These steels are largely selected as structural materials for existing and future reactor cores. Deep investigations of baffle former bolts which underwent service failure caused by this phenomenon systematically show intergranular failure of components exposed to: elevated doses, elevated temperatures and stress within a reactive environment. The fourth generation of reactors are planned to operate at higher temperatures and reach higher damage levels over the increased lifetime of reactor, possibly in a corrosive medium. Understanding and isolating factors causing and accelerating IASCC is a vast challenge because up to now involved mechanisms are not clearly defined and are still controversial. Indeed, IASCC is a very complex phenomenon. Among the various factors, RIS to irradiation-induced defects is undoubtedly involved.

Energetic collisions of neutrons with host atoms of a crystal provoke damage cascades resulting in the creation of a large amount of point defects, namely vacancies and self-interstitials (SIA). They can either annihilate by mutual recombination, collapse to form large vacancy or SIA clusters or migrate over long range to annihilate at the vicinity of pre-existing defects (e.g. grain boundaries) or newly created point defect clusters within grains (e.g. dislocation loops, vacancies). Defects that absorb point defects are defined as sinks. Point defect concentration evolution in time and space is a balance between their production rate and their annihilation rate which intimately dependent on the irradiation conditions (i.e. temperature, dose, dose rate), material thermomechanical history and the resulting sink strength.

Chemical species migration within an irradiated material is governed by exchanges occurring between chemical species and point defects. This thermally activated process is called diffusion. In unirradiated materials, diffusion of elements is only governed by vacancies. Because of their high formation energy, SIA concentration is too small to significantly influence diffusion. Vacancies equilibrium concentration rises with the temperature and faster diffusion kinetics. Under irradiation, point defects produced within collision cascades (i.e. vacancies and SIA) come to add to the vacancies created thermally. By increasing the overall number of point defects in the crystal lattice, first effect of irradiation is to enhance diffusion. As the number of point defects within the

lattice is high and at equilibrium at sinks, point defects fluxes toward sinks are created. Coupling between fluxes of point defects and chemical species will result in local enrichments or depletions of elements at sinks. This phenomenon is called radiation induced segregation (RIS).

Predict RIS is still challenging because of the lack of experimental diffusion data at the operating temperature range of nuclear reactors and the competition existing between the different identified mechanisms. The work presented here attempts to provide experimental insights for each issue.

Vacancy mediated diffusion kinetics are usually extrapolated from high temperatures diffusion experiments. While experimental data exist for binary alloys of the Fe-Ni-Cr system representative of the nuclear steels grades, database is poor for ternary alloys. Concerning SIA mediated diffusion, it is an even more difficult task.

Nevertheless, an experimental method gives hope to obtain these values experimentally under a reasonable experimental time. Interdiffusion coefficients are extracted from the concentration amplitude attenuation of a stack of nano-scaled diffusion couples resulting in a composition modulated structure. This kind of material can be fabricated by magnetron co-sputtering and can give access to a very large range of compositions. Two austenitic NiCr and FeNiCr model alloys have been studied within the operation temperature range of nuclear reactors both after thermal ageing and under ion irradiation. Atom probe tomography (APT) and transmission electron microscopy (TEM) are techniques scaled to these experiments where atom migration in nanoscale systems need to be tackled.

Because IASCC provokes a characteristic intergranular fracture, the large majority of experimental RIS studies are focused on grain boundaries. But RIS levels at a particular sink not only depend on the sink itself but on the overall sink strength. Intragranular defects can exhibit preferential absorption of a type of point defect. Depending on their respective bias, mechanisms involved in RIS can differ which influences RIS at other sinks vicinity, phases stability and precipitate-defect association. Thus, a deep investigation of the global microstructure evolution under irradiation is necessary to understand and anticipate ageing under irradiation faced by austenitic stainless steels components.

As far as irradiation induced features are concerned, austenitic stainless steels had been largely studied thanks to different atomic-scale techniques (TEM, APT, PAS...) revealing the presence of extended defects (cavities, dislocation loops) and chemical heterogeneities (segregations, solute clusters, precipitates). However, the nature of some solute clusters remains unclear by solely coupling techniques (precipitates of new phase or segregation to defect clusters) but using two different samples. In order to better understand the nature of these features and their mechanism of formation, correlative APT-TEM microscopy performed on a unique sample has been implemented on an optimized steel, 316L(N) provided by EDF. Linking composition to crystallography will help to fully characterize these defects and to understand their formation mechanisms.

Within the framework of the Generation IV Materials Maturity (GEMMA) European project (see APPENDIX) involving experts and users of the nuclear material community, a common effort is

made to give keys or answer to these numerous open questions. This collective involvement is essential to anticipate ageing of materials under irradiation for long term operation of existing reactor as well as for the development of a future generation.

The present work expects to provide new insights to appreciate RIS kinetics and mechanisms:

1. By the experimental determination of interdiffusion kinetics to improve diffusion of point defect models under irradiation in austenitic Fe-Ni-Cr system
2. By the study of RIS on intragranular sinks by implementing recent development in terms of nanoscale characterisations and their coupling on a 316L(N) austenitic stainless steel.

First chapter is dedicated to the literature review on microstructure evolution of austenitic stainless steels under thermal ageing and ageing under irradiation, processes involved in degradation mechanisms of reactor internals. Before introducing irradiation effect on microstructural evolution and diffusion kinetics, basic approach of the thermal diffusion theory in substitutional binary and ternary alloys is explained. Precipitates commonly encountered in thermally aged alloys are then listed. Extended vacancy and SIA defects encountered in damaged microstructure as well as current understanding on RIS phenomenon and precipitation under irradiation will be developed. Finally, the strategy chosen for this present work to improve RIS predictions will be justified and faced to the bibliography.

The second chapter will treat on the theoretical and practical aspects of the nanoscale experimental techniques employed in this work, namely: transmission electron microscopy (TEM) and atom probe tomography (APT). Strengths, limitations and complementarity of both techniques will be highlighted and recent advances on these techniques will be also exposed.

In the third chapter, theory and assumptions of the nanolayers method will be first introduced. Sample fabrication and specimen preparation as well as realized optimizations will be presented. The choice of ageing conditions will be justified based on predictive models. Results obtained for interdiffusion kinetics after thermal ageing and under irradiation on binary NiCr and ternary FeNiCr model alloys will be presented and criticized. Strengths and current limitations of the method will be pointed out and improvements will be proposed to overcome experimental issues and improve results interpretation. Finally, a matrix of experimental conditions will be proposed for both systems to access to SIA mediated diffusion kinetics.

Last chapter will be devoted to the study of RIS on intragranular defects of an optimized 316L(N) by the use of coupled and correlated experimental nanoscale techniques. As-received microstructure characterizations from the micron scale down to the nanoscale will be first described. Then, the implementation of TEM-APT correlative microscopy on an APT tip and a tip extracted from a pre-characterized TEM lamella will be detailed in a dedicated section. Microstructure evolution under ion irradiation will be characterized for each selected irradiation condition. Link between local chemical heterogeneities and defect crystallography will intend to be established to identify RIS mechanisms involved and complementary investigation will be proposed. Finally, the contribution of correlative microscopy to the present work will be discussed and improvements will be proposed regarding new advances on specimen preparation, data acquisition and data treatment.

The document will end with a conclusion and perspectives of this work.

CHAPTER 1

BIBLIOGRAPHIC REVIEW

I. Understanding and mitigating performance issues of austenitic stainless steels components in nuclear reactors.....	6
II. Microstructure evolution after thermal ageing.....	9
1. Austenite stability.....	9
2. Vacancy mediated substitutional diffusion.....	10
3. Precipitation	22
III. Microstructure evolution after ageing under irradiation	26
1. Neutron production and transmutations in nuclear reactors	26
2. Collision event and radiation damage.....	27
3. Radiation enhanced and modified diffusion: 4 regimes	29
4. Emulate neutrons with ions	30
5. Effect of radiation damage on resulting microstructure and microchemistry.....	32
5.1. Black dots.....	32
5.2. Stacking fault tetrahedra.....	32
5.3. Cavities.....	33
5.4. Dislocation loops and dislocation network evolution	35
5.5. Radiation induced segregation.....	36
5.6. Phase stability under irradiation	45
IV. Prediction of microstructural evolution up to 60 years of irradiation: focus on RIS.....	52
1. By the experimental determination of interdiffusion kinetics to improve diffusion of point defect models under irradiation in austenitic Fe-Ni-Cr system	53
2. Quantifying segregation levels on biased sinks by implementing recent development in terms of nanoscale characterisations on a 316L(N) austenitic stainless steel.	53

In the alarming context of climate change, nuclear power energy source is considered as part of the decarbonised electricity generation mix. Another requirement is economical. In order to provide low-cost and low-emission nuclear energy, long-term operation (LTO) of existing nuclear power plants is included in the strategy. Ensure a safe life extension asks for extra investigations on corrosion and neutron-induced materials degradation phenomena under an in-service severe environment. LTO allows existing nuclear light water reactors (e.g. Pressurized Water Reactors) to operate for a further 20 years beyond their initial 40-year operating licence period. An improved understanding of the synergistic fundamental mechanisms involved in microstructural evolutions under long term ageing is a concern for austenitic stainless steels structural core components which will experience higher irradiation doses both for LTO and GEN-IV 60-years concepts of reactors. In addition, next generations of reactors will operate at higher temperatures. A potential consequence of higher damage levels and higher operating temperatures is the appearance of new or unanticipated degradation modes.

Assess, understand and mitigate ageing performance issues of austenitic stainless steels structural core materials is a need for R&D of both existing and future nuclear reactors. Reliable predictive physical-based models should therefore be built to anticipate the maximum operating time of replaceable and non-replaceable components, in the scope of maintenance costs reduction and reactor lifetime definition [1].

I. Understanding and mitigating performance issues of austenitic stainless steels components in nuclear reactors

Austenitic stainless steels are widely employed for nuclear applications in current commercial reactors, e.g. Pressurized Water Reactors (PWR), they also appear to be good candidates for advanced nuclear systems, e.g. Sodium-cooled Fast Reactors (SFR) and are considered for fusion reactors [2].

It turns out that austenitic stainless steels demonstrate good mechanical and physical properties: they combine strength and ductility at both high and low temperatures, an excellent fatigue resistance and relatively good creep resistance. Furthermore, these materials are non magnetic, have a good thermal conductivity, are highly weldable and corrosion resistant. Thus, they had been selected as structural materials for components close to the core such as internals (e.g. 304L, 316L) for PWR and for the majority of the I^{ary} circuit components (i.e. 316L(N)) of future SFR. In this reactor, they are also candidates for fuel claddings (Austenitic Improved Material 1). In France, their chemical compositions are specified by RCC-M and RCC-MRx codes for nuclear reactors design of second and fourth generation respectively. They are listed in Table 1, except from AIM1 which is not qualified yet.

Table 1 - Chemical composition specifications* of the most common austenitic stainless steels (in wt.% - Fe bal.)

ASS	C	N	Mn	Si	Cr	Ni	Mo	P	Ti	Cu	B	S
304 304L	<0.08/ <0.03	<0.08	<2.0	<1.0	18.5- 20.0	9.0- 10.0	-	<0.045	-	<1	-	<0.03
316 316L	<0.08/ <0.03	<0.06	<2.0	<1.0	16.5- 18.5	10.0- 13.0	2.25- 2.75	<0.040	-	<1	-	<0.03
316L(N)	<0.03	0.06- 0.08	1.6-2.0	<0.5	17.0- 18.0	12.0- 12.5	2.30- 2.70	<0.030	-	<1	<0.002	<0.015
AIM1 [1]	0.08- 0.10	-	1.0-2.0	0.7-0.9	14.0- 16.0	14.0- 16.0	1.30- 1.70	0.030- 0.050	0.3-0.5	-	0.004- 0.008	-

* Cobalt content depends on the nuclear class of the component to limit activation and embrittlement : <0.2% for class 1, <0.05% for class 2, <0.001% for class 3.

Austenitic stainless steels are austenitic (γ) Fe-Ni-Cr rich alloys with a Face Centered Cubic (FCC) close-packed structure. After solution annealing (typically 30min - 1h at 1000 - 1200°C) followed by water quenching, their microstructure shows large grains ($\sim 50 \mu\text{m}$) of austenite. Small amount of δ -ferrite and inclusions can remain. They are stainless because their Cr contents greater than 11 wt.% render them a good corrosion resistance by surface passivation. Finally, they are steels because they are iron-based and contain carbon. L is added to grade names when the carbon content is low (< 0.03 wt.%).

Each solute element of austenitic stainless steels affects the microstructure and resulting properties. Ni, Mn, Co, Cu, C and N are γ stabilizers whereas Cr, Mo and Si tend to form ferrite. Nb and Ti are strong carbide and nitride formers. These types of carbides/nitrides cannot be totally dissolved in austenite during solution annealing if their concentrations exceed several tenth of wt.%. Carbide and/or nitride precipitation leads to precipitation strengthening. Addition of Mo will strengthen solid solution.

Solution and precipitation hardening are methods to improve the creep strength of austenitic stainless steels but usually austenitic stainless steels are not precipitation strengthened steels. Cold working (up to 30%) is a way to improve mechanical properties at the as-received state. Dislocation density can arise from $\sim 10^{12}$ for solution annealed austenitic stainless steels to 10^{15} to 10^{16} m^{-2} after cold working [3].

In operation, austenitic stainless steels structural materials will be subjected to low or intermediate temperatures, irradiation, static or cyclic stresses within a corrosive environment during tens of years (Table 2). Under these harsh conditions for components in service, the metastable austenite will evolve, deteriorating their fracture properties and will therefore limit components lifetime.

Degradation of austenitic stainless steels components can lead to reduced performance and, in some cases, unexpected failure. In normal operating conditions of Reactor Pressured Vessel (RPV) internals, temperature of some components can locally reach 380°C due to gamma heating and dose as high as 80 dpa. These conditions will lead to hardening and embrittlement. Adding the corrosive

environnement and stress, cracks can appear due to IASCC and fracture of components as baffle-former bolts.

Table 2 - PWR and SFR systems operation conditions and performance issues of austenitic stainless steels [2]. Coolants are water and sodium respectively.

System	Coolant inlet temperature (°C)	Coolant outlet temperature (°C)	Maximum dose (dpa*)	Pressure (MPa)	Main degradation mechanisms
PWR (GEN II)	290	320	100	16	IASCC ¹ , ageing under irradiation, thermal ageing, fatigue
SFR (GENIV)	370	550	200	0.1	+ swelling and irradiation creep

* displacement per atom. Dose unit defined and used by the nuclear material community to quantify and compare radiation damage from different radiation sources. N dpa means that each atom of the target material have been displaced N times from its lattice site.

Origins of mechanical properties deteriorations under irradiation are attributed to nano-scale changes within the microstructure such as defects nature, size, density and chemistry. Local chemical evolution at defects vicinity is attributed to solutes segregation. This phenomenon is known as radiation-induced segregation (RIS). While numerous experimental studies attend to validate identified RIS mechanisms, accurately predict RIS levels for various types of radiation-induced defects stays a key challenge to take up for lifetime extension purposes.

As temperature coupled with irradiation activate RIS, one should first understand how temperature influences solute transport in solids (i.e. thermal diffusion) and the consequences of long term thermal ageing on austenitic stainless steels microstructure modification (e.g. precipitation). Then a litterature review of radiation damage theory will help to understand how it affects both diffusion and microstructure depending on the applied conditions. Finally, focus will be made on RIS and precipitation under irradiation.

¹ Irradiation-Assisted Stress Corrosion Cracking (IASCC) is the premature failure of an alloy in the presence of a mechanical stress and an aggressive environment under irradiation, cracks typically propagate along grain boundaries.

II. Microstructure evolution after thermal ageing

Austenite is metastable at the operation temperatures of nuclear reactors. Especially for SFR where components could be subjected to higher ones. Under long term thermal ageing, the initial microstructure will evolve to tend to thermodynamic equilibrium.

1. Austenite stability

Stability of a system at a constant pressure is defined by the value of Gibbs free energy G . Any change/transformation in the system is possible when it results in a state with lower free energy. $\Delta G < 0$, with:

$$\Delta G = \Delta H - T\Delta S \quad (1)$$

where ΔH is the enthalpy variation, ΔS the entropy variation and T the temperature.

This minimum of energy is called the thermodynamic equilibrium. Phase diagrams give the stable phases at a given temperature predicted by thermodynamics. For simplification purpose, ternary systems representative of austenitic stainless steels nuclear grades are: Fe-20Cr-10Ni (for 304 SS) and Fe-18Cr-12Ni (for 316 SS). At thermodynamic equilibrium, in these particular model alloys, the microstructure should present two phases: austenite and ferrite (Figure 1.A) and Table 3). However, to obtain the required mechanical properties, commercial austenitic stainless steels are composed of a lot of alloying elements in addition to Ni and Cr as shown in Table 1. They can be classified as austenite or ferrite stabilizers and are expressed in terms of Ni and Cr equivalent concentrations. Pryce-Andrews diagram is not based on thermodynamics but predicts phase occurrence at room temperature in stainless steels after solution annealing followed by water quenching (Figure 1.B)). At this metallurgical state, 304 and 316-grades are almost fully austenitic and contain a small volume fraction of δ ferrite. Because of the quenching, alloying elements are supersaturated in the austenitic solid solution. In the operating temperature range of nuclear reactors (300-550°C), most of alloying elements concentrations are over their solubility limit resulting on precipitate nucleation. Precipitate growth is a kinetical process based on the diffusion of chemical species.

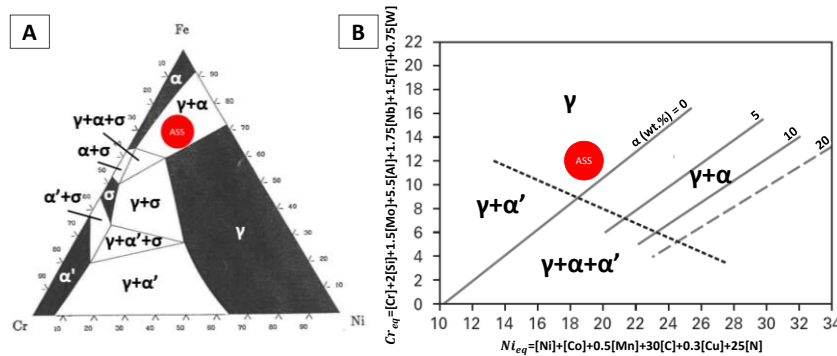


Figure 1 – A) Isothermal section of the FeNiCr ternary phase diagram at 400°C [4] and B) Pryce-Andrews diagram. Austenitic stainless steels 304 and 316-grades domain is represented in red, concentrations are in weight.%.

Table 3 – Austenite and ferrite characteristics. The reference number of the phase in COD crystallographic database is also given.

Nature <i>COD</i>	Major elements / Composition	Crystallographic Structure	Orientation relationship with the matrix
Austenite (γ) <i>9015071</i>	Fe-Cr-Ni	FCC Fm-3m (225) a=3.598 Å	-
Ferrite (α or δ) <i>9000657</i>	Fe-Cr-Mo	BCC Im-3m (229) a=2.866 Å	<u>Bain</u> : $\{001\}_{\alpha} \{001\}_{\gamma}$, $\langle 011 \rangle_{\alpha} \langle 001 \rangle_{\gamma}$, $\langle 001 \rangle_{\alpha} \langle 011 \rangle_{\gamma}$ <u>K-S</u> : $\{011\}_{\alpha} \{111\}_{\gamma}$, $\langle 111 \rangle_{\alpha} \langle 011 \rangle_{\gamma}$, $\langle 112 \rangle_{\alpha} \langle 112 \rangle_{\gamma}$ <u>N-W</u> : $\{011\}_{\alpha} \{111\}_{\gamma}$, $\langle 001 \rangle_{\alpha} \langle 011 \rangle_{\gamma}$, $\langle 011 \rangle_{\alpha} \langle 112 \rangle_{\gamma}$, <u>G-T</u> : $\{011\}_{\alpha} \{111\}_{\gamma}$ (1°) , $\langle 011 \rangle_{\alpha} \langle 112 \rangle_{\gamma} (2^{\circ})$ <u>Pitsch</u> : $\{011\}_{\alpha} \{001\}_{\gamma}$, $\langle 111 \rangle_{\alpha} \langle 011 \rangle_{\gamma}$, $\langle 112 \rangle_{\alpha} \langle 011 \rangle_{\gamma}$

2. Vacancy mediated substitutional diffusion

In periodically arranged crystals, atomic diffusion consists in random jumps between vacancies (vacant sites) and atoms of the lattice. Thermal vacancies are created when atoms diffuse from the interior of a crystal to the free surface, leaving behind vacant lattice sites by the Schottky mechanism (Figure 2).

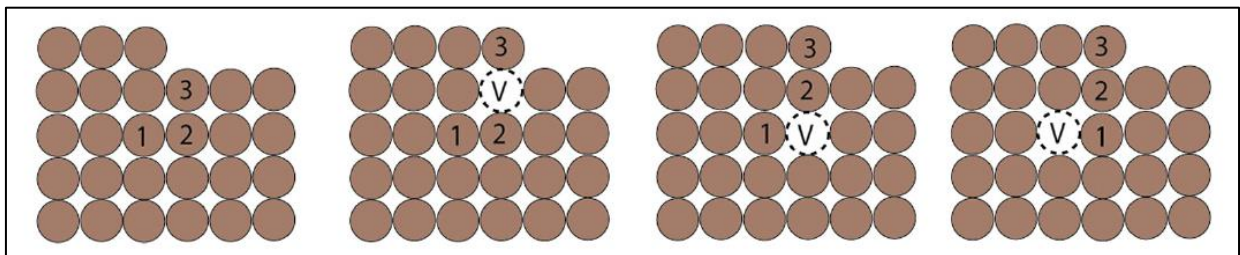


Figure 2 - Scheme of the formation a vacancy by the Schottky mechanism [5]

As diffusion is a thermally activated process, diffusion kinetics, expressed in term of diffusion coefficient, D obviously depends on the temperature, T and follows the general Arrhenius law:

$$D = D_0 e^{-Q/k_B T} \quad (2)$$

where D_0 is the frequency factor, Q is the activation energy and k_B is the Boltzmann constant. But it also depends on the local alloy composition, the crystallographic structure, internal or external stresses and the defects population (dislocations, grain boundaries, precipitate interface and free surfaces). Diffusion can occur in the absence, where components diffuse randomly, or in the presence of driving forces. Here, diffusion becomes driving force direction-dependant generating a flux of species. One can distinguish internal and external driving forces. The most common is the chemical (or thermodynamic) internal driving force created by a gradient of chemical potential. Temperature or stress gradients are examples of external driving forces which can be applied to the system. They won't take part in the following discussion. Depending on the studied system, different diffusion coefficients can be defined. They are presented in the form $D_{\text{solvent}}^{\text{solute}}$. Definitions of the most frequently encountered diffusion coefficients are expressed both for binary (A-B) and ternary (A-B-C) systems, details of demonstrations are available in referenced books [5–9].

In a two-component system A-B, diffusion coefficients are defined as follows:

- A in A, absence of thermodynamic driving forces (random atomic jumps)

Self-diffusion coefficient D_A^A : Self-diffusion is the diffusion of A atom into A matrix, just because of thermal vibration and in the absence of any other internal or external driving forces. It depends on the crystal structure and the temperature. Self-diffusion coefficient is given by the expression:

$$D_A^A = D_V c_V^{eq} = g a^2 \omega c_V^{eq} \quad (3)$$

where a is the lattice parameter, ω is the atomic jump frequency, g is a geometrical factor depending on the lattice and the defect type ($g=1$ for a monovacancy in FCC lattice). D_V is the vacancy diffusion coefficient and can be expressed thanks to an Arrhenius law where the activation energy is the Gibbs free energy of migration of vacancies ΔG_v^m :

$$D_V = D_0 e^{-\Delta G_v^m / k_B T} \quad (4)$$

c_V^{eq} is the vacancy mole fraction at equilibrium, the formation of vacancies depends on the Gibbs free energy ΔG_v^f :

$$c_V^{eq} = e^{-\Delta G_v^f / k_B T} \quad (5)$$

k_B is the Boltzmann constant and T the temperature. From this equation, it can be understood that vacancy equilibrium concentration rises with the temperature as well as their mobility - Eq. (4). Vacancies are more numerous and are more mobile when the temperature increases, vacancy mediated substitutional diffusion rate will be enhanced at elevated temperatures.

Radiotracer diffusion coefficient $D_A^{A^*}$: A way to deduce experimentally the self-diffusion coefficient is to follow the diffusion path of a radiotracer. A single vacancy is free to exchange position with any of the host atoms A or radioisotope A* surrounding. There are almost equal probabilities to exchange positions since the effect of mass difference of radiotracer and other components is very small. The correlation factor f is purely linked with the crystallographic structure of the system in this case.

$$D_A^{A^*} \approx f D_A^A \quad (6)$$

f is equal to 0.78 in FCC lattices.

- A in B, absence of thermodynamic driving forces

Solute (or impurity) diffusion coefficient D_A^B : In a substitutional alloy, A and B occupy sites of the same lattice. If the solute B is infinitely diluted in a solvent A, the probability of a vacancy to be present on a neighbouring site of a solute atom or of a solvent atom is not the same. The solute-vacancy pair interaction energy $\Delta G_{B(A)}^f$ is introduced. The resulting diffusion coefficient is:

$$D_A^B = f_2 D_V c_V^{eq} = f_2 g a^2 \omega_2 e^{\left(\frac{\Delta G_{B(A)}^f}{k_B T} \right)} c_V^{eq} \quad (7)$$

Here, the correlation factor f_2 and the atomic jump frequency ω_2 are different than in a pure metal A.

Solute and solute tracer diffusion coefficients are similar because the difference in mass is only one or two neutrons between them:

$$D_A^B \approx D_A^{B^*} \quad (8)$$

Radiotracers experiments consist in depositing a thin layer of radiotracers at the surface of a material (e.g. pure metal, binary alloy, commercial alloy) and follow tracers penetration within the host material after thermal annealing. Thus, they are not infinitely dilute in the material when the experiment starts at the vicinity of interface and gradient of chemical potential will be created. Nevertheless, if the deposited layer is thin enough compared with the diffusion length, gradient of chemical potential is neglected because the source of solute atoms is so limited that it tends to an infinite solute dilution.

- A in B, presence of thermodynamic driving forces

When the deposited layer is thicker or when two metals of different A-B compositions are coupled, the resulting chemical potential gradient cannot be neglected. The presence of driving force makes the jump rate of atoms higher in one particular direction. When two alloys are coupled together and show a difference in chemical potentials or activity of the components involved in both couples, a chemical potential gradient exist. This chemical potential gradient will drive interdiffusion (i.e.

mixing) of the species from a couple to the other to reach the thermodynamic (here chemical) equilibrium. The chemical potential of a particular element is defined as follows:

$$\mu_i = \mu_i^0 + RT \ln a_i = \mu_i^0 + RT \ln(X_i \gamma_i) \quad (9)$$

with R the gas constant, T the temperature, μ_i^0 the chemical potential of the component i at the standard state (25°C and 1 atmospheric pressure), X_i its mole fraction, a_i its activity and γ_i the activity coefficient of component i. For an ideal solid solution (i.e. following Raoult's law), $a_i = X_i$ and $\gamma_i=1$. In a real solid solution, γ_i deviates from 1 and $\gamma_i \rightarrow 1$ as T increase. If $\gamma_i=1$ (i.e. case of an ideal solid solution) the system tends to homogenise, $\gamma_i > 1$ for an endothermic mixing it will provoke phase separation and $\gamma_i < 1$ for an exothermic mixing it will lead to ordering.

In the presence of a chemical potential gradient, components diffuse generally down the chemical concentration gradient (negative sign) as expressed by the Fick's 1st law:

$$\vec{J} = -D \nabla \tilde{c} \quad (10)$$

When diffusion occurs, species fluxes from the two coupled material will mix solutes inside an interdiffusion zone. In a binary alloy, there is a single interdiffusion coefficient \tilde{D} that characterises interdiffusion, it is composition-dependent. However, diffusion kinetics of the two components taken apart are different. Consequently, two diffusion coefficients are defined as the intrinsic diffusion coefficients D_i , they depend on their local chemical environment. A atoms will diffuse towards the region with the poorest A content and contrariwise for B. As diffusion is vacancy mediated, if A atoms diffuse faster than B ones, this difference in diffusion kinetics give rise to a vacancy flux in the direction B flux called the vacancy wind and provoke a movement of the interface in the sample frame (i.e. Kirkendall effect). Contrarily to \tilde{D} , intrinsic diffusion coefficients are defined relatively to the lattice frame which is fixed to the crystal lattice and can move relative to the sample frame with a certain velocity.

Intrinsic diffusion coefficient D_A and D_B : According to Darken, intrinsic diffusion coefficients are related to the tracer diffusion coefficients in a binary A–B system by:

$$D_A = D_{AB}^{A*} \Phi \quad \text{and} \quad D_B = D_{AB}^{B*} \Phi \quad (11)$$

Φ is the thermodynamic factor. In the case of a binary system, Gibbs-Duhem relation of thermodynamics demonstrates that it is the same for both components:

$$\Phi = \frac{d \ln a_A}{d \ln X_A} = \frac{d \ln a_B}{d \ln X_B} = 1 + \frac{d \ln \gamma_A}{d \ln X_A} = 1 + \frac{d \ln \gamma_B}{d \ln X_B} \quad (12)$$

Where γ_A and γ_B are the activity coefficient of each component.

D_i , D_{AB}^{i*} and Φ (i=A or B) are composition dependant. It should be pointed out that, when $X_B \rightarrow 0$, $D_{B(0)}^I = D_A^{B*}$ because $\Phi \rightarrow 1$.

When diffusion is controlled by a vacancy mechanism, the flow of matter in one direction will be balanced by a flow of vacancies in the opposite direction, called the vacancy wind. In Darken's approximation, the vacancy wind effect is not considered leading to an overestimation of diffusion kinetics of faster diffusing component and an underestimation of the slower diffusion component. To include this effect, Manning introduced the s_i and S parameters respectively the individual and the total vacancy wind correction factors. Darken-Manning equations for intrinsic diffusion coefficients are given by:

$$\begin{cases} D_A = D_{AB}^{A*} \Phi s_A \\ D_B = D_{AB}^{B*} \Phi s_B \end{cases} \quad (13)$$

with

$$\begin{cases} s_A = 1 + \frac{(1-f)}{f} \frac{X_A(D_{AB}^{A*} - D_{AB}^{B*})}{X_A D_{AB}^{A*} + X_B D_{AB}^{B*}} \\ s_B = 1 + \frac{(1-f)}{f} \frac{X_A(D_{AB}^{B*} - D_{AB}^{A*})}{X_A D_{AB}^{A*} + X_B D_{AB}^{B*}} \end{cases} \quad (14)$$

where f is the correlation factor.

Interdiffusion coefficient \tilde{D}_{AB} : This coefficient measures the mixing rate inside the interdiffusion zone of a diffusion couple A/B. The Darken-Manning equation expresses the interdiffusion coefficient as follows:

$$\tilde{D}_{AB} = X_B D_A + X_A D_B = (X_B D_{AB}^{A*} + X_A D_{AB}^{B*}) \Phi S \quad (15)$$

here,

$$S = 1 + \frac{(1-f)}{f} \frac{X_A X_B (D_{AB}^{A*} - D_{AB}^{B*})^2}{(X_A D_{AB}^{A*} + X_B D_{AB}^{B*})(X_A D_{AB}^{B*} + X_B D_{AB}^{A*})} = 1 + \frac{2X_A X_B (D_{AB}^{A*} - D_{AB}^{B*})^2}{M_0 (X_A D_{AB}^{A*} + X_B D_{AB}^{B*})(X_A D_{AB}^{B*} + X_B D_{AB}^{A*})} \quad (16)$$

where $M_0 = 2f/(1-f)$ in FCC crystal is 7.15. If $D_{AB}^{A*}/D_{AB}^{B*} < 3$, $S < 1.07$ in a FCC structure and generally $\Phi \gg S$, in this case S can be neglected.

All the previously defined diffusion coefficients are summed up in Table 4.

Table 4 – Diffusion coefficients conventionally defined in pure and binary systems depending on the alloy concentration

System	Measured diffusion coefficient
Pure A	$D_A^A \approx f D_A^{A*}$
A-B and $C_B \rightarrow 0$	$D_{B(0)}^I = D_A^{B*}$
A-B concentrated alloy (diffusion couple)	$D_{AB}^{A*}, D_{AB}^{B*}, D_A, D_B, \tilde{D}_{AB}$
A-B and $C_A \rightarrow 0$	$D_{A(0)}^I = D_B^{A*}$
Pure B	$D_B^B \approx f D_B^{B*}$

Diffusion coefficients have the great advantage to be determined experimentally but they cannot be directly used to describe fluxes between species. Indeed, first Fick's law describes the linear relationship between fluxes and a measurable quantity, i.e. the concentration gradient, but the actual driving force for diffusion is the chemical potential gradient, $-\nabla\mu$. Onsager formalism has been proposed and linearly links fluxes and driving forces. The generalized flux equation is:

$$J_i = \sum_{j=1}^n L_{ij} X_j \quad (17)$$

where J_i is the fluxes matrix, L_{ij} the phenomenological coefficients of the Onsager matrix L and X_j is the driving force matrix. If the system is only constrained by internal thermodynamic driving forces (no external driving forces are applied to the system), hence $X = -\nabla\mu$. As under thermal ageing the vacancy concentration is at equilibrium, $-\nabla\mu_V = 0$.

Self-diffusion coefficient of A in pure A is related to Onsager coefficient this way:

$$D_A^A = \frac{L_{AA}}{X_A} k_B T \quad (18)$$

Therefore, diffusion coefficients are dependent on their local environment in terms of concentration and temperature. Contrarily to Onsager coefficients, coupling between fluxes cannot be uncorrelated. As phenomenological coefficients are purely kinetic quantities, they are used to model diffusion processes.

Because the phenomenological coefficients are not directly obtained experimentally, relations with the measurable diffusion coefficients have been established:

$$D_A^{A*} = \left[1 - \frac{L_{AA^*}}{L_{AA}} \frac{X_A}{X_{A^*}} \right] D_A^A \quad (19)$$

$$\begin{cases} D_A = \frac{L_{AA}}{X_A} \left(1 - \frac{L_{AB} X_A}{L_{AA} X_B} \right) k_B T \Phi \\ D_B = \frac{L_{BB}}{X_B} \left(1 - \frac{L_{AB} X_B}{L_{BB} X_A} \right) k_B T \Phi \end{cases} \quad (20)$$

Austenitic stainless steels can be either modelled by Ni-Cr binary or Fe-Ni-Cr ternary systems. In a N-ary system, N^2 L_{ij} exist. The diagonal terms describe the transport of one particular specie due to its own chemical potential gradient, whereas the off-diagonal terms describe how the chemical potential gradient of one specie can give rise to a flux of other species. Thanks to the Onsager reciprocity theorem, it is postulated that the L matrix is symmetric, $L_{ij} = L_{ji}$, hence $\frac{N^2 + N}{2}$ L_{ij} are independent.

In the case of interdiffusion for an A-B-C ternary system, the fluxes of chemical species can be expressed as a function of the 6 phenomenological coefficients (i.e. reciprocity) and the gradients of chemical potentials as follows:

$$\begin{cases} \vec{J}_A = -L_{AA}\nabla\vec{\mu}_A - L_{AB}\nabla\vec{\mu}_B - L_{AC}\nabla\vec{\mu}_C \\ \vec{J}_B = -L_{AB}\nabla\vec{\mu}_A - L_{BB}\nabla\vec{\mu}_B - L_{BC}\nabla\vec{\mu}_C \\ \vec{J}_C = -L_{AC}\nabla\vec{\mu}_A - L_{BC}\nabla\vec{\mu}_B - L_{CC}\nabla\vec{\mu}_C \end{cases} \quad (21)$$

They also can be written as a function of the 9 intrinsic diffusion coefficients in the lattice frame:

$$\begin{cases} \vec{J}_A = -D_{AA}\nabla\vec{c}_A - D_{AB}\nabla\vec{c}_B - D_{AC}\nabla\vec{c}_C \\ \vec{J}_B = -D_{BA}\nabla\vec{c}_A - D_{BB}\nabla\vec{c}_B - D_{BC}\nabla\vec{c}_C \\ \vec{J}_C = -D_{CA}\nabla\vec{c}_A - D_{CB}\nabla\vec{c}_B - D_{CC}\nabla\vec{c}_C \end{cases} \quad (22)$$

As $\nabla\vec{c}_C = -\nabla\vec{c}_A - \nabla\vec{c}_B$, one component, e.g. C (generally the main element), can be taken as the dependent one in order to simplify Eq. (22) and reduce the number of intrinsic diffusion coefficients to 6:

$$\begin{cases} \vec{J}_A = -D_{AA}^C\nabla\vec{c}_A - D_{AB}^C\nabla\vec{c}_B \\ \vec{J}_B = -D_{BA}^C\nabla\vec{c}_A - D_{BB}^C\nabla\vec{c}_B \\ \vec{J}_C = -D_{CA}^C\nabla\vec{c}_A - D_{CB}^C\nabla\vec{c}_B \end{cases} \quad (23)$$

and $D_{ij}^C = D_{ij} - D_{ic}$ with $j \neq C$.

Thanks to this approach, in a N-ary alloy $(N-1)^2 \tilde{D}_{ij}$ have to be determined. The fluxes of the two minor elements (A and B) in the sample frame can be written as a function of the 4 independent interdiffusion coefficients \tilde{D}_{ij}^k (i,j=A,B and k=C) for a ternary system since $J_A + J_B + J_C = 0$, $\tilde{D}_{AA}^C + \tilde{D}_{BA}^C + \tilde{D}_{CA}^C = 0$ and $\tilde{D}_{AB}^C + \tilde{D}_{BB}^C + \tilde{D}_{CB}^C = 0$:

$$\begin{cases} \vec{J}_A = -\tilde{D}_{AA}^C\nabla\vec{c}_A - \tilde{D}_{AB}^C\nabla\vec{c}_B \\ \vec{J}_B = -\tilde{D}_{BA}^C\nabla\vec{c}_A - \tilde{D}_{BB}^C\nabla\vec{c}_B \end{cases} \quad (24)$$

and $\vec{J}_C = -\tilde{D}_{CA}^C\nabla\vec{c}_A - \tilde{D}_{CB}^C\nabla\vec{c}_B$ is deduced.

It had been shown [10] that under thermodynamic and kinetics restrictions, \tilde{D}_{ij}^k have to comply to the next relations:

$$\begin{cases} \tilde{D}_{AA}^C + \tilde{D}_{BB}^C > 0 \\ \tilde{D}_{AA}^C\tilde{D}_{BB}^C - \tilde{D}_{AB}^C + \tilde{D}_{BA}^C > 0 \\ (\tilde{D}_{AA}^C + \tilde{D}_{BB}^C)^2 > 4(\tilde{D}_{AA}^C\tilde{D}_{BB}^C - \tilde{D}_{AB}^C\tilde{D}_{BA}^C) \end{cases} \quad (25)$$

and,

$$\tilde{D}_{AA}^C > 0 \quad \tilde{D}_{BB}^C > 0 \quad \tilde{D}_{AB}^C\tilde{D}_{BA}^C > 0 \quad (26)$$

\tilde{D}_{AB}^C and \tilde{D}_{BA}^C can be either positive or negative.

Whatever the element put in superscript, thanks to these subsequent relationships, every interdiffusion coefficient can be deduced from the four experimentally determined ones:

$$\begin{aligned}
\tilde{D}_{AA}^B &= \tilde{D}_{AA}^C - \tilde{D}_{AB}^C & \tilde{D}_{AC}^B &= -\tilde{D}_{AB}^C & \tilde{D}_{CA}^B &= \tilde{D}_{BB}^C + \tilde{D}_{AB}^C - \tilde{D}_{AA}^C - \tilde{D}_{BA}^C & \tilde{D}_{CC}^B &= \tilde{D}_{BB}^C - \tilde{D}_{AB}^C \\
\tilde{D}_{BB}^A &= \tilde{D}_{BB}^C - \tilde{D}_{BA}^C & \tilde{D}_{BC}^A &= -\tilde{D}_{BA}^C & \tilde{D}_{CB}^A &= \tilde{D}_{AA}^C + \tilde{D}_{BA}^C - \tilde{D}_{BB}^C - \tilde{D}_{AB}^C & \tilde{D}_{CC}^A &= \tilde{D}_{AA}^C - \tilde{D}_{BA}^C
\end{aligned} \tag{27}$$

As shown for the binary system, it is possible to link tracer diffusion coefficients (i.e. diffusion of A*, B* or C* tracers in a matrix ABC) to the interdiffusion coefficients [11,12]:

$$\begin{bmatrix} \tilde{D}_{AA}^C & \tilde{D}_{AB}^C \\ \tilde{D}_{BA}^C & \tilde{D}_{BB}^C \end{bmatrix} = \begin{bmatrix} S_{AA} \tilde{d}_{AA}^C & S_{AB} \tilde{d}_{AB}^C \\ S_{BA} \tilde{d}_{BA}^C & S_{BB} \tilde{d}_{BB}^C \end{bmatrix} \begin{bmatrix} \Phi_{AA} & \Phi_{AB} \\ \Phi_{BA} & \Phi_{BB} \end{bmatrix} \tag{28}$$

where

$$\begin{cases} \tilde{d}_{AA}^C = D_{ABC}^{A*} - X_A D_{ABC}^{A*} + X_A D_{ABC}^{C*} \\ \tilde{d}_{AB}^C = -X_A D_{ABC}^{B*} + X_A D_{ABC}^{C*} \\ \tilde{d}_{BA}^C = -X_B D_{ABC}^{A*} + X_B D_{ABC}^{C*} \\ \tilde{d}_{BB}^C = D_{ABC}^{B*} - X_B D_{ABC}^{B*} + X_B D_{ABC}^{C*} \end{cases} \tag{29}$$

with S_{ij} the vacancy wind terms as defined by Manning,

$$\begin{cases} S_{AA} = 1 + \frac{2X_A(X_B(D_{ABC}^{A*} - D_{ABC}^{B*}) + X_C(D_{ABC}^{A*} - D_{ABC}^{C*}))(D_{ABC}^{A*} - D_{ABC}^{C*})}{M_0((1 - X_C)D_{ABC}^{A*} + X_A D_{ABC}^{C*})(X_A D_{ABC}^{A*} + X_B D_{ABC}^{B*} + X_C D_{ABC}^{C*})} \\ S_{AB} = 1 + \frac{2}{M_0} \left(1 - \frac{D_{ABC}^{A*}}{X_A D_{ABC}^{A*} + X_B D_{ABC}^{B*} + X_C D_{ABC}^{C*}} \right) \\ S_{BA} = 1 + \frac{2}{M_0} \left(1 - \frac{D_{ABC}^{B*}}{X_A D_{ABC}^{A*} + X_B D_{ABC}^{B*} + X_C D_{ABC}^{C*}} \right) \\ S_{BB} = 1 + \frac{2X_B(X_A(D_{ABC}^{B*} - D_{ABC}^{A*}) + X_C(D_{ABC}^{B*} - D_{ABC}^{C*}))(D_{ABC}^{B*} - D_{ABC}^{C*})}{M_0((1 - X_C)D_{ABC}^{B*} + X_B D_{ABC}^{C*})(X_A D_{ABC}^{A*} + X_B D_{ABC}^{B*} + X_C D_{ABC}^{C*})} \end{cases} \tag{30}$$

and Φ_{ij} are the thermodynamic factors [12],

$$\begin{cases} \Phi_{AA} = \left(\frac{\partial \ln a_A}{\partial \ln X_A} \right)_{p,T,X_B} \\ \Phi_{AB} = \left(\frac{\partial \ln a_A}{\partial \ln X_B} \right)_{p,T,X_A} \\ \Phi_{BA} = \left(\frac{\partial \ln a_B}{\partial \ln X_A} \right)_{p,T,X_B} \\ \Phi_{BB} = \left(\frac{\partial \ln a_B}{\partial \ln X_B} \right)_{p,T,X_A} \end{cases} \tag{31}$$

Only three of these thermodynamic factors are independent because they are related to the fourth one as follows:

$$\Phi_{BA} = \frac{X_A}{(1 - X_A)} \left[\frac{(1 - X_B)}{X_B} \cdot \Phi_{AB} + \Phi_{BB} - \Phi_{AA} \right] \quad (32)$$

All the previously defined diffusion coefficients for a ternary system are summed up in Table 5.

Table 5 – Diffusion coefficients conventionally defined for a ternary system depending on the alloy concentration (SS here stands for solid solution)

System	Measured diffusion coefficient
A* in A-B-C SS	D_{ABC}^{A*}
B* in A-B-C SS	D_{ABC}^{B*}
C* in A-B-C SS	D_{ABC}^{C*}
A-B-C concentrated alloy (diffusion couple)	$D_{AA}^C, D_{AB}^C, D_{BA}^C, D_{BB}^C, D_{CA}^C, D_{CB}^C$ $\tilde{D}_{AA}^C, \tilde{D}_{AB}^C, \tilde{D}_{BA}^C, \tilde{D}_{BB}^C$

From Eq. (15) and (16) for a binary system and from Eq. (28) to (32) for a ternary system, by knowing the radiotracer diffusion coefficients of all components of a binary or a ternary system for a particular composition of the matrix and by calculating thermodynamic factors one is able to predict interdiffusion coefficients. These latter will be experimentally determined in this work.

In a N-ary system, a (N-1)x(N-1) matrix of thermodynamic factor is defined as follows [13]:

$$\Phi_{ij} = \delta_{ij} + X_i \frac{\partial \ln \gamma_i}{\partial X_j} \quad (33)$$

with δ_{ij} the Kronecker delta, i,j=A, B,...,n-1 and the thermodynamic matrix is linked to the gradient of chemical potential $\nabla \vec{\mu}_i$ by this relation:

$$\frac{X_i}{RT} \nabla \vec{\mu}_i = \sum_{j=1}^{n-1} \Phi_{ij} \nabla \vec{X}_j \quad (34)$$

Chemical potentials can be obtained via thermodynamic calculations thanks to the CALPHAD method [14] and permits to calculate the thermodynamic factors.

For austenitic stainless steels model alloys, most of the tracer diffusion coefficients are obtained at high temperature for bulk diffusion, well much higher than the operating temperatures of PWR or SFR (between 300 and 550°C). There is therefore a real lack of data within this temperatures range and diffusion coefficients are generally extrapolated from high temperatures. The database extracted from the literature is presented in Table 6 for the Ni-Cr system, then in Table 7 for the Fe-Ni-Cr system. Data available for all components within a system have been selected only. Most authors agree on the fact that $D_{NiCr}^{Cr*} > D_{NiCr}^{Ni*}$ in Ni-Cr and $D_{FeNiCr}^{Cr*} > D_{FeNiCr}^{Fe*} > D_{FeNiCr}^{Ni*}$ in Fe-Ni-Cr austenitic phase.

Table 6 – Arrhenius law parameters, see Eq. (2), of Ni and Cr tracer diffusion coefficients in Ni-Cr for extrapolation from high temperatures

Solid solution	Tracer X*	Temperature range (°C)	Frequency factor D^{X*}_0 (m ² /s)	Activation energy Q^{X*} (kJ/mol)	References
Ni-4.7Cr	⁵¹ Cr	950-1150	1.5×10^{-3}	301	[15]
	⁶³ Ni	950-1200	1.3×10^{-4}	280	[15]
Ni-14.3Cr	⁵¹ Cr	950-1150	5.8×10^{-4}	294	[15]
	⁶³ Ni	950-1200	2.3×10^{-4}	289	[15]
Ni-20Cr	⁵¹ Cr	900-1150	4.5×10^{-5}	255	[16]
	⁶³ Ni	950-1200	4.2×10^{-5}	264	[16]
Ni-22Cr	⁵¹ Cr	850-1200	6.1×10^{-5}	264	Dayananda (1979) from [17]
	⁶³ Ni	850-1200	1.5×10^{-5}	259	Dayananda (1979) from [17]
Ni-23.6Cr	⁵¹ Cr	950-1150	6.2×10^{-4}	296	[15]
	⁶³ Ni	950-1200	2.8×10^{-4}	293	[15]
Ni-29.4Cr	⁵¹ Cr	950-1150	3.0×10^{-4}	289	[15]
	⁶³ Ni	950-1200	1.0×10^{-4}	286	[15]
Ni-35Cr	⁵¹ Cr	890-1350	5.6×10^{-5}	262	[15,18]
	⁶³ Ni	950-1360	9.7×10^{-5}	276	[15,18]
Ni-38.4Cr	⁵¹ Cr	950-1150	2.2×10^{-4}	284	[15]
	⁶³ Ni	950-1200	1.4×10^{-4}	291	[15]
Ni-47.7Cr	⁵¹ Cr	950-1150	2.7×10^{-4}	284	[15]
	⁶³ Ni	950-1200	1.7×10^{-4}	289	[15]

Table 7 - Arrhenius law parameters of Fe, Ni and Cr tracer diffusion coefficients in Fe-Ni-Cr for extrapolation from high temperatures

Solid solution	Tracer X*	Temperature range (°C)	Frequency factor D^{X*}_0 (m ² /s)	Activation energy Q^{X*} (kJ/mol)	References
Fe-15Cr-20Ni	⁵⁹ Fe	960-1400	5.25×10^{-4}	308	[19]
	⁵¹ Cr	965-1400	8.27×10^{-4}	309	
	⁵⁷ Ni	960-1400	1.50×10^{-4}	300	
Fe-15Cr-45Ni	⁵⁹ Fe	960-1360	2.11×10^{-4}	288	[19]
	⁵¹ Cr	965-1365	4.00×10^{-4}	293	
	⁵⁷ Ni	960-1360	1.76×10^{-4}	295	
Fe-22Cr-45Ni	⁵⁹ Fe	960-1360	1.45×10^{-4}	286	[19]
	⁵¹ Cr	965-1365	4.10×10^{-4}	295	
	⁵⁷ Ni	960-1360	8.96×10^{-5}	289	
Fe-17Cr-12Ni	⁵⁹ Fe	600-1297	3.6×10^{-5}	280	[20]
	⁵¹ Cr	576-1295	1.3×10^{-5}	264	
	⁶³ Ni	603-1253	8.8×10^{-7}	251	[21]

Interdiffusion data in FCC Ni-Cr binary systems obtained by the diffusion couple method are presented Table 8. As in a binary alloy, only one interdiffusion coefficient have to be determined for a combination of composition and temperature, database covers a relatively large range of temperatures and compositions. However, in the case of ternary systems, accessible compositions are more numerous and the four interdiffusion coefficients for a certain composition and temperature are resolved at the intersection of two diffusion paths of two different diffusion couples.

Table 8 - Arrhenius law parameters, see Eq. (2), of interdiffusion coefficients in Ni-Cr for extrapolation from high temperatures

Solid solution	Temperature range (°C)	Frequency factor D_0 (m ² /s)	Activation energy Q (kJ/mol)	References
Ni-0.5Cr	1050-1375	5.97×10^{-4}	291	[22]
Ni-1Cr		4.94×10^{-4}	288	
Ni-1.5Cr		8.52×10^{-4}	287	
Ni-2Cr		4.66×10^{-4}	287	
Ni-2.5Cr		5.06×10^{-4}	288	
Ni-3Cr		5.32×10^{-4}	288	
Ni-3.5Cr		5.91×10^{-4}	289	
Ni-4Cr		5.97×10^{-4}	289	
Ni-4.5Cr		1.05×10^{-3}	296	
Ni-5Cr		6.61×10^{-4}	289	
Ni-5Cr	995-1300	1.14×10^{-4}	267	Ugaste (1967) from [17]
Ni-10Cr		1.34×10^{-4}	268	
Ni-15Cr		1.40×10^{-4}	268	
Ni-20Cr		1.46×10^{-4}	268	
Ni-30Cr		1.30×10^{-4}	268	
Ni-35Cr		1.60×10^{-4}	268	
Ni-40Cr		1.33×10^{-4}	268	
Ni-45Cr		8.06×10^{-5}	264	

Duh and Dayananda in 1985 [23] and Kale and al. in 1991 [24] have both determined interdiffusivities in various Fe-Ni-Cr FCC systems at only one temperature each, at 1100°C and 950°C respectively. Therefore, experimental results are missing to fit with an Arrhenius law. These authors observed that the cross coefficients (i.e. \tilde{D}_{CrNi}^{Fe} and \tilde{D}_{NiCr}^{Fe}) are either positive or negative and they are an order magnitude smaller than the main coefficients (i.e. \tilde{D}_{CrCr}^{Fe} and \tilde{D}_{NiNi}^{Fe}) meaning that the diffusional interactions between Ni and Cr are relatively small.

Both for binary and ternary system, authors [19,25–27] have shown that it is possible to extract fundamental parameters as the correlation factors, the atomic jump frequencies ratios (linked with the migration energy of vacancies) and the phenomenological coefficients from interdiffusion and tracers experiments. These are precious parameters to model processes driven by thermal diffusion but one should keep in mind that the experimentally determined coefficients all have been subjected to some approximations when fitted to the diffusion equations. The diffusion couple method, named Boltzmann-Matano, does not consider changes in the molar volume across the diffusion couple for example. Further, one should be aware of experimental sources of error associated with diffusion experiments.

The previous definitions introduced in this section are valid for bulk diffusion. However, in an alloy crystal defects such as grain boundaries, dislocations or free surfaces are always present and provide high-diffusivity paths or diffusion short-circuits as shown in Figure 3.A). In the case of tracer diffusion in polycrystals, an approximate expression for the effective diffusivity is given by:

$$D_{eff}^{A*} = gD_{GB}^{A*} + (1 - g)D_{Bulk}^{A*} \quad (35)$$

where g is the fraction of atomic sites in the grain boundary of the polycrystal and can be written as:

$$g = \frac{q\delta}{d} \quad (36)$$

where q is a constant depending on the grain shape ($q=1$ for parallel grain boundaries and $q=3$ for cubic grains), δ is the grain boundary width and d is the spacing between grain boundaries.

Figure 3.B) represents the evolution of the effective diffusion coefficient in terms of temperature. Grain boundary diffusion weight over bulk diffusion is larger at low temperature and for smaller grain size. The diffusivities estimated in the temperature range of PWR and SFR show a pronounced effect of grain boundaries.

This should be kept in mind when using diffusion coefficient data which have been determined by fitting to low-temperature diffusion data since the influence of high-diffusivity paths is more pronounced at lower temperatures. However, for well designed diffusion experiments (e.g. materials with large grains) and diffusion coefficients determined at high temperatures these short-circuits should generally do not have contributed to the volume-diffusion coefficient values reported or if they have, this contribution is taken into account and both bulk diffusion and diffusion at grain boundaries are determined [28].

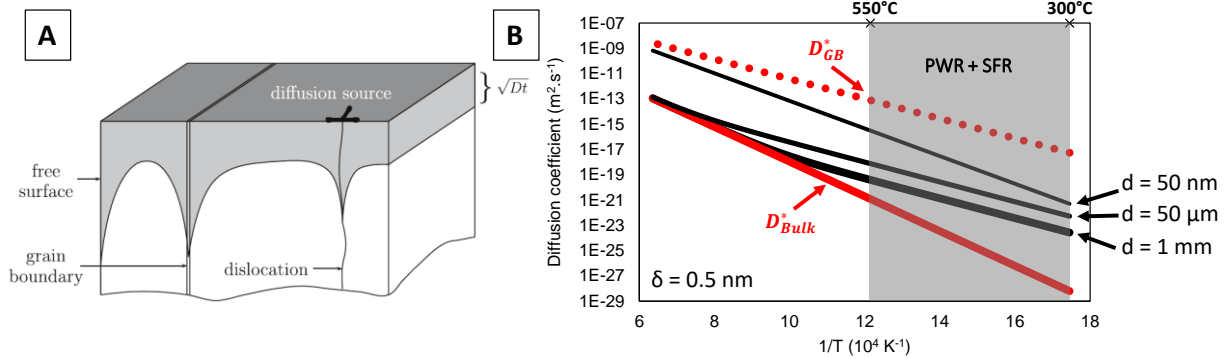


Figure 3 – A) Schematic representation of the fastest penetration of the diffusion source along defects[6]. B) Bulk, grain boundary and effective ^{51}Cr tracer diffusion coefficients in Ni-20Cr calculated from Eq. (35) for different GB spacing values with $q=1$. D_{Bulk}^* and D_{GB}^* are extrapolated from [16].

Diffusion processes are relevant for the kinetics of many microstructural changes that occur during elaboration of materials and in-service conditions. During long term thermal ageing, precipitation of second phases is the main diffusion-driven process responsible of mechanical properties evolutions. Next sub-section is dedicated to its description in nuclear austenitic stainless steels.

3. Precipitation

After solution annealing followed by rapid cooling, the austenitic microstructure shows large grains, annealing twins, residual δ ferrite and a small volume fraction of undissolved MX precipitates and/or inclusions (e.g. MnS). After thermal ageing, depending on the annealing temperature and time, precipitation can occur. Second phases population can be predicted with the help of a Time Temperature Precipitation (TTP) diagram (Figure 4). Phase occurrence is highly sensitive on the grade and also on the austenitic stainless steel composition and thermomechanical history.

Several reviews [29–34] dealt with the description of austenite stability after thermal ageing of austenitic stainless steels. Main conclusions are presented hereafter.

Carbon solubility in austenitic stainless steels decreases with temperature and particular elements addition (i.e. Cr, Mo). As carbon diffuses the fastest in austenite, carbides are generally the first to form. On the other hand, as substitutional elements required for the nucleation and growth of intermetallic phases diffuse slower, they generally appear at higher temperatures and longer times.

$M_{23}C_6$ carbides, where $M = \text{Cr, Fe, Mo and Ni}$, form at the early stage of precipitation in austenitic stainless steels. $M_{23}C_6$ are metastable carbides because they can partially dissolve at the expense of M_6C formation. $M_{23}C_6$ nucleates first at grain boundaries, at incoherent then at coherent twin boundaries, and finally along matrix dislocations. The formation of Cr_{23}C_6 at grain boundaries causes Cr-depletion at the carbide vicinity and thus a possible loss in stainless property promoting intergranular corrosion or IASCC.

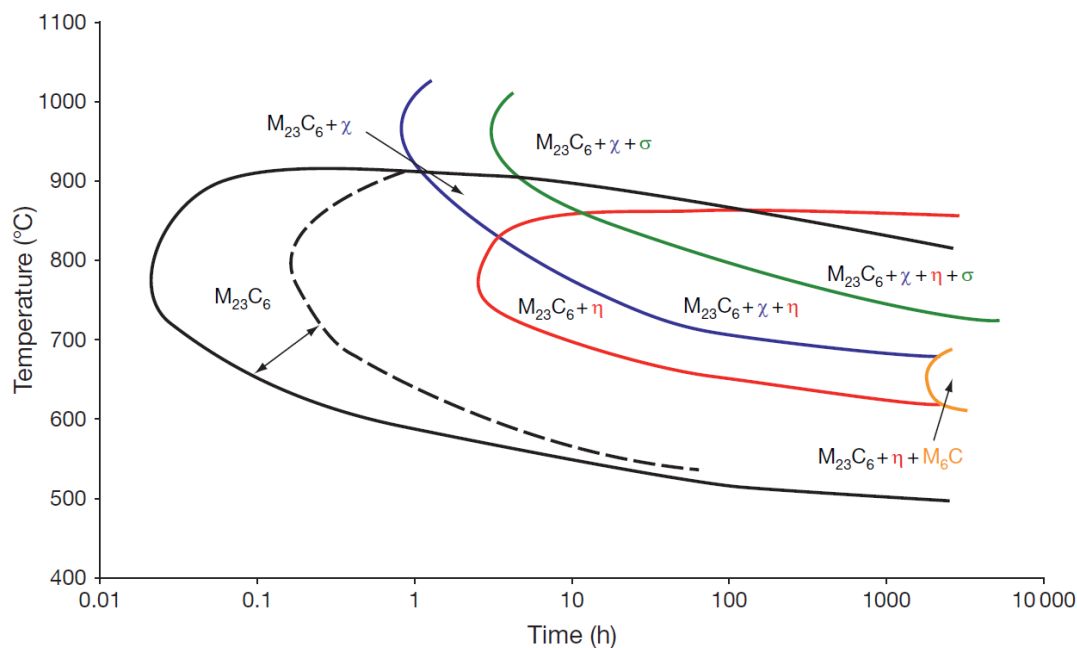


Figure 4 - Time-Temperature-Precipitation diagram of solution annealed 316L austenitic stainless steel. The dashed line represent a lower solution annealing temperature (1090°C vs. 1260°C) [33]

The presence of molybdenum in 316 austenitic stainless steel grade can cause the precipitation of M_6C carbide (η -carbide), where $M = Fe, Cr, Mo, Nb$ and V . It forms generally after long annealing times associated with $M_{23}C_6$.

The addition of “stabilizing elements” such as strong carbide formers Ti, Nb and V decreases the carbon solubility even more than Cr and Mo and promote the formation MC type carbides, where $M = Ti, Nb$ and/or V , against $M_{23}C_6$. They improve corrosion and creep resistance. Ti, Nb and V are also strong nitride formers promoting the formation of MN when the nitrogen content is high enough (from less than 0.1 wt.%). MN nitrides have the same crystalline structure as MC carbides, but they are even more stable and do not dissolve during solution annealing. MX precipitates can sometimes referred to carbonitrides $M(C,N)$. They have a characteristic cuboidal shape and can nucleate at grain boundaries, twins, stacking faults or on dislocation within the matrix. For short aging, MX precipitates are largely sub-stoichiometric and contain a large amount of chromium substituting for M .

The Z -phase is another nitride that can form in ASS containing Nb and N . In addition to Cr, N and Nb , the Z -phase can also contain Mo . Z -phase can nucleate at grain boundaries, twin boundaries or on matrix dislocations within a wide temperature range from 600 to 1200°C, so it can theoretically precipitate during solution annealing. The solvus temperature was estimated between 1300 and 1350°C.

The precipitation of hard and brittle sigma phase FeM , where $M = Cr$ or Mo , has a harmful effect on mechanical properties. Sigma phase precipitation depletes the adjacent matrix in Cr and Mo and thereby causes dissolution of carbides in this region. Sigma phase precipitation has a very slow kinetics in austenite. It precipitates mainly on grain boundaries, especially on triple junctions, and on incoherent twin boundaries and intergranular inclusions.

χ -phase precipitation can only occur in Mo or Ti -rich ASS. Sigma and χ -phase are very similar but can be distinguished with their respective composition because χ can dissolve C .

Laves phases Fe_2M , where $M = Mo$ or Nb , precipitate mainly intragranularly and occasionally at grain boundaries. Laves phases can be very densely faulted and grow from $M_{23}C_6$ carbide (Figure 5).

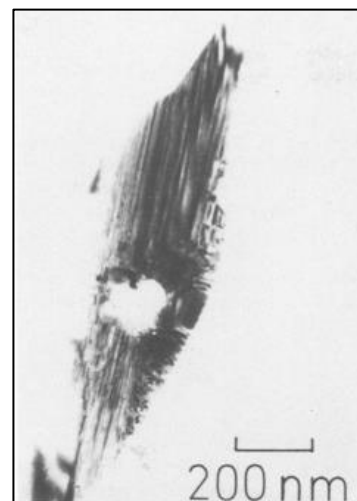


Figure 5 – Faulted Laves phase with a $M_{23}C_6$ nucleus [31]

In general, the most common phases to precipitate in SA 316 from 550 to 900°C are $M_{23}C_6$, M_6C , Laves, χ and sigma. During their growth they will relieve matrix supersaturations of Si, Mo, Cr , and C . While the matrix will soften, precipitates act as a barrier for dislocation gliding and tend to harden the material with an associated loss in ductility. Grain boundary sensitization will deteriorate ASS resistance to corrosion and fracture properties.

Precipitates characteristics (i.e. crystallographic structure) are summarized in Table 9.

Table 9 – Characteristics of the main precipitates observed in austenitic stainless steels after thermal ageing [29,35]. The reference number of the phase in PDF and COD crystallographic databases is also given.

Nature <i>PDF/COD</i>	Major elements / Composition	Crystallographic Structure	Particular orientation relationships with the matrix	Comments
MX 9008747 9008748 9008682 1011319 9008764 9008765	M =Ti, V, Nb and X=C,N or C+N	Ordered FCC Fm-3m (225) a=4.097-4.698 Å	Cube-on-cube	MN more stable than MC SA : partial dissolution of MC, no dissolution of MN
M ₂₃ C ₆ (τ-carbide) 14-407 5-721 25-405 2107332	Cr ₂₃ C ₆ (Cr ₁₆ Fe ₅ Mo ₂)C ₆ (Cr ₁₇ Fe _{4.5} Mo _{1.5})C ₆	FCC Fm-3m (225) a=10.57-10.68 Å	Cube-on-cube	cuboid or plate shape Early stage precipitation : metastable, can partially transform to M ₆ C
M ₆ C (η-carbide) 17-128 17-330 12-570	(Fe ₃ Mo ₃)C (Fe ₃ Nb ₃)C (Mn ₃ Mo ₃)C (CrCoMoNi) ₆ C (NbNi) ₆ C M ₅ SiC	Diamond cubic Fd-3m (227) a=10.95-11.28 Å	Cube-on-cube	Associated with M ₂₃ C ₆
Z-phase 1528599	Cr ₂ Nb ₂ N ₂	Tetragonal P4/nmm (129) a=3.037 Å c=7.391 Å	(001) _z [(001) _v [1-10] _z [(100) _v or [010] _z [(110) _v [111] _z [(100) _v [001] _z [(001) _v	cuboidal or rodlike shape stable, can precipitate during SA T _{solvus} =1300-1350°C
σ-phase 2310323	FeCr FeMo	Body centered tetragonal P42/mnm (136) a=8.7995-9.128 Å c=4.5442- 4.813 Å	(001) _σ [(111) _v [140] _σ [(011) _v or (001) _σ [(111) _v [-110] _σ [-110] _v	hard and brittle phase M ₂₃ C ₆ →σ Many variants
Laves phase (η) 1501464	Fe ₂ Mo Fe ₂ Nb	Hexagonal P63/mmc (194) a=4.6594 Å c=7.7433 Å	(10-13) _η [(111) _v or (-12-10) _η (-12- 1) _v or (0001) _η [(111) _v , [-1-120] _η [1-10] _v or (10-10) _η (-110) _v	Can exhibit stacking faults Associated with M ₂₃ C ₆ Fe ₂ Nb can partially transform to M ₆ C
χ-phase 9015334	(Fe,Ni) ₃₆ Cr ₁₂ Mo ₁₀ (Fe/Ni)15Cr26Mo (Fe/Ni)36Cr12Mo3Ti7	BCC I-43m (217) a=8.807-8.878 Å	(110) _χ [(111) _v , [-110] _χ [01-1] _v , [-211] _χ [001] _v	Form in the vicinity of carbide particles Many variants

To sum up

Thermodynamics and diffusion rule microstructural evolutions under thermal ageing.

In substitutional alloys, diffusion occurs via vacancy exchange with lattice atoms. Vacancy concentration is at equilibrium in the matrix and this concentration rises when the temperature is increased, accelerating diffusion at higher temperatures. Diffusion kinetics are therefore dependent on the temperature, but also on the crystal structure, composition, short-circuits density (e.g. grain boundaries) and driving forces. These driving forces allow fluxes of the species. Here, we focused on the chemical potential gradients neglecting external driving forces.

Diffusion coefficients have been defined and can be categorized this way: in the absence (i.e. dilute solution) or in the presence (i.e. concentrated alloy) of driving forces. In the absence of driving forces, self or impurity diffusion coefficients can be determined thanks to radiotracer experiments. When a driving force is applied, intrinsic and interdiffusion coefficients must be considered. They are commonly measured from diffusion couple experiments.

As Fe, Ni and Cr are slow diffusing elements in Ni-Cr and Fe-Ni-Cr austenitic alloys but also because the stability domain of austenite decreases with temperature, diffusion coefficients in the temperature range of PWR and SFR operation are mostly extrapolated from high temperatures. **A lack of data was highlighted for these temperatures both for binary and especially for the ternary system.** Knowledge of diffusion kinetics is crucial to predict microstructural evolution under long term thermal ageing which is directly linked to mechanical properties deteriorations.

Austenitic stainless steels are metastable at room temperature but become unstable after thermal ageing from 500°C (i.e. a concern for SFR components). This process will result in second phases precipitation. Elements in supersaturation in the matrix will diffuse to form and grow precipitates during thermal ageing. A large population of second phases can be observed in ASS (e.g. $M_{23}C_6$, MX, sigma-phase, Laves-phase, Z-phase) leading to hardening, loss of corrosion resistance and fracture properties.

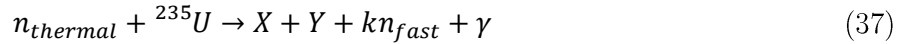
Identifying microstructure evolutions under thermal ageing is a first and necessary step to understand the additional effect of irradiation on austenitic stainless steels in the operation temperature range of nuclear reactors. The combination of temperature, time and flux of energetic particles will severely damage the structure and affect diffusion kinetics. This topic is largely reviewed in the next section.

III. Microstructure evolution after ageing under irradiation

1. Neutron production and transmutations in nuclear reactors

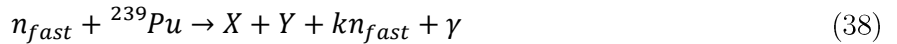
Depending on the reactor technology, austenitic stainless steels will experience different temperatures (Table 2), environment (fluid that transfers heat) and incident neutron energy, flux, spectra because the nuclear fission/fusion reaction involved to produce energy (electricity and sometimes heat) is different.

In PWR, the fuel is made of uranium oxide, enriched in ^{235}U . Fission reaction of ^{235}U produces fast neutron with average energy of 2 MeV. The capture cross section of a neutron by the ^{235}U fissile nuclei decreases as the neutron energy increases. Water is used not only as a coolant, but also as a moderator to slow down fast neutrons leaving them as thermal neutrons with only minimal kinetic energy (thermal and fast neutrons are classified regarding their energy, < 1 eV and > 1 MeV respectively). Thermal neutrons make more effective the fission chain reaction. The reaction proceeds via:



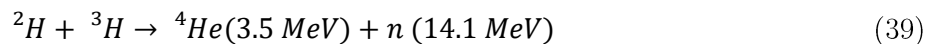
where X and Y are the fission products and $k=2.43$ is the average number of fast neutrons created from a single fission reaction. The energy produced during this reaction is mainly in the form of the kinetic energy of fission products and gamma rays.

For fast neutron spectrum reactors as SFR, the fuel contains ^{239}Pu . Sodium plays the role of coolant only. Fast neutrons can be captured by ^{239}Pu nuclei resulting in its fission. This reaction produces in average more neutrons than in thermal reactors. However, as the neutron capture cross section is lower, SFR fuel should be more enriched in fissile elements than PWR for the same efficiency level.



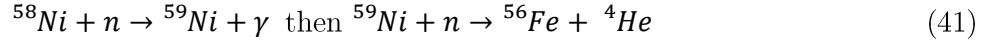
Here also, X and Y are the fission products and $k=2.89$ is the average number of fast neutrons created from a single fission reaction.

In the case of a nuclear fusion between two hydrogen isotopes, deuterium (^2H) and tritium (^3H), “ultra-fast” neutrons are produced following this reaction:



Atomic displacements from collision between an energetic particle and the target material atoms and the generation of helium, directly from fusion nuclear reaction or by nuclear transmutation reactions in fission reactors, are the two major components of the radiation damage.

In fission reactors, helium can be produced by the transmutation of boron contained in the primary water of PWR and transmutation of nickel, one of the major alloying elements of austenitic stainless steels [36]:



Although clear differences exist between these various reactor technologies, same classes of structural materials or alloys have been selected for specific components. Indeed, materials behavior is linked by the same underlying physics and the consequent radiation effects on properties.

2. Collision event and radiation damage

During a collision, if the transferred kinetic energy from a neutron to an atom of the target crystal (the primary knock-on atom - PKA) is higher than the displacement threshold energy, this atom will be removed from its lattice site, leaving behind a vacancy and insert into the crystal lattice as a self-interstitial atom (SIA). The pair of point defects created, a vacancy and a SIA, is called a Frenkel pair (Figure 6). If the energy transferred to the PKA is high enough, it becomes a projectile that can also transfer its energy to other atoms on its way within the crystal lattice. The subsequent atom-to-atom collisions will create additional knocked-on atoms: secondary KAs, tertiary KAs... and generate a collision cascade. Because of interactions with the crystal lattice, the initial PKA velocity will decrease during its travel and end as a SIA.

The collision cascade generated by a recoil atom cannot be observed experimentally because the time scale is too small, but it does thanks to molecular dynamics modelling (Figure 6). Two main stages can be distinguished during the collision cascade: the ballistic mixing phase (from 1 fs to 1 ps) and the thermal phase (from 1 ps to 10 ps). During the ballistic mixing, the number of low-order recoil atoms increases until their energy becomes lower than E_d , the displacement threshold energy. This corresponds to the thermal spike during which the local temperature increases. During the thermal phase, cooling down of the cascade occurs via lattice and electronic heat transfers. Most of the Frenkel pairs will recombine and leave behind single point defects or PD clusters as cascade debris. At larger time scales (from 10 ps to years) and higher temperatures, point defects will migrate thanks to diffusion creating new clusters and destructing or modifying ones that already exist.

As explained before, under irradiation, a type of point defects not present at thermal equilibrium will be created: self-interstitial atoms. They can theoretically arrange into different configurations (Figure 7). They can be in one of the usual octahedral or tetrahedral sites, in the number of 8 or 12 respectively for the FCC lattice, but these structures are uneasy to form. The most common is the dumbbell configuration in which two atoms will share the same lattice site. The center of mass of the two atoms is at the lattice site, and they are displaced symmetrically from it along one of the principal lattice directions: $\langle 100 \rangle$ the most favourable, then $\langle 111 \rangle$ or $\langle 110 \rangle$. The crowdion

is another option. It can be understood as a long chain compressed of atoms (around 10-20) along the $\langle 110 \rangle$ lattice direction which contains one extra atom. On the contrary, if an atom is removed and leave behind a vacancy, a relaxed chain of atoms, the voidion can appear.

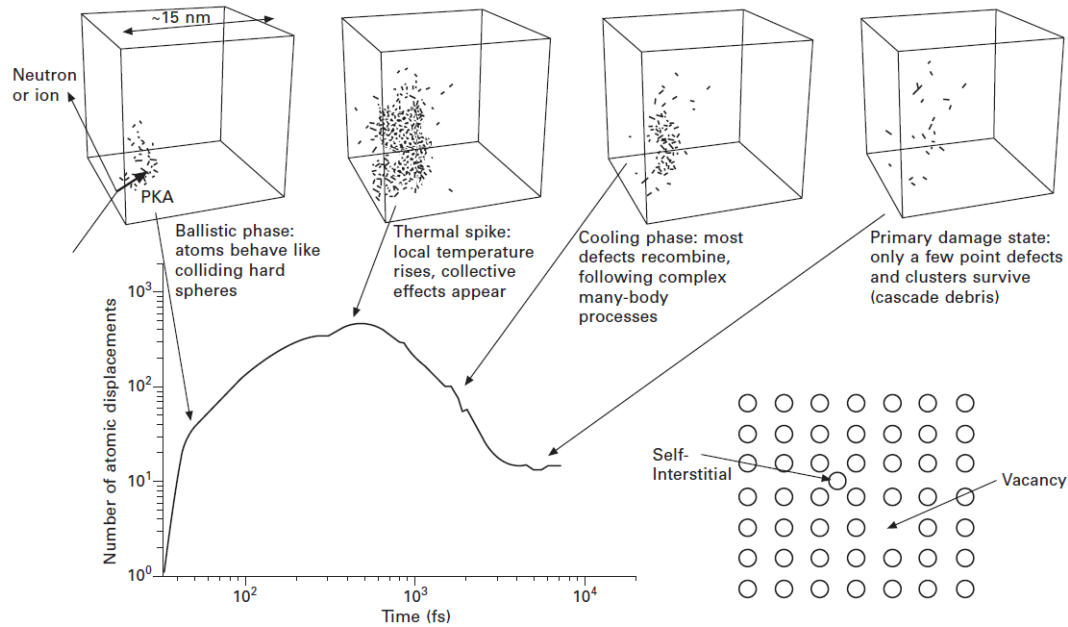


Figure 6 - Stages of the cascade development from MD modelling (10 keV in BCC iron simulated by D. Terentyev with molecular dynamics, only self-interstitials are visualised) and scheme of a Frenkel pair [37]

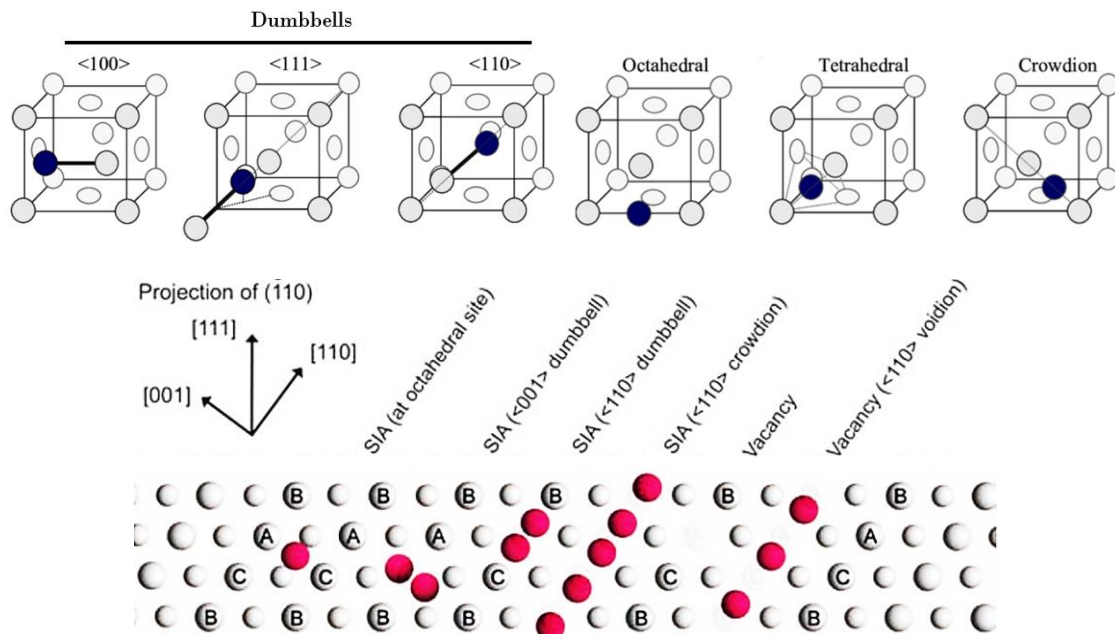


Figure 7 - Point defect configurations in FCC crystals [38,39]

Similarly to thermal diffusion, diffusion under irradiation is governed by migration of point defects in substitutional alloys. Depending on the applied temperature, different regimes are defined.

3. Radiation enhanced and modified diffusion: 4 regimes

Below $T \sim 50^\circ\text{C}$, SIA are the only diffusing point defects. Vacancies and SIA become both mobile from this temperature, but move with different diffusional modes and velocities, with interstitials diffusing much faster than vacancies. Therefore, all diffusion-driven processes will be strongly affected by irradiation. Depending on the temperature and the sink strength, freely migrating point defects (PD) will preferentially annihilate by mutual recombination or annihilate at sinks. 4 different regimes can be distinguished:

- **Low temperature:** PD are immobile, annihilation by mutual recombination happen between neighbouring interstitial/vacancy directly within the cascades. This regime is called the ballistic mixing. Here, PD concentration is proportional to the defects production.
- **Intermediate temperature, low sink strength:** PD are mobile and the equilibrium concentration of vacancies c_V^{eq} is low. Freely migrating PD can diffuse over longer distance to annihilate by mutual recombination if the sink strength is low. This is the so-called recombination regime.
- **Intermediate temperature, high sink strength:** PD are mobile and $c_V^{eq} < c_V^{irr} + c_I^{irr}$. Freely migrating PD can diffuse over longer distance and annihilate at sinks. Within this Radiation-Induced Segregation (RIS) temperature range, the temperature can change the relative weight of the competing migration mechanisms because of different migration activation energy of PD: $E_I^m > E_V^m$.
- **High temperature:** $c_V^{eq} \gg c_V^{irr} + c_I^{irr}$, the thermal emission of vacancies by linear and surface defects is high enough to provoke a back diffusion. Here, microstructure evolution is governed by thermal processes.

In pure metal, the evolution of the average PD concentrations is given by the integration over time of the rate theory equations:

$$\begin{cases} \frac{dc_V}{dt} = K_0 - Rc_Ic_V - \sum_s k_{V_s}^2 D_V (c_V - c_V^{eq}) \\ \frac{dc_I}{dt} = K_0 - Rc_Ic_V - \sum_s k_{I_s}^2 D_I c_I \end{cases} \quad (42)$$

where K_0 is the point defect production rate (dpa.s^{-1}) and it is proportional to the radiation flux, R is the recombination rate, $k_{PD_s}^2$ is the sink strength which depends on the nature and the density of sinks, D_{PD} and c_{PD} are vacancies and interstitials diffusion coefficients and concentrations respectively.

Depending on the regime, the self-diffusion coefficient will evolve following the way described in Figure 8.

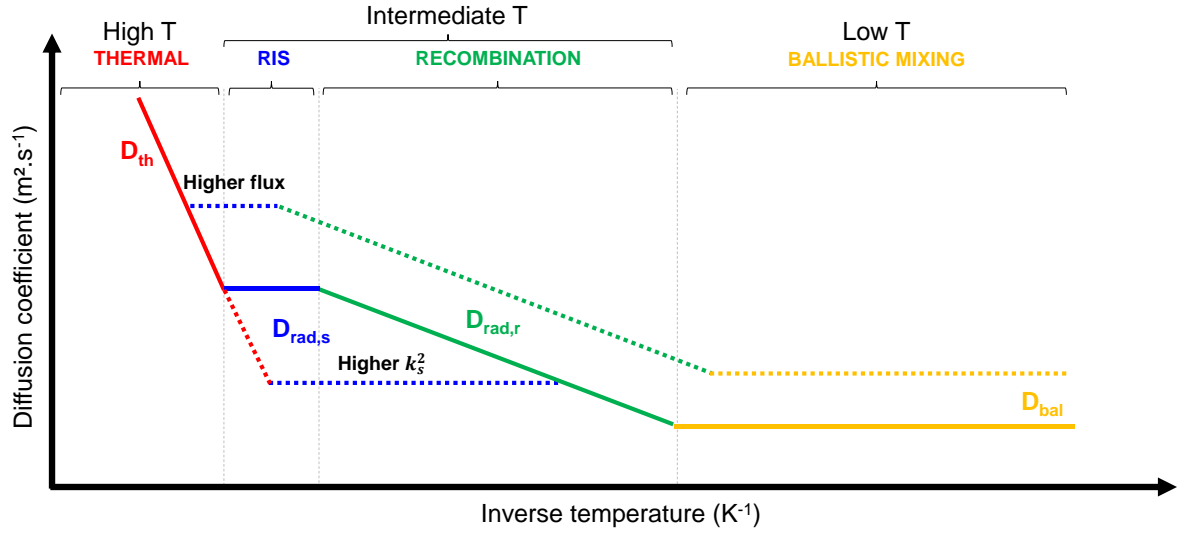


Figure 8 – Schematic representation of the self-diffusion coefficient trend under irradiation depending on the different temperature regimes. Flux (or dose rate) and sink strength effect are highlighted with dashed lines.

4. Emulate neutrons with ions

Neutron irradiations can be performed in either industrial or experimental reactors where the damage rate is equal to $\sim 10^{-7}$ dpa/s. Only 3 dpa will be reached within a year of operation. Thus they cost time and money. Furthermore, the induced radioactivity² of irradiated materials constrains to manipulate samples in dedicated facilities (i.e. hot cells) to protect workers from ionising radiations. For all these reasons, protons and heavy-ion irradiations are alternative to understand radiation damage mechanisms caused by neutron.

Compared with neutrons, which are light neutral particles, proton and heavy ions have a large cross section of interaction with the target steel atoms. Thus, protons and heavy ions will penetrate less deep in the material than neutrons, but they will produce same amount of damage in shorter time. However, by changing the incident particle, the resulting radiation-induced microstructure will be different. While it had been proved that proton irradiation can qualitatively and quantitatively emulate neutrons [40], the number of well-controlled studies that provide direct comparison of the effect of ion irradiation versus neutron on microstructure and properties of materials are few. Nevertheless, numerous heavy ion irradiations helped to date to understand basic mechanisms of radiation effect on microstructure and the associate mechanical properties evolution [41].

In order to compare the radiation damage from different radiation sources, Kinchin and Pease [42] first attempted to describe the total number of Frenkel pairs $N_{d,KP}(T)$ created from a single PKA of energy T by this relation :

$$N_{d,KP}(T) = \frac{T}{2E_d} \quad (43)$$

² Austenitic stainless steels are activated after neutron exposure due to presence of Ni and, in some cases, of Mo in their composition.

where T depends on the particle type and E_d on the target material. The previous expression is valid for $2E_d < T < E_c$ where E_c is a cut-off energy. When $T < E_d$, no atom is ejected from its crystal lattice, therefore $N_{d,KP}(T) = 0$. If $E_d < T < 2E_d$, a single Frenkel pair is created, so $N_{d,KP} = 1$. Above the cut-off energy E_c , the number of generated Frenkel pairs saturate, here $N_{d,KP}(T) = \frac{E_c}{2E_d}$.

To obtain this simple relation, several assumptions had been done [36]:

- The cascade is created by a sequence two-body elastic collisions between atoms.
- The displacement probability is 1 for $T > E_d$.
- There is no loss of energy due to inelastic interactions within the cascade.
- When $T < E_c$, the electronic stopping is ignored and only atomic collisions occur whereas above E_c , all additional energy contribute to electronic excitation.
- The energy transfer cross section is given by the hard sphere-model.
- The arrangement of the atoms in the solid is random (amorphous)
- It is an athermal reaction.

In 1975, Norgett, Robinson and Torrens [43], proposed a standard for dpa calculation. According to the NRT model, the number of Frenkel pairs $N_{d,NRT}(z)$ generated by a single recoil atom of damage energy \bar{T} per depth unit z is given by the following equation:

$$N_{d,NRT}(z) = \kappa \frac{\bar{T}(z)}{2E_d} \quad (44)$$

Here, \bar{T} , which depends of the PKA energy, is the part of the PKA energy available for displacements. In other words, the energy loss by electron excitation is taken into account in the term \bar{T} . κ is a constant equal to 0.8 that takes into account the cascade efficiency. SRIM (Stopping and Ranging of Ions in Matter) code calculates the NRT damage caused by ions in the target material, and give access to $N_{d,NRT}(z)$. The damage energy \bar{T} is given by the ion nature and energy. Even if E_d depends on crystallographic orientation, the average value of 40 eV is used for Fe and austenitic stainless steels.

Integration of the NRT damage function over the PKA energy spectrum and time will give the well-known dpa(z) (number of times an atom is displaced during irradiation at a certain depth z) [44]:

$$dpa(z) = \frac{N_{d,NRT}(z) \times \varphi \times t}{N} \quad (45)$$

where φ is the ion flux, t the irradiation duration and N is the atomic density.

The NRT model is handicapped by limitations (e.g. overestimation of defects produced within the cascade). Recently, Nordlund et al proposed a new formalism to offer a better prediction of radiation damage [45].

In the literature, the dose is sometimes given in terms of fluence Φ in n.cm^{-2} for $E > 1$ MeV instead of dpa for neutron irradiations. Even if it is not the most accurate way to convert the neutron fluence into dpa, the following equation is still commonly used:

$$dpa = \sigma_d \Phi \quad (46)$$

where σ_d is the displacement cross section in barns.

5. Effect of radiation damage on resulting microstructure and microchemistry

In-excess point defects within the matrix will either recombine, annihilate at sinks or form clusters. PD clusters can form directly within a damage cascade or indirectly between cascades by nucleation and growth processes. They can evolve into dislocation loops, stacking fault tetrahedra or cavities which are sinks for PD annihilation. Driven by the diffusion of freely migrating PD, elements will redistribute within the crystal leading to local enrichments, phase transformation and precipitation. All these evolutions can contribute to changes in both mechanical properties and dimension of the reactor components (i.e. creep and swelling). In the next sections will be presented microstructural and microchemical changes under irradiation that can be detected by TEM and/or APT in austenitic stainless steels.

5.1. Black dots

Black dots, or black spots, are the dominant microstructural features in the low temperature regime (10^{24} m^{-3} reachable from 0.1 dpa). These defects are detected by TEM but unresolved due to their small size ($< 2 \text{ nm}$). Thus, their nature is still unclear: are they vacancy or interstitial-type small Frank loops, SFTs?

Below $\sim 300^\circ\text{C}$, black dots and Frank loops are the main radiation induced defects. It was stated for a long time that Frank loops are only interstitial type. Regarding the point defect balance and the slow diffusivity of vacancies at low temperature limiting annihilation at sinks, black dots are suggested to be vacancy clusters products from the cascades (SFTs) [46]. Others [47], attempted to demonstrate that black dots are small Frank loops which, with sizes in the range of 1-30nm, can be either vacancy or interstitial type. To date, their nature remains unclear.

5.2. Stacking fault tetrahedra

In FCC metals presenting a low stacking fault energy (SFE) and/or high shear modulus, as it is the case for austenitic stainless steels with average values of 40 mJ.m^{-2} and 76 GPa respectively, a new vacancy-type of defect can appear: a three-dimensional stacking fault configuration lying on $\{111\}$ planes in the shape of a tetrahedron called stacking fault tetrahedron (SFT) as represented in Figure 9.A). In 2013, Schibli and Schäublin [48] reviewed the proposed formation mechanisms of SFT:

- From the dissociation of a vacancy-type Frank dislocation loop [49] under a critical size. This critical Frank loop size depends on the reduced stacking fault energy, defined as γ/Gb , where γ represents the SFE, G the shear modulus and b the Burgers vector modulus of a perfect dislocation in FCC structure. The reduced SFE should be smaller than $1/50$ to promote SFTs formation [50] which is the case for austenitic stainless steels.
- By absorption of freely migrating vacancies from a small triangular-shaped nucleus of vacancies, with an edge length of less than five atoms [51].

- From a void collapse [52].
- From the displacement cascade [53].

It should be noted that identification of small SFT from TEM images is not straightforward. 2 edge-on variants of Frank loops can overlap within the sample thickness when tilted to $\langle 011 \rangle$ zone axis and give a triangular shape contrast. Strain field of small defects can also result on wrong interpretation. In both cases, changing the diffraction conditions near this zone axis can help to clarify the defect nature [54].

According to the literature, they are more likely to form in high purity austenitic stainless steels, i.e. with lower impurity contents or model alloys [55,56] (Figure 9.B)) than in commercial steels. Indeed, in austenitic stainless steels, SFT should be the more stable vacancy-type defect under a temperature of about 300°C [50] but the addition of impurities as P or C seems to reduce their appearance. Despite a large number of publications dealing with 300-grades SS microstructure evolution under irradiation, few authors reported their presence [57]. Cavities and SFTs appear to be closely linked. Indeed, as shown in Figure 9.C), SFT can act as cavity nuclei.

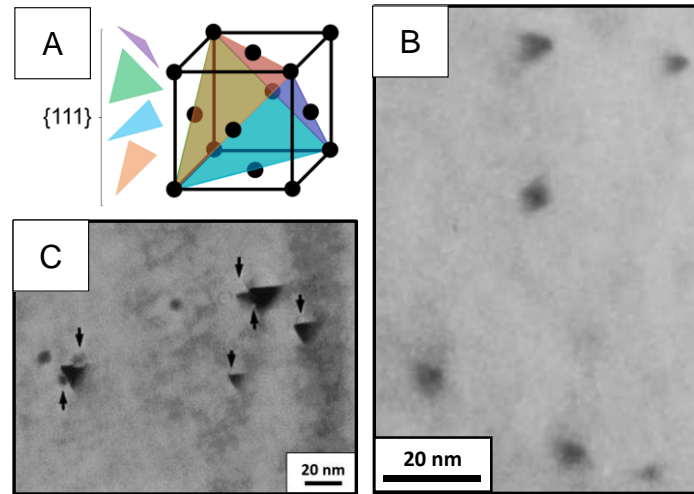


Figure 9 – A) Schematic representation of the 4 $\{111\}$ planes where SFT stacking fault lie in FCC crystals. B) SFT in Fe-13Cr-14Ni alloy electron irradiated at 300°C [58]. C) Cavities nucleation at the vicinity of SFT in Ag foils irradiated in-situ with electrons [59].

5.3. Cavities

Cavities are also three-dimensional defects created by the condensation of vacancies. If they are stabilized by a gas (He trapping), they are called bubbles, if not, they are considered as voids. Apart from He pre-injected samples or double-beam ion irradiations, self-ion irradiations cannot form bubbles because He is a transmutation product in neutron irradiated austenitic stainless steels. Cavities appear in the intermediate temperature regime from ~ 300 to 700°C in fission reactors. At lower temperatures, small cavities start to nucleate and compete with vacancy loops. The growth rate and size rise with temperature to a maximum around 470°C for neutrons irradiated austenitic stainless steels at $\sim 10^6 \text{ dpa.s}^{-1}$. At higher temperatures, cavities start to emit vacancies and shrink.

Only bubbles can remain in the microstructure at temperature above 700°C [60]. Cavities can be faceted along crystal directions as shown in Figure 10. A) and B).

Cavities induce components dimensional change known as swelling and expressed as follows: $\Delta V/V$ (%). Depending on the dose level, swelling exhibits three distinct regimes: incubation, transient and steady growth with a swelling rate of 1%/dpa. As shown in Figure 10. C), swelling is extremely sensitive to the initial metallurgical state, impurities and alloying elements content.

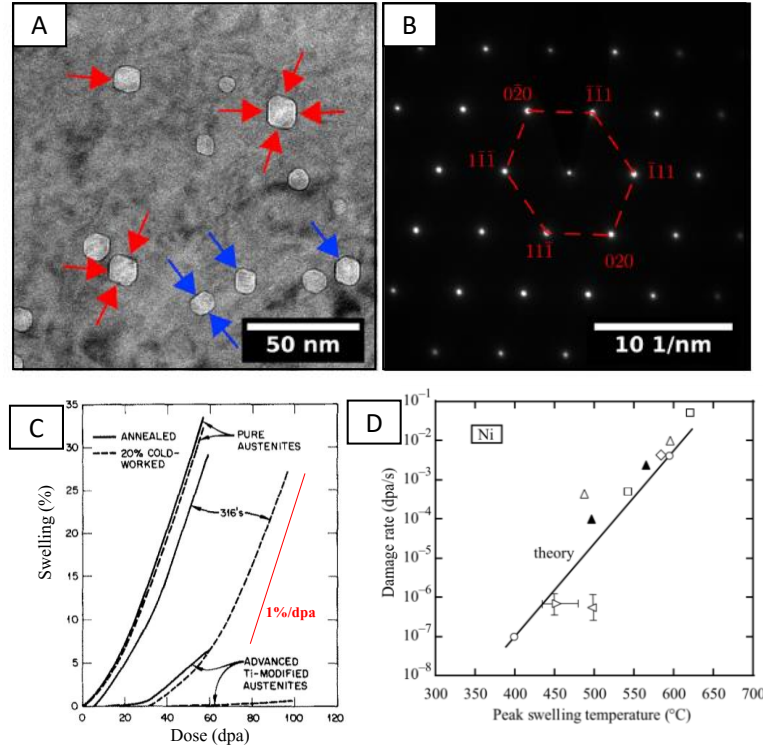


Figure 10 – A) TEM BF under-focus imaging of cavities in a 316L irradiated with protons up to 1.5 dpa at 380°C with facets lying on $\{111\}$ and $\{020\}$ planes, highlighted by red and blue arrows respectively, as shown from the $[101]$ associated SAED pattern in B) [61] C) Dose dependence of swelling of model, commercial and Ti-modified 316-type SS with different as-received states (SA or 20%-CW) [60]. D) Temperature shift of peak swelling as a function of dose rate in pure Ni, theory vs. experiments [36].

There is also a strong dependence of swelling to the dose rate, which can be a problem when emulating neutron radiation damage with ions. Mansur [62] demonstrated the possibility to reach the same swelling level by increasing the irradiation temperature. If one considers the invariance of the net flux of vacancies over interstitials toward cavities, in the recombination-dominated regime (with a relatively low sink strength), the temperature shift ($T_2 - T_1$) is expressed as follows:

$$T_2 - T_1 = \frac{\frac{k_B T_1^2}{E_m^v + 2E_f^v} \ln\left(\frac{K_{02}}{K_{01}}\right)}{1 - \frac{k T_1}{E_m^v + 2E_f^v} \ln\left(\frac{K_{02}}{K_{01}}\right)} \quad (47)$$

where k_B is the Boltzmann constant, K_0 is the dose rate, E_m^v and E_f^v are the vacancy migration and formation energies respectively.

Figure 10. D) shows the good agreement between experimental and predicted peak swelling temperature shift in irradiated pure Ni at different dose rates.

5.4. Dislocation loops and dislocation network evolution

In FCC crystals, the condensation of point defects between two $\{111\}$ close-packed planes will cause the creation of a stacking fault. In the case of vacancies, the stacking fault will be intrinsic with stacking sequence $ABCA\textcolor{red}{X}CABC\dots$ whereas for interstitials it will be extrinsic $ABCAB\textcolor{red}{A}CAB\dots$. The boundary line of such a fault is a dislocation loop called (faulted) Frank loop (Figure 11.A) and B)) with a Burgers vector perpendicular to the fault lying plane (i.e. prismatic loops): $\vec{b} = \frac{a}{3}\langle 111 \rangle$, a is the lattice parameter. Because the Burgers vector direction does not lie in the plane of the fault, Frank loops are sessile. Since they are unable to glide, they take part to hardening. Loop growth or dislocation interaction can unfault Frank loops into a glissile prismatic loop. Depending on their nature, the unfaulting reaction can be described as follows [63]:



Vacancy-type (intrinsic)

Interstitial-type (extrinsic)

where $\frac{a}{6}\langle 112 \rangle$ and $\frac{a}{2}\langle 110 \rangle$ are the Burgers vector of a Shockley partial dislocation and a perfect prismatic loop respectively. First, this process will form a perfect loop on the $\{111\}$ habit plane of the former faulted loop. Then, a rotation of the glide cylinder will change the habit plane from $\{111\}$ to $\{110\}$ on which they will be able to glide. Therefore, two families of perfect loops can coexist in irradiated FCC, one of them, $\frac{a}{2}\langle 110 \rangle\{110\}$, being prismatic.

In austenitic stainless steels, Frank loops are the most observed radiation-induced defect type. At low temperature ($<300^\circ\text{C}$), small Frank loops can theoretically either be vacancy or interstitial type. Because the number of interstitials and vacancies produced in the cascade are the same, a balance should exist between point defects clusters. Faulted loop density increases with the dose to a plateau from few dpa (Figure 11.C)). This saturation could be explained by unfaulting of Frank loops at higher dose as shown in Figure 11.E). At intermediate temperature ($300^\circ\text{C} < T < 700^\circ\text{C}$), vacancy-FL become thermally unstable and emit vacancies into the lattice, allowing cavities to form [64]. Then, only interstitial Frank loops will remain, their size will rise while their saturation density will decrease with temperature (Figure 11.D)). As the loops grow with temperature, faulted loops become closer to each other until they interact. It results in unfaulting of the loops and incorporation into the dislocation network, explaining this decrease of saturation density. Above $\sim 700^\circ\text{C}$, when thermal vacancies density exceeds radiation-induced PD, Frank loops will shrink.

Researchers distinguish the dislocation network (dislocation lines) from the dislocation loops observed after irradiation. Depending on the initial metallurgical state of the material (solution

annealed or cold worked), the total dislocation density (total = network) will evolve in a different way to reach a common plateau at high doses. At the first stage of irradiation, dislocation from the original network will rapidly disappear and Frank dislocation loops induced by irradiation will grow. Then, via unfaulding and interaction of loops, new dislocation lines will be generated so the initial network will be fully recovered.

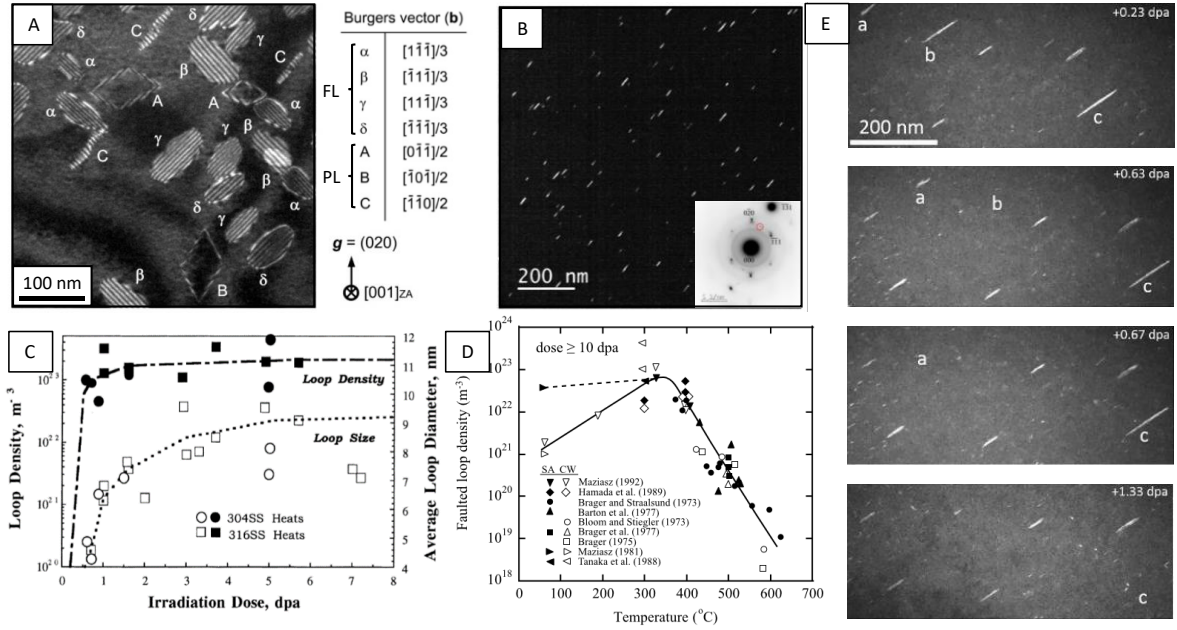


Figure 11 –A) WBDF TEM image of faulted Frank loops (FL) and perfect prismatic loops (PL) near B~[001], G=(020) imaging conditions with their associated Burgers vector in a CrFeCoNi-based alloy electron irradiated to 1 dpa at 400°C [65] B) DF TEM image at B=[011], $G=\frac{1}{2}(\bar{1}\bar{1}1)$ of one variant edge-on FL [66] C) FL number density and size evolution in terms of dose of 304 and 316SS neutron irradiated at approximately 280°C [67]. D) Effect of temperature and as-received state (SA or CW) on FL number density evolution of neutron-irradiated type-316 SS at dose levels higher than 10 dpa [60]. E) Room temperature in-situ ion irradiation showing the unfaulding process of Frank loops of an ion pre-irradiated Fe-21Cr-32Ni model alloy at 440°C to 1 dpa [68]

5.5. Radiation induced segregation

Radiation-induced solute segregation (RIS) refers to the redistribution of elements under irradiation due to a coupling between solute and point defect fluxes. Any preferential association between an atom and one type of defect will result in enrichment or depletion of that atom at defect sinks such as grain boundaries, void surfaces, dislocations, precipitate/matrix interfaces or free surfaces. During irradiation mixed phenomena will occur:

- as diffusion is governed by point defect motion and the total number of defects increases, diffusion, segregation and precipitation kinetics can be radiation-enhanced.
- as new point defects are created (interstitials) and the global PD concentrations are in far excess in the matrix and at equilibrium at the vicinity of defect sinks, PD-solute coupled fluxes will appear involving element redistribution in the alloy leading to radiation-induced segregation or modified precipitation.

- as the alloying elements redistribution will lead to local changes in composition in the matrix or at the grain boundaries/dislocations/interphase interfaces, precipitation can be induced or even retarded.

Preferential segregation of alloying elements or impurities at sinks is typically observed in the intermediate temperature regime when the sink strength is sufficiently high (Figure 8). RIS is a complex phenomenon and the proposed flux-coupling mechanisms involved are still subjects to discussion (Figure 12). The first one is the Inverse Kirkendall Effect (IKE). It takes its name from the Kirkendall Effect occurring during thermal annealing of a diffusion couple A/B. Under thermal ageing, when $D_A \gg D_B$, and the species concentration gradients are imposed, the difference in fluxes of A and B atoms will lead to a flux of vacancies (i.e. the vacancy wind) in the opposite direction of the net solute atoms flux. Under irradiation, PD concentration within the matrix is high and at equilibrium at sinks. This concentration gradient results in a flux of PD toward sinks. In the case of IKE, the vacancy flux is imposed and will cause solute fluxes in the opposite direction. The slow diffusing atoms B will be enriched at sinks; on the contrary, the sink will be depleted in A (fast diffuser). In γ -Fe, $D_{Mn}^* > D_{Cr}^* > D_{Fe}^* > D_{Ni}^*$ [19,67,69] (thermal behaviour). As predicted by IKE mechanism, atoms of Ni will preferentially segregate at sinks contrary to Cr and Mn. Depending on Fe-Ni-Cr alloy composition Fe can either enrich or deplete at grain boundary [70].

A solute size effect has also been underlined in RIS with a tendency of undersized solute atoms, i.e. Ni, Si and P atoms, to segregate at sinks while Cr, Mn and Mo oversized solutes typically deplete. Second mechanism was therefore proposed based on the migration of PD-solutes complexes toward sinks by vacancy and the interstitial drag (Figure 12). While interstitial binding of undersized solutes is proposed, the vacancy drag effect of oversized solutes is explained by the formation of V-S complexes.

Since the RIS resulting from IKE and PD-S complexes drag mechanisms are identical in Fe-Cr-Ni alloys, determining the dominant mechanism responsible for the segregation towards sinks is still open for discussion. Nevertheless, successful attempts to predict RIS in several Fe-Ni-Cr systems on grain boundaries have been made. Based on differences in atom-vacancy jump rates of the constituent atoms (the inverse Kirkendall effect), the model developed by Perks et al. [71] was able to reproduce RIS tendencies at grain boundaries in Fe-Ni-Cr systems at various irradiation conditions. This model predicts a strong dependence of segregation on the irradiation temperature with the segregation reaching a maximum between 300 and 500°C for irradiation conditions typical of a thermal reactor. Allen and Was [72] modified the IKE model of Perks to include composition dependent migration energies which incorporate short range ordering effects. This revised model, known as the MIK model, provides an accurate representation of grain boundary composition in irradiated Fe-Cr-Ni alloys and suggests that IKE mechanism should be the sole contributor to RIS. Nevertheless, Ni enrichment at grain boundaries has been observed and modelled at low temperature ($\sim 50^\circ\text{C}$) [73]. As at this temperature range, RIS cannot be explained by IKE because vacancies are practically immobile, contribution of interstitials to RIS is therefore believed to co-exist with the IKE mechanism. Unfortunately, RIS models that take into account for interstitial

binding seems to overestimate RIS levels [70]. To date, mutual weight of these two mechanisms to predict RIS is still unsolved.

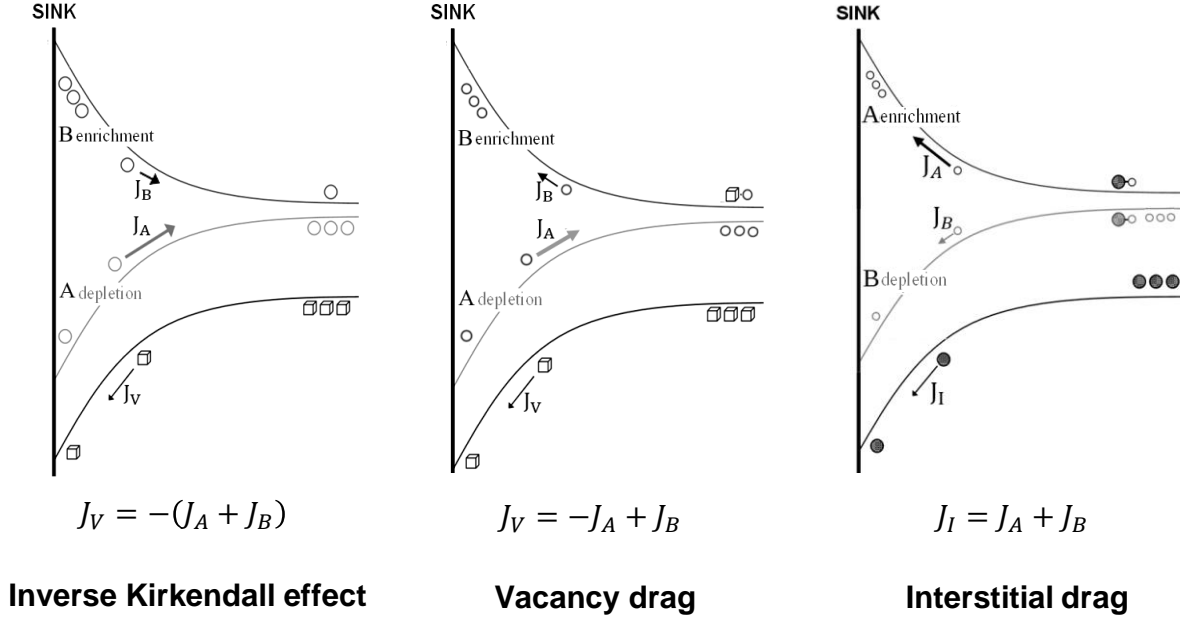


Figure 12 – RIS mechanisms adapted from [74]: if $D_A > D_B$, the IKE will lead to an enrichment of slow-diffusing solutes (left) and PD-solute complexes segregation (center and right).

RIS depends on alloying elements and impurities levels, crystal structure, sink nature, bias and strength and irradiation conditions, especially dose rate and temperature as shown in Figure 13.B). The temperature at which RIS levels are maximum shifts to higher values with increasing dose rate. In general, irradiation at a lower dose rate will result in a lower dose to reach steady state. The presented mechanisms are in competition, and their relative weight depends on the former conditions. General enrichment and depletion trends in 304 and 316-type ASS grades are summarized in Figure 13.A).

In addition to Ni segregation at sinks in austenitic stainless steels, minor alloying elements such as Si or impurities like P can strongly segregate on defects as illustrated on Figure 14. Pre-existing enrichment of Cr, Mo, B, C and P and depletion of Fe and Ni near grain boundaries can be observed before irradiation because of thermal segregation. While boron segregation levels does not seem to be affected by irradiation, extra segregation have been reported for phosphorous while C tends to deplete [75]. “W-shaped” Cr profile have been reported across grain boundaries due to a mix between the pre-existing enrichment and the depletion due to RIS [76].

Efforts to predict RIS were mainly done for grain boundaries. But point defects clusters as cavities and dislocations also exhibits RIS (Figure 14.B)). Because of their nature, they are biased meaning that preferential absorption of specific point defects at specific sinks exist, e.g. SIA for dislocations. Differences between measured and predicted RIS levels had been highlighted on He bubbles [77] suggesting that competing mechanisms also depends on sink type. There is a severe lack of studies comparing experimental and predictions levels of RIS on biased defect.

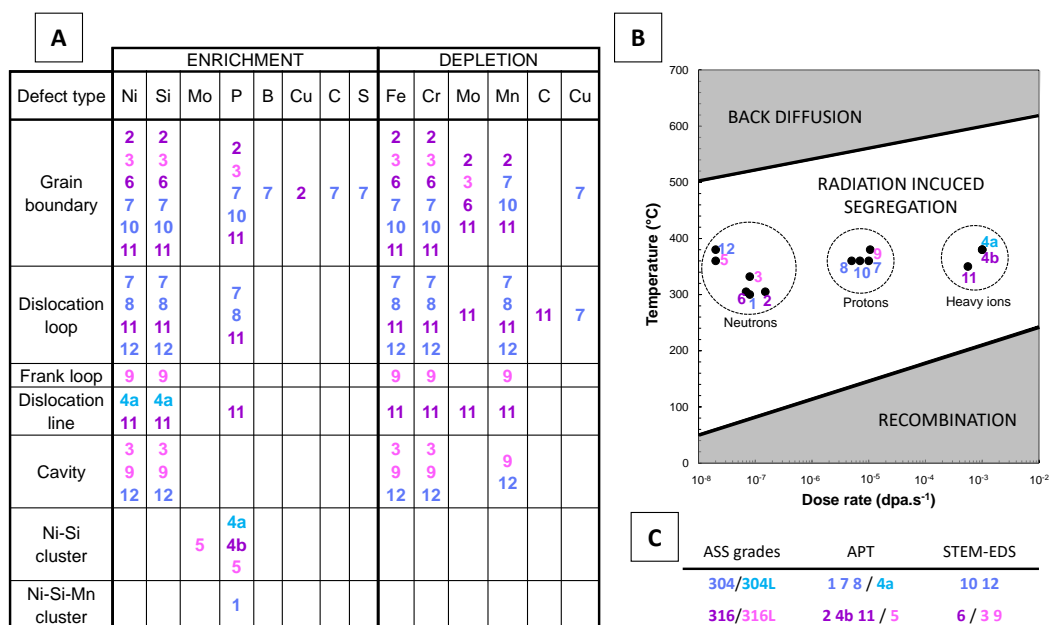


Figure 13 – A) Elements enrichment and depletion at different sink-types depending on C) the measurement technique in different austenitic stainless steels (1[78,79] 2[80] 3[64] 4a,b[81] 5[82] 6[46] 7[75] 8[83] 9[84] 10[85] 11[86] 12[87]) and B) the associated predicted RIS regime regarding the radiation temperature and dose rate.

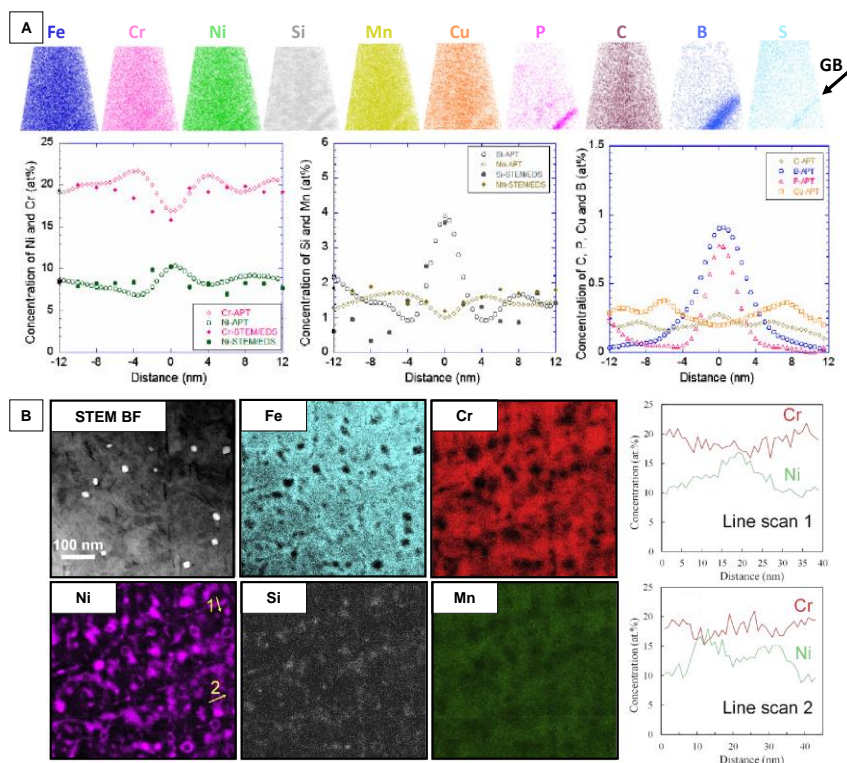


Figure 14 – A) APT volumes and associated concentration profiles showing enrichments and depletions at a grain boundary in a 304 SS following irradiation at 360°C to 5 dpa [75] B) STEM-EDS elemental maps and associated concentration profiles drawn on a dislocation loop and a cavity of a neutron-irradiated austenitic stainless steel 304 [87].

Presented in the first part of this section, mechanisms and general trends had been based on RIS reviews [88–91]. The second part will now focus on the theoretical description of RIS kinetics as introduced by Wiedersich et al. [92] and Lam et al. [93] in binary and ternary systems respectively.

- RIS in concentrated binary system A-B

After irradiation, SIA and V concentrations are not at equilibrium anymore. The resulting evolution of PD and solutes concentrations are described by the following set of equations [89]:

$$\left\{ \begin{array}{l} \frac{\partial c_V}{\partial t} = -\nabla \cdot \vec{J}_V + K_0 - R c_I c_V - \sum_S k_{VS}^2 D_V (c_V - c_V^{eq}) \\ \frac{\partial c_I}{\partial t} = -\nabla \cdot \vec{J}_I + K_0 - R c_I c_V - \sum_V k_{IS}^2 D_I c_I \\ \frac{\partial c_A}{\partial t} = -\nabla \cdot \vec{J}_A \\ \frac{\partial c_B}{\partial t} = -\nabla \cdot \vec{J}_B \end{array} \right. \quad (48)$$

Assuming that there is no solute drag by vacancies, fluxes must balance (negative sign for vacancy flux because vacancy and atom diffusions are in opposite direction):

$$\vec{J}_A + \vec{J}_B = -\vec{J}_V + \vec{J}_I \quad (49)$$

A flux of interstitials drives a flux of A and B atoms and reciprocally. Similarly, a flux of vacancies drives a flux of A and B atoms and reciprocally. Finally fluxes of A and B atoms imply the contribution of both IKE and interstitial mechanisms. Coupled solute-PD partial fluxes are then defined according to Figure 12:

$$\vec{J}_A = \vec{J}_{AV} + \vec{J}_{AI} \quad \vec{J}_B = \vec{J}_{BV} + \vec{J}_{BI} \quad \vec{J}_V = -(\vec{J}_{AV} + \vec{J}_{BV}) \quad \vec{J}_I = \vec{J}_{AI} + \vec{J}_{BI} \quad (50)$$

with $\vec{J}_{iV} = \vec{J}_i^V - \vec{J}_V^i$ and $\vec{J}_{iI} = \vec{J}_i^I + \vec{J}_I^i$ (i=A,B)

Fluxes of atoms and point defects are linearly dependent on the gradients of chemical potentials of all elements and defects. The partial fluxes can be therefore expressed in terms of the phenomenological coefficients L_{ij} :

$$\left\{ \begin{array}{l} \vec{J}_{AV} = -L_{AA}^V \nabla(\mu_A - \mu_V) - L_{AB}^V \nabla(\mu_B - \mu_V) \\ \vec{J}_{BV} = -L_{BB}^V \nabla(\mu_B - \mu_V) - L_{AB}^V \nabla(\mu_A - \mu_V) \\ \vec{J}_{AI} = -L_{AA}^I \nabla(\mu_A + \mu_I) - L_{AB}^I \nabla(\mu_B + \mu_I) \\ \vec{J}_{BI} = -L_{BB}^I \nabla(\mu_B + \mu_I) - L_{AB}^I \nabla(\mu_A + \mu_I) \end{array} \right. \quad (51)$$

In comparison with the thermal diffusion, gradients of point defect chemical potential are nonnegligible. Under irradiation, L_{ij} coefficients vary with point defect concentrations evolution. New constants associated with temperature, a crystallographic structure and an alloy composition were defined, the partial diffusion coefficients d_{ij} (i=A,B and j=V,I):

$$d_{ij} = \frac{1}{6} \lambda_j^2 Z_j \omega_{ij} \quad (52)$$

where λ is the jump length, Z_i is the number of nearest neighbours to the atom i and ω is the effective jump frequency of an atom-point defect pair.

They are linked to the partial fluxes by these relations:

$$\vec{j}_i^j = d_{ij} x_j \Phi \nabla c_i \text{ and } \vec{j}_j^i = d_{ij} x_i \nabla c_j \text{ (i=A,B and j=V,I)} \quad (53)$$

with c the concentration and x the atomic fraction.

In order to simplify the expression of the total fluxes, total diffusion coefficients are defined:

$$D_V = d_{AV} x_A + d_{BV} x_B \quad D_I = d_{AI} x_A + d_{BI} x_B \quad D_A = d_{AV} x_V + d_{AI} x_I \quad D_B = d_{BV} x_V + d_{BI} x_I \quad (54)$$

Fluxes of atoms and defects are given as:

$$\begin{cases} \vec{J}_A = \vec{j}_A^V + \vec{j}_A^I - \vec{j}_V^A + \vec{j}_I^A = -D_A \Phi \nabla c_A + (d_{AV} \nabla c_V - d_{AI} \nabla c_I) x_A \\ \vec{J}_B = \vec{j}_B^V + \vec{j}_B^I - \vec{j}_V^B + \vec{j}_I^B = -D_B \Phi \nabla c_B + (d_{BV} \nabla c_V - d_{BI} \nabla c_I) x_B \\ \vec{J}_V = -(\vec{j}_A^V + \vec{j}_B^V - \vec{j}_V^A - \vec{j}_V^B) = (d_{AV} - d_{BV}) x_V \Phi \nabla c_A - D_V \nabla c_V \\ \vec{J}_I = \vec{j}_A^I + \vec{j}_B^I + \vec{j}_I^A + \vec{j}_I^B = -(d_{AI} - d_{BI}) x_I \Phi \nabla c_A - D_I \nabla c_I \end{cases} \quad (55)$$

where Φ is the thermodynamic factor and $\nabla c_B = -\nabla c_A$, see equation (12).

As $x_B = 1 - x_A$, solute and defects atomic fraction evolution can be expressed by three independent equations:

$$\begin{cases} \frac{\partial c_A}{\partial t} = -\nabla \cdot [-D_A \Phi \nabla c_A + (d_{AV} \nabla c_V - d_{AI} \nabla c_I) c_A \Omega] \\ \frac{\partial c_V}{\partial t} = -\nabla \cdot [(d_{AV} - d_{BV}) c_V \Omega \Phi \nabla c_A - D_V \nabla c_V] + K_0 - R c_I c_V - \sum_S k_{VS}^2 D_V (c_V - c_V^{eq}) \\ \frac{\partial c_I}{\partial t} = -\nabla \cdot [-(d_{AI} - d_{BI}) c_I \Omega \Phi \nabla c_A - D_I \nabla c_I] + K_0 - R c_I c_V - \sum_V k_{IS}^2 D_I c_I \end{cases} \quad (56)$$

Here $c_i = x_i \Omega$ the atomic fraction can be expressed in terms of volume concentration and the average atomic volume Ω .

The RIS model can account for preferential interstitial binding by adding a binding energy term E_b^{Ai} for a particular solute, i.e. solute A. The resulting partial mixed dumbbell concentrations are given as:

$$\begin{cases} c_{Ai} = c_i \frac{c_A \times e^{E_b^{Ai}/k_B T}}{c_A \times e^{E_b^{Ai}/k_B T} + c_B} \\ c_{Bi} = c_i \frac{c_B}{c_A \times e^{E_b^{Ai}/k_B T} + c_B} \end{cases} \quad (57)$$

As equal numbers of PDs are produced and annihilate by mutual recombination or at sinks (if there is no sink bias), when the steady state is reached, we have:

$$\vec{J}_A = \vec{J}_B = 0 \text{ and } \vec{J}_i = \vec{J}_V \quad (58)$$

From equalities of III-22 and expressions of fluxes III-19, at the stationary state, we get:

$$M_A = \frac{\nabla c_A}{\nabla c_V} = \frac{c_A c_B d_{Bi} d_{Ai}}{\Phi(d_{Bi} c_B D_A + d_{Ai} c_A D_B)} \times \left(\frac{d_{AV}}{d_{BV}} - \frac{d_{AI}}{d_{BI}} \right) \quad (59)$$

As the vacancy concentration always decreases towards a defect sink, if A is preferentially transported via vacancies than via SIA, in comparison to B, in others words, if,

$$\frac{d_{AV}}{d_{BV}} - \frac{d_{AI}}{d_{BI}} > 0 \quad (60)$$

then the gradient of concentration of A is in the same direction than the vacancy one. In that case, RIS will result in A depletion and B enrichment at sinks.

The ratio $\frac{d_{AV}}{d_{BV}}$ of the partial diffusion coefficient of solutes A and B against vacancies should be the same as the ratio $\frac{D_{AB}^A}{D_{AB}^B}$ determined from tracer diffusion coefficient after thermal ageing. Therefore, if the variations of diffusivity and migration energy with changing composition follow the variation of the self-diffusion coefficient and self-diffusion energy, the segregation is consistent with a vacancy mechanism [70]. Therefore, thermal diffusion data are useful keys to understand RIS vacancy mechanism. Unlike vacancies, the diffusion of interstitial cannot be measured from thermal diffusion experiment. Because of their high formation energy, concentration of this type of point defect is extremely low under thermal ageing. Thus, interstitial diffusivities information can only be obtained after irradiation, there is a crucial lack of diffusion data on this field.

- RIS in concentrated ternary system A-B-C

In a ternary system, solutes and point defects total fluxes in the alloy are related to partial fluxes by these expressions:

$$\left\{ \begin{array}{l} \vec{J}_A = \vec{J}_{AV} + \vec{J}_{AI} = \vec{j}_A^V + \vec{j}_A^I - \vec{j}_V^A + \vec{j}_I^A \\ \vec{J}_B = \vec{J}_{BV} + \vec{J}_{BI} = \vec{j}_B^V + \vec{j}_B^I - \vec{j}_V^B + \vec{j}_I^B \\ \vec{J}_C = \vec{J}_{CV} + \vec{J}_{CI} = \vec{j}_C^V + \vec{j}_C^I - \vec{j}_V^C + \vec{j}_I^C \\ \vec{J}_V = -(\vec{J}_{AV} + \vec{J}_{BV} + \vec{J}_{CV}) = -(\vec{j}_A^V + \vec{j}_B^V + \vec{j}_C^V - \vec{j}_V^A - \vec{j}_V^B - \vec{j}_V^C) \\ \vec{J}_I = \vec{J}_{AI} + \vec{J}_{BI} + \vec{J}_{CI} = \vec{j}_A^I + \vec{j}_B^I + \vec{j}_C^I + \vec{j}_I^A + \vec{j}_I^B + \vec{j}_I^C \end{array} \right. \quad (61)$$

Partial diffusion coefficients are linked to the partial fluxes by these relations:

$$\vec{j}_i^j = d_{ij} x_j \Phi_i \nabla c_i \text{ and } \vec{j}_j^i = d_{ij} x_i \nabla c_j \text{ (i=A,B,C and j=V,I)} \quad (62)$$

Giving,

$$\left\{ \begin{array}{l} \vec{J}_A = -D_A \Phi_A \nabla c_A + (d_{AV} \nabla c_V - d_{AI} \nabla c_I) x_A \\ \vec{J}_B = -D_B \Phi_B \nabla c_B + (d_{BV} \nabla c_V - d_{BI} \nabla c_I) x_B \\ \vec{J}_C = -D_C \Phi_C \nabla c_C + (d_{CV} \nabla c_V - d_{CI} \nabla c_I) x_C \\ \vec{J}_V = (d_{AV} - d_{CV}) x_V \Phi_A \nabla c_A + (d_{BV} - d_{CV}) x_V \Phi_B \nabla c_B - D_V \nabla c_V \\ \vec{J}_I = -(d_{AI} - d_{CI}) x_I \Phi_A \nabla c_A - (d_{BI} - d_{CI}) x_I \Phi_B \nabla c_B - D_I \nabla c_I \end{array} \right. \quad (63)$$

As $x_C = 1 - x_A - x_B$, solute and defects atomic fraction evolution can be expressed by four independent equations:

$$\left\{ \begin{array}{l} \frac{\partial c_A}{\partial t} = -\nabla \cdot [-D_A \Phi_A \nabla c_A + (d_{AV} \nabla c_V - d_{AI} \nabla c_I) \Omega c_A] \\ \frac{\partial c_B}{\partial t} = -\nabla \cdot [-D_B \Phi_B \nabla c_B + (d_{BV} \nabla c_V - d_{BI} \nabla c_I) \Omega c_B] \\ \frac{\partial c_V}{\partial t} = -\nabla \cdot [(d_{AV} - d_{CV}) \Omega c_V \Phi_A \nabla c_A + (d_{BV} - d_{CV}) \Omega c_V \Phi_B \nabla c_B - D_V \nabla c_V] + K_0 - R c_I c_V - \sum_S k_{VS}^2 D_V (c_V - c_V^{eq}) \\ \frac{\partial c_I}{\partial t} = -\nabla \cdot [-(d_{AI} - d_{CI}) \Omega c_I \Phi_A \nabla c_A - (d_{BI} - d_{CI}) \Omega c_I \Phi_B \nabla c_B - D_I \nabla c_I] + K_0 - R c_I c_V - \sum_V k_{IS}^2 D_I c_I \end{array} \right. \quad (64)$$

Here again, $c_i = x_i \Omega$.

By analogy with the binary system, the preferential mixed dumbbell formation for the solute A can be written:

$$\left\{ \begin{array}{l} c_{Ai} = c_i \frac{c_A \times e^{\frac{E_b^{Ai}}{k_B T}}}{c_A \times e^{\frac{E_b^{Ai}}{k_B T}} + c_B + c_C} \\ c_{Bi} = c_i \frac{c_B}{c_A \times e^{\frac{E_b^{Ai}}{k_B T}} + c_B + c_C} \\ c_{Ci} = c_i \frac{c_C}{c_A \times e^{\frac{E_b^{Ai}}{k_B T}} + c_B + c_C} \end{array} \right. \quad (65)$$

At steady state, if the thermodynamic factors are taken as unity, the discriminants of RIS M_i (i=A,B,C) are defined by these equations:

$$\begin{cases} M_A = \frac{\nabla C_A}{\nabla C_V} = \frac{C_A(d_{AV}d_{BI}C_BD_C + d_{AV}d_{CI}C_CD_B - d_{AI}d_{BV}C_BD_C - d_{AI}d_{CV}C_CD_B)}{d_{AI}C_AD_BD_C + d_{BI}C_BD_CD_A + d_{CI}C_CD_AD_B} \\ M_B = \frac{\nabla C_B}{\nabla C_V} = \frac{C_B(d_{BV}d_{CI}C_CD_A + d_{BV}d_{AI}C_AD_C - d_{BI}d_{CV}C_CD_A - d_{BI}d_{AV}C_AD_C)}{d_{AI}C_AD_BD_C + d_{BI}C_BD_CD_A + d_{CI}C_CD_AD_B} \\ M_C = \frac{\nabla C_C}{\nabla C_V} = \frac{C_C(d_{CV}d_{AI}C_AD_B + d_{CV}d_{BI}C_BD_A - d_{CI}d_{AV}C_AD_B - d_{CI}d_{BV}C_BD_A)}{d_{AI}C_AD_BD_C + d_{BI}C_BD_CD_A + d_{CI}C_CD_AD_B} \end{cases} \quad (66)$$

Here again, the sign of M_i gives the RIS tendency for element i:

$$\begin{cases} M_i > 0 \rightarrow \text{i depletion} \\ M_i < 0 \rightarrow \text{i enrichment} \end{cases}$$

Despite the relative complexity of the continuum model of RIS, especially due to the experimental difficulties to measure independently all of the input terms, a lot of phenomena occurring during irradiation (Table 10) are not taken into account.

Table 10 – Pros and cons of the continuum model of RIS

+	-
<p>IKE and interstitial drag mechanisms are taken into account</p> <p>PD concentration gradients and evolution (Production-Annihilation)</p>	<p>Only substitutional elements</p> <p>Vacancy drag mechanism and sink bias are not considered</p> <p>Cluster defects (dislocation loops, cavities, ...) are not considered</p> <p>Chemical potential gradients are the only driving forces</p> <p>Correlation factors are removed for simplicity</p> <p>Effect of local composition change is neglected</p> <p>Solubility limit and precipitation are excluded</p>

However, the development of accurate models for RIS relies on knowing the diffusivities for all elements, PD-solute interactions and solubility limits. Three ways to obtain them - from experiments, from CALPHAD database or first principles simulation (*ab initio*) - can be envisaged. Unfortunately, in practice, it is very difficult to get such information from experimental measurements, especially for concentrated and multicomponent alloys, and for interstitials diffusion. Nevertheless, few experimental results have been widely used to fit mean-field or Monte Carlo simulations of RIS in the Fe-Ni-Cr system:

- Rothman's [19] performed tracer diffusion experiment in thermally aged Fe-Ni-Cr system. He was able to extract effective jump frequencies ratios and correlation factors for each element (most of the time taken equal to unity in RIS models).
- Dimitrov et al. [94–98] performed resistivity experiments on Fe-Ni-Cr alloys irradiated at low temperature where PD are immobile. The increase of resistivity induced by the PD

formation during irradiation was recovered nonuniformly during isochronal annealing on a large temperature range. The mobility of point defects was deduced from the recovery behaviour. Average jump frequency activation energies can be obtained by analysing the change of resistivity variation-rate which results from a change of annealing temperature. As resistivity variation can be due either to the defect-jump rate or to a change in atomic order promoted by defect jumps (formation of PD clusters), the resulting activation energies are approximated. Major conclusions on RIS understanding were made thanks to their set of experiments. Unirradiated and irradiated samples show the same resistivity level above 800K, where back diffusion happens because the thermal vacancy concentration largely increase. Regarding the electrical resistivity variations, three different recovery stages can be distinguished: below 200K, from 200K to 600K and above 600K. Below 200K, the resistivity decrease was attributed to the recombination of close Frenkel pairs involving only few jumps of the more mobile defect (self-interstitial) and these take place in the strain-field of the antagonist defect (vacancy). From 200K to 600K, the resistivity increased because long-range migration of self-interstitial starts followed by vacancies one. Above 600K, decrease of resistivity was connected to the dissociation of defect clusters or of defect-impurity clusters. The joint results of resistivity and positron lifetime measurements during the isochronal recovery annealing allowed the respective mobility of self-interstitial and vacancy-type defects to be determined. The mobility of self-interstitials increases with increasing nickel content, whereas the increase in Cr content reveals an opposite effect. On the contrary, the mobility of vacancies seems to be independent of the variation in composition in both cases.

- Watanabe and al. [99] performed electron irradiations at 50°C where the interstitial mechanism of RIS is dominating and revealed Ni enrichment, Cr and Fe depletion at grain boundary.
- Allen and Was [70] - with the help of a systematic comparison of RIS at grain boundaries observed by Auger spectroscopy in Fe-Cr-Ni as a function of temperature, nominal composition, and irradiation dose - successfully implemented the Modified Inverse Kirkendall (MIK) model to predict RIS in irradiated austenitic Fe-Cr-Ni alloys. In the MIK model, diffusivities are dependent on the local chemical potential gradients.

Despite successful attempts to reproduce RIS levels at grain boundaries of different model alloys, RIS is still challenging to predict for trace elements and other sink types because of competing mechanisms and a lack of reliable diffusion data under irradiation (especially for self-interstitials).

5.6. Phase stability under irradiation

Phase stability is a concern as it can influence mechanical properties, deformation mode and corrosion behaviour. Due to solute redistribution, RIS can lead to areas with local concentrations that are significantly different from the bulk composition. Solubility limits can be locally reached at the vicinity of sinks and lead to radiation-induced precipitation (RIP) as shown in Figure 15.A). Other effects include radiation-modified, -enhanced, or -retarded precipitation or $\gamma \rightarrow \alpha$ phase transformation because of the segregation of austenite stabilizers at sinks [100]. Main precipitates

and solute clusters (i.e. precursor or small precipitates depending on their stoichiometry) observed in irradiated austenitic stainless steels are summarized in Table 11.

Table 11 – Precipitation/clustering under irradiation in 300-series austenitic stainless steels [60,80,101,102]

Radiation retarded thermal phases	Radiation enhanced thermal phases	Radiation modified thermal phases	Radiation induced precipitates
$M_{23}C_6$, MC, σ , χ	M_6C , Laves	M_6C , Laves	γ' , G-phase, MP, M_2P , M_3P , Cu clusters, Ni-Si solute clusters, Si atmospheres, Ni-Si-Mn clusters, Ni-Si-Mo-P clusters, Cu-rich or C-rich clusters

Precipitates formation depends on the alloy composition, the metallurgical state (solution annealed or cold-worked) and irradiation conditions. Precipitation occurs in the intermediate temperature regime, when long-range migration of PD happens, and tend to increase with dose (Figure 15.B)). The main phases induced by irradiation are the silicides γ' and G and the phosphides MP, M_2P and M_3P (Table 12 and Figure 15.C)). The former phase appear also as a thermal phase in P-doped 304L [103].

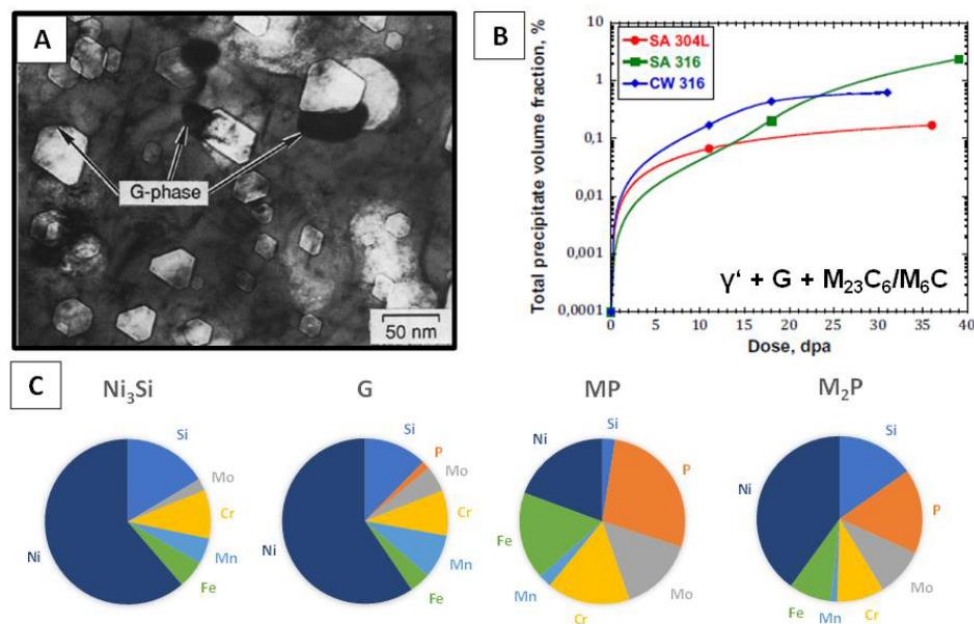


Figure 15 - A) G-phase/cavity association in Fe-14Cr-16Ni-2Mo steel irradiated with neutrons to 11 dpa at 500°C [104]. B) Precipitate volume fraction evolution with dose [105]. C) Radiation induced precipitates composition determined from EDS spectra on replicas in a solution annealed 316 after neutron irradiation at 500-625°C to 8.4 dpa [104].

γ' phase has a stoichiometric composition of Ni_3Si and exhibits a L1_2 ordered structure. It is the most observed precipitate after irradiation. Part of the Si may be replaced by Al, Nb or Ti, and the phase can dissolve other elements as Fe, Cr and Mo. γ' phase has almost the same lattice parameter as the austenite with little or no misfits. RIP of this phase seems to be encouraged in 316 compared to 304L because of higher Ni and Si contents [105]. Dislocations are privileged sites for their nucleation. They have been observed to form near Frank loops in a temperature range between 300 and 500°C [104].

The G-phase have the general formula $\text{M}_6\text{Ni}_{16}\text{Si}_7$, where M can be Ti, Nb, Mn or Cr. This precipitate is difficult to distinguish from M_{23}C_6 using conventional TEM because they have the same crystalline structure, with similar lattice parameter. However, they can be differentiated by their composition. The G-phase can show several crystallographic variants (different orientation relationships with the matrix). This phase is predominant in SA 316 compared to CW 316. The formation of G-phase doesn't seem to occur in 304L compared to 316 [105]. Radiation-induced G phase has been observed to form near voids in a temperature range of 400–650°C (Figure 15.A)) [104]. It forms at higher temperatures and higher doses than the γ' phase [35].

Phosphides can be also encountered. Three types have been reported in irradiated 316 austenitic stainless steels: MP (i.e. FeP with an orthorhombic structure), M_2P (i.e. Fe_2P with a hexagonal structure) and M_3P (i.e. Cr_3P with a body-centered tetragonal structure). They are often found to be associated with voids. Phosphides are minor precipitates in SA 316 found between 400-650°C after 5-30 dpa neutron irradiation. They can apparently dissolve at higher dose [104]. Microstructurally, the M_2P and M_3P phases are often observed as thin needles with axes parallel to $\langle 100 \rangle_\gamma$.

Thermodynamically stable phase formation could be enhanced or retarded by irradiation, depending of the effects of RIS. Enrichments of Ni and Si (and Mo, Cr depletions) due to RIS tend to favor M_6C and Laves formation while retarding formation of M_{23}C_6 , sigma, and χ phases in type 316 stainless steel. Irradiation can also modify phases, i.e. Laves phase can show additional amounts of Ni and Si. Precipitation becomes nearly similar to the one observed under thermal ageing in the high temperature regime [102].

Table 12 – Characteristics of radiation induced precipitates [35,104]

Nature <i>COD</i>	Major elements / Composition	Crystallographic Structure	Orientation relationship with the matrix
G-phase <i>4031670</i>	$M_6Ni_{16}Si_7$ (M=Ti, Nb ,Mn,Fe,Cr) (Ni,Fe,Mo,Cr) $16(Nb,Mn,Cr,Ti)6Si_6$ or 7 (Ni,Fe,Cr) $16(Nb,Ti)6Si_6$	FCC Fm-3m (225) a=11.154 Å	cube-on-cube or random several variants
γ' <i>1538633</i>	Ni_3Si . $Ni_3(Si,Al,Ti,Nb)$ and high solubility of Fe, Cr and Mo	Primitive cubic Pm-3m (221) a=3.542 Å	cube-on-cube : $1/2\{220\}_{\gamma} = \{110\}_{\gamma'}$
MP <i>9008932</i>	FeP	Orthorhombic Pnm/Pbnm (62) a = 5.793 Å b = 5.187 Å c = 3.093 Å	-
M_2P <i>9011403</i>	Fe_2P	Hexagonal-centered trigonal P321 (150) a=6.04 Å c=3.60 Å	$(0001)_{Fe_2P} (001)_{\gamma}$ $(1210)_{Fe_2P} (110)_{\gamma}$ needle axe parallel to $\langle 100 \rangle_{\gamma}$
M_3P	Cr_3P	Body Centered Tetragonal I4 (79) a=9.186 Å c=4.558 Å	needle axe parallel to $\langle 100 \rangle_{\gamma}$

Depending on the technique used for microstructural investigations, precipitates can be clearly identified by the combination of chemical and crystallographic information (TEM). From APT analyses, atmospheres (i.e. diffuse clusters) or clusters can be seen, corresponding to local enrichments (generally in Ni, Si, P) as shown on Figure 16. Ni, Ni-Si, Ni-Si-P, Ni-Si-Mn and Ni-Si-Mo-P clusters have been observed thanks to APT analyses. These clusters are suggested to be precursors or radiation induced-precipitates of γ' and G-phase depending on their stoichiometry (Figure 16). Comparison of their composition and concentration ratios with the literature help to classify these clusters as precursors or precipitates. Post-irradiation annealing [78] demonstrate that radiation-induced precipitates tend to dissolve, they are thermodynamically unstable.

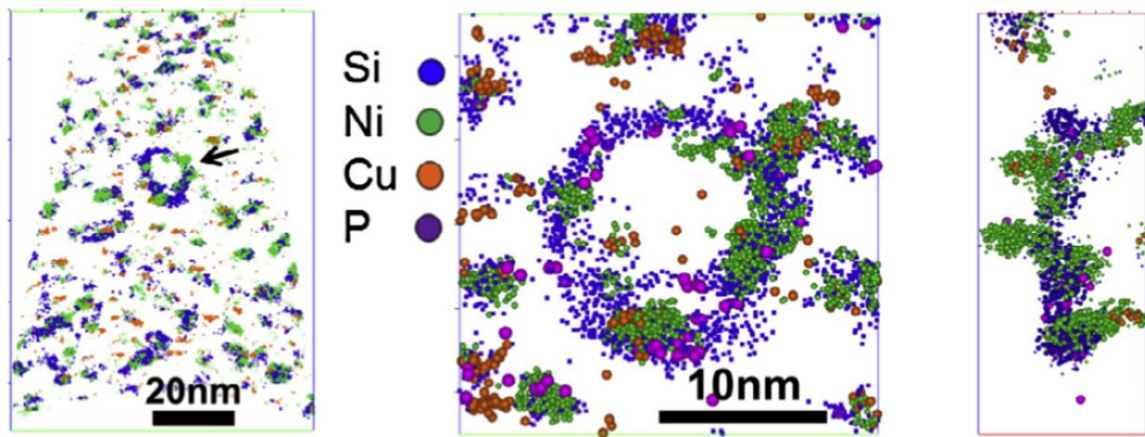


Figure 16 – Filtered APT volume of a 304 SS irradiated with protons at 360°C up to 10 dpa highlighting Si, Ni, Cu and P local enrichments (left) and close-up on a Si-rich dislocation loop pointed by a black arrow decorated with Ni-rich clusters (front view in the center and side view on the right)[83]

To sum up

In nuclear reactors core, when a neutron collides with an atom of the target material, a pair of point defects (PD), i.e. a vacancy and a self-interstitial, known as Frenkel pair, is created. Numerous of PD will be produced in cascade and the total number of point defects will be in far excess compared to thermal vacancies, especially at low temperature where their concentration is low, accelerating diffusion kinetics. Linear, planar and bulk defects interfaces act as sinks for PD. As at sinks, PD concentration is at equilibrium, PD fluxes inside grains arise towards them. Diffusion-driven processes, e.g. segregation and precipitation, will be therefore enhanced, induced, modified or retarded under irradiation.

Depending on the irradiation temperature, 4 regimes can be distinguished:

- at low temperature, PD are immobile and annihilation by short-range mutual recombination happens and small PD clusters are directly created within the cascades (i.e. cascade debris). These defects are too small to be detected either by TEM or APT.
- at intermediate temperature and low sink strength: PD become mobile. SIA start to diffuse first and migrate faster than vacancies. PD can diffuse over longer distance to recombine if the sink strength is low. As diffusion is activated, PD clusters will grow and their number density will decrease with temperature. They become now visible by TEM and APT: black dots, stacking fault tetrahedra, cavities (i.e. He bubbles or voids), faulted Frank loops and perfect loops are features commonly observed in irradiated microstructures.
- at intermediate temperature and high sink strength: PD are mobile and can diffuse over longer distance to annihilate at sinks. Under these conditions, radiation-induced segregation (RIS) is observed at grain boundaries and PD clusters defects created by irradiation. Enrichments of undersized alloying elements as Ni and Si enrichments are observed at sinks while depletion oversized solutes as Cr, Mn and Mo occur. Fe can either segregate or deplete depending on alloy composition and segregation of trace elements as P is also largely observed. Different mechanisms have been identified: the inverse Kirkendall effect and PD-drag, undersized atoms being preferentially linked with SIA. As in Fe-Ni-Cr alloys both mechanisms lead to the same RIS tendencies, their mutual weight in this process is still unclear and is believed to depend on elements/composition, sink bias and irradiation conditions. Solute redistribution is responsible to phase instabilities. Solubility limit can be locally reached at sinks leading to radiation induced precipitation, silicides γ' and G-phase being the most reported ones.
- at high temperature: thermal vacancies equilibrium concentration is higher than the PD concentration created by irradiation, leading to back diffusion and PD defects shrinkage follow by their disappearance as the temperature increases (i.e. recovery stage). This regime is governed by thermal processes, and microstructural changes are similar to the ones expected in section II. Stabilized gas-bubbles can remain at high temperature.

Apart from temperature, other parameters, gathered under the general term of irradiation conditions, have also a considerable impact on microstructure evolution:

- particle type and its energy spectrum: to study neutron irradiated materials is time/cost-consuming and ask for dedicated facilities to protect workers from radiations. Ions irradiations are extensively used to emulate neutrons irradiations and understand fundamental mechanisms involved in damaged microstructures. Heavy ions are interesting particles because they also create PD in cascades. While neutrons energy spectrum is large, ions are quasi-monokinetic. Because of their neutrality and size, neutrons deeply damage the microstructure while ions penetrate materials within a depth of a few microns maximum. Ions do not activate materials and transmutation events that produce He do not happen.
- dose (or fluence): in order to compare the radiation damage from different radiation sources, dose is expressed in terms of displacements per atoms (dpa). Size and number density features induced by radiation damage (i.e. PD defects and RIS/P) increase with dose to a steady state reached after few dpa. This steady state level closely depends on others irradiation conditions, alloy composition and as-received state (solution annealed or cold-worked).
- dose rate (or flux): at higher dose rate, higher PD generation under a short period of time promotes annihilation by mutual recombination versus diffusion at sinks. By increasing temperature, this difference in annihilation modes tends to be reduced and steady state segregation levels can be reached. A temperature shift to higher temperatures due to the higher dose rate is dependent on the microstructure feature of interest (e.g. location of the peak swelling temperature).

All features nature, density and size depend on the material (concentrated elements and impurities, thermomechanical history) and irradiations conditions (particle nature and linked energy spectrum, dose, dose rate and temperature). In order to compare results to the literature, one should carefully describe unirradiated and irradiated microstructure regarding selected irradiation conditions.

Efforts are done by the nuclear materials community to establish relationships between:

- irradiation conditions and the resulting microstructure;
- irradiation conditions and the resulting mechanical properties;
- irradiated microstructure and the mechanical properties.

To do so, mechanisms of processes involved during irradiation should be clearly identified and understood for predictions. As radiation-induced segregation is pointed to play a role on the majority of degradation mechanisms identified for nuclear reactors components, its study is under great interest. **To optimize RIS models, diffusion kinetics under irradiation is a need and suffers from a lack of data, especially for SIA. RIS at grain boundaries has been intensively studied but we showed that radiation PD defects also act as sinks and can be biased. The relative weight of the mechanisms involved can therefore be impacted, furthermore RIS tendencies are usually drawn for major and minor alloying elements, a focus on impurities should be made as well.**

IV. Prediction of microstructural evolution up to 60 years of irradiation: focus on RIS

Long term ageing under irradiation is a major concern for both existing and future generations of reactors. In the context of reduction of PWR maintenance costs during long time operation, ensure reliable mechanical resistance over longer time of use of austenitic stainless steel components is a must. First, to decrease the replacement frequency of components that can be. Second, increase the reactor lifetime limited by the time of use of components difficult to replace. It also applies to SFR with a design life of 60 years, where austenitic stainless steels have been selected for the majority of the primary circuit components, including the irreplaceable reactor pressure vessel. Well understand and finely link microstructural evolution under irradiation to its mechanical response is a key for reliable components lifetime prediction and austenitic stainless steels optimization.

Suspected or confirmed role of RIS on different degradation mechanisms of structural components of the reactors core explains why understanding and modelling RIS is of prime importance for lifetime extension purpose and radiation-resistant material design for new reactor concepts. While grain boundaries sensitization to corrosion caused by Cr depletion and trace element segregation promote embrittlement and intergranular cracking under stress known as irradiation-assisted stress corrosion cracking, RIS on He bubbles affects swelling and RIS on dislocation loops takes part to hardening.

To date, unanswered questions remain:

- Models based on the inverse Kirkendall effect (e.g. Perks and MIK models) validate their input parameters by comparing the calculated diffusion coefficients under irradiation with experimental thermal diffusion coefficients (e.g. ratio of tracer coefficients) [106]. Diffusion kinetics are well established at high temperature in the Ni-Cr binary system. Nevertheless, diffusion coefficients database is poor at the operation temperature ranges of PWR and SFR, especially for the Fe-Ni-Cr ternary system as highlighted in sub-section II.2. The gap of knowledge is even worse under irradiation, and no quantitative data is available to date for diffusion kinetics of SIA due to severe difficulties to decorrelate diffusion occurring via each PD type in the intermediate temperature range.
- Mutual weight of RIS mechanisms for defect sinks other than grain boundaries has not yet been determined, particularly when sinks are biased for a certain type of PD (e.g. cavities, dislocations). Moreover, impurity levels at these sinks are less reported, for two main reasons. First, because of the matrix contribution, signal from trace elements at targeted sinks can be close to the detection limit in STEM-EDS. In addition, this spectroscopy technique is less sensitive to light elements. Second, despite a high chemical sensibility of APT, measured segregation levels cannot be directly and unambiguously linked to the crystallographic nature of sink.

This present work expects to provide new insights to appreciate RIS kinetics and mechanisms:

1. By the experimental determination of interdiffusion kinetics to improve diffusion of point defect models under irradiation in austenitic Fe-Ni-Cr system

It had been shown [107] that nanolayers can be used to obtain interdiffusion coefficients at low temperature under a reasonable time. These coefficients are determined from the concentration profiles amplitude evolution after thermal ageing and have been obtained by APT at 440°C. In parallel, TEM investigations have been performed to characterize the microstructure. To highlight irradiation effect on diffusion kinetics, the same method is applied and radiation damage is finely quantified.

Towards improvement of physical diffusion point defect models under irradiation in austenitic stainless steels (e.g. MIK), model alloys are studied both theoretically and experimentally in the framework of the GEneration IV Materials Maturity (GEMMA) European project (APPENDIX).

Concerning interdiffusion, experiments under isothermal annealings and under ion irradiation have been run on Ni-Cr and Fe-Ni-Cr nanolayers to calibrate and assess the validity of the atomistic kinetic models.

2. Quantifying segregation levels on biased sinks by implementing recent development in terms of nanoscale characterisations on a 316L(N) austenitic stainless steel.

Conventional austenitic stainless steels (i.e. 316/L and 304/L) are continuously developed to give improved service performance, e.g. to reduce swelling (AIM1-type steels) or improve creep properties 316L(N). Study improved steels is a need to validate the choice of these material candidates.

As explained in sub-section III.5.5, RIS completely modify chemical distribution of an alloy leading to phase instabilities. Many authors observed RIS on different types of sinks, i.e. grain boundaries, dislocation loops and lines and cavities. Some of them are biased, meaning they preferentially absorb one type of PD: interstitials for dislocation loops and vacancies for cavities. As model validation is based on the fit of experimental data, it is crucial to characterise RIS and associated sinks as precisely as possible. Taking benefits from recent methodological and instrumental developments can help to provide direct correlations between microstructural and microchemistry evolutions.

(S)TEM and APT are extensively used to study microstructural features induced by radiation damage because of their complementarity: accurate crystallography information for TEM and accurate composition measurements for APT. Technological innovations, such as the multiple (2 or 4) Silicon Drift Detector (SDD) configurations for EDS microanalysis, provide significant improvements in EDS solid angle for data acquisition, and have greatly improved microstructural investigations of irradiated materials. STEM-EDS spectrum imaging, which combines STEM imaging with pixel-by-pixel EDX spectra, can clearly reveal RIS on grain boundaries and

irradiation-induced defects. However, EDS is not able to give quantitative enrichments of light trace elements. APT can but is not able to give crystallographic information.

Correlative TEM-APT studies have illustrated the direct comparison of the same features visible via each technique, which can offer both compositional and crystallographic information [108]. Correlative microscopy has been recently used as a new tool to study radiation damage [83,109–111] and will be applied to study RIS in an ion irradiated 316L(N) austenitic stainless steel.

CHAPTER 2

EXPERIMENTAL TECHNIQUES

I.	Analytical Electron Microscopy	56
1.	Basic principle.....	56
2.	Real space to reciprocal space: imaging with diffraction.....	62
3.	Other types of contrast	71
4.	Defect characterization	72
4.1.	Foil thickness estimation	72
4.2.	Black dots imaging	73
4.3.	Cavities imaging	74
4.4.	Stacking fault tetrahedra imaging	76
4.5.	Dislocations lines and loops imaging.....	76
4.6.	Solute segregation measurement	84
4.7.	Precipitates identification.....	87
II.	Atom Probe Tomography	90
1.	Basic principle.....	90
2.	Data acquisition and data treatment	100
2.1.	Acquisition parameters definition	100
2.2.	Reconstruction parameters determination	102
2.3.	Composition measurement.....	104
2.4.	Clusters analysis	106

In order to study diffusion kinetics based on concentration profiles amplitude extraction (i.e. nanolayers method) and to quantitatively characterize RIS on defects in austenite, the techniques chosen should be scaled to the features of interest. Transmission Electron Microscopy (TEM) and Atom Probe Tomography (APT) allow to study crystal (TEM) and chemical (AEM and APT) heterogeneities at the nanoscale. AEM stands for Analytical Transmission Microscopy and includes elemental analysis techniques in addition to TEM ones. Their strengths and limitations make them complementary, and, thanks to a similar specimen size, it is even possible to correlate them to extract the maximum of information from a confined location. This chapter aims to describe basic principle and limitations of each technique taken apart. A focus will be also done on data acquisition and data treatment as they were used to obtain and extract results for this present work.

I. Analytical Electron Microscopy

1. Basic principle

A Transmission Electron Microscope (TEM) is an instrument combining different imaging, diffraction and chemical analysis techniques that cover a large range of scales: from microscopic to sub-atomic scale. The Rayleigh resolution criterion defines that the minimum separation distance between two objects is in the range of the wavelength of the illumination beam. According to this criterion and to the relationship I-1, an electron beam accelerated under a voltage V of 200kV has a wavelength λ_{200kV} allowing a theoretical resolution in the picometer range:

$$\lambda_{200kV} = \frac{h}{\sqrt{2m_0eV(1 + \frac{eV}{2m_0c^2})}} = 2.51 \text{ pm} \quad (67)$$

with h the Planck's constant ($6,626 \cdot 10^{-34} \text{ J.K}^{-1}$), m_0 the electron mass ($9.109 \cdot 10^{-31} \text{ kg}$), e the elementary charge ($1.602 \cdot 10^{-19} \text{ C}$) and c the speed of light in vacuum ($2.997 \cdot 10^8 \text{ m/s}$). Because of the finite size of circular apertures of this optical system, a focused diffracted wave will result in Airy disks instead of a well defined spot. As the aperture size decrease, the disks tend to spread decreasing the ultimate resolution. Therefore, spatial resolution is first limited by diffraction.

Nowadays, many TEM are equipped with Field Emission Guns (FEG) offering high coherency to the beam with small energy spread (i.e. reduced chromatic aberration). Astigmatism, caused by a non-uniform magnetic field because of an imperfect cylindrical symmetry of the lenses, can be corrected by dedicated lenses. Therefore, the most limiting aberrations are:

- the spherical aberration - the on-axis and off-axis rays fail to converge at the same point - which is always positive can be balanced by a defocus (i.e. Scherzer defocus). The defocus magnitude depends on the microscope optics. Aberration-corrected S/TEM can correct it. In this case, high-resolution images are obtained when the sample is at the exact focus (i.e. eucentric position).
- the diffraction limit, which deteriorate spatial resolution when apertures size is reduced.

The best spatial resolution is a bit below 0.1 nm for aberration-corrected S/TEM, permitting to “image” atomic columns. Increasing the accelerating voltage can also help to enhance the spatial resolution but radiation damage can become significant and thereby not relevant for irradiation effect characterizations [112]. Sample thickness is also a key parameter affecting resolution because the beam can broaden when passing through it. Usually in austenitic stainless steels, depending on the technique used and the purpose of investigation, the sample thickness is between 50 nm (e.g. High Resolution imaging) and 150 nm (e.g. dislocation density measurements). For defects quantification, sample is thicker to reduce surface effects (i.e. defects can escape from the surface).

Most of the transmission electron microscopes can work in two different modes: TEM and Scanning TEM (STEM). Each mode gives access to numerous of diffraction and imaging techniques depending on the selected rays, the projected plane by the projection lenses (for TEM) or the camera length, condenser aperture (C2) size and the selected camera or detector and the beam scanning (for STEM).

In TEM mode (Figure 17), the beam is broad, static and quasi-parallel (the convergence semi-angle α_{TEM} is small). Passing through the specimen, part of the electrons are diffracted by atomic planes of the crystal at specific angles. The interatomic distances correspond to the length between the direct beam spot (at the center of the diffraction pattern) and the corresponding diffracted spot. The back-focal plane of the objective lens is the diffraction plane. The diffracted rays are coming from the region of the specimen selected by a selected-area aperture located in the image plane. To image the diffraction pattern, the diffraction plane is projected by intermediate lenses (i.e. projection system) on the camera in CTEM-SAED mode. To obtain a bright field or a dark field image (CTEM-BF or CTEM-DF modes), the direct or diffracted rays are either selected by an objective aperture located in the diffraction plane. The size of the objective aperture defines the collection semi-angle β_{TEM} . The smaller the aperture, the larger the angle. To obtain an image, the projection system projects the image plane on the camera. Finally, in High-Resolution TEM mode, both direct and diffracted rays are necessary to form the image. A large objective aperture can be used to enhance contrast of HR-TEM images.

In STEM mode (Figure 18), a convergent beam scans the specimen. Because of a higher beam convergence ($\alpha_{\text{TEM}} \gg \alpha_{\text{STEM}}$), spots become disks. Disks radius depends on the convergence semi-angle: the larger the angle, the larger the radius. The beam convergence is defined by the condenser aperture size. A single diffraction pattern is obtained at each scan step. An image is formed by selecting un/scattered rays thanks to annular detectors. A BF image is obtained by selecting the unscattered rays, an annular DF image (ADF) is obtained by selecting the diffracted rays and an high-angle annular DF image (HAADF) is obtained by selecting the rays scattered at high angles. Practically, contrasts are often mixed because of disk overlapping (avoidable by reducing α_{STEM}) and not well defined collection angles of the detectors. In order to control the detectors collection angles, user have to change the camera length (i.e. the distance from the sample to the projected image). The larger the camera length, the smaller the distance between disks and the smaller the collection semi-angle β_{STEM} . Obtaining “pure” images ask to sacrifice intensity and resolution (e.g.

when avoiding disk overlapping by decreasing C2 aperture size, the diffraction-limited aberration will increase).

Annular Bright field imaging (not represented in Figure 18) consists to cover the BF detector center with the beam stop. An image is obtained on each detector when the probe is scanned over an area defined by the user: the higher the magnification, the smaller the scanned area. As the lateral resolution is defined by the probe size, if the probe is small enough (i.e. α_{STEM} is large) and the crystal is oriented on a zone axis, atomic resolution is reached by all imaging techniques.

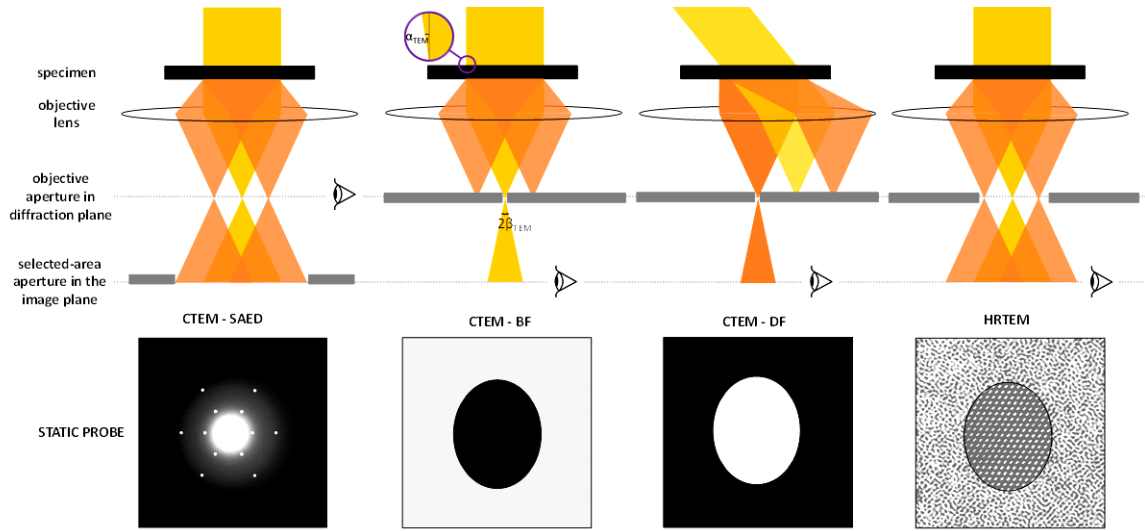


Figure 17 – Ray diagrams of diffraction and imaging techniques in TEM “parallel” mode (from left to right): conventional TEM Selected Area Electron Diffraction (SAED), Bright Field (BF), Dark Field (DF) and High Resolution (HR) TEM. Bottom part: scheme of recorded images by the CCD camera of a gold particle on-axis on an amorphous carbon film depending on the technique used and the projected plane (diffraction or image plane). The diffraction pattern shows spots (from the crystal) and a diffuse hallow (from the amorphous film). In TEM mode, the probe is static, the convergent semi-angle α_{TEM} is small and the collection semi-angle β_{TEM} is controlled by the objective aperture size.

There are three main differences between these two modes for imaging:

- In TEM, the beam is static and parallel whereas in STEM a convergent beam scans the area of interest;
- In TEM, the magnification is controlled by intermediate lenses of the projection system whereas in STEM the magnification depends on the size of the scan dimensions on the specimen.
- In TEM, high resolution images are formed by the interferences (phase shift) between the coherent unscattered beam and the coherent elastically scattered beams whereas in STEM image resolution is directly linked to the probe size.

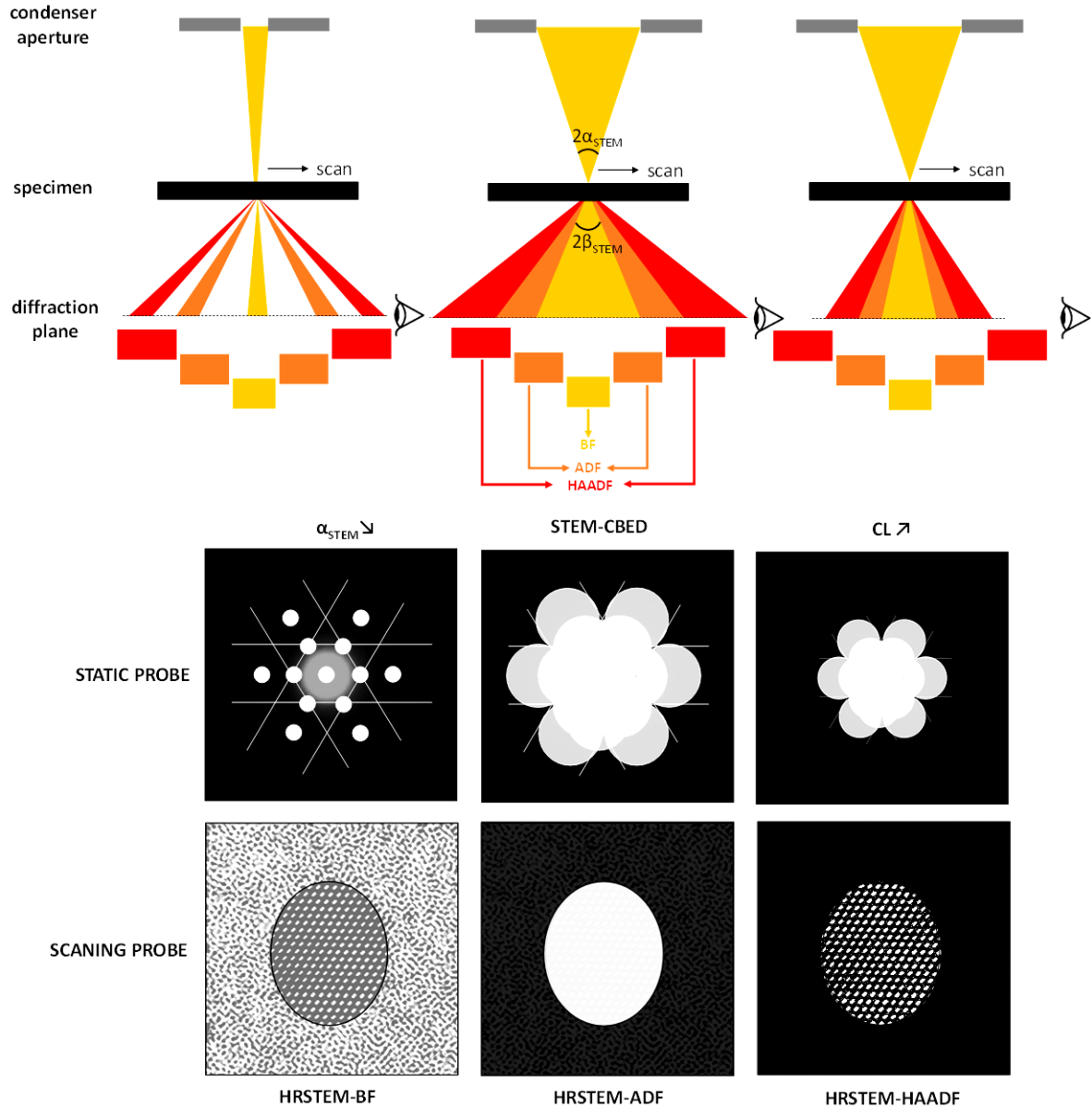


Figure 18 - Ray diagrams of diffraction and imaging techniques in STEM convergent mode. If the probe is static, the Convergent Beam Electron Diffraction (CBED) pattern at the probe location is recorded on a CCD camera (here on the on-axis gold particle of Figure 17). As the beam is convergent, the diffraction pattern shows Kikuchi bands and disks instead of spots which overlap when the convergent semi-angle α_{STEM} is large enough. The collection semi-angle β_{STEM} is controlled by the camera length (CL). When CL is decreased, the CBED pattern is magnified and change the relative contribution of the direct beam (yellow), diffracted beam (orange) and incoherent quasi-elastic scattered electron beam (red) collected by the Bright Field (BF), the Annular Dark Field (ADF) and the High Annular Dark Field (HAADF) detectors.

At a thickness of tens of nanometers range, the sample is “transparent” to electrons (depends on material density). The large majority of the incident electrons are transmitted without interacting with the sample. Nevertheless, the minor part of electrons interacting with matter gives rise to substantial information. As it is summarized on Figure 19.A, scattered electrons can be classified into 3 categories described here after [113]. Depending of the type of scattered electron or secondary beam collected, different imaging and analysis techniques can be defined (Figure 19.B).

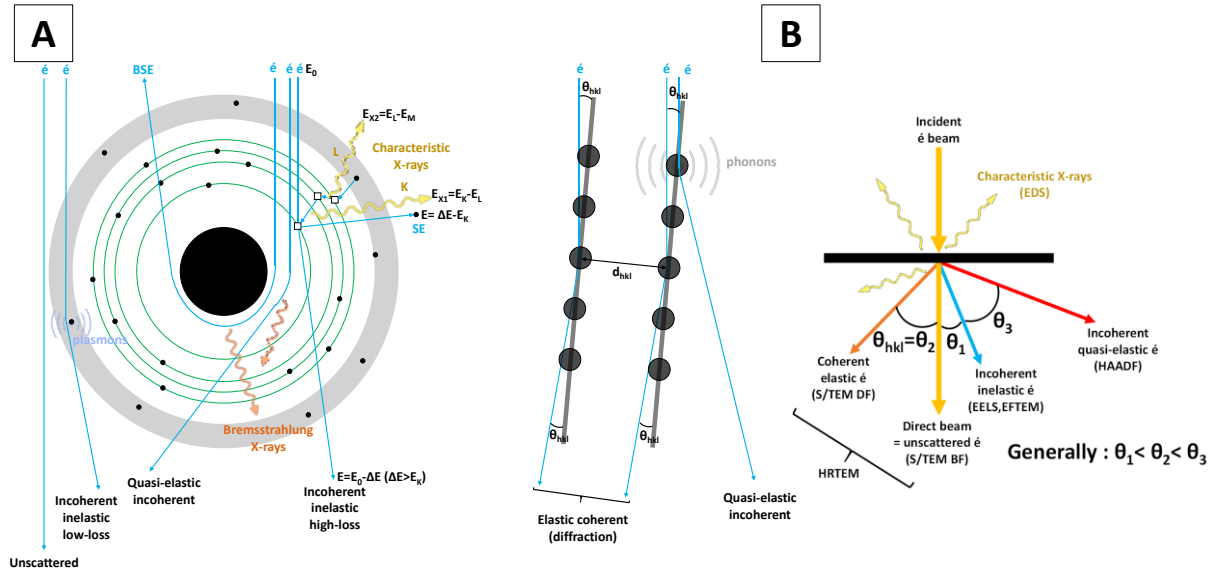


Figure 19 – A) Electron scattering within the atom (left) and within the crystal (right) B) Electrons interactions within a thin specimen, associated scattering angles and techniques

- Incoherent inelastic scattering

Because incident electrons and atomic electrons have the same mass, the energy exchange is efficient. Therefore, depending on the shell level excitation (i.e. outer or core), primary electrons can lose a significant amount of energy. If the electron beam passes through an assembly of free electrons (i.e. conduction band of metals), the transfer of energy can induce collective oscillations inside the electron gas that are called plasmons. Plasmon excitations involve low energy loss (<50 eV) and can repeat several times through the sample thickness. Therefore, the total amount of lost energy by plasmon excitations can be used to estimate the sample thickness thanks to the Energy-Filtered TEM technique (EFTEM).

If the incident electron has enough energy to knock out an inner shell electron, the atom will be ionized. The ejected electron is called a secondary electron. In the case of heavy atoms, an electron from an upper shell drops to fill the vacancy and the atom comes back to its fundamental energy level emitting a photon X. The photon energy is characteristic of a particular element and a particular electronic transition (Figure 20). For light elements, this electronic transition to an inner shell will favour the ejection of an electron from the outer shell called Auger electron, instead of photon X emission. Finally, as the primary electron transferred a consequent energy to allow the expulsion of an electron from the atom core shell, high energy loss has occurred. It corresponds to the threshold energy that is necessary to promote an inner shell electron from its energetically favoured ground state to the lowest unoccupied energy level (>100 eV, Figure 20Figure 17). The electron that ionized the atom is deviated through an angle of $<\sim 10$ mrad. The loss of energy of the primary electron and the energy of the generated photon X are used for chemical analysis, i.e. Electron Energy Loss Spectroscopy (EELS) and Energy Dispersive X-ray Spectroscopy (EDS) respectively, and elemental mapping (EFTEM, EELS and EDS) as shown in Figure 20.

- Incoherent quasi-elastic scattering

If an incident electron transfers a part of its energy to an atom, this atom starts to vibrate. Since all atoms are linked together in a crystal, the vibration of an atom will lead to a collective vibration: the phonons. Phonons can also be generated by other inelastic processes occurring within the atom (e.g. energy of Auger or X-ray emission). Any shaking of the atoms is equivalent to heating up the specimen. Typically, a phonon vibration causes a very small energy loss of < 0.1 eV and the phonon-loss electrons are scattered out to angles of 5–15 mrad. These electrons account for the diffuse background intensity present in electron diffraction patterns.

An electron can be deflected into high angles (> 50 mrad) or even back scattered by the Coulomb field of an atom nucleus (i.e. Rutherford scattering). It is a quasi-elastic interaction because the energy exchange (electrons and atomic nucleus have a great mass difference) is small and emits Bremsstrahlung (Figure 20). The heavier the atom is, the higher the scattering angle is. The coherency of the scattered electrons is related to their angle of scattering (θ). As this angle becomes larger, the degree of coherency decreases and electrons that are Rutherford-scattered out to high angles are incoherent. High angles scattered electrons cause a mass-thickness contrast in High-Angle Annular Dark Field (HAADF) images.

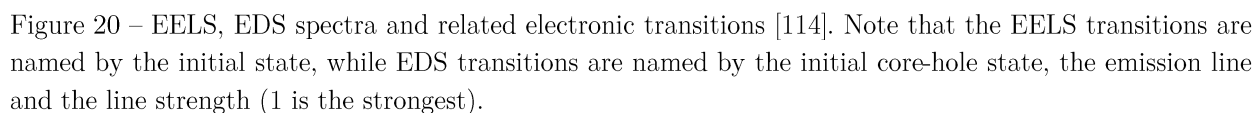
- Coherent elastic scattering

In contrast to Rutherford scattering, electrons that are scattered elastically through angles below 50 mrad are coherent. The intensity of this “low-angle” scattering is strongly affected by the arrangement of atoms within the specimen. Such collective scattering by the atoms refers to diffraction and can only be understood if the electron is treated as a wave. Diffraction is controlled by the angle of incidence of the electron beam, the electrons wavelength λ and the crystallographic structure of the specimen and described in the real space by the Bragg law:

$$n\lambda = 2d_{hkl}\sin(\theta_{hkl}) \quad (68)$$

where n is the order of reflection (integer), d_{hkl} is the interatomic distance between (hkl) planes and θ_{hkl} is the Bragg angle (i.e. at which electrons are reflected).

Coherent elastic scattering is used to identify a structure or to study imperfections of the crystal thanks to Bright Field/Dark Field (BF/DF) imaging, Selected Area Electron Diffraction and Convergent Beam Electron Diffraction (SAED/CBED).



A crystal has two lattices: one in the real space (or direct space), the second in the reciprocal space (Figure 21). It is a convenient representation to understand diffraction patterns generation in TEM.



If the electron beam is diffracted by the specimen in the real space, the space where the electron diffraction pattern forms is the reciprocal space and the image plane is back again in the real space. The transformation from the real space to the reciprocal space is mathematically given by the Fourier transform.

The incident and diffracted beams have wave vectors \mathbf{k}_0 and \mathbf{k}_{hkl} respectively. The difference between those vectors is defined as the scattering vector \mathbf{G}_{hkl} and the angle between them is equal to $2\theta_{hkl}$ with θ_{hkl} the Bragg angle. In the case of diffraction (elastic interaction), \mathbf{k}_0 and \mathbf{k}_{hkl} have the same magnitude ($1/\lambda$), so they define a sphere of radius $1/\lambda$ called the Ewald's sphere (Figure 23.A)) with λ being the wavelength of the electron beam. The observed diffraction pattern is the part of the reciprocal lattice that is intersected by the Ewald sphere, each diffraction spot on the diffraction pattern is described by a particular scattering vector \mathbf{G}_{hkl} from the pattern center (i.e. the direct beam spot). Diffraction occurs when the condition $\mathbf{k}_{hkl} - \mathbf{k}_0 = \mathbf{G}_{hkl}$, \mathbf{G}_{hkl} being defined also as the crystal's reciprocal lattice vector. In electron diffraction, due to the extremely small wavelength, the Ewald sphere is almost flat and intersects with many reciprocal lattice points at the same time. The reciprocal vector \mathbf{G}_{hkl} is normal to the family of lattice planes (hkl) in the direct space and the magnitude of the reciprocal lattice vectors is proportional to the reciprocal of the length of the direct lattice vectors: $G_{hkl} = 1/d_{hkl}$ with d_{hkl} the distance between (hkl) atomic planes. For the n-ary order of diffraction, $nG_{hkl} = n/d_{hkl}$.

At certain orientation of the crystal relative to the beam direction, many sets of planes families are in diffraction conditions. A zone axis is the common direction $\mathbf{B} = [\text{UVW}]$ shared by several (hkl) crystal planes. Crystal planes obeying this relation: $hU + kV + lW = 0$ belongs to \mathbf{B} . As λ is extremely small, the reflecting lattice planes are almost parallel to the direct beam. Thus, the incident electron beam represents approximately the zone axis of the reflecting lattice planes. Note that a zone $[\text{UVW}]$ is represented as a vector in real space but as a plane (i.e. the corresponding diffraction pattern) in the reciprocal space.

A useful tool to link the real space to the reciprocal space (i.e. to link crystal orientation to the recorded diffraction pattern) is the stereographic projection (Figure 22), a graphical representation of 3D directions in a 2D drawing which preserves angular relations. Its construction is well described in [115]. Plane normals (poles) and crystallographic directions are represented on the same projection even if they are not parallel to one another. The angle between the normal of planes (hkl) is the angle between those poles on the projected sphere. It also corresponds to the angle between the corresponding reflections \mathbf{G}_{hkl} in the diffraction pattern. All the plane normals in a particular zone axis $[\text{UVW}]$ will lie on a single great circle of the sphere. These poles at the $[\text{UVW}]$ zone axis represent the possible diffracting planes. So if $[\text{UVW}]$ is in the center of the projection, the hkl reflections will be around the circumference of the projection (the primitive great circle). Stereographic projection helps to index reflections in a diffraction pattern but it is also really useful to determine the tilt and/or rotation angles we should use to image the crystal at the desired diffraction conditions.

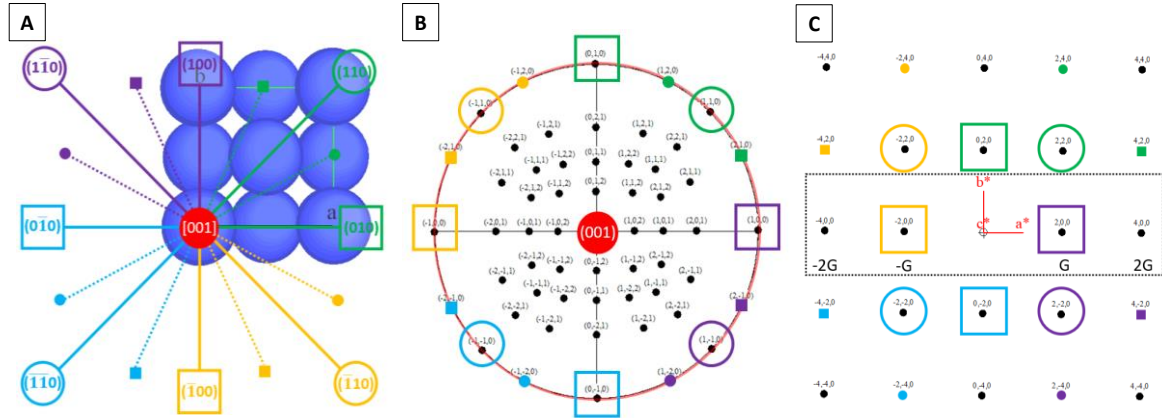


Figure 22 – (hkl) planes belonging to the [001] zone axis of a FCC structure A) in real space, B) in the stereographic projection and C) in the reciprocal space (i.e. as seen on a diffraction pattern). Definition of nG and $-nG$ with n an integer.

As λ is extremely small at 200kV, the part of the sphere projected on the diffraction plane or on the CCD camera is almost flat (Figure 23.B) and C)). Lattice planes appear as rel-rods in the reciprocal space because the specimen is thin.

The Ewald's sphere can be affected by several parameters (Figure 23.D) to I)).

If the sample is thicker, the incident wave vector can be diffracted more than once within sample thickness giving rise to extra spots, namely double diffraction spots (Figure 23.E)). Moreover, relrods are less elongated, therefore the farthest reflections from the direct beam spot fade.

If the direct lattice of the crystal in the real space is tilted, so do its reciprocal lattice in the reciprocal space (Figure 23.F)). So, if the specimen is tilted, the relrods move but the Ewald sphere does not.

Now, if the beam is tilted and not the specimen, the Ewald sphere moves, because the center of the sphere moves too (Figure 23.G)). As the radius of the Ewald sphere is equal to the inverse of electrons wavelength, if the accelerating voltage of the electron beam is decreased, their respective wavelength increases so the radius of the sphere decreases. In this case also, some reflections can fade (Figure 23.H)).

A beam convergence will give rise to numerous of spheres with different center positions (Figure 23.I)).

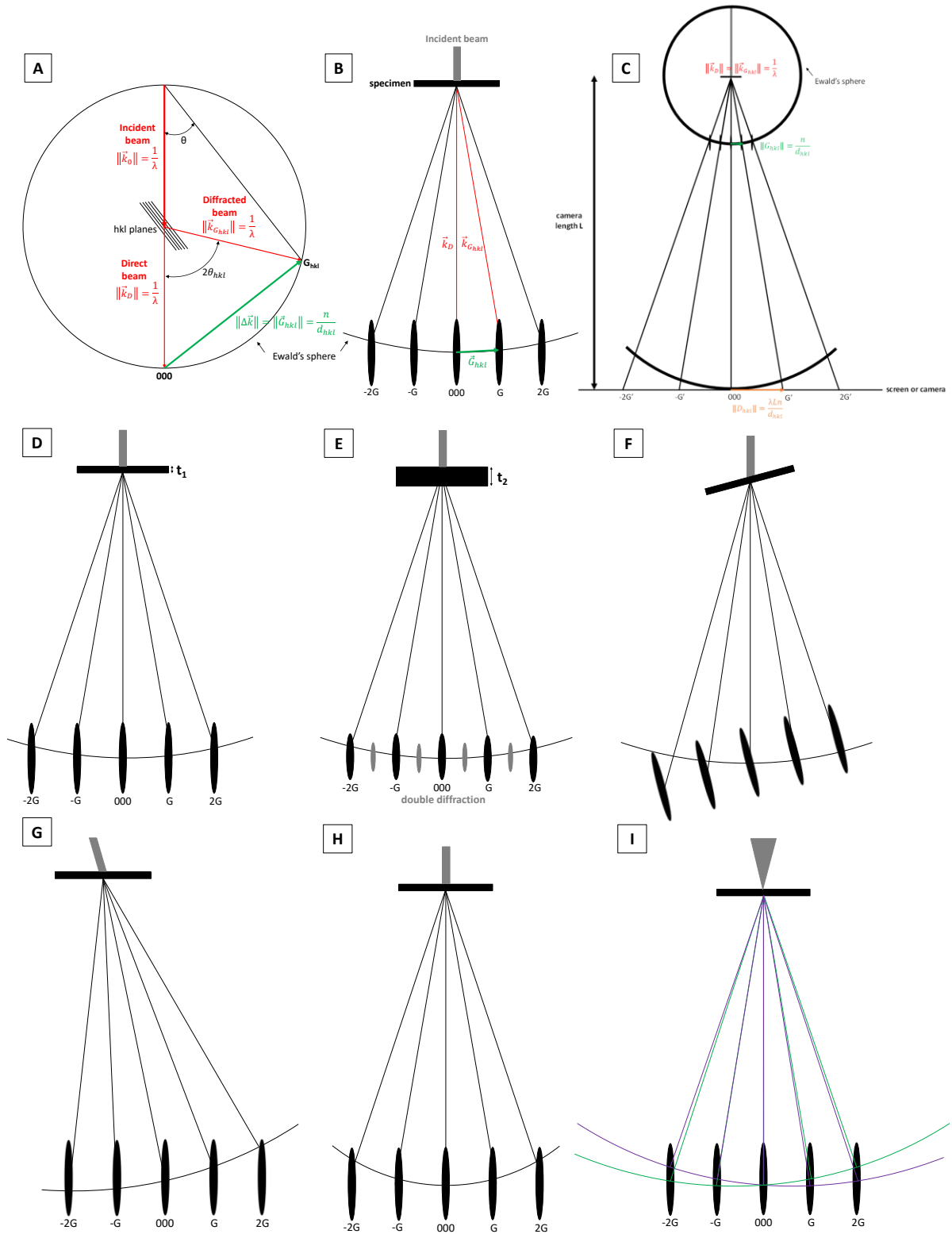


Figure 23 – A) Ewald's sphere construction. The radius of the sphere is equal to $1/\lambda$. B) Ewald's sphere in the diffraction plane, reflecting planes appear as rel-rods because the specimen is thin (reciprocity). C) Projection of the Ewald's sphere on the CCD camera. Effect of E) sample thickness, F) sample tilt, G) beam tilt, H) accelerating voltage (lower V) and I) beam convergence on Ewald sphere reference D).

Information about crystal defects is obtained from different diffraction conditions:

- Multi-beam conditions (zone axis)

Useful information can be extracted from low index zone axis (i.e. h,k,l have small integer values) of high symmetry.

Second phases can give rise to extra spots and be identified from SAED patterns. Orientation relationship with the matrix can be deduced (Figure 24.A)) and they can be imaged thanks to DF-TEM by isolating a spot from the precipitate in the diffraction plane with an objective aperture. One should be careful and generate a DF-TEM image from each extra spot present in the diffraction pattern in order to check if all spots belong to the same precipitates. Indeed, several crystallographic variants can coexist (even in a single particle).

Nanocrystalline materials will generate a ring pattern (Figure 24.B)), each ring radius corresponds to different interplanar spacings of (hkl) planes of a particular phase.

Twinned materials exhibit a mirror symmetry in the diffraction pattern (Figure 24.C)). The common direction between the mirror plane and the diffraction pattern plane is perpendicular to the twinning plane.

If the number density of stacking faults is large enough, on-axis SAED patterns can show spots with streaks running through them (Figure 24.D)). These streaks run perpendicular to on-edge stacking faults bands.

Double diffraction occurs when a diffracted beam traveling through a crystal is rediffracted either within the same crystal (same orientation but thick specimen or different orientation within the thickness) or when it passes through a second crystal. If the initial diffraction vector of the beam is \mathbf{G}_1 and it is rediffracted by reflection \mathbf{G}_2 , then the resulting diffraction vector of the double-diffracted beam is $\Delta\mathbf{G} = \mathbf{G}_1 - \mathbf{G}_2$. If \mathbf{G}_2 is not allowed reflection in the first crystal, the double diffracted beam is characteristic of neither the first nor the second crystal (Figure 24.E)).

Interpretation of diffraction patterns is sometimes not straightforward (Figure 24.F)). Understanding the effect on SAED pattern of each feature separately is necessary.

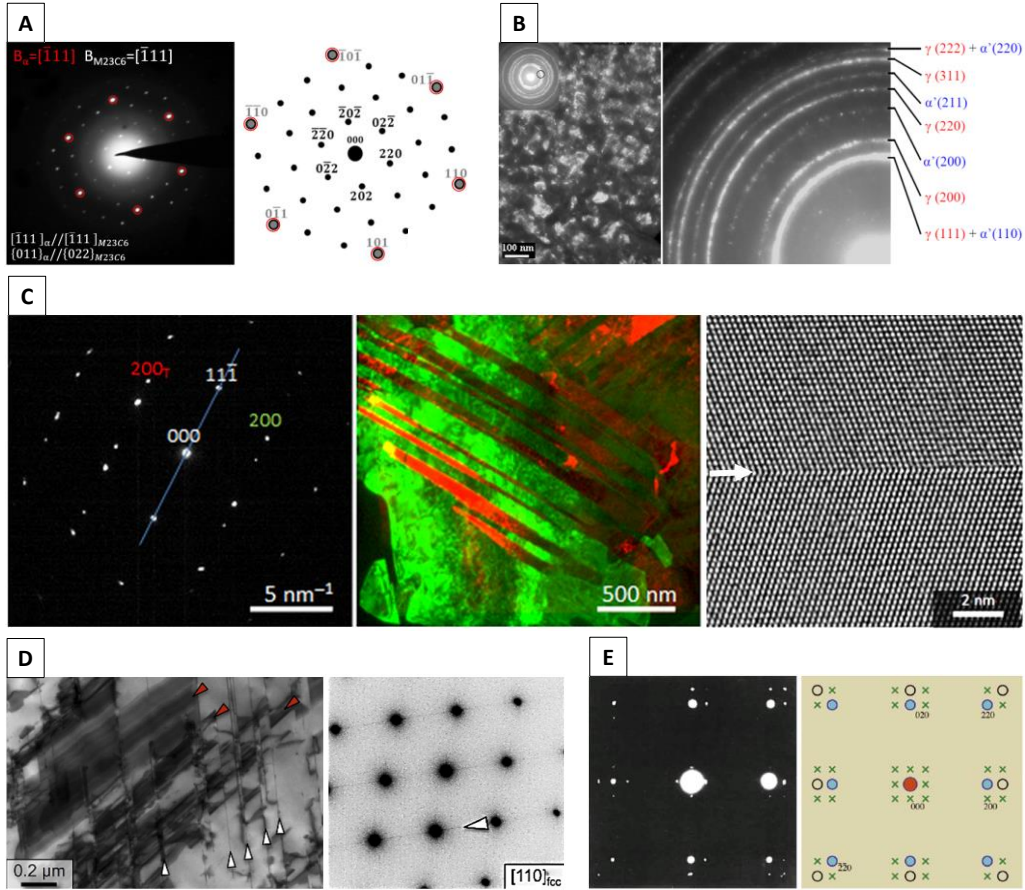


Figure 24 – Signature of common crystal defects on SAED patterns. A) Second phase identification and orientation relationship with the matrix from a single grain B) Typical ring pattern from nanocrystals, second phase identification and associated DF image of a selected region on the pattern by the objective aperture (black circle) [74]. C) Mirror symmetry of a twinned grain along $[11\bar{1}]$ in a FCC crystal highlighted by the blue line (edge-on plane) on SAED pattern with $B=[110]$. Color-coded overlay of TEM-DF images of the matrix in green and twins in red $\{200\}$ reflections. HRTEM image of a twin boundary (white arrow)[116]. D) Streaks formation on SAED spots normal to the edge-on stacking fault direction of the corresponding TEM-BF image (white arrows). No visible contribution in the SAED pattern of the stacking faults closed to in-plane orientation marked with red arrows [117]. E) Experimental and simulated SAED pattern of two aligned crystals oriented on $B=\langle 001 \rangle$ zone axis. Closed circles correspond to crystal 1, open circles to crystal 2 and crosses to double diffraction of rediffracted beams from crystal 1 by crystal 2 [115].

- 2-beam conditions

Within a grain containing a high number density of defects, diffraction contrasts can become challenging to interpret. Under 2-beam conditions, the beam will be scattered by a single set of planes. Sample is oriented in a way that only two spots are excited in the diffraction pattern, the direct spot and one \mathbf{G} . As \mathbf{G} should be known for further analyses, the crystal is first oriented to a zone axis, where the diffraction pattern is indexed, and then tilted to 2-beam conditions following $-g/g$ Kikuchi bands revealed by increasing the beam convergence (Figure 25). The distance in reciprocal space between the $-g$ and g Kikuchi lines is G . If the direct beam is exactly parallel to the plane (hkl) , the g and $-g$ Kikuchi lines are symmetrically displaced about 000 spot with the g Kikuchi line “passing through” $G/2$ and the $-g$ line “passing through” $-G/2$.

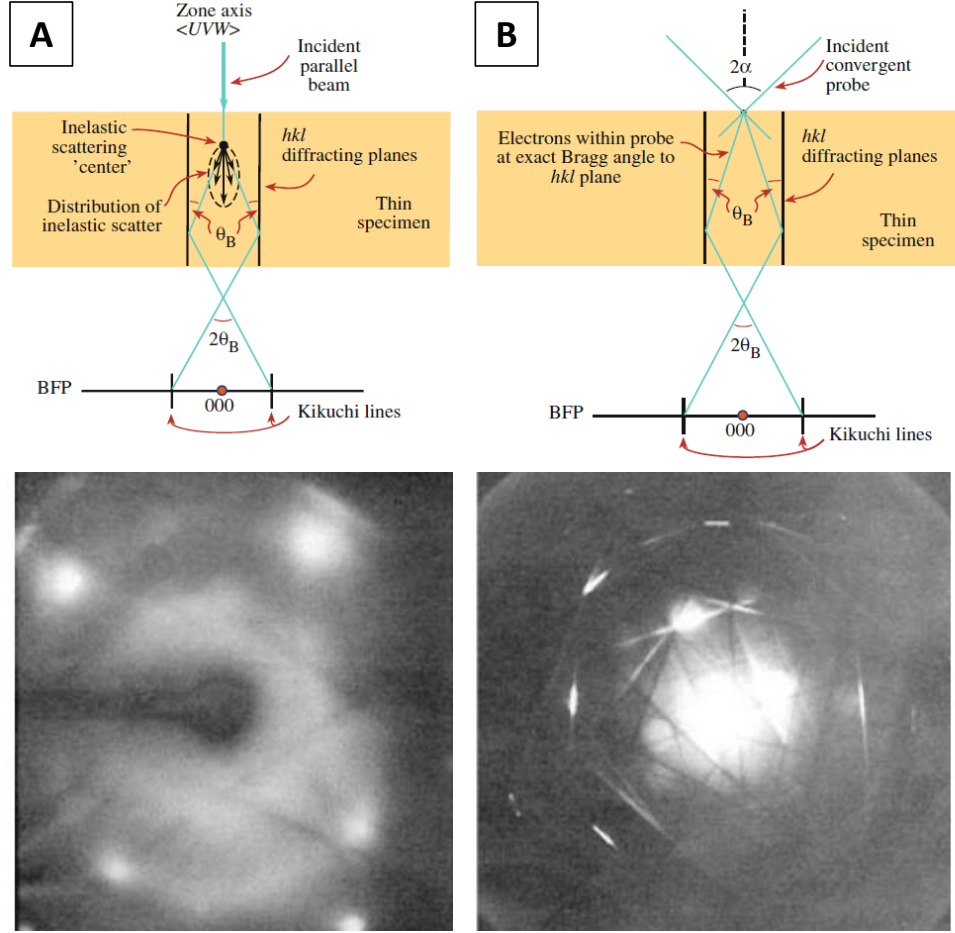


Figure 25 – Kikuchi lines generation from A) a secondary scattering event: diffraction of inelastically scattered electrons in a thick specimen in TEM when the beam is parallel and B) a primary scattering event: diffraction of incident electrons when the beam is convergent. When the specimen is thin enough and the electron beam is parallel, Kikuchi lines do not appear in the diffraction pattern, only spots [115].

A reflection \mathbf{G} is strongly excited when the Kikuchi line g passes through the spot \mathbf{G} whereas \mathbf{NG} is excited when Ng passes through \mathbf{NG} . If g (or Ng) deviates from \mathbf{G} the spot intensity becomes weaker, that means that the Ewald's sphere doesn't intersect exactly the rel-rod center of \mathbf{G} anymore. This deviation from Bragg is defined by s_G , the excitation error also called Bragg deviation parameter. By convention $s_G < 0$ when the Ewald's sphere intersects the upper part of the rel-rod (g line between the direct spot and \mathbf{G}) and $s_G > 0$ when it cuts the lower part. The distance between g and \mathbf{G} (or Ng and \mathbf{NG}) on the diffraction pattern is X (in nm^{-1}) and it is linked with s_G by these following equations:

$$n = \frac{2(NG + X)}{G} - N \quad (69)$$

$$s_G = \frac{1}{2}(n - 1)G^2\lambda \quad (70)$$

where n is the order of diffraction (not necessary an integer except when $s_G = 0$), N is the order of diffraction of the closest diffraction spot (here N is an integer), G is the magnitude of the first order diffraction vector and λ is the electrons wavelength.

In 2-beam conditions, an oscillatory contrast is observable due to periodical extinctions within the sample thickness. The diffraction contrast, either in bright or dark-field images, follows this periodicity, showing maxima or minima along the length of the inclined defect (planar or linear). The spatial extinction period is called the extinction distance ξ_G . It is a characteristic length measured in nanometers for a particular material, reflection G and electrons wavelength:

$$\xi_G = \frac{\pi \cdot V_c \cdot \cos(2\theta_{hkl})}{\lambda \cdot F_G} \quad (71)$$

where V_c is the volume of the unit cell, θ_{hkl} is the Bragg angle and F_G is the structure factor of the reflection G. Depending on the 2-beams diffraction conditions chosen, ξ_G will change.

The kinematical theory describes the evolution of the diffracted beam intensity I_G :

$$I_G = \left(\frac{\pi}{\xi_G}\right)^2 \frac{\sin^2(\pi \cdot t \cdot s_G)}{(\pi \cdot s_G)^2} \quad (72)$$

This equation has only one variable, the thickness t . We can note that $I_G=0$ when $t=\frac{x}{s_G}$ where x is an integer including 0. This equation is only valid when s_G different from 0.

The direct beam and diffracted beam intensities, I_0 and I_G respectively, are complementary:

$$I_G = 1 - I_0 \quad (73)$$

This theory is only valid for very thin specimen or for weak-beam conditions ($s_G \gg 0$) when the intensity of the diffracted beam is much less than the incident beam intensity. In practice, when $s_G \sim 0$, the dynamical theory is applied (i.e. strong beam conditions). I_0 and I_G are not strictly complementary anymore because of absorption effects. I_G expression becomes:

$$I_G = \left(\frac{\pi}{\xi_G}\right)^2 \frac{\sin^2(\pi \cdot t \cdot s_{G,eff})}{(\pi \cdot s_{G,eff})^2} \quad (74)$$

Effective excitation error $s_{G,eff}$ and extinction distance $\xi_{G,eff}$ are defined:

$$|s_{G,eff}| = \sqrt{s_G^2 + \xi_G^{-2}} \quad (75)$$

$$\xi_{G,eff} = \xi_G / \sqrt{1 + (\xi_G \cdot s_G)^2} \quad (76)$$

We can notice that if $s_G=0$, $|s_{G,eff}| = \xi_G^{-1}$ and $\xi_{G,eff} = \xi_G$, meaning that $I_G=0$ when $t=x\xi_G$ with x an integer. Thanks to this property, thickness can be locally determined for a wedge-shaped specimen or the size of a inclined defect in a flat specimen (e.g. stacking fault or dislocation). On the other hand, if $s_G \gg 0$, $|s_{G,eff}| \sim s_G$ and $\xi_{G,eff} \rightarrow 0$, kinematical theory can be applied.

Strong-beam conditions ($s_G \sim 0$) give a broad contrast. The width of the dislocation line image is $\sim \xi_G/3$ whereas for weak-beam image, it decreases to $\sim \xi_{G,eff}/3$ (Figure 26). Hence, crystal defects studies are generally performed under weak-beam conditions. Weak-beam images can be obtained either in bright field or in dark field imaging. The most common technique is the weak-beam dark

field (WBDF) imaging in $\mathbf{G}/n\mathbf{G}$ conditions (Figure 27), conditions specific for the studied material are presented in Table 13. This notation refers to the diffracted spot in the optical axis, \mathbf{G} , selected by the objective aperture to form the image after beam tilt. The Ewald's sphere cuts the row of systematic reflections at $n\mathbf{G}$ where n is not necessarily an integer. It is recommended to use $s_G=0.2 \text{ nm}^{-1}$ (valid whatever the studied material) when defects are studied quantitatively because simulations show that the position of the image can then be directly related to the position of the defect under these conditions. Either for strong or weak beam images, it is recommended to use $s_G>0$. As the value of s_G increases, the intensity of the \mathbf{G} beam decreases very rapidly. The exposure time needed to record an image is long and drift can blur image. Indeed, $s_G=0.2 \text{ nm}^{-1}$ is not a strict rule and the user should find the best compromise for s_G to image defects. If few nanometers defects have to be imaged, it is of course advised to get closer to s_G "magic number".

Table 13 – Values of interatomic distances d , magnitude of \mathbf{G} vector, extinction distance ξ_G , effective excitation error $s_{G,\text{eff}}$ and extinction distance $\xi_{G,\text{eff}}$, nearest excited spot $n\mathbf{G}$ by the $n\mathbf{G}$ Kikuchi line, the corresponding offset X and the corresponding weak-beam dark field conditions taking $s_G=0.2 \text{ nm}^{-1}$ for different sets of diffracting planes in a FCC crystal with a cell parameter equal to 0.359 nm .

(hkl)	$d \text{ (nm)}$	$ \mathbf{G} \text{ (nm}^{-1}\text{)}$	$\xi_G \text{ (nm)}$	$s_{G,\text{eff}} \text{ (nm}^{-1}\text{)}$	$\xi_{G,\text{eff}} \text{ (nm)}$	Excited spot $n\mathbf{G}$ / offset X of $n\mathbf{G}$ line from $n\mathbf{G}$ spot (nm^{-1})	Weak beam DF conditions
(111)	0,2073	4,82	35,50	0,2020	4,95	$6\mathbf{G} / -0.3$	$\mathbf{G}/7.9\mathbf{G}$
(002)	0,1796	5,57	40,97	0,2015	4,96	$4\mathbf{G} / +0.4$	$\mathbf{G}/6.1\mathbf{G}$
(022)	0,1270	7,88	60,79	0,2007	4,98	$\mathbf{G} / -1,7$	$\mathbf{G}/3.6\mathbf{G}$
(113)	0,1083	9,24	75,50	0,2004	4,99	$\mathbf{G} / -0,6$	$\mathbf{G}/2.9\mathbf{G}$
(222)	0,1037	9,65	80,50	0,2004	4,99	see 111	see 111
(400)	0,0898	11,14	101,31	0,2002	4,99	see 200	see 200
(133)	0,0824	12,14	117,89	0,2002	5,00	$\mathbf{G} / 0,5$	$\mathbf{G}/2.1\mathbf{G}$

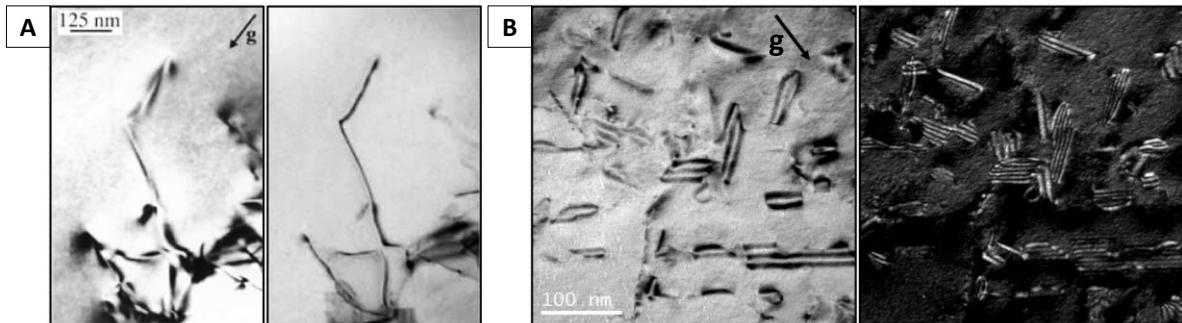


Figure 26 – A) Variation of the diffraction contrast for $s_G=0$ (left) and $s_G>>0$ (right) in CTEM-BF 2-beam conditions $[11\bar{5}]$ B) Frank loops imaged under 2-beam BF-TEM (left) and WBDF $\mathbf{G}/3\mathbf{G}$ (right) conditions. Stacking fault fringes spacings are smaller and better defined in the WBDF image.

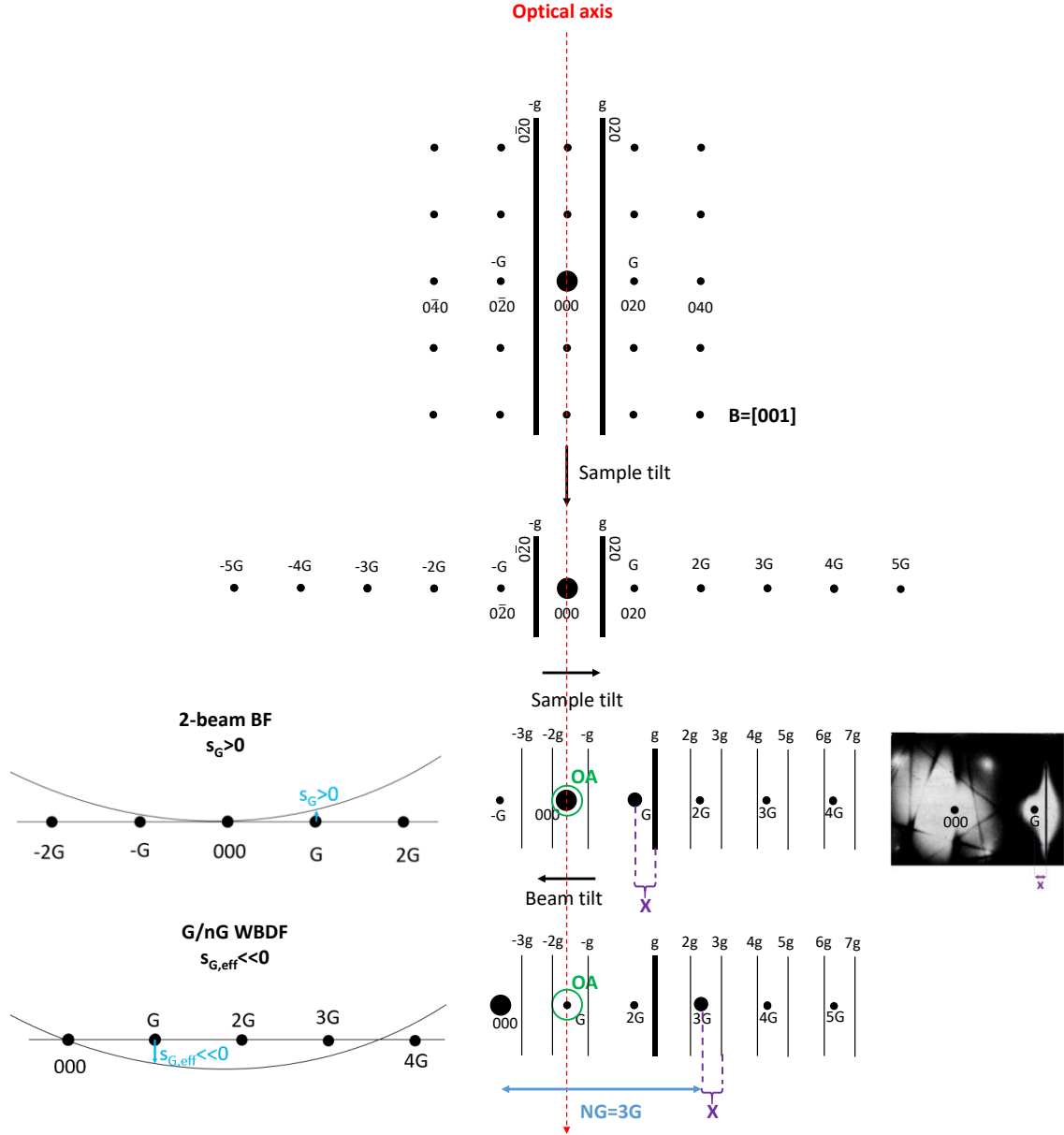


Figure 27 – Weak-beam dark field imaging G/nG near $B \sim [001]$, step-by-step. OA is the objective aperture. In the present example $0 < s_G < 0.2 \text{ nm}^{-1}$.

3. Other types of contrast

- Mass-thickness contrast

At a constant thickness, a phase (crystalline or amorphous) with high Z will strongly scatter electrons and at higher angles (Rutherford scattering) than a low Z phase. In a TEM-BF image, the heavier phase will appear darker. For crystals, a difference in composition will affect the structure factor F_G . As $I_G \propto F_G^2$, the diffracted beam intensity will also change.

STEM-HAADF detector collects quasi-elastic incoherent scattered electrons. The higher Z , the larger the scattering angle: lighter phases appear darker. The thicker, the more scattered electrons: thinner areas appear darker.

- Phase contrast

Contrast in HRTEM images is developed by the interference of two waves: one which doesn't interact with the sample and one which undergoes a phase shift due to the interactions with the sample crystal structure. Atom columns appear in dark.

Fresnel contrast is developed by the interference of two waves, reference vacuum wave and one which scatters off the edges in the sample causing a path length difference and phase shift, resulting in fringe patterns that depend on the focus setting of the microscope.

This first section explained origins of contrasts, based on electron-matter interactions and optical configuration, for interpretation of S/TEM images and diffraction patterns. As described in CHAPTER 1, depending on irradiation conditions, austenitic stainless steels can exhibit a high density of various types of defects. A non-exhaustive review of the techniques used to image/identify/quantify each defect type is presented in the following section.

4. Defect characterization

TEM investigations were performed at 200 kV on the JEOL-ARM200F (cold-FEG, HR pole piece) aberration-corrected both in probe (STEM mode) and in image-forming optics (TEM mode). This electron microscope is equipped with a Gatan Imaging Filter Quantum ER (i.e. for thickness measurements in this present work) and a single JEOL Centurio EDS SDD detector. The high collection solid angle of 0.98 steradians from a detection area of 100 mm² provides high count rates. A double tilt analytical specimen holder was used to reduce shadowing effect during STEM-EDS acquisitions. Specimens were tilted to reach targeted diffraction conditions for imaging and diffraction. In the case of EDS elemental analyses, no tilt was applied. EDS data were collected and post-treated with JEOL Analysis Station software.

4.1. Foil thickness estimation

Because S/TEM images are 2D projections of the sample across its thickness, thickness estimation is a need for defects quantification (e.g. number density) and EDS composition measurements (e.g. X-rays absorption or matrix contribution to the signal). Among the numerous techniques existing for specimen-thickness evaluation, EELS log-ratio technique have been selected for this work.

Plasmons peak intensity in EELS spectrum, I_n , is related to the thickness of the sample. Indeed, plasmon resonance process can occur several times within the sample thickness. The mean free plasmon path Λ_p is the characteristic distance over which the probability of a plasmon event is equal to 1. Along the thickness t of the sample, the probability of producing n plasmon events follows a Poisson law [118]:

$$P(n) = \frac{I_n}{I_{total}} = \frac{\left(t/\Lambda_p\right)^n}{n!} \times e^{-\left(t/\Lambda_p\right)} \quad (77)$$

According to the 0-loss peak this formula can be rewritten:

$$\frac{I_0}{I_{total}} = \frac{\left(\frac{t}{\Lambda_p}\right)^0}{0!} \times e^{\left(\frac{t}{\Lambda_p}\right)} = e^{\left(\frac{t}{\Lambda_p}\right)} \quad (78)$$

The specimen thickness can be obtained this way:

$$t = \ln\left(\frac{I_0}{I_{total}}\right) \Lambda_p \quad (79)$$

A typical error of 15-20% in thickness measurement by this technique is generally reported in the literature at 200 kV, without objective aperture. Under these conditions, Λ_p is very close to 100 nm for austenitic stainless steels [119,120].

4.2. Black dots imaging

As a reminder, back dots, because of their small size (< 2 nm), are defined as unresolvable defects which appear as black spots in TEM bright field S/TEM images.

On TEM on-axis images, black dots can be seen but, under these strong beam conditions, the background diffraction contrast can mask such small defects. Weak-beam dark field imaging gives a better-defined contrast to visualize and quantify them (here they appear as white dots). However, depending on their depth in the foil and the diffraction conditions chosen for imaging, they can be out-of-contrast. Schäublin and al. [121] showed that increasing beam convergency up to 5 mrad can suppress oscillatory contrast related to the effective extinction distance and thus reveals all defects existing within the foil depth. If black dots are small dislocations loops, they will obey the invisibility criteria $\mathbf{G} \cdot \mathbf{b} = 0$ (see section 0), meaning that for particular \mathbf{G} values, black dots will be invisible. WBDF images taken for various \mathbf{G} are therefore necessary for a complete analysis.

Black dots number density is given by this formula:

$$\rho = \frac{N}{A \times t} \quad (80)$$

where N is the number of black dots calculated from the TEM image surface area A, and t is the thickness.

The average size is:

$$\bar{D} = \frac{1}{N} \sum_{i=1}^N D_i \quad (81)$$

with D_i is the diameter of an individual black dot.

The errors in the determination of the density and average size are calculated this way [122]:

$$\varepsilon_\rho = \rho \sqrt{\left(\frac{\sqrt{N}}{N}\right)^2 + \left(\frac{\varepsilon_t}{t}\right)^2} \quad (82)$$

$$\varepsilon_D = \sqrt{\left(\frac{\sigma}{\sqrt{N}}\right)^2 + \varepsilon_m^2} \quad (83)$$

with ε_t is the error of thickness measurement, σ is the standard deviation of the size measurement and ε_m is the measurement error taken as the size of a pixel in the image.

4.3. Cavities imaging

Cavities can either be voids or bubbles filled with gas. In the case on single-beam ion irradiation, only voids can be formed.

- Imaging cavities in TEM mode: bright field (BF) out-of-focus method

In BF TEM, the defocus will cause a phase shift between electrons passing through the cavity and electrons passing through the adjacent perfect crystal giving rise to Fresnel fringes (phase contrast) near the edge of the cavity. Cavities appear as white dots surrounded by a dark fringe in underfocused images, and as dark dots surrounded by a bright fringe in overfocused images. In order to limit diffraction contrast from the other features present in the region of interest, it is advised to tilt the sample away from a low index zone axis. Acceleration voltage, absolute value of defocus and sample thickness will affect the cavity size measurements, especially for small cavities (Figure 28). Small precipitates can also give similar contrast than small cavities. In this case, combination of techniques (e.g. EDS, out-of-focus TEM BF, STEM HAADF) is necessary to conclude on their nature.

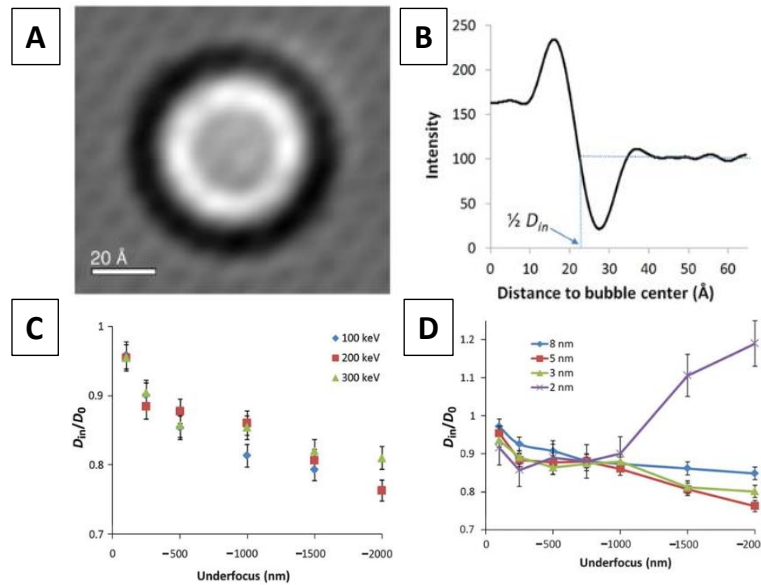


Figure 28 – A) Simulated TEM image of a He bubble with a size of $D_0 = 5$ nm, an accelerating voltage $V = 200$ keV and an underfocus value $\Delta f = -500$ nm and B) the corresponding intensity profile of half of the image with the bubble radius measurement $\frac{1}{2} D_{in}$. Bubble size is under estimated under these conditions. C) and D) Influence of underfocus value and accelerating voltage (in keV not in kV) or bubble size respectively on size measurement (D_{in}/D_0) [123].

- Imaging cavities in STEM mode: HAADF mass-thickness contrast and BF out-of-focus method

Using complementary STEM HAADF imaging is useful to provide an accurate measurement of cavity of small size < 5 nm. In STEM HAADF mode, cavities have a darker contrast than the surrounding matrix because the thickness of material is locally reduced (Figure 29B). However, low-Z precipitates can be confused with cavities. Switching from TEM to STEM mode implies to realign the electron beam and it can sometimes be tricky to find the same imaged zone. Thanks to the TEM and STEM reciprocity theorem (Figure 29A and C)), the out-of-focus method commonly used in TEM to reveal cavities can be achieved in STEM mode, if $\alpha_{\text{STEM}} \approx \beta_{\text{TEM}} \gg \beta_{\text{STEM}} \approx \alpha_{\text{TEM}}$. As in conventional TEM mode, users are working with a near-parallel beam, the aperture semi-angle α_{TEM} is very small and the corresponding collection semi-angle β_{STEM} should be small too whereas the collection semi-angle β_{TEM} , controlled by the objective aperture is larger than α_{TEM} in TEM, so do α_{STEM} within the same angles range. α_{STEM} and β_{STEM} can be tuned by choosing the good condenser aperture C2 and camera length respectively. On one hand, the smaller the C2 aperture (poorer resolution because of the diffraction limit), the smaller α_{STEM} . As in standard STEM operation mode, $\alpha_{\text{STEM}} \gg \beta_{\text{STEM}}$, the use of small condenser aperture is required to reach TEM-STEM reciprocity conditions. On the other hand, the larger the camera length, the larger β_{STEM} . By using these two complementary techniques, one is able to distinguish cavities from small precipitates and provide a reliable cavity size measurement.

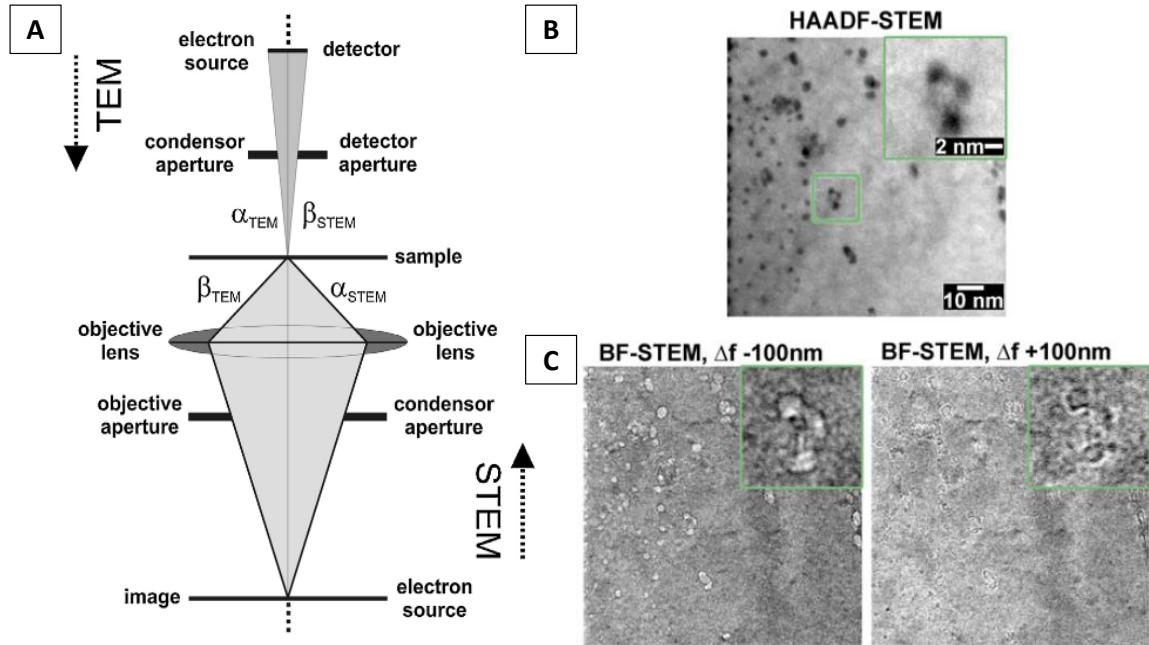


Figure 29 – A) Ray diagrams for TEM (left) and STEM (right) modes. The reciprocal theorem is valid when $\alpha_{\text{STEM}} \approx \beta_{\text{TEM}} \gg \beta_{\text{STEM}} \approx \alpha_{\text{TEM}}$ [124] B) in-focus STEM HAADF mode and C) out-of-focus STEM BF images showing the same Fresnel fringes contrast as in TEM-BF mode [125].

The number density and size of cavities are determined as defined from Eq.(80) to (83) for black dots.

4.4. Stacking fault tetrahedra imaging

Stacking fault tetrahedron is another 3D vacancy-type defect. Because of their small size in FeNiCr austenitic alloys or steels, WBDF imaging with $s_G=0.2 \text{ nm}^{-1}$ is highly recommended for SFT analysis (Figure 30.C)). Thomson's tetrahedron is a schematic representation of SFT structure with its four $\{111\}$ faces that are bounded by stair-rod partial dislocations with $\mathbf{b}=1/6\langle 110 \rangle$. It helps to predict SFT projection shape on a particular zone axis (Figure 30.A) and B)). On $\langle 111 \rangle$ zone axis, it is an equilateral triangle with its sides parallel to three different $\mathbf{G}=\{220\}$, whereas on $\langle 011 \rangle$ it has an isosceles triangle shape with its two equal sides parallel to $\mathbf{G}=\{111\}$ and the third one parallel to $\mathbf{G}=\{220\}$. High-resolution (i.e. on-axis) TEM or STEM is also a way to image them (Figure 30.D)).

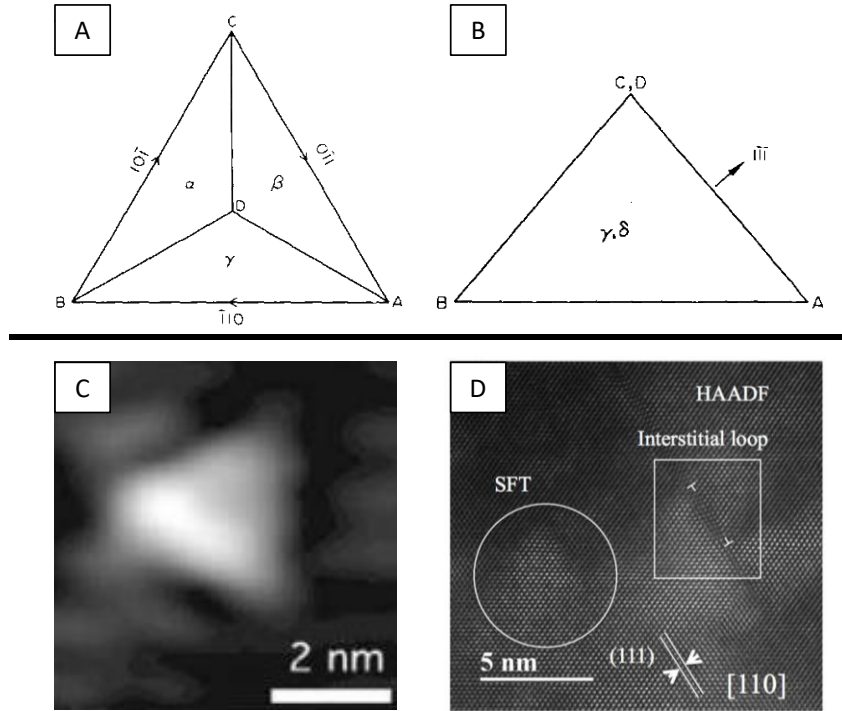


Figure 30 –Thomson's tetrahedron viewed along A) $[1\bar{1}\bar{1}]$ and B) $[1\bar{1}0]$ zone axis [126]. C) WBDF imaging of a nanometre-scale SFT in $G/6G$ diffraction conditions with $\mathbf{G}=\{200\}$ near $B\sim\langle 011 \rangle$ [127] D) HRSTEM-HAADF image taken at $B=\langle 011 \rangle$ illustrates crystal lattice distortions due to a vacancy-type SFT and an interstitial Frank loop [128].

The number density and size of stacking fault tetrahedra are determined as defined from Eq. (80) to (83) for black dots.

4.5. Dislocations lines and loops imaging

Dislocations loops are dislocations whose periphery consists of a dislocation line closed inside the crystal. As for dislocation lines, they are characterized by their Burgers vector \mathbf{b} and it is possible to determine as well their density inside the analysed volume. Other characteristics specific to the loops can be determined : their size, their habit plane and their nature (vacancy or interstitial-type).

- Imaging a dislocation line

Dislocations cause severe local distortions of the surrounding crystal. It is, in fact, the strains in the crystal that provide the diffraction contrast of the dislocation, not the core of the dislocation itself. In the weak beam dark field (WBDF) technique, with large tilts away from a symmetrical diffraction pattern, only the severely-bent Bragg planes near the core of the dislocation contribute to the image contrast [115,129,130]. If s_G is increased, then the planes must bend more to satisfy the Bragg condition, which means the observed peak will move closer to the dislocation core (Figure 31). $s_G=0.2 \text{ nm}^{-1}$ is recommended since it satisfies the requirements that the image should have a narrow width and shows a well-defined contrast between the defect and the background matrix. The intensity of \mathbf{G} spot in diffraction pattern (DP) is weak even though a relatively intense peak may occur in the image close to the defect core because DP averages over a large area. The weak beam dark field image shows the diffraction from bent planes near the core of the dislocation.

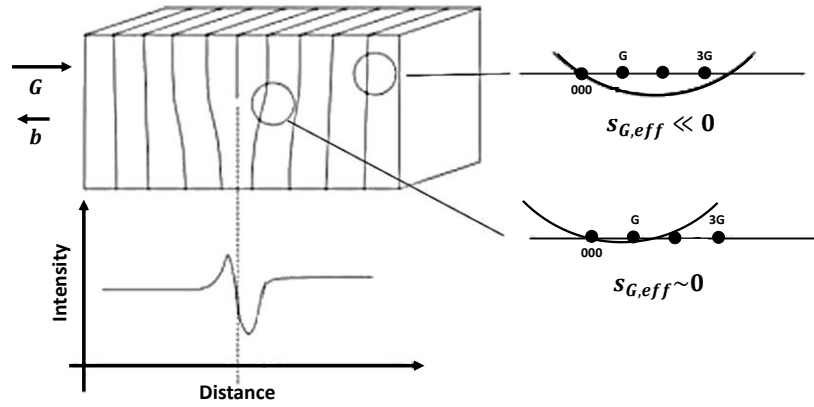
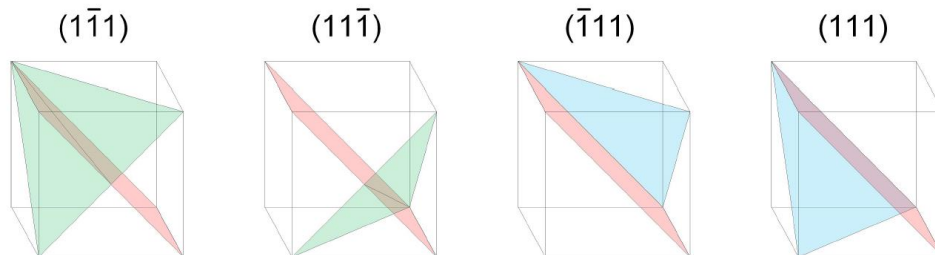


Figure 31 – Change in diffraction conditions at the vicinity of dislocation core and intensity profile of the imaged dislocation [131]. Far from the dislocation core, crystal planes are under weak-beam conditions while at the vicinity of the dislocation core, because they are severely bent, planes are under strong beam conditions.

- Determine loops habit planes

A prismatic loop has its Burgers vector perpendicular to its habit plane. Thus, both faulted Frank loops with $\mathbf{b} = \frac{a}{3}\langle 111 \rangle$ and perfect loops with $\mathbf{b} = \frac{a}{2}\langle 110 \rangle$ and their respective habit planes $\{111\}$ and $\{110\}$ are prismatic. Among the two families of perfect loops, having a perfect crystal at the interior plane of the loop, with a common Burgers vector magnitude $\mathbf{b} = \frac{a}{2}\langle 110 \rangle$ and lying on $\{111\}$ or $\{110\}$ planes, only one is prismatic. Their habit plane can be determined from their projected shape when the specimen is tilted near a zone axis (Figure 32 and Figure 33).



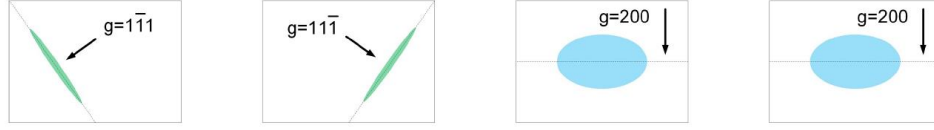


Figure 32 - Scheme of faulted Frank and perfect dislocation loops lying on $\{111\}$ planes (green and blue) imaged near $B \sim [011]$ assuming that loops are circular, the plane in pink corresponds to (011) plane. Loops lying on $(1-11)$ and $(11-1)$ planes (green ones) are viewed edge-on [132]. Here $g = \mathbf{G}$ as it was described before.

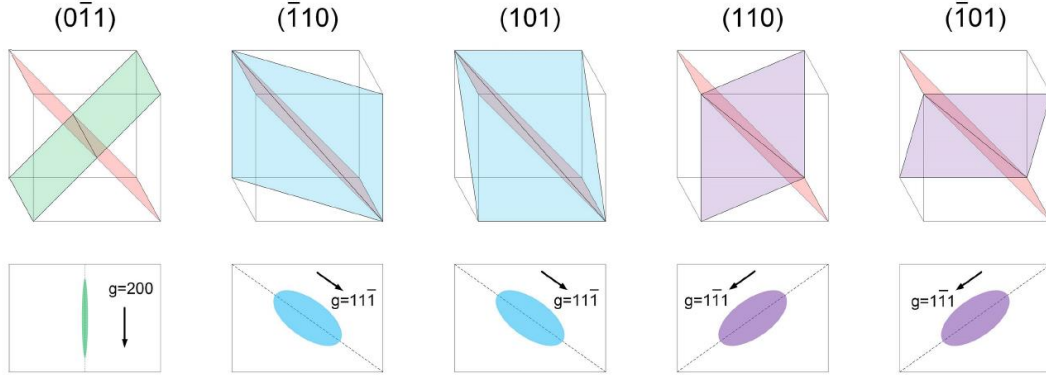


Figure 33 - Scheme of a perfect prismatic dislocation loops lying on $\{110\}$ planes (green, blue and purple) imaged near $B \sim [011]$ assuming that loops are circular. Loops lying on (011) , plane in pink, are invisible for all \mathbf{G} belonging to this zone axis [132].

Images can be either obtained on-axis or in strong or weak 2-beam conditions in TEM-BF or DF mode. On-axis TEM BF image will show almost all dislocation loops population at the same time (except for pure screw loops lying on the plane perpendicular to the selected zone axis) but strong and broad diffraction contrasts can make the analysis difficult. WBDF images will provide well defined loops images but their number density should be corrected because, depending on \mathbf{G} , some of them can be out-of-contrast.

- Determine loops Burger vector

$\mathbf{G} \cdot \mathbf{b}$ analysis is the common method to determine loops Burger vectors \mathbf{b} . Dislocations are invisible when \mathbf{b} is perpendicular to the active \mathbf{G} (i.e. $\mathbf{G} \cdot \mathbf{b} = 0$). This rule is always valid for a pure screw dislocation, where $\mathbf{b} \parallel \mathbf{u}$ with \mathbf{u} the dislocation line vector. For a pure edge dislocation, where $\mathbf{b} \perp \mathbf{u}$, the invisibility criterion only applies when $\mathbf{G} \cdot \mathbf{b} = 0$ and $\mathbf{G} \cdot (\mathbf{b} \times \mathbf{u}) = 0$. As an example, the Figure 34 shows that dislocation segments of the same prismatic loop can be visible or not since the second condition is not fulfilled for all segments. In practice, dislocations are visible only when $|\mathbf{G} \cdot \mathbf{b}| > 1/3$ [130].

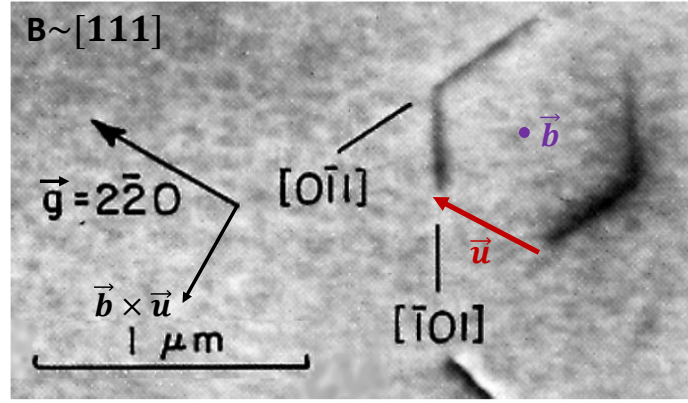


Figure 34 – Hexagonal-shaped Frank loop lying on (111) plane. Loop segments are invisible when \vec{u} and \vec{G} are colinear, even though $\vec{G} \cdot \vec{b} = 0$ for the whole loop. Even if the loop is faulted, no fringes are visible on the image because stacking faults are out-of-contrast when $\vec{G} \cdot \vec{R} = n$ where n is an integer including 0 where $\vec{R} = \frac{a}{3} \langle 111 \rangle$ is the displacement vector (i.e. the shift necessary to produce a stacking fault) [130].

In order to determine loops Burgers vectors, images should be recorded for several 2-beams conditions with different \mathbf{G} (from BF or WBDF images). To ensure a reliable analysis, $\mathbf{G} \cdot \mathbf{b} = 0$ criterion should be fulfilled twice for a unique dislocation. An example of $\mathbf{G} \cdot \mathbf{b}$ analysis is shown Table 14.

Table 14 - $|\mathbf{G} \cdot \mathbf{b}|$ analysis for perfect (PL) and Frank (FL) dislocation loops of an FCC crystal in 2-beam conditions near [011] zone axis. Yellow cells highlight the \mathbf{G}/\mathbf{b} combination for which dislocations should be invisible.

	Habit plane	\mathbf{b}/\mathbf{G}	$11\bar{1}$	$\bar{1}1\bar{1}$	200	02 $\bar{2}$	31 $\bar{1}$	$\bar{3}1\bar{1}$	$\bar{1}3\bar{3}$	13 $\bar{3}$
PL	(111) or ($\bar{1}\bar{1}1$) / (0 $\bar{1}1$)	$1/2[0\bar{1}1]$	1	1	0	2	1	1	3	3
	($\bar{1}\bar{1}1$) or (11 $\bar{1}$) / (011)	$1/2[011]$	0	0	0	0	0	0	0	0
	(111) or (11 $\bar{1}$) / ($\bar{1}10$)	$1/2[\bar{1}10]$	0	1	1	1	1	2	2	1
	($\bar{1}\bar{1}1$) or (11 $\bar{1}$) / (101)	$1/2[101]$	0	1	1	1	1	2	2	1
	($\bar{1}\bar{1}1$) or ($\bar{1}\bar{1}\bar{1}$) / (110)	$1/2[110]$	1	0	1	1	2	1	1	2
	(111) or ($\bar{1}\bar{1}1$) / ($\bar{1}01$)	$1/2[\bar{1}01]$	1	0	1	1	2	1	1	2
Visible PL fraction			1/2	1/2	2/3	5/6	5/6	5/6	5/6	5/6
FL	($\bar{1}\bar{1}1$) extrinsic	$1/3[1\bar{1}1]$	1/3	1	2/3	4/3	1/3	5/3	7/3	5/3
	(11 $\bar{1}$) extrinsic	$1/3[11\bar{1}]$	1	1/3	2/3	4/3	5/3	1/3	5/3	7/3
	($\bar{1}\bar{1}1$) extrinsic	$1/3[\bar{1}\bar{1}1]$	1/3	1/3	2/3	0	1	1	1/3	1/3
	(111) extrinsic	$1/3[111]$	1	1	2/3	0	1	1	1	1
Visible FL fraction			1/2	1/2	1	1/2	3/4	3/4	3/4	3/4

- Distinguishing between perfect and Frank loops

Frank loops are faulted loops whereas perfect loops are not. Hence, Frank loops can be distinguished from any perfect loops by forming a 2-beam images of their enclosed stacking-fault in suitable reflections (e.g. (200) reflections with \mathbf{G} vectors not lying in the loop plane $\{111\}$). If $s_G=0$, the number of dark fringes n in the BF image is such that $(n-1)\xi_G=d$, with d the loop size. For small loops, weak-beam dark field method is recommended because the effective extinction distance is much smaller than in a strong 2-beam bright field image reducing space between fringes.

If the Burgers vector had already been determined without ambiguity, then both types of loops are easily differentiated because Frank loops have a Burgers vector equal to $a/3\langle 111 \rangle$ parallel to their (111) habit plane normal, whereas perfect dislocation loops can have 3 different Burgers vectors type $a/2\langle 011 \rangle$ perpendicular to their (111) habit plane normal.

- Intrinsic (vacancy-type) or extrinsic (interstitial-type) Frank loop

For large Frank loops (large enough to contain several fringes), the method is the same as for stacking faults [130]. In strong 2-beam conditions where $s_G=0$ or s_G slightly positive, inside-outside contrast method on TEM-BF or TEM-DF images permits to determine the loop nature (Figure 35). For large loop, the top and bottom of the stacking fault should first be determined thanks to tilt series of the sample. Then, depending on the visible contrast at the edges of the stacking fault (bright or dark) and the selected \mathbf{G} (or $-\mathbf{G}$) spot, it is possible to determine stacking fault (i.e. loop) nature. For small Frank loops, depending on the inclination of the loop, in BF images, dark fringes will appear inside or outside the loop. If they exhibit the same contrast, they can be differentiated by their inclination (Figure 35.A)). To determine the loop inclination, images taken at different tilt angles with the same \mathbf{G} are necessary.

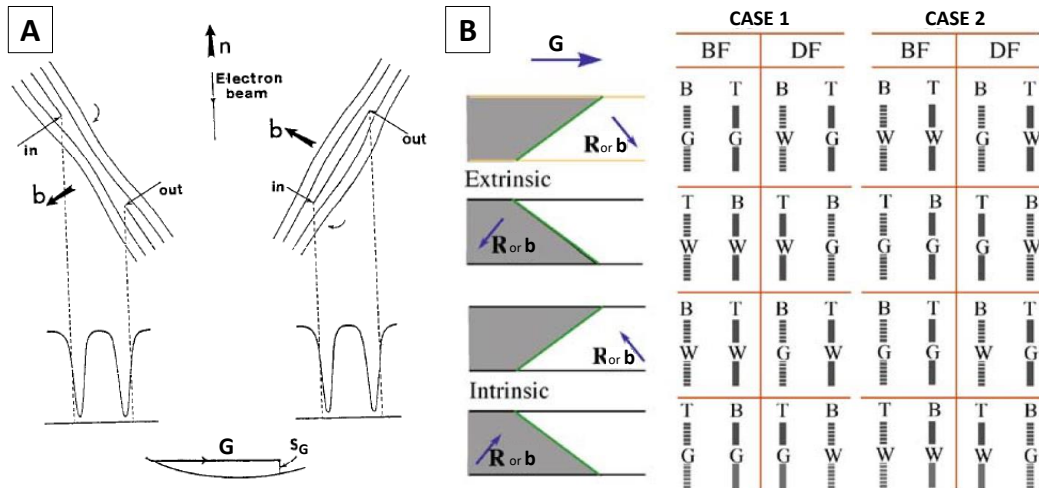


Figure 35 – Schemes of the inside-outside technique for loop nature determination. A) For small loops [129]. B) For large loops or stacking faults. T stands for top and B for bottom of the foil, W for bright fringes and G for dark fringes [115]. Cases 1 and 2 refer to \mathbf{G} or $-\mathbf{G}$ spot selected for imaging.

If the loop is seen edge-on (it is the case for two Frank loop variants at $B=\langle 011 \rangle$), by selecting $\{111\}$ \mathbf{G} and $-\mathbf{G}$ spots in the Fast Fourier Transform (FFT) of a HR-TEM or HR-STEM image will directly reveal the loop nature (Figure 36).

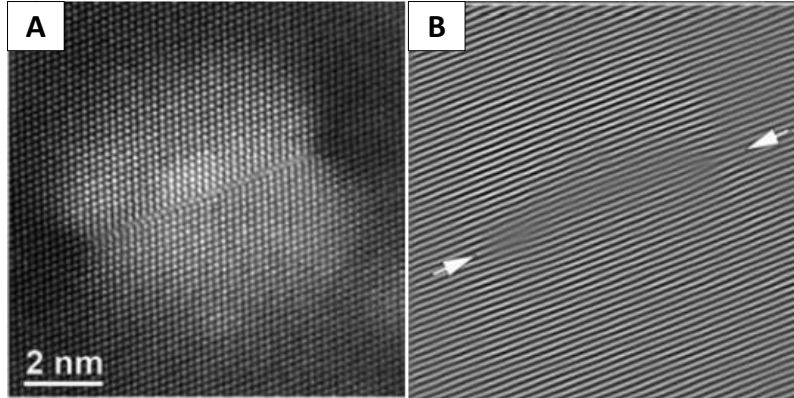


Figure 36 – A) ADF HR-STEM image of an edge-on extrinsic Frank loop. B) Fourier filtered pattern using $\{111\}$ components. The arrows indicate the extra half-plane $[133]$.

- Number density and size of dislocation loops

The most common technique to image Frank loops is the Rel-Rod Dark Field (RRDF technique). The sample is tilted away from $\langle 110 \rangle$ zone axis in 2-beam conditions with $\mathbf{G}=\{113\}$ to intensify streaks between $\{200\}$ and $\{111\}$ reflections. Streaks are then selected by an objective aperture (Figure 37.A) and C)). This technique allows to image 2 variants viewed edge-on for one $\langle 110 \rangle$ zone axis. It is sometimes possible to reach on the same grain a second $\langle 110 \rangle$ zone axis to image the third Frank loop variant. Nevertheless, it is not possible to image the 4 families of Frank loops within a grain by this technique. Assuming that Frank loops are homogeneously distributed in size and number density for all variants, it is possible to multiply results obtained for one variant by 4.

Thanks to the satellite spot method (Figure 37.B) and D)), it is possible to image all Frank loops population. The sample is tilted away from $\langle 100 \rangle$ zone axis in 2-beam conditions with $\mathbf{G}=\{022\}$, satellite spots near $\{200\}$ reflections are then selected by an objective aperture. Since the four variants have the same inclination (55°), the comparative variant measurements are done with more accuracy. As it is not possible to exclude completely matrix contribution of $\{200\}$ spot from satellite spots, images are not as well contrasted than for the RRDF technique.

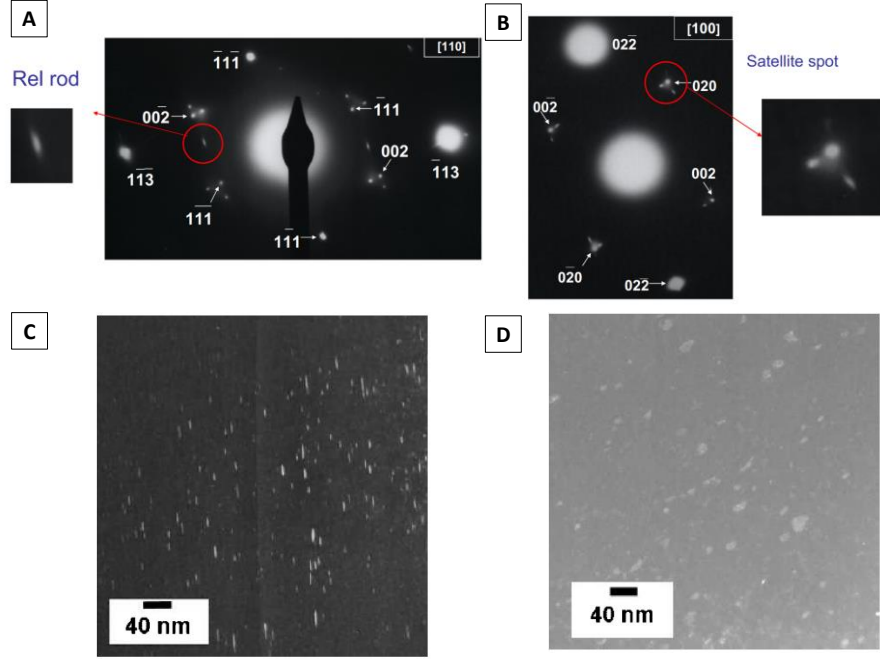


Figure 37 – SAED pattern and corresponding TEM-DF image for A) and C) the RRDF method and B) and D) the satellite spot method to image Frank loops [134].

As perfect loops are not faulted, these previous methods cannot be applied. Conventional WBDF technique should be used and loops should be identified, counted and measured manually.

The number density and size of dislocation loops are determined as defined from Eq. (80) to (83) for black dots.

- Network dislocation density

For as-received specimen characterization, if the dislocation network only exhibits dislocation lines. The dislocation density is given by:

$$\rho_{DN} = \frac{l}{V} = \frac{l}{At} \quad (84)$$

where V is the volume of observed material determined by multiplying the corresponding area A by the sample thickness t . l is the length of dislocation lines, it is related to the projected length of dislocation lines, l_p by this formula [135]:

$$l = \frac{4}{\pi} l_p \quad (85)$$

The projected length can be obtained thanks to image post-processing by multiplying the total number of pixels belonging to dislocations by the pixel size, with the line width equal to one pixel. User should always have in mind that dislocations can be invisible for particular diffraction conditions. On-axis TEM BF imaging permits to reveal almost all dislocations except for pure screw dislocations having a Burgers vector parallel to the beam direction. Bend contours can make the image post-processing harder in TEM images. Thanks to a higher convergence semi-angle in STEM mode, this unwanted diffraction contrast is suppressed (because a convergent beam give access to several deviation parameters s_G). On-axis STEM-BF or ADF (with all G spots detected) is then

advised if the dislocation density is low enough (i.e. if dislocations doesn't overlap within sample thickness). Other features (e.g. precipitates) can contribute to diffraction contrast, they should of course be removed for the analysis. For dislocation density measurements, it is advised to work on thick specimens (i.e. ~ 150 nm for steels) to reduce the proportion of dislocations which have escaped from surfaces of the foil. However, working with thick specimen will limit access to other techniques as high-resolution imaging (i.e. $t < 50$ nm). A sample 80-100 nm thick is a good compromise.

For post-irradiation characterization, if the initial dislocation network totally recovered to leave room to dislocation loops, WBDF technique is more suitable for this kind of analysis. Assuming circular loops, the dislocation length of a loop corresponds to the loop circumference given by:

$$l = \pi d \quad (86)$$

with d the longest length of the projected tilted loop.

The total length of a loop family will therefore be obtained by adding all single loop lengths. For a particular loop nature (i.e. Frank or perfect loop), the total dislocation length is the sum of the total length of each family. However, for certain diffraction conditions loops can be invisible. For $\{200\}$ G reflections near $B \sim \langle 011 \rangle$, all Frank loops variants are visible and 5/6 of perfect loops are visible (Table 14). The total length of all dislocation loops is therefore given by:

$$l = \sum_4 l_{FL} + \frac{1}{6} \times \sum_4 l_{PL} \quad (87)$$

where l_{FL} and l_{PL} are the total dislocation length of a variant of Frank and perfect loops respectively. Equation (84) is then applied.

After irradiation, black dots can also be present. Black dots can be added in the dislocation network density calculation but, as their nature is unknown, one should give a careful interpretation of the result.

If the irradiated sample shows both dislocation loops and lines, their respective density can be determined as presented previously then added.

- Imaging dislocations and stacking faults in STEM

Extensive strain fields around defects makes difficult to obtain exact size and density data in TEM BF. STEM holds many advantages over TEM, under particular conditions, it can suppress bend contours and it is more convenient for thicker samples. It is also possible to access to lower magnification, scan rotation (i.e. image rotation) is useful for features tracking and elemental analysis maps can be acquired without switching mode allowing to correlate defects crystallography to their local enrichment (in some restricted cases - see section 4.6). Thanks to the reciprocity theorem (Figure 29.A)), under specific imaging conditions controlled by several parameters: condenser aperture size, objective aperture size and camera length, traditional **G.b** and **G.R** invisibility criteria are still valid. This requires a complete calibration of the convergence and

collection semi-angles over these latter parameters and the corresponding detectors opening range angles. Examples of applications are presented in Figure 38 and Figure 39.

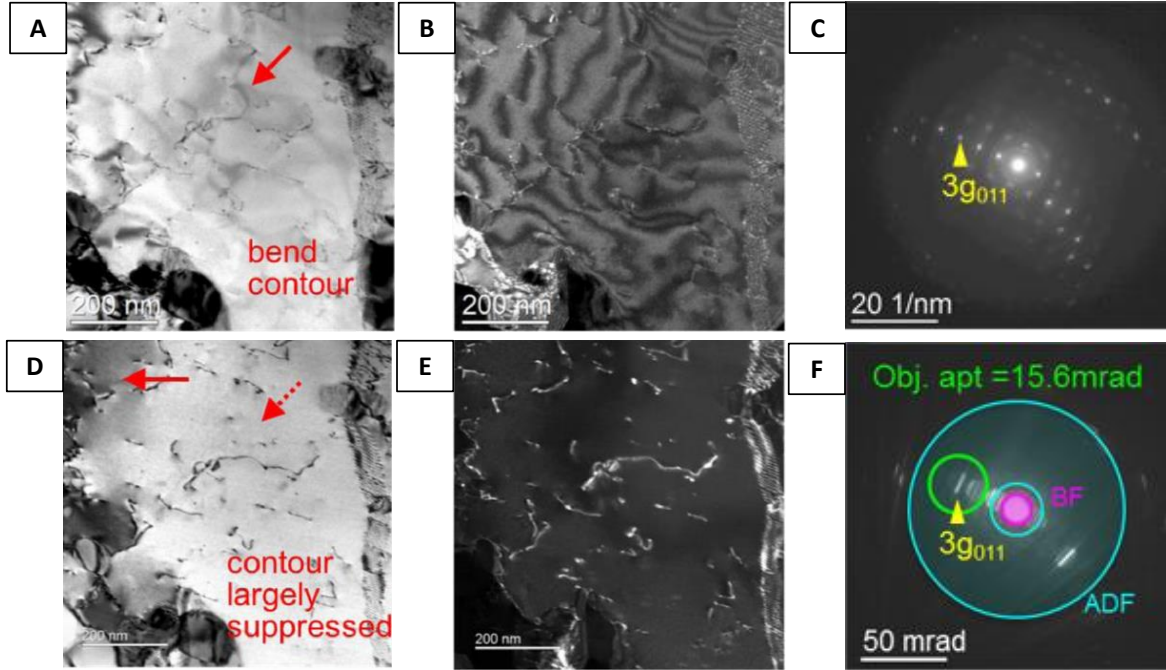


Figure 38 – TEM A) BF, B) WBDF G/3G with $G=011$ near $B \sim \langle 001 \rangle$ and C) the corresponding SAED pattern. STEM D) BF, E) ADF image with 3G selected by a 15.6 mrad objective aperture and F) the corresponding CBED row pattern. STEM images were obtained using $\beta_{\text{STEM}}=6.2$ mrad and $CL=40$ cm [136].

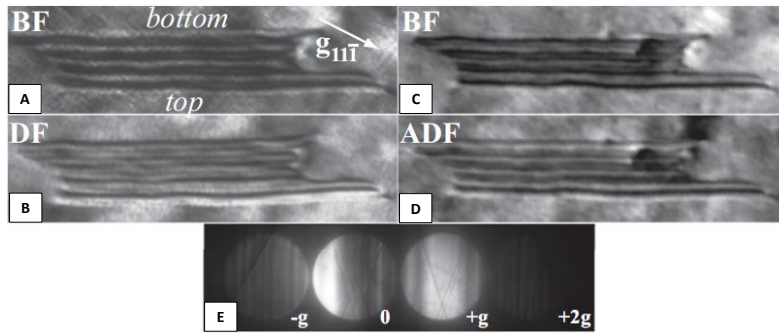


Figure 39 – Imaging of an extrinsic stacking fault with displacement vector $\mathbf{R}=\frac{1}{3}[\bar{1}\bar{1}\bar{1}]$ on the $(\bar{1}11)$ plane in 2-beam A) TEM-BF, B) TEM-DF, C) STEM-BF, D) STEM-ADF and E) the CBED row pattern with $\mathbf{G}=11\bar{1}$ [137].

4.6. Solute segregation measurement

Most of TEM dedicated to irradiation defects analysis are equipped with two elemental spectroscopy techniques: Energy Dispersive X-ray Spectroscopy (EDS or EDXS) and Electron Energy Loss Spectroscopy (EELS). The latter won't be developed thereafter since it is not used in this work.

X-rays energies are characteristic of a particular element and a particular electronic transition. For light elements, this electronic transition to an inner shell will favour the ejection of an electron from the outer shell called Auger electron, instead of the emission of a photon X. Adding the absorption of low energies by the specimen, EDS can therefore detect elements from beryllium for last

generations of spectrometers and fails to accurately quantify light elements. EDS conjugates qualitative and semi-quantitative elemental analysis. EDS spectrum displays the number of detected photons (intensity) as a function of their energy in keV. In STEM mode, elemental maps and profiles can be drawn permitting to link the microstructural defects to their microchemistry. Chemical analysis in EDS is semi-quantitative because the sum of the concentration of identified elements is equal to 100% and a lot of parameters starting from sample geometry to spectrum treatment can affect the resulting quantification.

X-rays from atom deexcitation are emitted in all directions (i.e. 4π sr) but only a small amount is collected ($< \sim 1$ sr) by the EDS detector tilted off the optical axis. In order to perform defect analysis, the sample needs to be tilted to reach certain Bragg conditions (except for cavities). This tilt can shadow X-rays toward the detector. Analytical electron microscopes with multiple SDD EDS detectors allow to collect X-rays by selecting 1 detector or more facing sample surface. As the JEOL-ARM200F used in this study is equipped with a single SDD EDS detector (with a collection solid angle of 0.98 sr), the specimen had been prepared in the required orientation in order to reduce specimen tilt to access to most of desired information. By doing so, it is possible to link defect crystallography with their chemistry. Nevertheless, except for large defects crossing the all sample depth (e.g. grain boundary analysed edge-on to minimize profile broadening), matrix will always contribute to the signal. If the defect is located within specimen depth and depending on its depth, X-ray absorption will be different because the X-ray path through the sample is different. For small enrichments, or for small defects, solute enrichments or depletions can be detected only if enough counts are collected and they are characterized in a qualitative way only. STEM-EDS permits to build spectrum images where each pixel corresponds to a spectrum to highlight elemental distribution in the analysed area. In order to reduce the acquisition time, the dwell time of each acquisition step is very short (few μ s) and pixel spectra suffer of a high background level. Line profiles are preferred for quantitative analysis (e.g. grain boundary). The technique cannot give accurate measurement of light elements because they are highly absorbed, they are often convolute with L-lines of heavier elements and X-ray emission probability is low for light elements. Elements lighter than Be cannot be detected and carbon quantification is not possible because of carbon contamination happening during the acquisition. X-ray signal intensity depends on the mass, but also on specimen thickness. It is advised to acquire spectra on a relatively flat area.

There are two ways to improve considerably EDS maps quality: to obtain high-collection-efficiency X-ray spectrum images (this requires a detector with a high collection solid angle, a well tilted specimen, a high beam current and long acquisition time) and to post-process raw data with the multivariate statistical analysis (MVSA) method of optimally scaled principal component analysis. MVSA post-treatment (Figure 40) will qualitatively assign pixels in the spectrum image to one phase or another to find the underlying spectral contributions to the noisy spectrum image, as well as the spatial distribution of these spectral contributions. This provides a statistically noise filter, which allows to greatly improve the analysis of the X-ray mapping data and the visibility of key features (e.g. grain boundary segregation, small-scale clustering), and the elemental identity of the features [125,138,139].

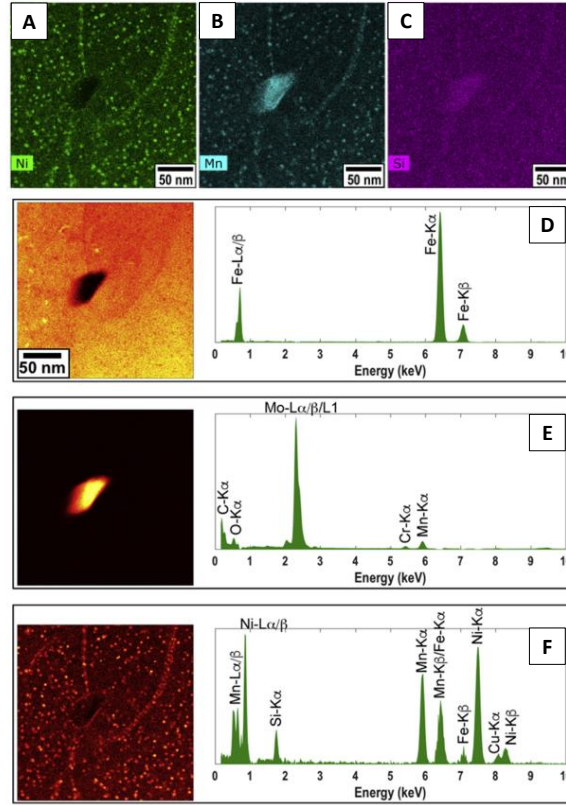


Figure 40 – Raw, unprocessed EDS spectrum images for A) Ni, B) Mn and C) Si. MVSA analysis showing D) the matrix, E) a large Mo-rich precipitate and F) distribution of Ni-Mn-Si-rich precipitates with their respective global spectrum [139].

In this study, EDS data have been collected and post-treated thanks to JEOL Analysis Station commercial software. Acquisition parameters for the STEM-EDS spectrum image dataset collection were a compromise between a sufficient spatial resolution, low spurious X-rays contribution to the signal and high statistics:

- Accelerating voltage = 200 kV ;
- Magnification > 1 Mx for RIS measurements ;
- Use of a high-visibility double-tilt specimen-holder ;
- Dead time ~ 20% ;
- 2nd largest condenser aperture C1 ;
- “large” spot size: 4C ;
- Area = 256x256 px² ;
- Dwell time = 0.5 msec ;
- Total acquisition time ~2h (i.e. until specimen starts to drift).

The STEM-EDS spectrum image dataset post-treatment consisted in:

- Binning = 3x3 ;
- Background subtraction ;
- Automatic peak deconvolution following a careful peak identification ;
- When the studied specimen contained a detectable content of Mo (e.g. 316L(N)), if a Mo grid was used, Mo content was overestimated. Contribution of the grid to the signal was

estimated by the difference in measured Mo concentration within the matrix between the same material welded on a Cu grid and Mo grid. Mo contribution from the grid was subtracted and concentrations were then normalized.

Neither k-factors quantification method nor absorption correction factors provided by the software have been applied because EDS quantification claims for a dedicated study to optimize post-processing parameters. As this optimization had not been performed, obtained results are qualitative and aim to highlight trends.

Linear profiles extracted from EDS spectrum images were smoothed thanks to a moving average while error bars have been defined thanks to a moving standard deviation. For light elements (i.e. X-rays absorption), Mo (i.e. grid) and Si (i.e. detector) as calculated errors had been multiplied by 2.

4.7. Precipitates identification

Precipitates can be classified according to the level of the coherency of their crystal lattice with the matrix one as: coherent, semi-coherent or incoherent precipitates.

- Coherent precipitates

Coherent precipitates match all the matrix crystal planes but cause distortion because of a small difference in lattice parameter (Figure 41.A)). There is, however, undistorted planes that run right through the center of the precipitate. This absence of distortion causes a line of no contrast that runs through the image of the particle perpendicular to the active G vector (Figure 41.B)). Changing the orientation of G changes, the orientation of this line of no contrast. Strain diffraction contrast therefore permit to reveal them in BF-TEM 2-beam conditions. HRSTEM HAADF is another useful technique to study them (Figure 41.C)).

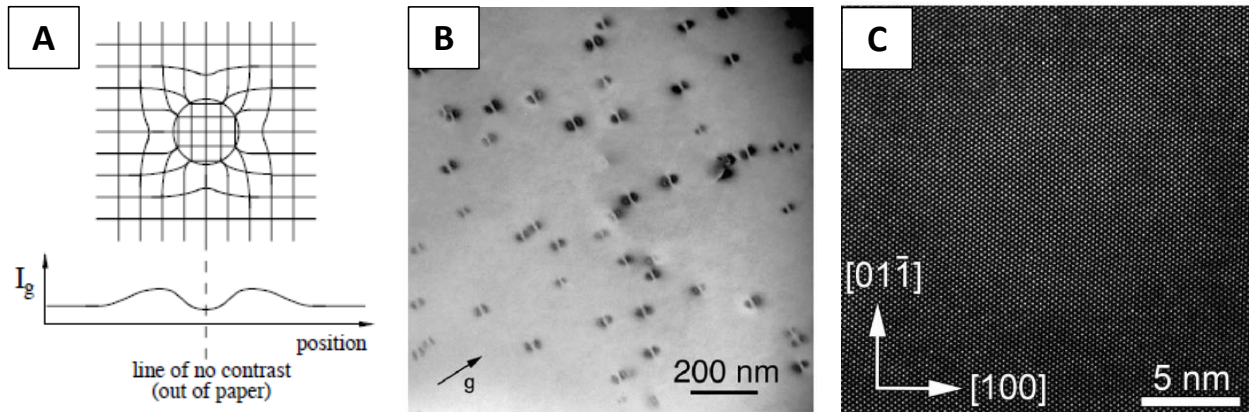


Figure 41 – A) Scheme of a spherical coherent precipitate with a lattice parameter smaller than the matrix showing bending of matrix lattice planes. Intensity profile for diffraction from the vertical planes $[130]$. B) BF-TEM image in 2-beam conditions of coherent precipitates $[140]$. C) HRSTEM HAADF a coherent precipitate with a mean Z higher than the matrix appear brighter $[141]$.

- Semi-coherent and incoherent precipitates

For semi-coherent and incoherent precipitates, if their volume fraction is high enough to be detected extra spots will appear in SAED pattern. By isolating a precipitate spot from the matrix with an objective aperture in the diffraction plane, TEM Dark-Field imaging will allow to visualize their distribution within the analysed area.

For semi-coherent precipitates, orientation relationships can be determined if precipitates and matrix spots are aligned in the diffraction pattern or if their respective zone axis are superimposed (Figure 24.A)). In order to reduce matrix contribution within the diffraction pattern, it is possible to tilt the sample in strong 2-beam conditions ($s_G=0$) so only one matrix spot will be excited (Figure 42).

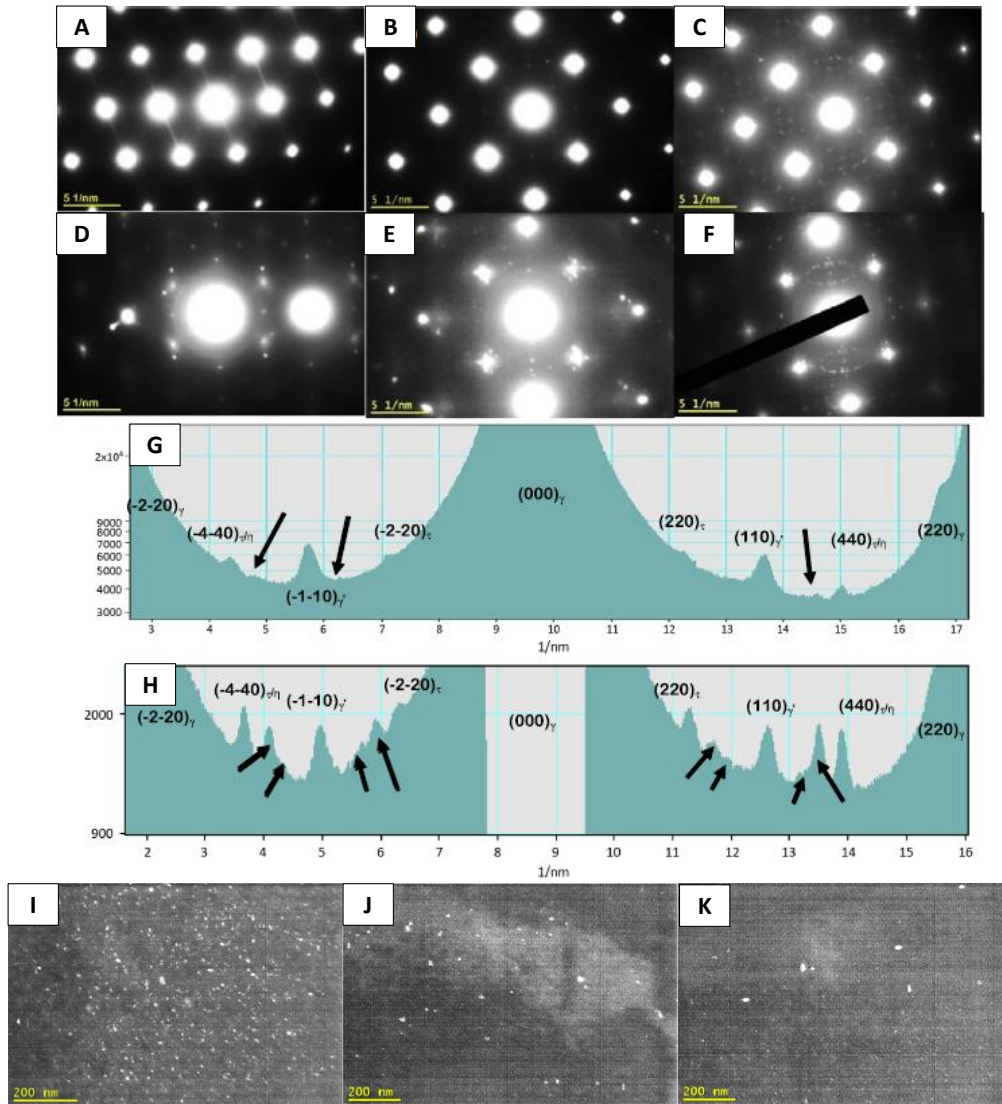



Figure 42 – A) $[\bar{1}10]$ and B), C) $[001]$ zone-axis SAED patterns; D) $B \sim [\bar{1}10]$, $G = (220)$ and E), F) $B \sim [001]$, $G = (220)$ 2-beam SAED patterns and G), H) intensity profiles between the (220) and $(\bar{2}\bar{2}0)$ reflections respectively shown in E) F). I), J) and K) DF-TEM images showing the various precipitates in the matrix with $B \sim [001]$ $G = (220)$. They were taken respectively from $(110)_{\psi}$, $(440)_{\psi\eta}$ and the reflections located between ψ' and τ/η reflections [105].

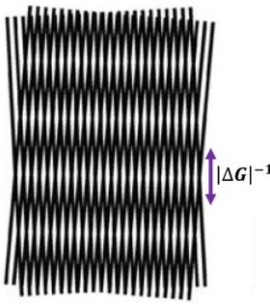
If the volume fraction of precipitates is not high enough to be detected in SAED, one way to determine the crystallography of second phases is to analyse HRTEM images and their Fast Fourier Transform (FFT). In high resolution images of semi-coherent precipitates, a pseudo-lattice can appear giving rise to extra spots in the FFT image (Figure 43). If two crystals are superimposed through the thickness of the sample, a pseudo-lattice with spacings an order of magnitude higher than the original ones will be produced. The so-called Moiré pattern corresponds to interferences between a pair of beams, G_1 and G_2 . If G_1 is generated in the upper crystal and G_2 in the lower, then, each reflection G_1 in crystal 1 acts as an incident beam for the lower crystal and will result in the creation of a vector of magnitude $|\Delta G|$.

The superposition of two crystal lattices with the same orientation but different interplanar distances - d_1 for the matrix and d_2 for the precipitate - will produce translation Moiré fringes. If the two crystals have the same interplanar spacing but are rotated, rotation Moiré fringes will be produced. If both interplanar distance and rotation change between these two crystals, mixed Moiré fringes will be produced. From the pseudo-lattice spacing, knowing the interplanar distance of the matrix and the rotation that occurred, it is possible to deduce the interplanar distance of the precipitate (Figure 43).



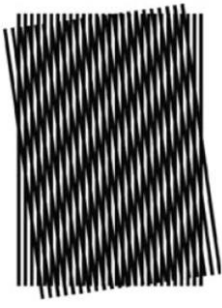
$$d_{tm} = |\Delta G|^{-1} = \frac{d_1}{1 - \frac{d_2}{d_1}}$$

88



$$d_{rm} = |\Delta G|^{-1} = \frac{d}{2 \sin \frac{\beta}{2}}$$

89



$$d_{gm} = \frac{d_1 d_2}{((d_1 - d_2)^2 + d_1 d_2 \beta^2)^{1/2}}$$

90

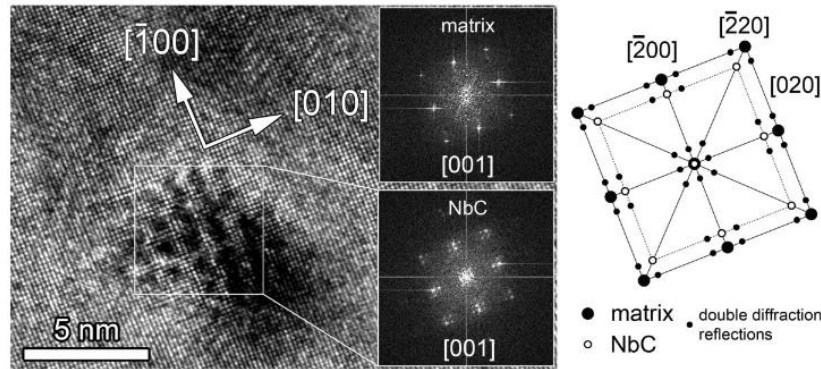


Figure 43 – (Upper part of the figure) From left to right: translation, rotation and mixed Moiré fringes with the corresponding interfringes distance d_{tm} , d_{rm} and d_{gm} [115]. (Lower part) BF-HRTEM image of a semi-coherent precipitate and comparison of FFT images from the matrix and the precipitate (with the scheme of the corresponding indexed spots on the right) [141].

It had been shown that Transmission Electron Microscopy, can reveal radiation-induced nanodefects nature by choosing the appropriate specimen orientation and the corresponding imaging, diffraction or chemical analysis technique. While defect crystallography can be fully characterized by TEM, issues regarding fine quantification of light and trace elements in STEM EDS were highlighted. Indeed, low energy X-rays absorption and matrix contribution to the acquired spectrums can make difficult to precisely quantify segregation levels on nanosized intragranular defects. To this end, Atom Probe Tomography is a very powerful complementary technique to obtain accurate composition of 3D nano-features.

II. Atom Probe Tomography

1. Basic principle

Atom Probe Tomography (APT) is an analytical microscopy technique that provides three-dimensional elemental mapping of a small volume of material (\sim hundreds of thousands of nm^3) with a near atomic spatial resolution. APT is based on the time-controlled ‘single’ evaporation of ionized atoms by a very intense electric field ($\sim 10 \text{ V.nm}^{-1}$) from the surface of a needle-shaped specimen held at cryogenic temperature (\sim tens of K) under ultra-high vacuum (10^{-10} mbar). Short voltage or laser pulses trigger the field evaporation process. Ions are accelerated by the applied electric field and projected towards a time and position sensitive detector through a counter-electrode and, for energy compensated atom probes, through a reflectron (Figure 44). Initial atom positions on the tip surface are calculated from a back-projection algorithm while the depth assignment is incrementally calculated, based on the sequence of evaporation. Their chemical nature is determined by time-of-flight mass spectrometry.

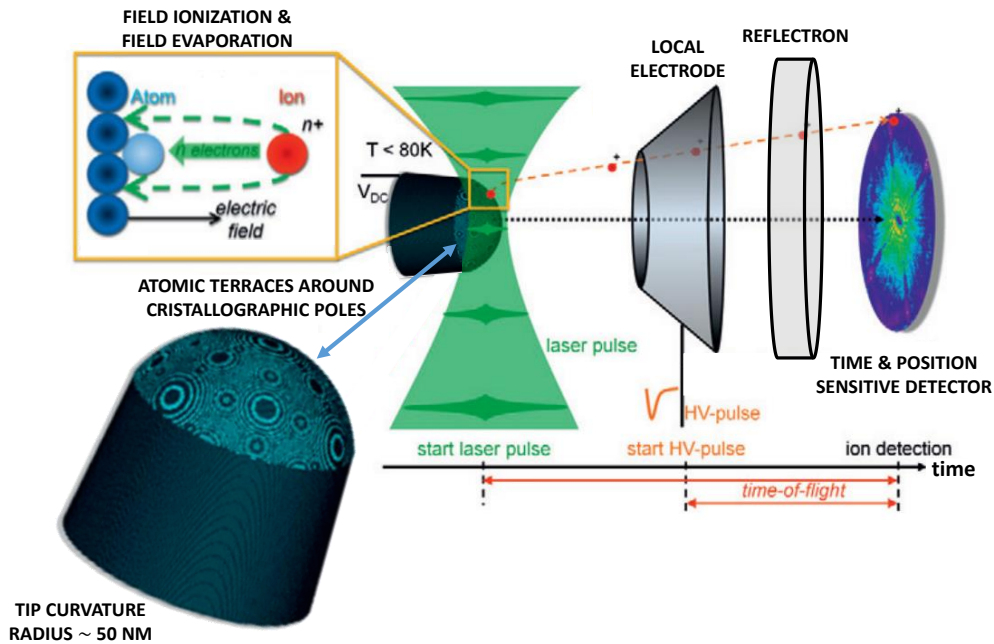


Figure 44 – Schematic representation of an Atom Probe Microscope (type LEAP 4000 XHR) and the basic principle of the APT technique data acquisition [142]

- Field evaporation and ions travel from the tip surface to the detector

A tip is conventionally described as a truncated cone ended by a quasi-hemispherical end cap. The electric field at tip apex is linked to the tip shape and the total applied voltage as:

$$F = \frac{V}{k_F R} \quad (91)$$

where R is the radius of curvature of the tip and k_F the field factor depending on the electrostatic environment (ranges from 3 to 8). Thus, the required radius for an atom to be able to be evaporated is in the range of tens of nm for an applied voltage of few kilovolts.

The electric field required to field evaporate an atom is generally called the evaporation field. The field evaporation is a thermally activated process specific to each element and phase in the material and has an activation energy dependent on the applied electric field strength. The highest strength, the lowest activation energy. Thus, under high electric fields (typically ~ 10 V/nm), surface atoms evaporation can happen even at very low temperature (tens of K). Atoms first field evaporate as singly charged ions. Then, electrons can be stripped from evaporated atoms by a tunnelling process generating positive ions (field ionization). Then, ion charge state is controlled by the postionisation mechanism, a higher charged state is reached for a higher electric field. Kingham [143] determined this postionisation probability for a large range of elements depending on the intensity of the applied electrical field.

A positive DC voltage is applied to reach approximately 80% of the evaporation field where the evaporation probability is almost 0. This constant electric field controls ions trajectories. In order to control ions evaporation, at a time t_{start} , an electric pulse or a laser pulse is superimposed to the DC voltage, which will bring the missing potential energy (the 20% left) or decrease the energy barrier to expulse ions from the surface. The ions are accelerated by the surface electric field. The ions are expected to follow the field lines defined by the electrostatic field and should hence follow exactly same trajectories whatever their mass or charge-state, at any applied voltage. The electrostatic field lines are bent by the presence of the shank of the specimen. Because of this bending, ion projection trajectory is not stereographic but quasi-stereographic. Due to energy conservation, ions kinetic energy will allow ions to travel with a high velocity toward the detector.

When an ion hits the detector, at the time t_{end} , the impact position will be recorded on the detector. The ion impact signal is amplified by the creation of a cascade of secondary electrons (uncorrelated with the ion chemical nature) by a microchannel plate assembly (MCP). It is constituted of a thin disc with a regular array of microchannels densely distributed over the whole surface. The physical transparency of MCP strongly affects the detection efficiency which reaches 36% for the LEAP 4000X HR used in this work. MCP assembly gives access to the related analogic signal that can be used to extract t_{end} . At least, two independent delay line anodes placed just behind the MCP allows to convert the electron cloud output into position information [144]. The first delay line is used to define the X position and the second is used to define the Y position. Each delay line will record two “electron charge” travelling time: T_{X1} and T_{X2} for the X line and T_{Y1} and T_{Y2} for the Y line. Five timing information are then extracted by the MCP and the delay lines (Figure 45). The combination of the four timing information collected on each extremity of the delay line give access

to the X and Y coordinates while t_{end} collected on the MCP will gives access to the time of flight ($t_f = t_{\text{end}} - t_{\text{start}}$) of the detected atom, in other words its chemical nature. Therefore, one can notice that both mass resolution and spatial resolution depend on time measurement accuracy.

Continuous developments such as reflectrons [145], local (or counter) electrodes [146], high frequency pulsers, delay-line detectors and laser-assisted APT [147] considerably improved instruments capability.

Reflectrons are energy compensation systems made of electrostatic mirrors which aim to equalize ion flight time by causing ions of higher energy to take longer pathways toward the detector. All ions with the same mass-to-charge ratio evaporated at the same standing voltage have the same flight time. Thus, mass resolution is improved.

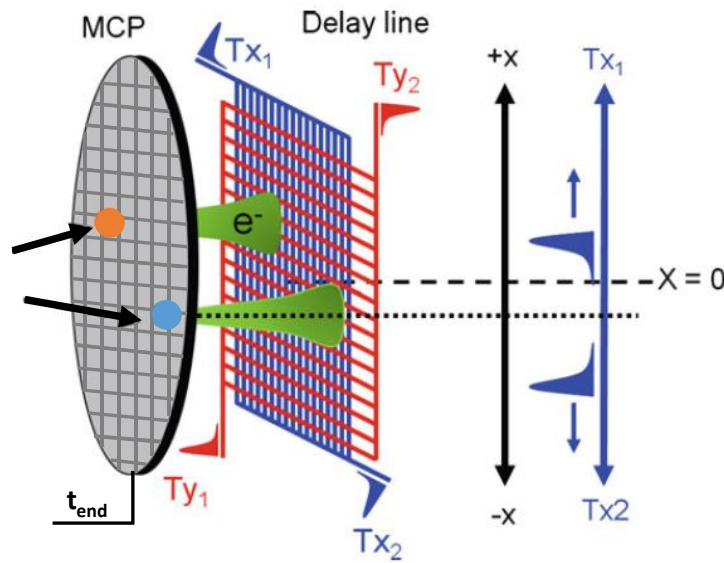


Figure 45 – Scheme of a delay line detector assembly and the timing measurements [148]

The local electrode gives access to a local enhancement of the electric field at the end of the tip. Tips can be prepared by electropolishing from sticks of material or by selecting a region of interest thanks to Focused-Ion Beam (FIB) and mount it on presharpended microtips (pretips). A single pretip can be prepared by electropolishing but, thanks to the local electrode, it is now possible to use a large range of tip holder geometries such as micro-coupons (22 or 36-pretips grid) or also TEM grids with pretips. Local electrode combined with high frequency pulsers help to faster acquisition times since much higher pulse repetition rates may be achieved at lower voltages.

Delay-line detectors can combine excellent multi-hits capability and good time separation limit (i.e. short time resolving power or dead time) which both reduce composition biases.

Voltage-pulse APT restricts analysis to conductive materials (i.e. metals). Laser-assisted APT enlarged considerably the field of application of this technique to non-metals such as semi-conductors and insulators.

- Time of flight spectroscopy

The mass-over-charge ratio of the ion is determined by equating the potential energy of the ion just prior to field evaporation to its kinetic energy just after field evaporation (conservation of energy):

$$neV = \frac{1}{2}mv^2 \quad (92)$$

where n is the number of electrons removed during the field ionization process (i.e. ion charge state), e is the elementary charge, V is the total voltage on the specimen, m is the mass of the ion and v the ion velocity. In the case of laser pulsing, V is the direct current (DC) voltage applied to the sample. In the case of electric pulsing, V is the sum of the DC voltage and the pulse voltage amplitudes.

As the ion flies toward the detector with a nearly constant velocity, ion velocity is related to the flight length L_f in this simple way:

$$v = \frac{L_f}{t_f} \quad (93)$$

with $t_f = t_{\text{end}} - t_{\text{start}}$, the time of flight.

Thus, according to Eq. (92) and (93), the mass-over-charge ratio is given by:

$$\frac{m}{n} = \frac{2eVt_f^2}{L_f^2} \quad (94)$$

$\frac{m}{n}$ is often given in atomic mass units (amu) or daltons (Da).

All the mass-over-charge ratios of the detected ions or are represented in a so-called mass spectrum graph where number of ions are recorded as a function of their measured masses (a.m.u.). Different peaks can be attributed to the same chemical element depending on element isotopes and charge states. For example, Ni has five isotopes per charge state. Ni ions can be charged positively once or twice. Thus, ten peaks are attributed to Ni in a mass spectrum if no association of Ni ions with other ions, so-called molecular ions, is observed. On the contrary, a peak can be attributed to different elements due to peak overlapping (e.g. $^{28}\text{Si}^{2+}$ and $^{14}\text{N}^+$ at 14 Da) or molecular ions (e.g. $^{52}\text{Cr}^{16}\text{O}^{2+}$ at 34 Da). Composition can be obtained from the relative intensity of the summed peaks mass range integrated intensity attributed to each element, corrections are made in case of peak overlapping or molecular ions and will be developed later. The background noise in the spectrum is mainly due to the random detection of ionized gaseous atoms/molecules coming from the analysis chamber or atoms/molecules adsorbed at the surface of the specimen (e.g. H_2O). These atoms/molecules being ionized at the DC voltage, are detected at any time of the acquisition. The detection system can sometime generate spontaneously electrons that are detected as impacts on the detector, but it constitutes a minor contribution to mass spectrum background.

Mass resolution $\frac{M}{\Delta M x\%}$ is calculated by the ratio of $M=m/n$ over the width of the mass peaks at $x\%$ of the maximum peak height, $\Delta M x\%$, where $x\%$ is often equal to 10 or 1%. The mass resolution

depends on ions energy dispersion and the relative timing accuracy of the detection system. In voltage pulsed mode, a time-varying voltage pulse is used to trigger ions emission. If most of the ions are emitted at the topmost of the voltage pulse, some field evaporated ions leave the sample at slightly different times relative to the pulse maximum (start time). This causes these ions to acquire slightly smaller kinetic energies, and therefore slightly slower velocities compared with the peak maximum, resulting in a mass tail in the mass spectrum. This deficit and energy can be compensated, to the detriment of detection efficiency, using a reflectron. In the laser assisted mode, a laser is focused on the tip apex. The light energy is absorbed and induces a heating of the sample. The increase of the temperature triggers the evaporation process by a thermal pulse (i.e. field evaporation is thermally activated). As the heating process is faster than the cooling process, the temperature curve profile is asymmetric, and a thermal tail is observed during the cooling period. This slow cooling down tail has a direct effect on the mass spectrum leading to a mass tail. It can severely reduce mass resolution and increase peak overlap if the illumination conditions are not carefully chosen, it is also material (i.e. thermal conductivity) and tip shape dependant (i.e. shank angle).

On one hand, measurement precision is defined by the mass resolution. On the other hand, measurement accuracy can be affected by chemical composition biases. Three main possible origins are isolated:

- Multi-hit events (co-evaporation and molecular dissociation)
- Preferential evaporation/retention
- Peak overlap (see section 2.3)

Multi-hit events happen when more than one atom is detected on the same pulse. The ability of the electronic system to discriminate two similar signals with the shorter time difference Δt is defined as the Time Resolving Power (TRP) or dead time (remember that both XY position and t_{end} , i.e. time of flight, are measured in time units). If $\Delta t > \text{TRP}$, the system discriminates the two atoms and calculates the time of flight and the XY position of each atom. If $\Delta t < \text{TRP}$, the result of the discrimination depends on the relative XY position of the atoms. The spatial difference can permit the individual ions of the multi-hit event to be resolved even if the ions have the same t_{end} . TRP thus corresponds to a physical “dead zone” that surrounds each ion impact site on the detector, where a second ion cannot be detected if it arrives within a specified time interval.

There are two types of multiple events: coevaporation, where neighbour surface atoms or molecules are evaporated in a short time interval [149], and molecular dissociation [150]. Molecular ions can sometimes, assisted by the intense electric field, split into two or more charged or neutral fragments.

Coevaporation is often correlated in time (same mass over charge ratio) and space (neighbour atoms). This phenomenon is particularly enhanced at the centre of low index poles because the electric field increase as the pole terrace diameter decreases. It mainly affects the main isotope of major element but also atoms subjected to preferential retention. The overall dataset (total events or hits) can be divided in 3 categories: single-hits, partial-hits and multi-hits. Coevaporation of certain type of ions (e.g. C+) will induce multi-hits at poles level. By filtering multi-hits only, it

can help to image and identify these poles. Poles identification will then help to define the reconstruction parameters. Data mining of multiple hits can help to correct composition bias induced as well.

Preferential evaporation will lead to specific loss of the atoms with the lowest evaporation field, the reverse is true for preferential retention. In the case of preferential evaporation, atoms with lower evaporation field can be evaporated between pulses if the chosen DC voltage is not sufficiently low to reduce evaporation probability to 0. Thus, atoms evaporated out of the pulses won't be detected because they are out of the detection window or detected as noise because of an unclassified apparent time of flight. It is particularly true in the case of copper in iron [151]. Some elements which require a large electric field to induce their field evaporation are subject to preferential retention such as boron [152].

- Volume reconstruction: back projection

As the specimen is evaporated, the xy position of the atom is determined from its XY hit coordinates on the detector. Its **z**-position (depth into the specimen along its long axis) is determined from the sequence of evaporation. The point projection model for the 3D reconstruction is presented Figure 46, from Bas et al. [153].

Because of the shank angle of the truncated cone, ions trajectories are compressed, thus the projection point P_0 doesn't coincide with the hemisphere cap center O_0 , having a radius R_0 before evaporation. After increment in evaporation depth, Δz , new P, O positions and R value are defined. The distance OP is equal to mR with m a constant. The distance between the projection point and the tip surface ξR is equal to $(m + 1)R$, where ξ is the image compression factor (ICF). ICF is also linked to the small angles θ and θ' defined in the Figure 46 :

$$\xi = \frac{\tan \theta}{\tan \theta'} \approx \frac{\theta}{\theta'} \quad (95)$$

As it will be shown in section 2.2, this equation will be useful for ICF determination from pole figures. The shortest distance between z axis and the position of the evaporated atom at the surface, s of the tip is d and the projected distance on the detector of surface S is D.



Figure 46 – Schematic view of point projection model [153]

Magnification M is defined as follows:

$$\frac{X}{x} = \frac{Y}{y} = \frac{D}{d} = M \quad \text{and} \quad \frac{S}{s} = M^2 \quad (96)$$

M is linked to the tip-detector distance, L by this relationship:

$$M = \frac{L}{\xi R} \quad (97)$$

From Eq. (96) and (97), atom coordinates on the tip surface (x, y) are related to the ion impact coordinates on the detector (X, Y) by these following relations:

$$x = \frac{\xi^R}{L}X \quad \text{et} \quad y = \frac{\xi^R}{L}Y \quad (98)$$

The depth z of the evaporated atom is given by:

$$z = dz + dz' \quad (99)$$

with dz and dz' defined on the Figure 46.

It is possible to write the volume which have already been evaporated this way:

$$V_{ev} = s. dz = N. V_{at} \quad (100)$$

with s the tip surface, N the number atoms within V_{ev} and V_{at} the average atomic volume.

As detection efficiency Q underestimate the number of evaporated atoms, N is corrected:

$$N = \frac{N_D}{Q} \quad (101)$$

with N_D the number of detected ions.

The evaporated volume can thus be rewritten:

$$V_{ev} = s \cdot dz = \frac{N_D}{Q} \cdot V_{at} \quad (102)$$

with $s = \frac{1}{M^2} \times S$ and $S = \pi \frac{D_D^2}{4}$ where D_D is the detector diameter.

Since $R = \frac{V}{F \cdot k_f}$, thus:

$$dz = \frac{N_D}{Q} \cdot V_{at} \frac{M^2}{S} = \frac{N_D \cdot V_{at}}{Q \cdot S} \left(\frac{L}{\xi R} \right)^2 = \frac{N_D \cdot V_{at}}{Q \cdot S} \left(\frac{L \cdot F \cdot k_f}{V \cdot \xi} \right)^2 \quad (103)$$

dz' is deduced from trigonometry:

$$dz' = R - c = R - R \cdot \cos \theta = R(1 - \cos \theta) \quad (104)$$

$$dz' = R \left(1 - \sqrt{\cos^2 \theta} \right) = R \left(1 - \sqrt{1 - \sin^2 \theta} \right) \quad (105)$$

$$dz' = R \left(1 - \sqrt{1 - \left(\frac{d}{R} \right)^2} \right) = R \left(1 - \sqrt{1 - \frac{x^2 + y^2}{R^2}} \right) \quad (106)$$

Therefore,

$$dz' = \frac{V}{F \cdot k_f} \left(1 - \sqrt{1 - \frac{x^2 + y^2}{\left(\frac{V}{F \cdot k_f} \right)^2}} \right) \quad (107)$$

According Eq. (103) and (107), the final expression of z is:

$$z = dz + dz' = \frac{N_D \cdot V_{at}}{Q \cdot S} \left(\frac{L \cdot F \cdot k_f}{V \cdot \xi} \right)^2 + \frac{V}{F \cdot k_f} \left(1 - \sqrt{1 - \frac{x^2 + y^2}{\left(\frac{V}{F \cdot k_f} \right)^2}} \right) \quad (108)$$

For the i^{th} atom detected, the incremental z_i is:

$$z_i = \left(\sum_1^i \left(\frac{L}{V_i} \times \frac{F \cdot k_f}{\xi} \right)^2 \frac{V_{at(i)}}{Q \times S} \right) + \frac{V_i}{F \cdot k_f} \left(1 - \sqrt{1 - \frac{x_i^2 + y_i^2}{\left(\frac{V_i}{F \cdot k_f} \right)^2}} \right) \quad (109)$$

Finally, the space coordinates of the i^{th} detected ion are:

$$(x_i, y_i, z_i) = \left(\frac{\xi V_i}{LF \cdot k_f} X, \frac{\xi V_i}{LF \cdot k_f} Y, \left(\sum_1^i \left(\frac{L}{V_i} \times \frac{F \cdot k_f}{\xi} \right)^2 \frac{V_{at(i)}}{Q \times S} \right) + \frac{V_i}{E \cdot k_f} \left(1 - \sqrt{1 - \frac{x_i^2 + y_i^2}{\left(\frac{V_i}{F \cdot k_f} \right)^2}} \right) \right) \quad (110)$$

V_i is the total applied voltage that triggers evaporation of the i^{th} atom, S , L and Q are instrument constants and the evaporation field F is defined as the evaporation field of the major element (tabulated value). All these previous parameters are known; nevertheless, two constants need still to be adjusted: k_f and ξ , commonly designed as the reconstruction parameters. Actually, it had been shown that the reconstruction parameters evolve during acquisition and can bias the reconstructed volume. Hatzoglou and al. [154] proposed a dynamic reconstruction model where k_f and ξ are not constants anymore. It has to be noticed that this model is not yet implemented into the reconstruction software commonly used.

Spatial resolution is anisotropic. Generally, 0.2 nm resolution is reached in depth and close to 1 nm for lateral resolution. Loss of depth resolution is observed close to the volume border due to the influence of lateral resolution for these large angles. Tip shape or large difference in evaporation field between a feature and the surrounding matrix within the material can lead to strong reconstruction biases. Local compression or dilatation of the feature of interest, so-called local magnification effects.

In the case of a low-field precipitate (Figure 47) compression occurs laterally, matrix ion trajectories cross precipitate ones and composition bias in the core can occur. The reverse is true for high-field precipitate (i.e. lateral dilatation and no composition bias in the core).

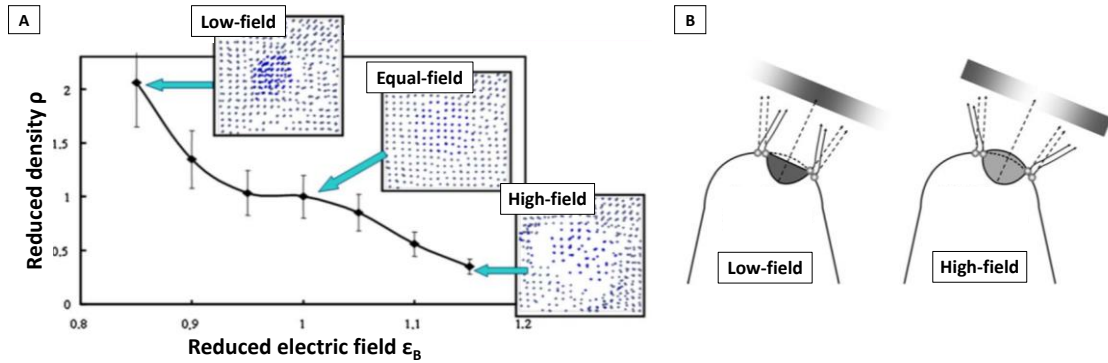


Figure 47 - Local magnification effects. B) Trajectory overlaps are shown to occur at a spherical precipitate interfaces (view on XY plane), containing only B atoms in pure A solid solution. Reduced density $\rho = \frac{n}{n_0}$ (with n the measured density and n_0 the matrix one) measured inside the precipitates and their evolution in terms of reduced electric field $\epsilon_B = \frac{F_B}{F_A}$ [155]. Schematic representation of ion trajectories and the observed density on the detector (higher density = darker) for low and high field precipitates [156].

Cavities can lead to either an increase or a decrease in local atomic densities in the APT reconstruction. Local density variations near voids are controlled by the evaporation fields of the shell atoms (Figure 48).

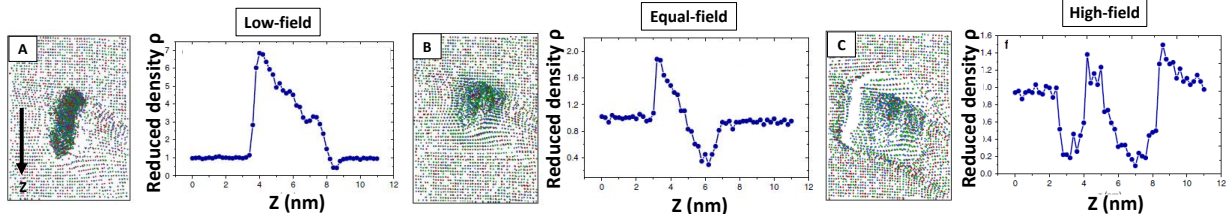


Figure 48 - Atom distributions in the YZ plane and 1D local density profiles near cavities based on field-evaporation simulations in the case of A) low-field, B) equal-field and C) high-field cavities shell. The corresponding 1D density profiles are oriented parallel to the evaporation direction (z-axis) of the simulated APT reconstruction. Evaporation field difference with the matrix of the void shell lead to very specific density profiles. [157].

In the case of irradiated material where radiation-induced precipitation (RIP) and radiation-induced segregation (RIS) at cavity-matrix interface can occur, field-evaporation simulation is a very helpful tool to be able to distinguish between such kind of defects and correct/identify composition biases.

- Voltage vs. laser pulse mode

Laser-assisted APT (La-APT) opened new field for nano-scaled investigation of nonconductive materials [147]. But, one of the main advantages of La-APT for conductive materials is the risk reduction of tip fracture. Indeed, contrary to voltage mode, no repeated mechanical stress induced by electrical pulses is applied to the sample.

In the case of La-APT, field evaporation is triggered by the increase in temperature induced by absorption of the laser light by the specimen (Figure 49). The peak temperature that can be reached depends on the material thermal conductivity, the tip shank angle and various parameters linked to the laser pulse itself: pulse duration, wavelength, energy, focusing conditions and the position of the spot on the tip. A thermal peak tail is usually observed on the mass spectrum. This is due to the time needed to heat spread, that increases the duration during which ions can be evaporated. Large shank angles of the specimen provide a larger heat sink and thus a faster cooling and reduce the extent of the thermal tails in the mass spectrum. But the shank angle shouldn't be too large because the tip radius will rapidly increase during the analysis and consequently, voltage will rapidly reach the instrument voltage limit.

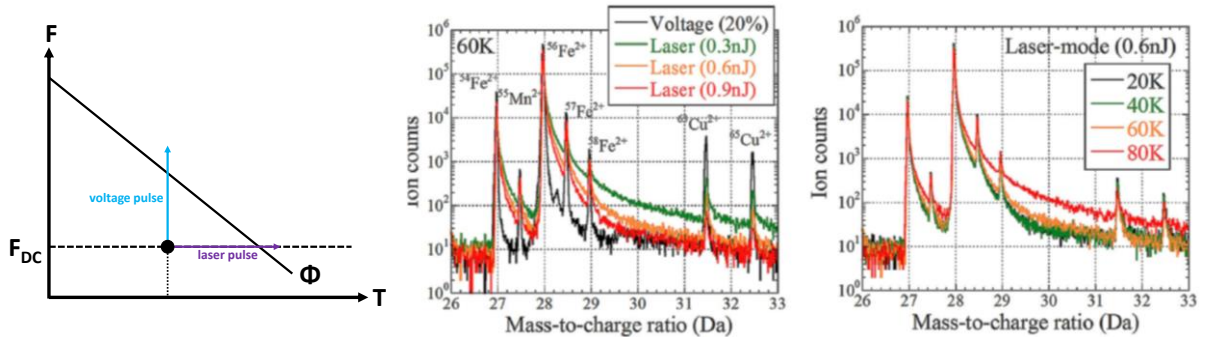


Figure 49 – (left) Mechanisms of field evaporation triggered by voltage pulse (electric field increase) and laser pulse (temperature increase), Φ is the evaporation rate. (center) Mass spectrum at 60K in laser-mode with various pulse energies and in voltage-mode with a pulse fraction of 20%. (right) Mass spectrum of various specimen temperatures in laser-mode with a laser pulse energy of 0.6nJ [158].

2. Data acquisition and data treatment

2.1. Acquisition parameters definition

Both composition measurement accuracy and spatial resolution strongly depend on the studied material, tip shape and acquisition parameters. To ensure satisfying data quality, preferential evaporation/retention and multi-hit events should be avoided, mass spectra with a low background noise and good statistics are highly recommended. To achieve this goal, compromise should be found between the four parameters that can be tuned during the analysis: the base temperature, the detection rate, the voltage pulse fraction or the laser pulse energy and the pulse frequency [159].

Base temperature ranges between 20 and 90K. As the field evaporation is a thermally activated process, the field needed to maintain a given evaporation rate is lower at higher base temperature. Consequently, the applied DC voltage is lower too so the electrostatic stress applied to the sample is lowered and the risk of fracture as well. Higher temperature will promote residual gas ionization which increases the background level. Preferential evaporation is also an issue for some elements if the temperature is too high, and can sometimes be unavoidable [160].

The detection rate (DR) is the number of ions detected each 100 pulses. It ranges from 0.01 to 1. A high DR will decrease the time of analysis because the tip will evaporate faster on one hand. On the other hand, the field-induced stress on the specimen rises because, maintaining a higher DR requires a higher electric field. It could result in an early tip failure. Furthermore, too high DR will encourage multi-hit events. If the DR is too low, the signal to noise ratio is degraded. Working at constant detection rate is not recommended because the number of ions detected per unit area (i.e. flux) will progressively decrease during tip evaporation (i.e. the presence of a shank angle cause an increase in radius, and thus an increase of the analysed surface, all along the analysis). As the tip radius and subsequently the field of view increase, the evaporation field will lower over time. Thus, DR should be progressively increased during the analysis to counterbalance this effect and obtain a constant evaporation flux (ion/s/nm^2). However, it is recommended to work with a constant flux.

The voltage pulse fraction is a percentage of the applied DC voltage. It corresponds to the increase of the voltage brought by the pulse to trigger field evaporation, it ranges from 1% to 20% of the standing voltage. Insufficient pulse fraction can cause preferential evaporation of low evaporation field elements and/or preferential retention of high evaporation field elements. To avoid preferential evaporation, DC voltage must be low enough so that there is nearly zero probability of field evaporation, while the DC voltage plus pulse voltage should provide similar probabilities of field evaporation for all surface elements.

Laser pulse energy refers to the thermal energy brought to provoke field evaporation, like the voltage pulse fraction in HV pulse mode. It ranges from pJ to nJ. Insufficient laser pulse energy requires evaporation at higher DC fields and can lead to a higher background level and shorter specimen lifetime. On the contrary, excessive laser pulse energy can reduce spatial resolution by providing nonuniform evaporation and increases surface diffusion. Molecular evaporation is also encouraged. This complexifies mass spectrum treatment because peak identification is sometimes not straightforward, and the probability of peak superimposition rises. Higher pulse energy can be

associated to higher cooling rate for materials with sufficiently high thermal conductivity and reduces the extent of the peak tail.

Pulse frequency (PF) is the number of pulses repetitions per second. It ranges from 25 to 200kHz. Higher PF permits faster data collection but the repeated application of a pulse results in mechanical fatigue (i.e. in voltage mode) and promotes specimen breakage, even though higher pulsing rates are generally desirable. However, the maximum pulse repetition rate is limited by the longest ion flight times expected, i.e. too long to be detected within one detection windows between pulses, inducing a specific loss of these ions. In HV-pulsing mode, a higher pulsing rate involves a longer time during which the specimen is held at a higher electric field longer on average. At higher electric field, residual-gas are ionised farther from the surface and are generally not detected. Thus, background noise is reduced. In contrast, in laser mode, high pulsing rates can be problematic. If the time between two pulses is too short to enable heat transfer, the temperature increases. A higher temperature favours residual-gases ionisation and the background level is higher.

Generally, for metals, it is recommended to run analysis at low temperature, high pulse fraction or high pulse energy, and high pulse frequency. Under these conditions, sample failure is highly promoted. Depending on the material sensibility to preferential evaporation/retention, multi-hit events and breakage, acquisition parameters should be adjusted. This requires a set of experiments with different acquisition conditions and to compare composition measurements with a reference composition acquired with another technique if possible to ensure reliable data, moreover if studied material is new [160]. For this present work, depending on the material studied (i.e. nanolayers or bulk material) and the selected mode (i.e. voltage or laser) the following parameters ranges were used:

- temperature: from 60 (most of the experiments) to 80 K (correlative microscopy) in order to limit tip fracture;
- pulse fraction: 20%;
- equivalent pulse energy (PE_{eq}): from 15 to 25 pJ calculated for an effective pulse fraction of 20% at the beginning of La-APT analysis as explained in Figure 50 ;
- detection rate: varies from 0.05 to 0.2 i/pulse in order to work under a constant flux of ~ 0.15 i/s/nm² all along the specimen analysis;
- pulse frequency: 200kHz in voltage mode, 250kHz in laser mode.

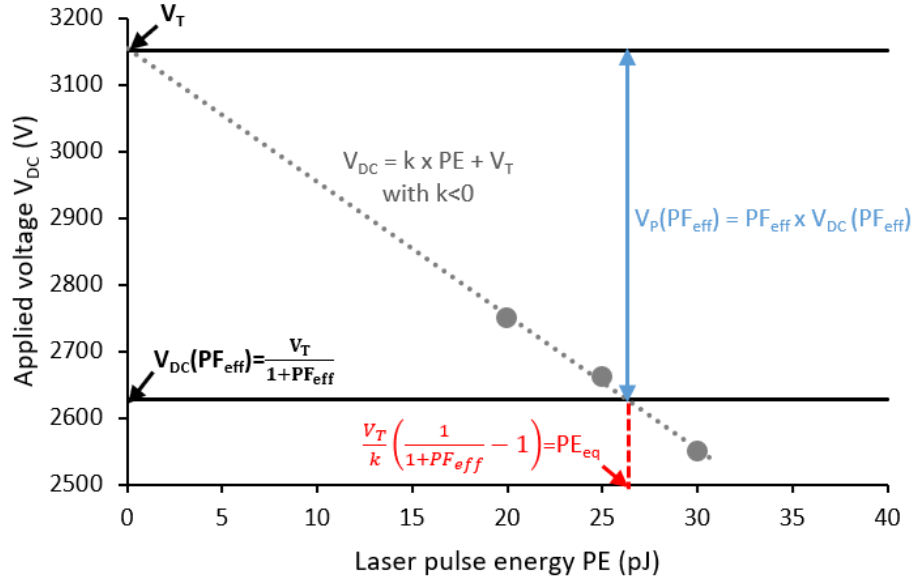


Figure 50 – Laser pulse energy calibration curve. Measurements of the applied voltage as a function of the laser pulse energy are made at the beginning of the La-APT analysis. Linear fit of experimental points permits to determine the equivalent pulse energy PE_{eq} for an effective pulse fraction PF_{eff} of 20%. Here k corresponds to the slope of the linear fit, V_T is total applied voltage extrapolated at $PE = 0$ pJ, V_{DC} is the standing voltage and V_P is the pulse voltage.

2.2. Reconstruction parameters determination

As previously demonstrated, the space coordinates of the i^{th} detected ion are :

$$(x_i, y_i, z_i) = \left(\frac{\xi V_i}{LF \cdot k_f} X, \frac{\xi V_i}{LF \cdot k_f} Y, \left(\sum_1^i \left(\frac{L}{V_i} \times \frac{F \cdot k_f}{\xi} \right)^2 \frac{V_{at(i)}}{Q \times S} \right) + \frac{V_i}{E \cdot k_f} \left(1 - \sqrt{1 - \frac{x_i^2 + y_i^2}{\left(\frac{V_i}{F \cdot k_f} \right)^2}} \right) \right) \quad (111)$$

And the radius is expressed this way:

$$R = \frac{V}{F \cdot k_f} \quad (112)$$

Therefore, coordinates expression can be rewritten:

$$(x_i, y_i, z_i) = \left(\frac{\xi R_i}{L} X, \frac{\xi R_i}{L} Y, \left(\sum_1^i \left(\frac{L}{\xi R_i} \right)^2 \frac{V_{at(i)}}{Q \times S} \right) + R_i \left(1 - \sqrt{1 - \frac{x_i^2 + y_i^2}{R_i^2}} \right) \right) \quad (113)$$

In Eq. (110) the two unknowns are k_F , the field factor and ξ , the compression factor. These two parameters will be determined from the reconstruction from poles method. In Eq. (113) the two unknowns are R_i and ξ . Thanks to correlative microscopy, the variable R_i is obtained from the initial curvature radius of the tip R_0 and the shank angle α . ξ can be adjust to match features shape and size if they can be seen by both techniques, i.e. APT and TEM. Otherwise, a standard value is used.

- From poles

When the tip reaches its equilibrium shape, the tip surface roughness is due to the formation of atomic terraces and induces an inhomogeneous electrical field distribution at the tip apex. The size of these terraces is directly related to the crystallographic poles. Lower index poles, are larger and show more electric field heterogeneities. This property results in an inhomogeneous ion density at poles Figure 51.

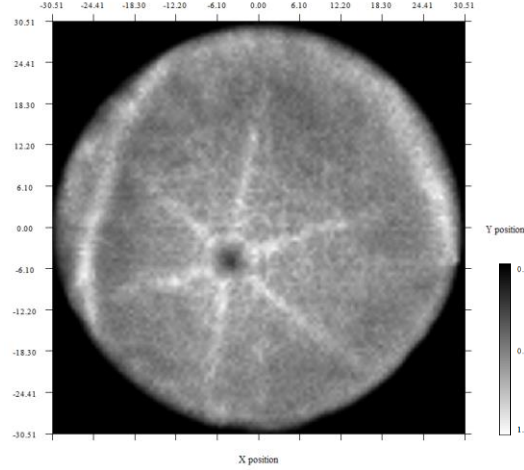


Figure 51 – Density variations near $\langle 111 \rangle$ pole in FCC.

The first step of this method is to identify poles. Once it is done, the interplanar distance has to be calculated and k_F should be adjusted in order to measure the theoretical distance inside the reconstructed volume. A first reconstruction should be done with “standard” parameters, i.e. $k_F=3.3$ and $\xi=1.6$. Then, the resulting interplanar distance is measured d_{hkl}^{false} . From the theoretical value of interplanar distance d_{hkl}^{true} of the identified pole (hkl), the true field factor is calculated:

$$k_{true} = k_{false} \sqrt{\frac{d_{hkl}^{true}}{d_{hkl}^{false}}} \quad (114)$$

If more than one pole is visible, the compression factor can be determined. By definition, stereographic projection preserves angles, and ion trajectories is quasi stereographic. Thus, compression factor can be determined from the distance, D between two poles on the impact density map on the detector, and the crystallographic angle, θ between these two poles.

$$\xi = \frac{L\theta}{D} \quad (115)$$

with L the distance between the tip and the detector.

ξ depends on the shank angle and the electrical field, it ranges between 1 (i.e. radial projection) and 2 (i.e. stereographic projection). If only one pole is invisible, the standard value, i.e. 1.65, should be used for the LEAP 4000X HR.

Poles are less visible on the detector events map when the temperature is increased. Their visibility strongly depends also on the material, i.e. its crystallography and the amount of alloying elements or impurities it contains. It is often hard to see poles in austenitic stainless steels. In this case, correlative microscopy should be performed.

- From correlative microscopy

Correlative microscopy method can be performed from SEM or S/TEM micrographs. In this case, both cap hemisphere radius R_0 and shank angle α have to be determined. As shown in Figure 52, they can lead to strong uncertainties.

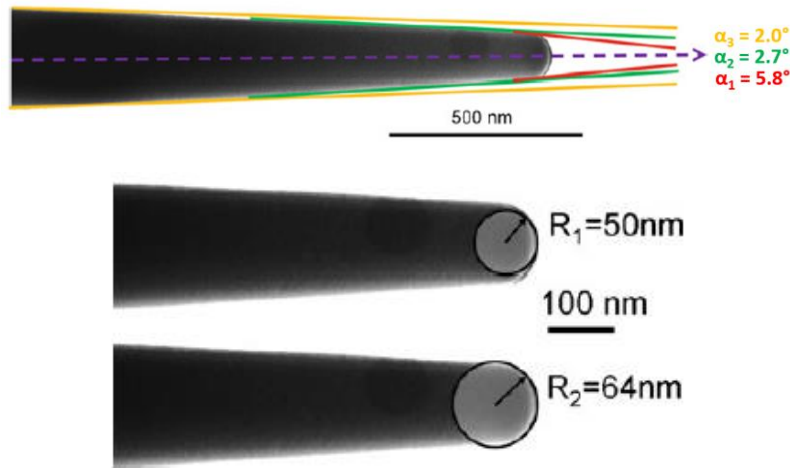


Figure 52 - (Upper) various possible definition of α (Lower) various possible definition of R_0 [148].

In order to ensure a reliable reconstruction, reconstruction parameters should be adjusted to be able to superimpose features revealed by both techniques (APT and TEM).

2.3. Composition measurement

At the beginning of the analysis, mass spectrum is highly contaminated by surface oxides, water condensation and gallium contamination (in the case of specimen prepared by FIB). This contamination is not representative of the material composition so the first tens or hundreds of thousands of atoms detected are always removed prior to further analyses.

To measure chemical specie concentrations, all peaks should be carefully identified. The corresponding mass ranges are defined including peak tails and the background is subtracted. Hydrogen ions and H_2O molecular ions are not considered for quantification. The total number of ions detected for a particular element is equal to the sum of all peak intensities corresponding to this element. For example, nickel has five isotopes and can be ionized once Ni^+ or twice Ni^{2+} , nickel oxides molecular ions can also form, five peaks will again appear for each charge state. Thus, in this case, the total number of Ni ions detected is the sum of the intensity of these 20 peaks. If overlaps between peaks occur, a decomposition based on the natural abundance of isotopes is performed. Concerning Fe, Ni and Cr ions charged twice, peaks at 27 and 29 Da are subjected to peak overlaps (Figure 53).

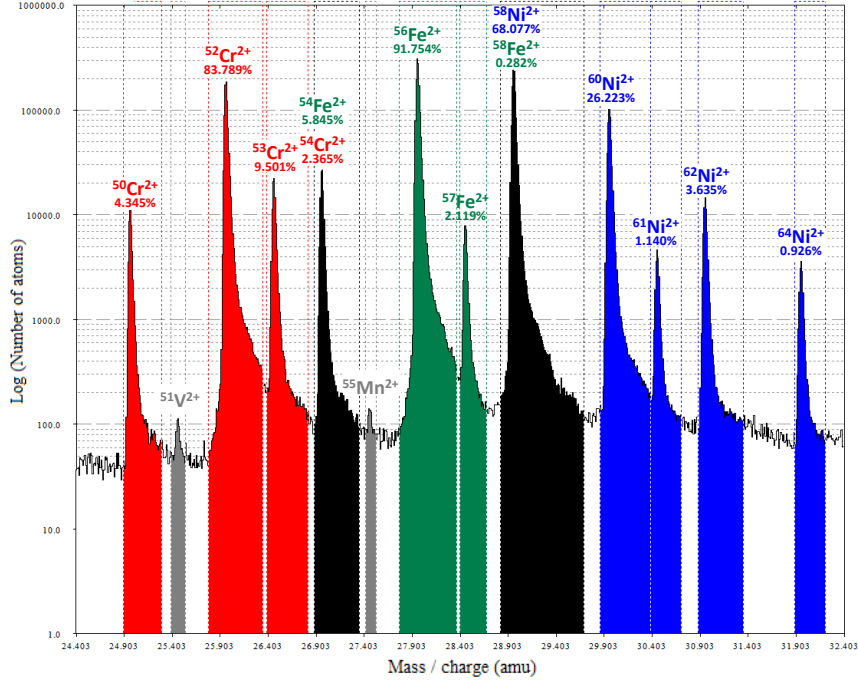


Figure 53 - Mass spectrum peak overlaps of Fe, Ni, Cr $^mX^{n+}$ isotopes and their corresponding natural abundances.

In the peak at 27 Da, the contribution of $^{54}\text{Cr}^{2+}$ and $^{54}\text{Fe}^{2+}$ isotopes is expressed as:

$$N^{\text{exp}}(27) = N^{\text{rel}}(^{54}\text{Cr}^{2+}) + N^{\text{rel}}(^{54}\text{Fe}^{2+}) \quad (116)$$

where $N^{\text{exp}}(27)$ is the number of ions in the peak at 27 Da directly extracted from the mass spectrum.

The number of $^{54}\text{Cr}^{2+}$ and $^{54}\text{Fe}^{2+}$ ions in the peak at 27 Da is calculated from the theoretical number of $^{54}\text{Cr}^{2+}$ and $^{54}\text{Fe}^{2+}$ determined from their natural abundances:

$$N^{\text{rel}}(^{54}\text{Cr}^{2+}) = \frac{N^{\text{th}}(^{54}\text{Cr}^{2+})}{N^{\text{th}}(^{54}\text{Cr}^{2+}) + N^{\text{th}}(^{54}\text{Fe}^{2+})} \times N^{\text{exp}}(27) \quad (117)$$

$$N^{\text{rel}}(^{54}\text{Fe}^{2+}) = \frac{N^{\text{th}}(^{54}\text{Fe}^{2+})}{N^{\text{th}}(^{54}\text{Cr}^{2+}) + N^{\text{th}}(^{54}\text{Fe}^{2+})} \times N^{\text{exp}}(27) \quad (118)$$

Thus, the theoretical number of Cr^{2+} ions at 27 Da is given by:

$$N^{\text{th}}(^{54}\text{Cr}^{2+}) = 2.365 \times N^{\text{th}}(\text{Cr}^{2+}) \quad (119)$$

where the theoretical total number of Cr^{2+} can be determined from the peaks of Cr^{2+} isotopes which show no overlap in the mass spectrum:

$$N^{\text{th}}(\text{Cr}^{2+}) = \frac{N^{\text{exp}}(^{50}\text{Cr}^{2+}) + N^{\text{exp}}(^{52}\text{Cr}^{2+}) + N^{\text{exp}}(^{53}\text{Cr}^{2+})}{4.345 + 83.789 + 9.501} \quad (120)$$

Then,

$$N^{\text{th}}(^{54}\text{Cr}^{2+}) = \frac{2.365}{97.635} \times (N^{\text{exp}}(^{50}\text{Cr}^{2+}) + N^{\text{exp}}(^{52}\text{Cr}^{2+}) + N^{\text{exp}}(^{53}\text{Cr}^{2+})) \quad (121)$$

and the theoretical number of Fe^{2+} ions at 27 Da is calculated in the same way (the peak at 29 Da of Fe^{2+} is not taken into account because of overlap with Ni^{2+}):

$$N^{th}(^{54}Fe^{2+}) = \frac{2.365}{91.754 + 2.119} \times (N^{exp}(^{56}Fe^{2+}) + N^{exp}(^{57}Fe^{2+})) \quad (122)$$

Experimental abundance of each isotope is calculated and compared to natural one in order to check composition measurement accuracy:

$$ab^{exp}(^{50}Cr^{2+}) = \left(\frac{N^{exp}(^{50}Cr^{2+})}{N^{exp}(^{50}Cr^{2+}) + N^{exp}(^{52}Cr^{2+}) + N^{exp}(^{53}Cr^{2+}) + N^{cal}(^{54}Fe^{2+})} \right) \times 100 \quad (123)$$

This can only be done if an element has several isotopes. Sometimes, more than two peaks overlap. It is the case for isotopes of Ni, P and Nb at 31 Da. Furthermore, P and Nb only have a single isotope, thus the previous treatment can't be applied. The theoretical number of Ni^{2+} ions at 31 Da is given by:

$$N^{th}(^{62}Ni^{2+}) = \frac{3.635}{26.223 + 1.140 + 0.926} \times (N^{exp}(^{60}Ni^{2+}) + N^{exp}(^{61}Ni^{2+}) + N^{exp}(^{64}Ni^{2+})) \quad (124)$$

The contribution of Ni^{2+} is then subtracted from the total number of ions in the peak at 31 Da and directly give the number of P^+ or Nb^{3+} :

$$N(^{31}P^+) = N^{exp}(31) - N^{th}(^{62}Ni^{2+}) \quad (125)$$

$$N(^{93}Nb^{3+}) = N^{exp}(31) - N^{th}(^{62}Ni^{2+}) \quad (126)$$

Composition is calculated twice, first with the contribution of P^+ , then with Nb^{3+} in the peak at 31 Da. Concentrations and uncertainties are given respectively by determining the mean and standard deviation in concentration between the two calculations. Uncertainties are determined as statistical errors if only one measurement is possible or as standard deviation between different measurements in the same volume or from different analyses.

2.4. Clusters analysis

Two methods are commonly used for cluster identification: the Maximum Separation Method (MSM) and the Isoposition Method (IPM). MSM [156,161,162] defines the maximum distance between a solute atom A and its N^{th} nearest neighbour solute atoms B (with $A=B$ or $A \neq B$) to form a cluster. NNN stands for the order N of Nearest Neighbours. The higher the order, the more difficult is the detection of small clusters. The second method, IPM [156], consists in the definition of a local composition associated to every single atom of the volume. Atoms belonging to a cluster are then filtered thanks to a threshold concentration in one or several species. Hyde and al. [163] compared these two methods to analyse a simulated dataset of known cluster size and density in a dilute matrix. Both methods give similar results for clusters ≥ 1 nm in radius whereas IPM have shown to give better results for smaller clusters. IPM method was kept for cluster analysis and is described in detail.

- Step 1: assign a composition to each atom inside a 3D grid

A composition 3D grid is calculated inside the global volume (Figure 54). The size of a cubic sampling volume in x, y, z dimension is defined by the magnitude of its basis vectors. Dimensions have to be chosen in order to obtain a good compromise between high spatial resolution and small dispersion in the concentration values C_i of each identified element i.e $C_i = N_i / N_{\text{samp}}$ are calculated for each subvolume (voxel) and attributed at their geometrical center. 1 nm had been selected, for a resulting sampling volume of 1nm^3 . In the case of austenite, the number of atoms inside this volume is:

$$N = \frac{N}{V_{\text{cell}}} Q \sim 31 \text{ atoms.nm}^{-3} \quad (127)$$

where N is the number of atoms per cell (4 for FCC), V_{cell} the volume of a cell with a lattice parameter equal to 0.359 nm and Q is the detector efficiency (36% for the LEAP 4000X HR).

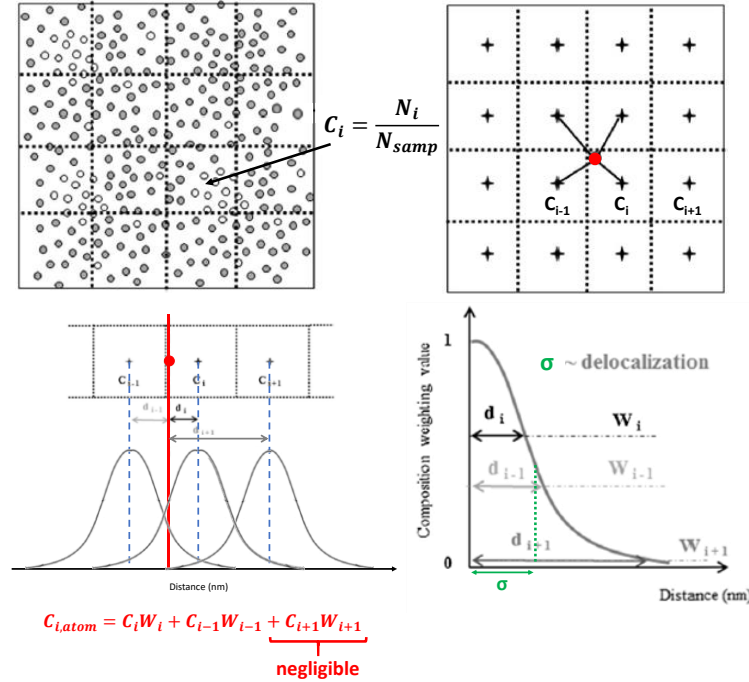


Figure 54 – A 3D grid is built with a user defined size (1 nm), the composition inside each box is calculated and attributed to the center of each box. A Gaussian function with a user defined standard deviation (0.5 nm) is superimposed to the center of each box. Depending on the relative position of an atom to the neighbouring boxes, a weighted average composition is calculated for this atom [156].

A Gaussian function with a user defined standard deviation, σ is associated to each voxel and centered on the center of this subvolume. In one dimension, if an atom is at a distance d_i from the center of the voxel i , and at a distance d_{i-1} from the neighboring box $i-1$; then, the atom composition corresponds to the weighted average of the composition at the center of boxes i and $i-1$.

This approach allows to attribute a composition to each set of x, y and z coordinates, so that to each atom.

- Step 2: define a threshold concentration C_{lim} to filter solute/solvent atoms

As each atom has an assigned composition, it is therefore possible to filter all the atoms with a threshold concentration. To do so, the distribution of concentration of an element is compared to a randomized distribution. The threshold concentration C_{lim} is defined at the concentration where the two distributions start to diverge. All atoms with a defined concentration below C_{lim} belong to the matrix and are filtered out.

- Step 3: define clusters D_{max} and N_{min}

After the filtering step, a new 3D grid with an edge equal to D_{max} is built. D_{max} is generally equal to σ or slightly smaller. The remaining atoms that belong to the same voxel or the adjacent ones are assigned to the same cluster. Only clusters containing at least N_{min} solute atoms are kept (atoms into clusters smaller than N_{min} are reassigned to the matrix). To define N_{min} , the volume is randomized, then the 3D composition grid is calculated again. N_{min} is the threshold value from which no clusters are visible in the randomized volume for a defined C_{lim} and D_{max} (statistical fluctuations are therefore eliminated).

- Step 4: cluster identification is checked by visual inspection

Merged clusters are split, split clusters are merged. Different classes of size can appear, if it is the case, only clusters of the same size are selected for erosion.

- Step 5: assorting near-interface atoms as cluster or matrix atoms

Generally, at the end of the identification step, matrix atoms close to the interface are identified as cluster atoms. To re-assort these atoms to the matrix, an erosion profile is plotted and the interface is moved. To plot an erosion profile, the distances between each cluster atom and matrix atoms are calculated. Thus, the minimal distance for each cluster atom is determined. All clusters atoms with similar minimal distance are sort in the same negative distance class, allowing to calculate a composition for this distance class. The same calculation is done for each matrix atom. In this latter case, the minimum distance between each matrix atom and clusters atoms is considered as positive. This approach allows to plot a concentration profile whatever the shape of the selected clusters. The distance "zero" corresponds to the identified interface (Figure 55). It has to be noticed that in order to avoid interface bias, clusters atoms are subtracted from the overall volume and the matrix composition is determined from the remaining ones at this step.

To define properly cluster-matrix interface (or core-shell interface, or shell-matrix interface), the interface is moved back of a negative distance d and set at the half-maximum of the cluster core composition. Every cluster atom distant of d from the previous interface are reinjected into the matrix. This step is the erosion 1 (Figure 55). At this stage of erosion, cluster size, volume fraction and number density of clusters are calculated.

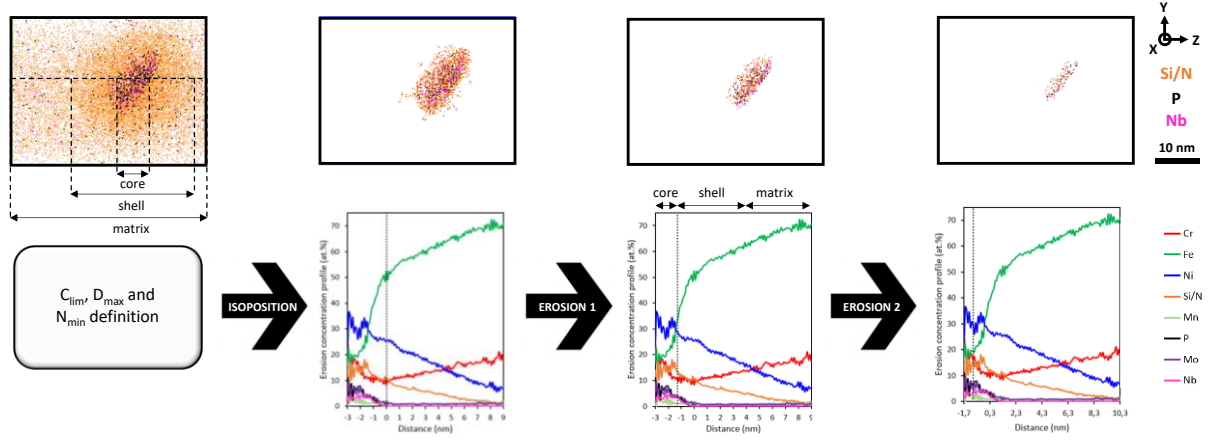


Figure 55 – From left to right. Erosion profiles after isoposition, interface cluster-matrix definition (erosion 1), cluster core (erosion 2) of an elongated core-shell cluster and the corresponding 3D-volumes.

To minimize interface bias, cluster core composition is calculated after a second erosion: erosion 2 (Figure 55). Here, the interface is set at the maximum of the cluster core composition. Erosion 1 and 2 are completed for each class of cluster size.

- Step 6: cluster analysis

Assuming spherical clusters with a uniform atom density, clusters radii can be given either by the Guinier radius R_G :

$$R_G = \sqrt{\frac{5}{3}} R_g \quad (128)$$

with R_g the gyration radius, given by:

$$R_g = \sqrt{\frac{\sum_{i=1}^n \{(x_i - x_0)^2 + (y_i - y_0)^2 + (z_i - z_0)^2\}}{n}} \quad (129)$$

where (x_0, y_0, z_0) are the coordinates of the center of mass of the cluster, (x_i, y_i, z_i) the coordinates of the i^{th} atom and n the number of atom in the cluster.

Or by the radius deduced from the volume of a sphere R_S and corrected by the detector efficiency Q :

$$R_S = \sqrt[3]{\frac{3nV_{at}}{4\pi Q}} \quad (130)$$

The resulting cluster size D is given by multiplying R_G or R_S by 2, clusters at the edge of the volume are not taken into account for the size measurement.

An atom density profile drawn through a particle can reveal a difference of evaporation field between this particle and the surrounding matrix. If it is the case, the shape of the particle will evolve after being evaporated (Figure 56), as already explained in Figure 47.

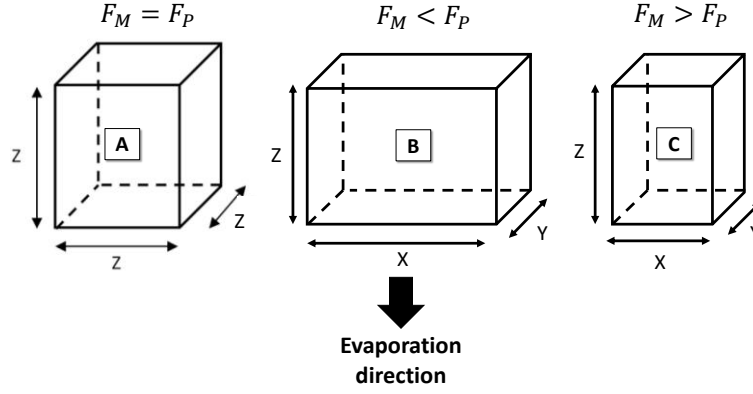


Figure 56 – Effect of local magnification of a cubic particle A) before, B) after field evaporation of a high-field particle and C) a low field particle. In both cases, the size in the z direction is slightly affected by the field difference but for the low field particle, the core composition cannot be experimentally measured without matrix contribution if the field difference is too high or the particle is too small. An analytical model had been developed to correct the measured composition for this latter case [164].

A high field precipitate ($F_M < F_P$) will cause a lateral dilatation and a low field precipitate ($F_M > F_P$) will result in a compression on the xy plane (the plane perpendicular to the analysis direction). Dimension in the analysis direction, z shouldn't be affected. Therefore, in this case, previous equations cannot be applied directly. The particle size is given as the size in z direction. Nevertheless, complementary simulations or correlative microscopy are useful complementary tools in order to provide the exact size of particles.

The volume fraction of clusters can be calculated in three different ways:

$$f_V = \frac{N_{clusters}}{N_{matrix}} \quad (131)$$

with $N_{clusters}$ and N_{matrix} are the number of atoms lying in clusters and in the matrix respectively.

$$f_V = N_V \frac{4}{3} \langle R^3 \rangle \quad (132)$$

with N_V the number density of clusters and $R=R_G$ or $R=R_S$.

$$f_V = \frac{C_0 - C_m}{C_c - C_m} \quad (133)$$

with C_0 , C_m and C_c the global, matrix and cluster concentrations respectively.

Finally, if no compositional bias is expected, cluster composition is given by as the average of all single cluster of a given class size.

To sum up

Depending on the irradiation conditions, the resulting damaged microstructure of austenitic stainless steels can contain a high density of defects with size ranging from the sub-angstrom scale (point defects) to the sub-micron scale (e.g. large precipitates). Transmission Electron Microscopy covers a large range of scales to identify most of as-induced defects. These defects are characterized by their crystallography and their chemistry. Both aspects can be resolved by TEM with some limitations concerning chemical analysis, mostly due to the matrix contribution and information superimposition over the depth of the foil.

Extract the composition of an object (i.e segregation at dislocations, cavities or precipitate/matrix interface) within the surrounding matrix can be done by performing a 3D chemical analysis. 3D EDS or 3D EELS offer this possibility in a TEM [165]. Both of these promising techniques require further developments to compete with Atom Probe Tomography in terms of detectability limit and composition measurement accuracy.

TEM and APT are intensively used in parallel to study microstructure evolution under irradiation. While correlative microscopy has seen rapid expansion over the past few years, only scarce experiments were done on irradiated materials. Combining their strengths, they allow to completely describe nanodefects and give new keys to understand basic mechanisms of radiation-induced segregation.

CHAPTER 3

IRRADIATION EFFECT ON DIFFUSION KINETICS

Experimental determination of interdiffusion coefficients after thermal annealing and under irradiation via the nanolayers method in Ni-Cr and Fe-Ni-Cr model alloys

I.	Introduction.....	114
II.	Theoretical approach of the nanolayers method.....	114
1.	In the binary system.....	114
2.	In the ternary system.....	117
III.	Experimental implementation.....	118
1.	Ageing conditions: annealing and irradiations.....	118
2.	Nanolayers elaboration and optimizations.....	122
3.	Specimen preparation.....	126
IV.	Interdiffusion kinetics in Ni/Ni-20Cr system after thermal ageing and under irradiation.....	128
1.	Microstructure evolution.....	128
2.	Concentration amplitude evolution.....	135
3.	Interdiffusion coefficients.....	142
4.	Discussion.....	144
V.	Interdiffusion kinetics in Ni-40Fe-25Cr/Ni-35Fe-20Cr system after thermal ageing and under irradiation.....	149
1.	Microstructure evolution.....	149
2.	Concentration amplitude evolution.....	152
3.	Interdiffusion coefficients.....	155
4.	Discussion.....	157
VI.	General discussion.....	161
VII.	Conclusion.....	164

I. Introduction

Input parameters of radiation induced segregation (RIS) models are fitted or compared for validation on thermal diffusion kinetics. Unfortunately, the interdiffusion kinetics database is poor for binary NiCr alloys at low temperature (below 550°C) and, to our knowledge, inexistent in the FeNiCr system. Another important parameter that have not been yet measured experimentally is the self interstitial atom (SIA) mediated diffusion coefficient under irradiation. The aim of this study is to bring quantitative data about interdiffusion kinetics both under thermal diffusion and irradiation at low temperature (i.e. between 400 and 550°C) to improve models of RIS.

For given diffusion length and diffusion kinetics, the lower the temperature the longer the time. To obtain interdiffusion kinetics at low temperature under reasonable (or even feasible) time, the nanolayers method is well suited. Interdiffusion kinetics as low as $10^{-26} \text{ m}^2\text{s}^{-1}$ are accessible by this method. Interdiffusion coefficients are extracted from the concentration amplitude attenuation of a stack of nano-scaled diffusion couples resulting in a composition modulated structure. This kind of material can be fabricated by magnetron co-sputtering and can give access to a very large range of compositions.

To extract experimentally amplitude evolution, experimental techniques should be scaled to the diffusion length. In the present case, APT, used to extract concentration amplitude and to study the elemental distribution was combined with TEM, to characterize the microstructure and to interpret obtained results.

Two austenitic NiCr and FeNiCr model systems have been studied within the operation temperature range of nuclear reactors both after thermal ageing and under irradiation in the scope of the Generation IV Materials Maturity (GEMMA) project (see APPENDIX).

II. Theoretical approach of the nanolayers method

1. In the binary system

For binary systems, review of the method can be found here: [107,166–169].

Nanolayers consist in a stack of nanometric diffusion couples. In the case of substitutional diffusion in a binary system A-B, composition modulations evolution of an element A can be modelled by a sinusoid:

$$X_t(z) - \bar{X} = A_t \cos[g(\Lambda)z] \quad (134)$$

with $X_t(z)$ the atomic fraction at the depth z for the ageing time t and \bar{X} the mean atomic fraction of the element A. The factor $g(\Lambda)$ depends on the modulation wavelength Λ . Amplitude modulation at the time t is given by:

$$A_t = A_0 e^{-g(\Lambda)^2 \tilde{D}_{AB,A} t} \quad (135)$$

where A_0 is the amplitude at $t=0$ and $\tilde{D}_{AB,\Lambda}$ the effective interdiffusion coefficient. $\tilde{D}_{AB,\Lambda}$ is extracted from the concentration amplitude evolution via this expression:

$$\tilde{D}_{AB,\Lambda} = \frac{\ln(A_0) - \ln(A_t)}{g(\Lambda)^2 t} \quad (136)$$

Assuming small modulations in composition, $\tilde{D}_{AB,\Lambda}$ is invariant for a given nominal composition and temperature. In order to define the bulk interdiffusion coefficient \tilde{D}_{AB} in terms of $\tilde{D}_{AB,\Lambda}$, one needs to describe first the studied system regarding the theory. Four cases are distinguished and detailed in Table 15:

- For thin multilayers with $\Lambda > 10$ nm, with d the interatomic distance, (i.e. smooth concentration gradients), Eq. (136) can be applied directly. Here, the system is uniform, a continuum model is used to describe the free energy of the system giving $g(\Lambda) = \frac{2\pi}{\Lambda}$ and $\tilde{D}_{AB,\Lambda} = \tilde{D}_{AB}$.
- For ultrathin multilayers with $10 \text{ nm} > \Lambda > 6d$ (i.e. steep concentration gradients), Cahn and Hilliard [170] proposed a continuum model to describe the dependency of the local Helmholtz free energy on the local composition gradient. In a region of nonuniform composition, the local free energy will depend both on the local composition and on the composition of the immediate environment. Consequently, the 2nd Fick's law expression is redefined considering the composition gradient. In this case, $\tilde{D}_{AB,\Lambda} \neq \tilde{D}_{AB}$.
- For ultrathin multilayers valid for all $\Lambda < 10$ nm (i.e. steep concentration gradients), Cook et al. [171] shown that the continuum model failed to describe modulation evolution below $\Lambda=6d$. They proposed a discrete model for the free energy description.
- For elastically strained ultrathin multilayers valid for all $\Lambda < 10$ nm (i.e. steep concentration gradients). Strain in multilayers can arise from lattice parameter variation with composition, especially when coherency is maintained in epitaxial materials. Elastic strain contribution to diffusion can be neglected when the atomic size difference is below about **10%** or if interfaces between layers are partially coherent or incoherent because the presence of dislocations can relieve the strain. In the Ni-Cr and Fe-Ni-Cr systems studied, deposited layers are not grown in epitaxy and atomic radius variations are: Ni/Cr $\sim 12\%$, Ni/Fe $\sim 6\%$, Cr/Fe $\sim 8\%$. In the present study, strain effect on diffusion can reasonably be neglected.

Authors tried to establish a criterion for Λ from which gradient energy becomes significant: > 10 nm can be found [171], > 1 nm [172] or $> 10d$ in [167]. As it depends on the average composition of the studied system, Λ effect on the measured effective interdiffusion coefficient should be estimated with respect to this system.

Table 15 – Analysis of interdiffusion in crystalline binary solid solution with small periodic variations of composition in one dimension (i.e. nanolayers)

Studied system	Thin $\Lambda > 10$ nm (=bulk diffusion) No change in atomic radius Absence of coherence strains	Ultrathin $\Lambda < 10$ nm Valid for $\Lambda > 6d$ No change in atomic radius Absence of coherence strains	Ultrathin $\Lambda < 10$ nm Valid for all Λ No change in atomic radius Absence of coherence strains	Ultrathin $\Lambda < 10$ nm Valid for all Λ Change in atomic radius Presence of coherence strains
Free energy model of the system	Homogeneous system Continuum model Smooth concentration gradients	Nonhomogeneous system Continuum model Steep concentration gradients	Nonhomogeneous system Discrete model Steep concentration gradients	Nonhomogeneous system Discrete model Steep concentration gradients Elastic strain
Ref.	[173]	[170]	[174,175]	[171,176,177]
2 nd Fick's law	$\frac{\partial X}{\partial t} = \tilde{D}_{AB} \left(\frac{\partial X}{\partial z} \right)^2$	$\frac{\partial X}{\partial t} = \tilde{D}_{AB} \left(\frac{\partial X}{\partial z} \right)^2 - \tilde{D}_{AB} \frac{2\kappa}{f_0''} \left(\frac{\partial X}{\partial z} \right)^4$	$\frac{\partial X}{\partial t} = \frac{\tilde{D}_{AB}}{d^2} \left(\frac{\partial X}{\partial z} \right)^2 - \frac{\tilde{D}_{AB}}{d^4} \frac{2\kappa}{f_0''} \left(\frac{\partial X}{\partial z} \right)^4$	$\frac{\partial X}{\partial t} = \tilde{D}_{AB} \left[1 + \frac{2\eta^2 Y}{f_0''} \right] \left(\frac{\partial X}{\partial z} \right)^2 - \tilde{D}_{AB} \frac{2\kappa_c}{f_0''} \left(\frac{\partial X}{\partial z} \right)^4$
$g(\Lambda)^2$	$\left(\frac{2\pi}{\Lambda} \right)^2$	$\left(\frac{2\pi}{\Lambda} \right)^2$	$\frac{2}{d^2} \left[1 - \cos \left(\frac{2\pi d}{\Lambda} \right) \right]$ For wavevectors along $\langle 111 \rangle$ in FCC structures	$\frac{2}{d^2} \left[1 - \cos \left(\frac{2\pi d}{\Lambda} \right) \right]$ For wavevectors along $\langle 111 \rangle$ in FCC structures
\tilde{D}_{AB} vs $\tilde{D}_{AB,\Lambda}$ with $\tilde{D} = \tilde{D}_{\Lambda \rightarrow \infty}$	$\tilde{D}_{AB} = \tilde{D}_{AB,\Lambda}$	$\tilde{D}_{AB} \left(1 + \frac{2\kappa}{f_0''} g(\Lambda)^2 \right) = \tilde{D}_{AB,\Lambda}$	$\tilde{D}_{AB} \left(1 + \frac{2\kappa}{f_0''} g(\Lambda)^2 \right) = \tilde{D}_{AB,\Lambda}$	$\tilde{D}_{AB} \left(1 + \frac{2\eta^2 Y}{f_0''} + \frac{2\kappa}{f_0''} g(\Lambda)^2 \right) = \tilde{D}_{AB,\Lambda}$

Here d is the interplanar spacing, κ is the gradient energy coefficient, $\eta = \frac{d \ln a}{dc}$ and $f_0'' = \frac{\partial^2 f_0}{\partial X^2}$ are the distortion parameter, with a the lattice parameter, and the second derivative of the Helmholtz free energy of an homogeneous system are evaluated for $X=X_0$, Y is the elastic coefficient. $Y_{\langle 111 \rangle} = \frac{6(C_{11}+2C_{12})C_{44}}{4C_{44}+C_{11}+2C_{12}}$ in case of anisotropy along $\langle 111 \rangle$ direction in a cubic crystal and $Y = \frac{E}{(1-\nu)}$ for the isotropic case with C_{ij} the elastic constants E the Young modulus and ν the Poisson ratio.

If no coherency strains or variation of the lattice parameter must be considered, in order to estimate \tilde{D}_{AB} with respect to measured $\tilde{D}_{AB,\Lambda}$, the use of regular solutions [170] (i.e. for an ideal configurational entropy and an enthalpy of mixing varying parabolically with composition) established for f_0'' and κ is particularly usefull.

For a regular solution with only nearest neighbour interactions, the second derivative of the free energy with respect to the atomic fraction of an homogeneous system for an average composition c_0 is given by [178]:

$$f_0'' = \frac{1}{\bar{X}(1-\bar{X})} - 2Z\Omega \quad (137)$$

with Z the number of nearest neighbors and Ω the interaction parameter: $\Omega = E_{AB} - \frac{1}{2}(E_{AA} + E_{BB})$, where E_{ij} corresponds to the bonding energies between i and j atoms.

And,

$$\kappa = 2\Omega \quad (138)$$

2. In the ternary system

For ternary systems, reviews or experimental applications of the method can be found here: [168,179–185].

In an A-B-C ternary system, concentration modulations of elements A and B (C is put as reference, with $X_A + X_B + X_C = 1$) in the z direction are expressed as:

$$\begin{cases} X_{A,t} - \bar{X}_A = [\alpha_{AA}e^{-g(\Lambda)^2\tilde{D}_1t} + \alpha_{AB}e^{-g(\Lambda)^2\tilde{D}_2t}] \cos(g(\Lambda)z) \\ X_{B,t} - \bar{X}_B = [\alpha_{BA}e^{-g(\Lambda)^2\tilde{D}_1t} + \alpha_{BB}e^{-g(\Lambda)^2\tilde{D}_2t}] \cos(g(\Lambda)z) \end{cases} \quad (139)$$

Expressions between square brackets describe sinusoidal amplitude $A_i(t)$ of the modulations. Constants α_{il} can be defined at $t=0$ with $A_A(t=0) = \alpha_{AA} + \alpha_{AB}$ and $A_B(t=0) = \alpha_{BA} + \alpha_{BB}$.

As explained in CHAPTER 1, four interdiffusion coefficients need to be determined. They are linked to the apparent interdiffusion coefficients \tilde{D}_1 and \tilde{D}_2 by these following relations:

$$\begin{cases} \tilde{D}_{AA} = \frac{\tilde{D}_A T_A - \tilde{D}_B T_B}{T_A - T_B} \\ \tilde{D}_{AB} = -\frac{(\tilde{D}_A - \tilde{D}_B)T_A T_B}{T_A - T_B} \\ \tilde{D}_{BB} = -\frac{\tilde{D}_A T_B - \tilde{D}_B T_A}{T_A - T_B} \\ \tilde{D}_{BA} = \frac{\tilde{D}_A - \tilde{D}_B}{T_A - T_B} \end{cases} \quad (140)$$

where $T_A = \frac{\alpha_{AA}}{\alpha_{BA}}$ and $T_B = \frac{\alpha_{AB}}{\alpha_{BB}}$.

In order to determine experimentally interdiffusion coefficients at one temperature, more than one annealing time is necessary. The logarithm of the amplitude attenuation of the slowest element (here element A) plotted against annealing time shows a slope break of the curve. From the slope and intercept linear part of the curve, value of \tilde{D}_1 and $\frac{\alpha_{AA}}{\alpha_{AA}+\alpha_{AB}}$ are obtained. As amplitude values at $t=0$ are known as well, all unknowns are solved. Determined interdiffusion coefficients must comply to the equations (25) and (26) presented in CHAPTER 1.

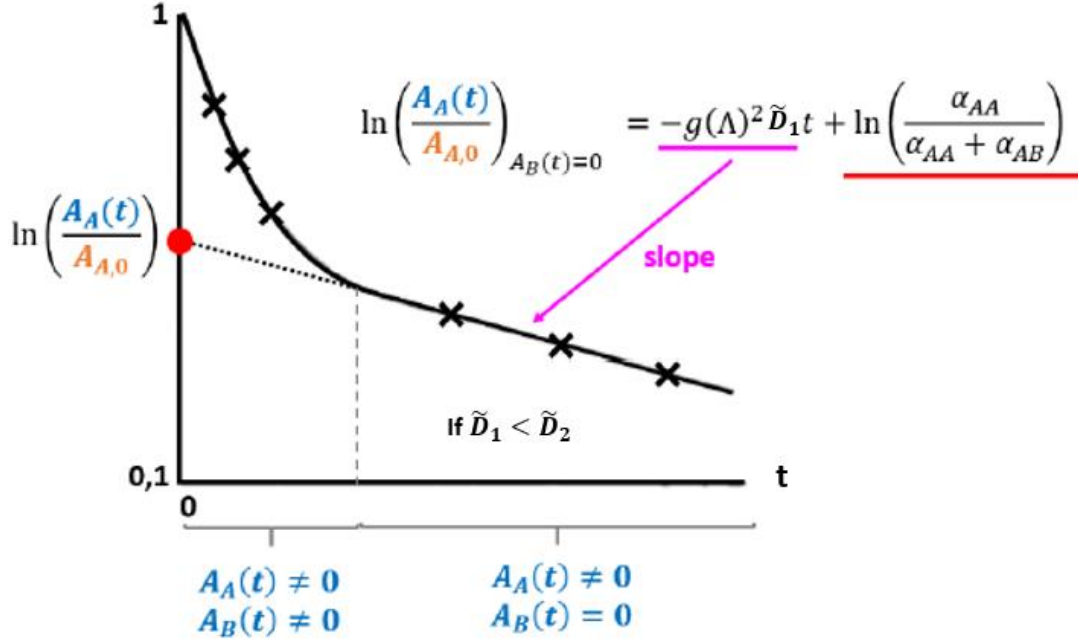


Figure 57 – Schematic representation of parameters determination from amplitude attenuation evolution with annealing time in a ternary system.

Similarly to the binary system, for the ternary system a gradient energy term can be added [183] while Morral and Cahn [186] proposed a correction factor for elastic strains. For the same reasons than for the binary, it was decided to ignore any elastic contribution to diffusion.

III. Experimental implementation

Nanolayers have been elaborated by magnetron co-sputtering by A. Billard from UTMB (Montbéliard). Sputtering is a physical vapor deposition (PVD) method consisting in the condensation on a substrate of atoms ejected from the surface of a target material by energetic particles. Principle is described briefly in the following section, more details about the theory can be found here: [187–190].

1. Ageing conditions: annealing and irradiations

In order to select the appropriate annealing and irradiation conditions, extrapolations and simulations were performed based on the as-deposited microstructure of each system. To do so, the wavelength and the sink strength were experimentally determined (see sections IV-1 and V-1).

The modulation wavelength is equal to 4.3 ± 0.3 nm and 5.3 ± 0.1 nm for the binary and the ternary systems respectively. The sink strength magnitude range is $10^{17} < 10^{18} < 10^{19}$ m⁻² for both systems. Wavelength and sink strength determination helped to predict amplitude attenuations and adapt ageing conditions (i.e. thermal and irradiations).

In CHAPTER 1, it has been shown that Darken-Manning approximation expresses interdiffusion coefficients in a binary or a ternary alloy in terms of atomic fractions, impurity diffusion coefficients, thermodynamic factors and vacancy wind factors (themselves being functions of atomic fractions and impurity diffusion coefficients). To choose annealing conditions (i.e. time and temperature), theoretical interdiffusion coefficients were calculated for temperatures ranging from 400 to 550°C for both systems.

Thermodynamic factors were derived from chemical potentials obtained thanks to Thermo-Calc (Ni V8.1 database) while impurity diffusion coefficients were calculated from Campbell et al. [191] atomic mobility assessment (NIST Ni-based diffusion mobility database available here: <https://materialsdata.nist.gov/handle/11256/942>), these coefficients have also been used to calculate the vacancy wind factors. Both databases were chosen for their compatibility. Calculation of the theoretical interdiffusion coefficients followed the same procedure than described in the Appendix B of [192] in the case of the binary system and was adapted for a system of three components using equations presented in CHAPTER 1.

Assuming that modulation wavelengths are large enough to neglect any gradient energy contribution (i.e. $\tilde{D}_A = \tilde{D}$), Equation (136) for thin multilayers and Equations (139) & (140) permitted to calculate amplitude attenuations in terms of annealing time between 400 and 550°C for the binary and the ternary systems respectively. Results are presented in Figure 58. An annealing temperature of 450°C appears to be a good compromise to neglect heating and cooling stages and obtain interdiffusion kinetics under a reasonable time (<1 week) for both systems.

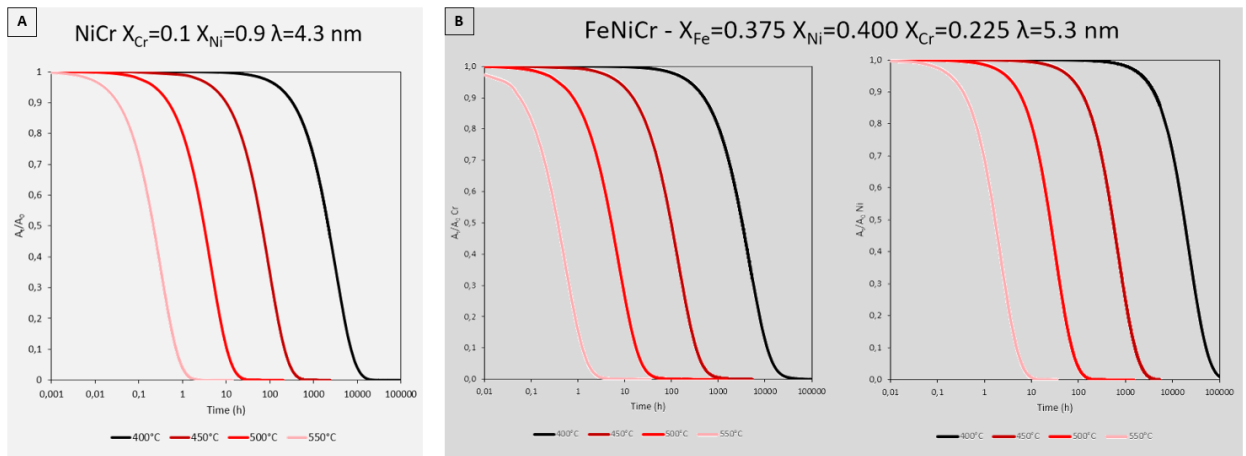


Figure 58 – Amplitude attenuations evolution in terms of annealing conditions (i.e. time and temperature) for Ni and Cr for the A) Ni/Ni-20Cr and B) Ni-40Fe-25Cr/Ni-35Fe-20Cr systems.

Chunks were plasma cleaned prior to annealing. A Zr sheet was placed in the quartz tube of a tubular oven nearby the Mo grid to act as an O getter. 24h of pumping permitted to reach a

vacuum level of 10^{-6} - 10^{-7} mbar before starting the thermal treatment. The heating rate was 0.27°C per second and after 48h of annealing at $440 \pm 10^{\circ}\text{C}$, the oven was slid away from the tube. The thermocouple placed at the vicinity of the grid did not registered the cooling stage. At the beginning of the temperature curve (Figure 59.A)), a temperature peak is observed. The temperature reached temporarily 460°C . Since 1h annealing at 460°C would have provoked an amplitude attenuation of 0.98 for the binary system, which is within the experimental error, it can be neglected. To avoid this peak and minimize heat-up time, the oven can be slide to the tube when preheating is complete. During annealing the chunk bent (Figure 59.B)). Mo from the grid may have diffuse inside de nanolayers at the welding level. Oversized atoms of Mo probably induced a stress gradient between the intermixing zone and the zone free from Mo. It can be also justified by a stress relaxation of the nanolayers.

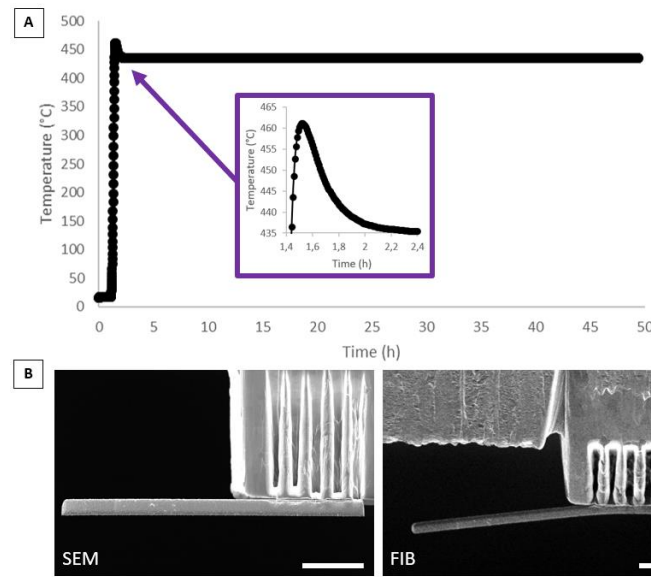


Figure 59 – A) Temperature curve and B) SEM and FIB view of the chunk after nanolayers annealing during 48h at 440°C . Scale bars = $5\text{ }\mu\text{m}$.

In order to predict approximately amplitude attenuations under heavy ions irradiations at 440°C and select the appropriate accessible conditions (i.e. dose rate and time), interdiffusion coefficients within a large range of dose rates and sink strengths have been determined by modelling for the Ni-10Cr system (Figure 60.A)). The developed analytical model [193] describes diffusion fluxes of single species (i.e. Ni, Cr, vacancies (V) and SIA) and five type of clusters (i.e. Cr, V and SIA monomers and the two pairs Cr-V and Cr-SIA) based on the Onsager formalism (see CHAPTER 1). Phenomenological coefficients are calculated thanks to the self-consistent mean-field theory [194] from the ab initio atomic jump frequencies. Partial (independent on PD concentration) and intrinsic diffusion (dependent on PD concentration) coefficients are calculated from phenomenological coefficients and the steady-state point defects (PD) bulk concentration. Long-range diffusion of atoms under irradiation depends on the steady-state PD bulk concentration determined from the reaction rate theory (see CHAPTER 1). The model accounts for the PD production (defined as replacement per atom per second in rpa.s^{-1} , proportional to the well-known dpa.s^{-1}), the forced atomic relocation events taking place in a displacement cascade (restricted to the first near neighbour interactions), mutual recombination, and the overall sink strength of the microstructure

controlling the elimination of PDs at unbiased sinks (i.e. no elastic effect). Calculations were done for the case of a dilute alloy, it is therefore reasonable to ignore interactions larger than pairs and to take thermodynamic factors equal to unity. Finally, interdiffusion coefficients have been calculated thanks to the Darken approximation. Ballistic mixing is also considered in the model.

Based on the model result (Figure 60.A)) and the calculated magnitude of the sink strength, interdiffusion coefficient under irradiation for the binary system ranges between 5×10^{20} and $1 \times 10^{21} \text{ m}^2 \cdot \text{s}^{-1}$ (for a PD bulk concentration determined at steady state). As shown in Figure 60.B), at the lowest accessible dose rate of $1.6 \times 10^{-5} \text{ dpa} \cdot \text{s}^{-1}$, amplitude mitigates extremely fast with a full attenuation ranging from few seconds to approximately one hour of irradiation time.

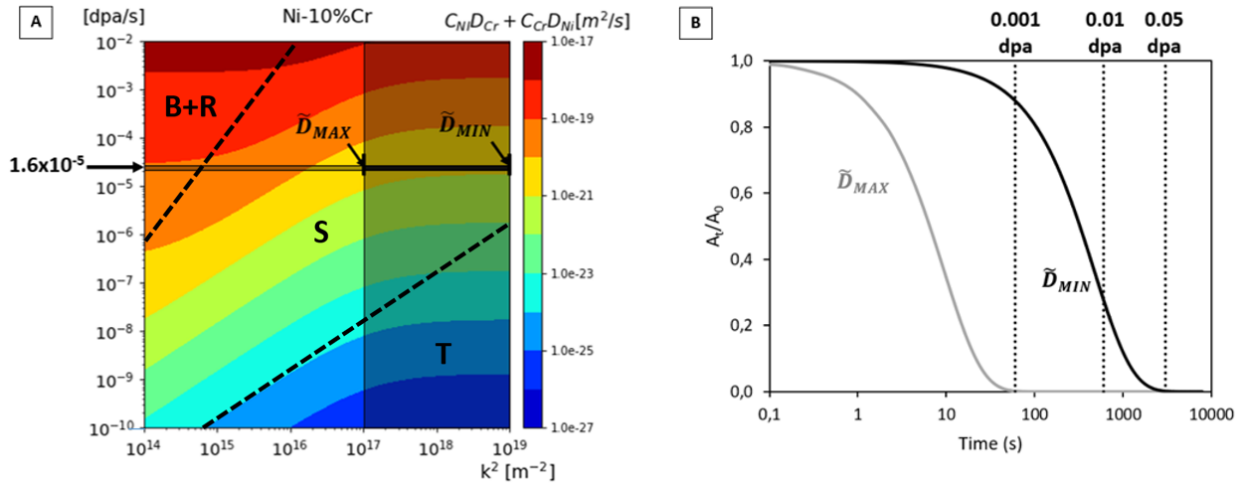


Figure 60 – A) Evolution of the interdiffusion kinetics in terms of dose rate and sink strength at 440°C (acknowledgments Liangzhao Huang). Their magnitude is indicated on the graph by grey windows. The regime limits are drawn with dashed lines for: T stands for thermal (or back diffusion), S for elimination at sinks and B+R for ballistic and recombination. B) The corresponding predictions of amplitude attenuation for \tilde{D} extrema (here $\tilde{D}_A = \tilde{D}$) and the irradiation durations necessary to reach 0.001, 0.01 and 0.5 dpa.

As uncertainties are large regarding predicted interdiffusion kinetics, we processed to a multi-dose irradiation. It consists to uncover regions of the specimen holder gradually during irradiation to let the beam illuminate specific samples only (Figure 61). Irradiation time had to be comprised between 1 min and 1h to ensure reliable flux measurement and prevent from a non-negligible thermal diffusion. Selected times were 1, 10 and 50 min to reach 0.001, 0.01 and 0.05 dpa.

Irradiations were performed in JANNuS Saclay triple ion beam facility (see CHAPTER 4 for details). The beam energy with Fe^{5+} ions was 10 MeV corresponding to an implantation peak depth at $2.3 \mu\text{m}$ (i.e. out of the nanolayers chunks) at a damage rate of $1.6 \times 10^{-5} \text{ dpa} \cdot \text{s}^{-1}$. According to SRIM calculations, target doses were reached in the region of interest: between 400 and 1100 nm for the NiCr and the FeNiCr systems having a total nanolayers thickness of 1.5 and $1 \mu\text{m}$ respectively.

The vacuum level was below $7 \cdot 10^{-8} \text{ mbar}$. Four thermocouples positioned at the vicinity of the samples recorded an average temperature of 441°C and the thermal camera shown a homogeneous temperature distribution at samples level during irradiations.

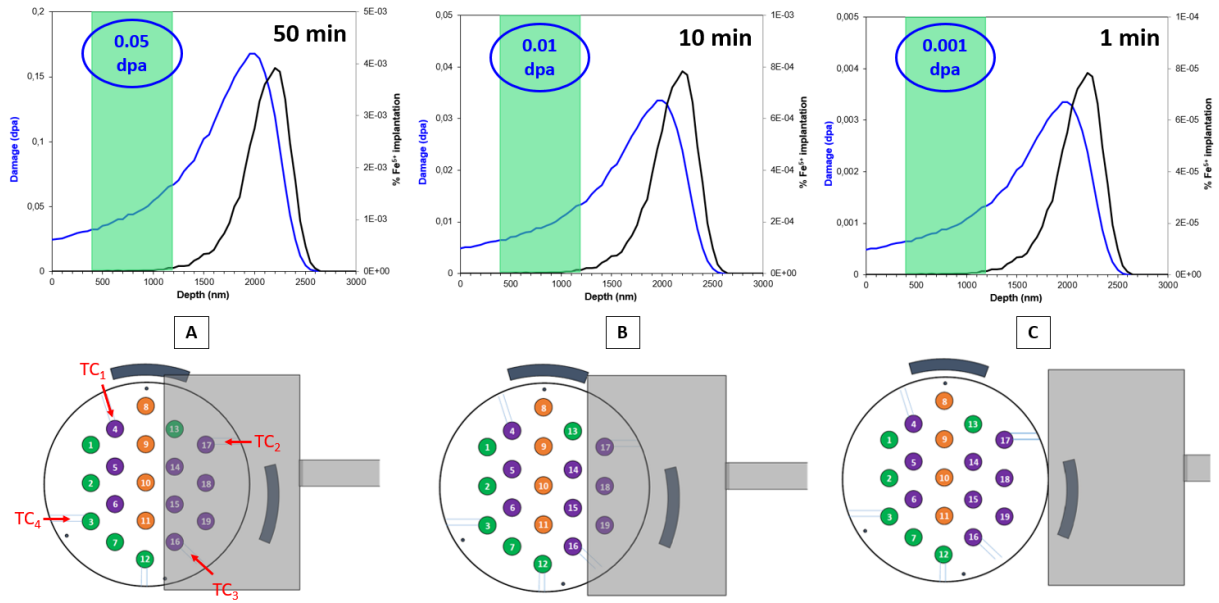


Figure 61 – Multi-dose irradiations and selected conditions, nanolayers positions are indicated by circles filled in purple and the 4 thermocouples are indicated by red arrows. Cover position A) at the beginning of irradiation B) after 40 min C) after 49 min after and the corresponding damage and implantation profiles.

Unfortunately, a grid felt before being irradiated and a large amount of “free welded” chunks broke away. Only two conditions are available per system: 0.001 and 0.05 dpa for the binary system, 0.001 dpa and 0.01 dpa for the ternary system. Obtained results are presented in the next sections.

2. Nanolayers elaboration and optimizations

The reactor is first placed under a secondary vacuum. Then, an inert gas, here Ar, is injected inside the reactor. A plasma is generated nearby the negatively biased target (i.e. cathode, reactor walls playing the role of anode) by discharge glow. The plasma is confined thanks to a magnetron and positive ions are accelerated to the target. The use of a magnetron allows to access to high sputter yield and stabilizes discharge under low pressures (low pressures promote compact structures versus columnar ones) [188]. Energetic ions collide with surface atoms and eject them from their host lattice. In the case of co-sputtering, this process is repeated on, at least, two different targets. As-sputtered atoms loose energy passing through the plasma before their condensation on a rotating substrate. A high rotation speed of the substrate permit to mix sputtered materials and obtain thin films with homogeneous composition approaching the average composition of the two targets. Indeed, the angular distribution of the sputtered materials depends, inter alia, on elements nature and affects coating composition. In order to obtain nanolayers, rotation speed is decreased and a wall is interposed between targets approaching as close as possible to the surface to be coated (Figure 62). The closer, the steeper the concentration gradient. At constant sputter yield, the lower the rotation speed, the thicker the layers. The total deposited layer thickness depends on the deposition duration. Substrates were held at room temperature to prevent from interdiffusion during deposition and reduce oxygen contamination due to degassing. No bias was applied to the substrate to reduce internal stresses within the coating.

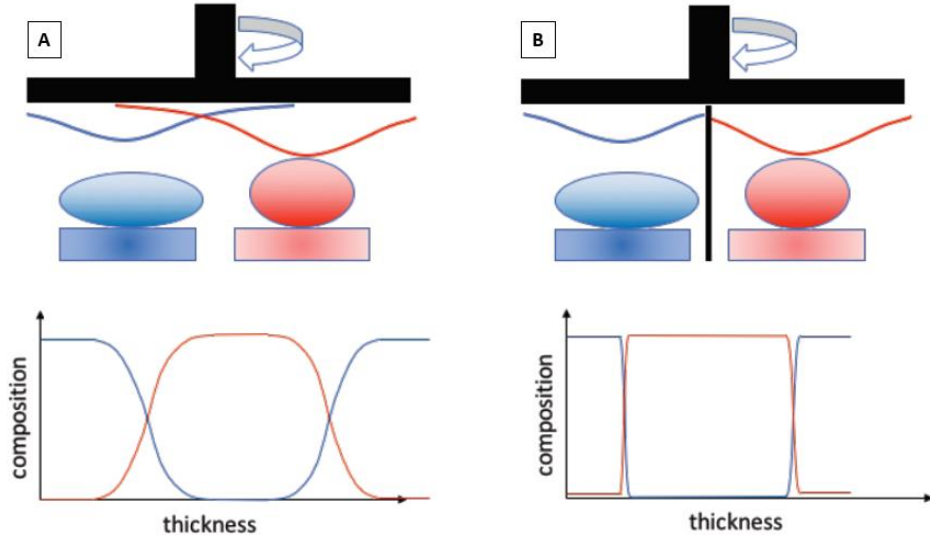


Figure 62 – Thickness profiles regarding the angular distribution (blue and red ellipsoids) of sputtered target materials and the respective concentration profiles in terms of deposited thickness A) with or B) without placing a wall between targets [195].

For the Ni-Cr binary system, the aim was to obtain nanolayers having a fully austenitic structure with the largest amplitude in composition. A Thermo-Calc calculation of the phase diagram (Figure 63.A)) permitted to select the composition of the layers (i.e. the targets): Ni and Ni-20Cr.

For the ternary system, to obtain a fully austenitic structure and a composition representative of 316/L steels (Fe-18Cr-12Ni) within the temperatures of interest is not feasible by magnetron co-sputtering. Indeed, biphasic austenite/ferrite domains represent the largest part of the equilibrium ternary diagram (Figure 63.B)). Compromises must be done.

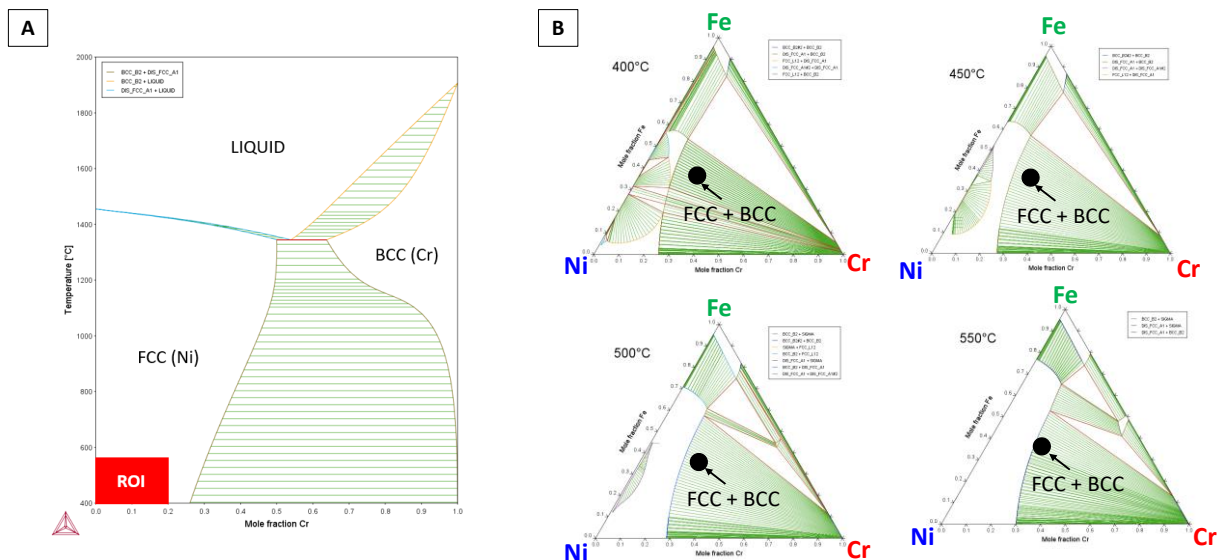


Figure 63 – A) Ni-Cr binary and B) Fe-Ni-Cr ternary phase diagrams calculated with Thermo-Calc. The red square on A) represent the region of interest (ROI) in terms of composition and temperature. Black spots in B) represent the average composition Ni-37.5Fe-22.5Cr of the selected system.

Furthermore, because of very high cooling rate of approximately 10^{12} K.s^{-1} [188,196] associated to vapor-quenching during metallic vapor condensation, metastable ferrite or sigma phase can be formed (Figure 64) [197,198]. In order to diminish the probability to analyse ferrite instead of austenite, the structure should be mostly austenitic ($\geq 90\%$). Therefore, choice was made to work on a Ni-based system with limited composition variations. Retained layers composition are Ni-40Fe-25Cr and Ni-35Fe-20Cr.

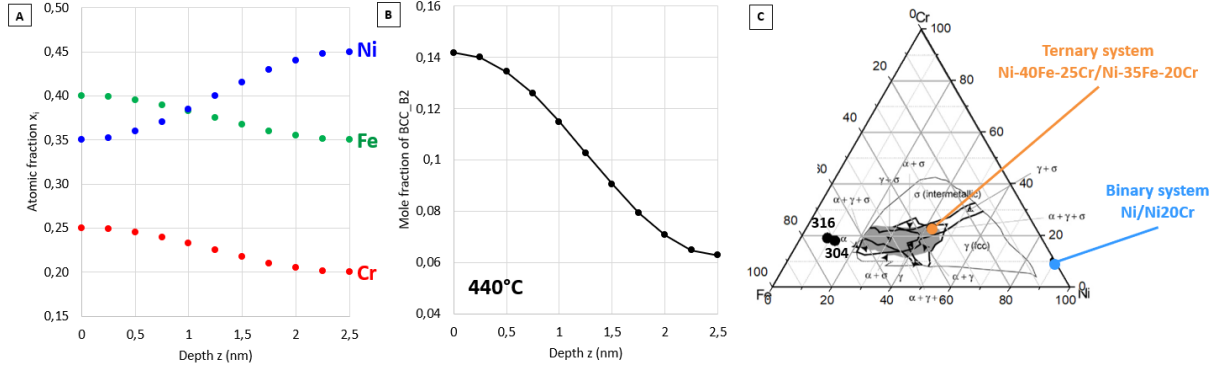


Figure 64 – A) Composition evolution of half of a modulation period for the selected composition. B) Calculated mole fraction of ferrite within this composition range. C) As-deposited ternary phase diagram at room temperature by PVD. The grey area marks the non-equilibrium phase domain [198].

Thanks to their very low surface roughness (typically $< 1 \text{ nm}$) and excellent flatness, single crystal Si wafers substrates ensure low rugosity of the deposited nanolayers. Since they are conductors when doped, further characterizations in electron microscopes and the use of APT electrical mode are facilitated.

Ensure a good adhesion between the coating and the substrate is also an important factor. Doped Si wafers show a relatively good bonding with iron-based metals. A metallic layer between the substrate and the nanolayers can be deposited to enhance adhesion if necessary.

On one hand, to access rapidly to interdiffusion kinetics at low temperature, wavelength should be as small as possible. On the other hand, to neglect the gradient energy term, wavelength selected for the selected systems should be larger than 10 nm or 10 times the interatomic distance d . FCC structures deposited by magnetron sputtering often exhibit strong $[111]$ crystallographic texture. In austenitic Fe-Ni-Cr systems, $d_{111}=0.2 \text{ nm}$, thus $10d$ criterion gives 2 nm minimum to neglect the gradient energy term. A value in between was finally kept: 5 nm both for the binary Ni-Cr and ternary Fe-Ni-Cr systems.

Finally, contamination should be minimised to avoid carbides and oxides formation and not to disturb major elements diffusion of the studied systems after annealing and irradiation. This implies to use high purity targets (i.e. $> 99.9 \text{ at.}\%$) and to start deposition under a base vacuum as low as possible. To do so, a degassing procedure of the water vapor adsorbed on the reactor walls was performed before carrying out coating synthesis. First, the reactor is pumped during at least 18h to obtain a base vacuum of 3.10^{-6} mbar , then the reactor is heated by a resistance up to 300°C during 6h minimum. This degassing procedure permitted to decrease the base vacuum level down to $6\text{--}7.10^{-7} \text{ mbar}$ [195].

In order to avoid oxygen contamination during further treatments, a thin layer (~ 50 nm) of sub-stoichiometric silicon oxide SiO_x was deposited on the top of the nanolayers [199]. To prevent diffusion of Si into the nanolayers, the native silicon oxide at substrate surface was kept to act as a diffusion barrier (Figure 65 - "Before").

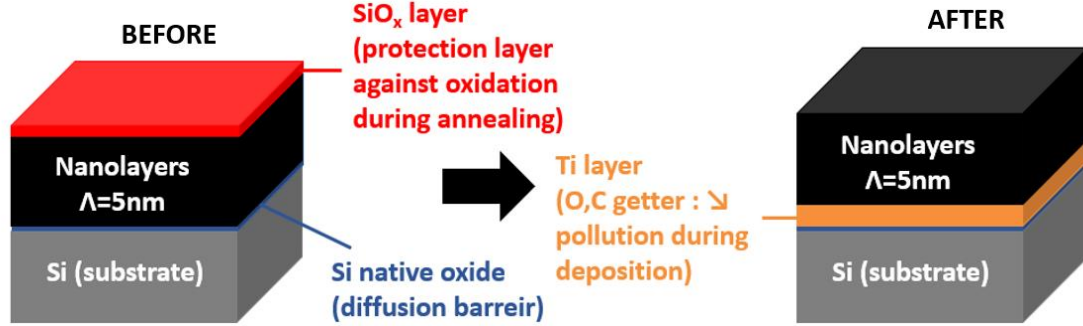


Figure 65 – Optimization of coating architecture

First set of samples prepared with this architecture were highly contaminated with oxygen and carbon (Table 16) and a real lack of adhesion between the substrate and the nanolayers was observed after thermal annealing. No reliable interdiffusion coefficients could have been determined from these samples because of large amplitudes irregularities and dense oxides precipitation after annealing. Contamination was detected to come from nanolayers fabrication, not during annealing. It was also observed that SiO_x top layer did not adhere well to the nanolayers. Thus, the elaboration process was optimized. In the optimized architecture (Figure 65 - "After"), additional optimizations successfully helped to overcome this contamination issue (Table 16) :

- Nanolayers were not covered by SiO_x cap to avoid adhesion problem of this cap.
- A Ti layer was deposited between the SiO_2 native layer and the nanolayers. Ti has proven to adhere very well with SiO_2 [200]. It plays also the role of a getter for oxygen and carbon thanks to his good affinity with these elements. Finally, it acts as a buffer layer regarding its linear thermal expansion coefficient being between the Si and nanolayers ones.
- Originally, substrate was stuck to the rotating substrate holder thanks to a Kapton adhesive tape. It was replaced by silver paint.
- Increase sputter yield decreases oxygen capture. Increasing sputter yield imposes to increase at the same time the rotation speed of the substrate to obtain the same wavelength.

Table 16 – APT volumes global composition in at.% at the as-deposited state before and after optimizations

	Al	C	Cr	Fe	Mn	Ni	O	Si	N	Purity
Before	0.02 ± 0.01	0.60 ± 0.2	12.3 ± 0.1	0.3 ± 0.1	0.09 ± 0.07	81.3 ± 0.3	5.3 ± 0.1	0.03 ± 0.04	0.04 ± 0.05	93.6
After	0.02 ± 0.00	0.08 ± 0.01	10.4 ± 0.4	0.37 ± 0.08	0.006 ± 0.001	89.0 ± 0.4	0.04 ± 0.01	0.04 ± 0.01	0.03 ± 0.01	99.4

3. Specimen preparation

The optimized architecture is in line with expectations and was kept to study interdiffusion for both systems. The resulting microstructure and obtained results will be described in sections IV and V. Nevertheless, first annealing of the optimized architecture revealed that Ti diffused within the nanolayers coating. Thus, specimen preparation should be adapted as well. Optimized specimen preparation based on the first annealing characterizations is described in this section.

As-deposited microstructure of the binary system is presented Figure 68. 400 nm Ti layer is deposited on a Si wafer substrate and coated with nanolayers over 1500 nm. Interfaces between coatings are abrupt thus no intermixing happened during elaboration. Coatings are dense, i.e. no cavities are observed. Columnar grains, tens of nm width and 1500 nm long, grew within the nanolayers coating. APT characterizations (Figure 75 and Figure 76.A)) confirmed that composition modulations are well defined in all grains at the as-deposited state.

After annealing under vacuum 25h at 440°C (acknowledgments Marie Loyer-Prost), the microstructure of the binary system Ni/Ni-20Cr with optimized architecture, as presented in Figure 65, evolved. The resulting microstructure is presented Figure 66. Grain growth, recrystallisation, large cavities formation (probably due to the Kirkendall effect) at the former Ti/nanolayers interface and reactive interdiffusion between Ti and Ni from nanolayers was observed from TEM investigations. Despite such microstructure evolution, STEM EDS concentration profile shows that, between cavities and coating surface, the average nanolayers composition looks still fine. Nevertheless, APT analyses revealed a heterogeneous diffusion. Indeed, within grains contaminated with Ti, composition modulations completely vanished whereas in other grains nanolayers are still visible. Grain boundaries are high diffusivity paths, Ti certainly diffuse from its former layer to the nanolayers region through grain boundaries.

Regarding the detrimental effect of Ti on interdiffusion kinetics in nanolayers, decision was made to remove both substrate and Ti before treatment (only nanolayers was kept). Nanolayers free of Ti and Si were welded on Mo TEM grids to facilitate their manipulation. Chunks were prepared thanks to the SEM-FIB Dual beam (Plasma) Helios Thermofisher. The use of Xe⁺ ions instead of Ga⁺ reduces both the implantation and the radiation damage depth induced by the ion beam [201]. Because standard Pt welding is a Pt/C mixture and C can diffuse rapidly within the studied nanolayers systems, we opted for the “free welding” method. This method consists in bonding materials together (here the nanolayers to the TEM grid) thanks to Mo redeposition during FIB milling. As the nanolayers coating is 1.5 µm and 1 µm thick for Ni-Cr and Fe-Ni-Cr systems respectively, it was necessary during the preparation process to save as much material as possible (to prevent from surface effect during treatments) and ensure to have removed all of the Si and Ti layers. To do so, after lift-out, the chunk was welded to a transfer Cu grid titled to have the nanolayers deposition direction perpendicular to the focused ion beam.

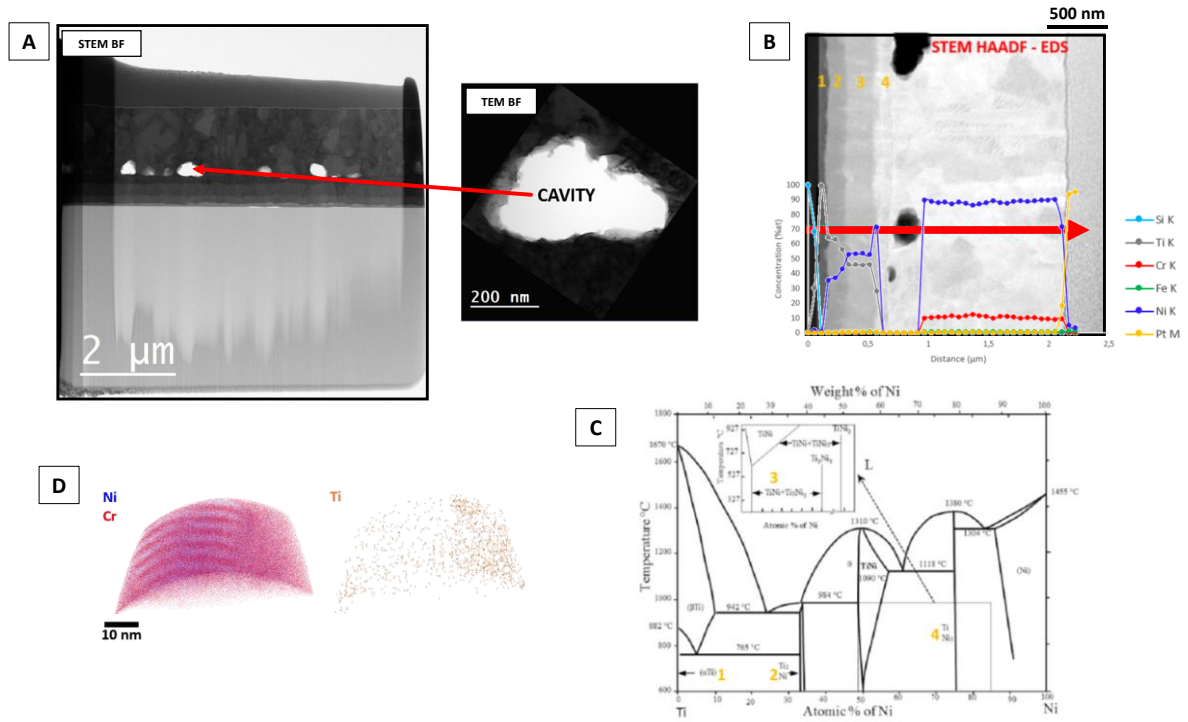


Figure 66 – A) Microstructure evolution after 25h at 400°C annealing (for comparison with the as-deposited state see Figure 68). B) STEM-EDS profile drawn along the deposition direction reveals reactive interdiffusion between the former Ti layer and Ni from nanolayers. The four distinct regions (1 to 4) exhibit different grey levels in STEM HAADF (i.e. different composition because the thickness is the same). C) Each region has a composition close to the phases α -Ti, Ti_2Ni , TiNi and TiNi_3 of the Ti-Ni binary phase diagram. D) Cr+Ni and Ti distribution within a 3D APT volume. Modulations vanished in the Ti-rich grain while they are well defined in the neighbour grain.

Ti and Si were removed by ion milling while keeping almost all nanolayers coating thickness. During this step, after removal of the Si substrate, the chunk bent and straighten back after removing the Ti layer (Figure 67.A)). Deflection direction indicates that Ti layer contained tensile residual stresses. Presence of a stress gradient, i.e. driving force for diffusion, within the Ti layer certainly explain why reactive interdiffusion happened so fast between Ti and Ni from nanolayers.

As thinned nanolayers were finally transferred to the Mo grid and “free welded” (Figure 67.B)). No Pt protection layer was deposited on the top of the nanolayers during the FIB preparation for the same reason that nanolayer were not welded to the Mo grid with Pt. Furthermore, a diffusion couple would have been created between Pt and the nanolayers. Actually, even with the “free welding” method a diffusion couple is created between Mo and the nanolayers. As prepared nanolayers chunks were long (total length $\sim 50 \mu\text{m}$), so that the diffusion length of the Mo-nanolayers diffusion couple for the selected treatment conditions should be shorter than the chunk “free” length (i.e. the length not in contact with the grid).

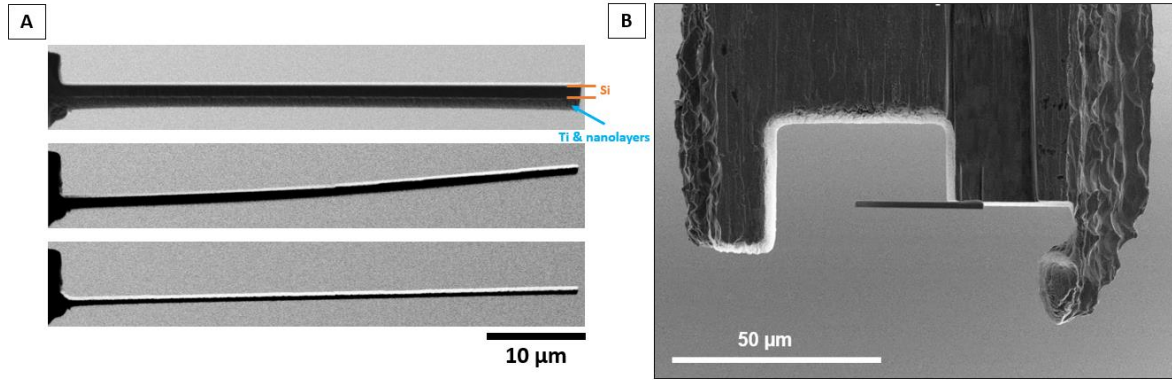


Figure 67 – A) Chunk bending during FIB thinning. B) As-prepared chunks by the “free welding” method for annealing and irradiations. The deposition direction z is perpendicular to the (x,y) plane of the image.

On each grid, two chunks were welded, one of each studied system (i.e. NiCr and FeNiCr). Except for the as-deposited state, all specimens presented in sections IV and V are prepared by this method before ageing (i.e. thermal and irradiation) to study interdiffusion. TEM lamellae and APT tips have been prepared from the aged chunks by standard methods with the Ga^+ XB-540 SEM-FIB from ZEISS at 30kV and cleaned with low voltage ions at 2 kV in the FIB for APT tips and with the PIPS II at 0.5 kV in the case of TEM lamellae.

IV. Interdiffusion kinetics in Ni/Ni-20Cr system after thermal ageing and under irradiation

1. Microstructure evolution

Coating architecture and microstructure at the as-deposited state were investigated by transmission electron microscopy (TEM) with the S/TEM JEOL-ARM200F at 200kV (see CHAPTER 2 for details). All measurements were performed at 0° tilt on cross-sectioned lamellae prepared by focused ion beam (FIB) with the Ga^+ XB-540 SEM-FIB from ZEISS at 30kV. Post-FIB examinations helped to characterize the global architecture at low magnification. Then, an Ar^+ ion cleaning with the PIPS II at 0.5 kV was done before high magnification STEM and HR-TEM imaging of the nanolayers. Indeed, as the thinning rates are quite different between Si, Ti and the nanolayers, after few minutes of cleaning only nanolayers left.

Ti film of 400 nm thickness was deposited on $\{002\}$ Si single crystal (Figure 68.B)). Ni/Ni-20Cr nanolayers thickness is 1.5 μm approximately (Figure 68.A)). HCP-Ti layer has its $\{0002\}$ planes parallel to the plane of the film [202] while nanolayers exhibit a $\{111\}$ texture, as commonly observed for FCC metals deposited by this technique [203]. Columnar grains grew perpendicularly to the Si substrate both for Ti and the nanolayers. Their width is tens on nm large while their length corresponds to the thickness of the coating. Grain length generally equals to the film

thickness for small thicknesses $\sim < 1\mu\text{m}$ [187]. Difference between Ti and Ni/Ni-20Cr grain structure lies on the very high density of stacking faults perpendicular to the growing direction in the nanolayers part (Figure 68.C) & D)).

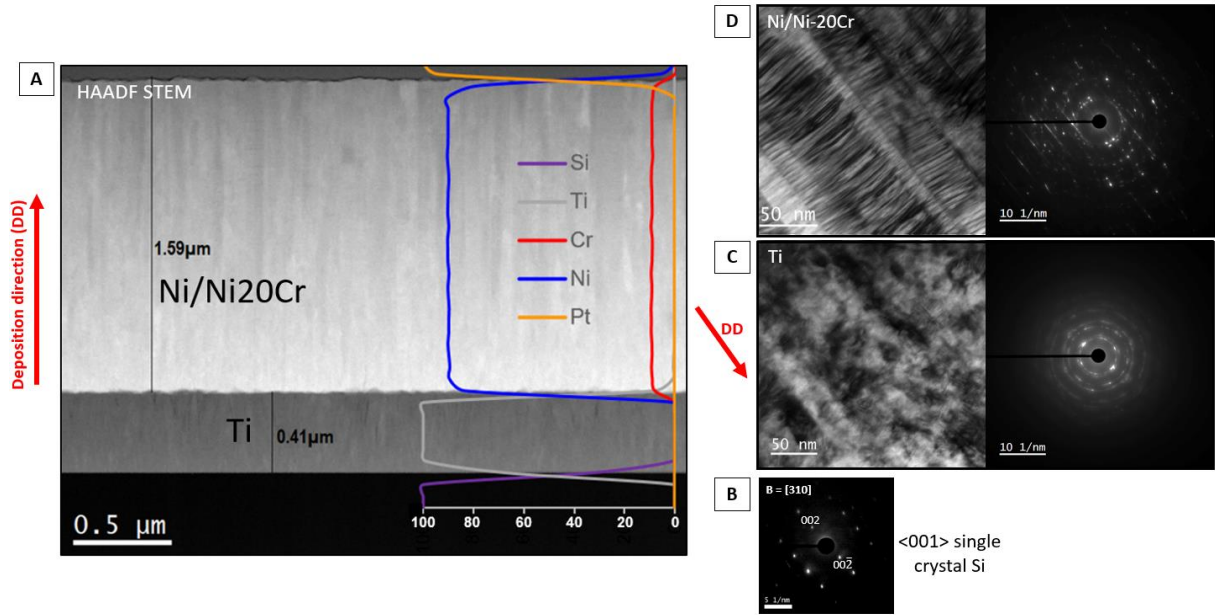


Figure 68 – Cross-sectional view of the as-deposited coating. A) Superimposed STEM-HAADF image and STEM-EDS linear concentration profile (at.%) showing the coating architecture. Columnar growth structure of C) Ti and D) nanolayers films on Si single crystal B). Orientation relationships along the growing direction $\langle 001 \rangle_{\text{FCC-Si}} // \langle 0001 \rangle_{\text{HCP-Ti}} // \langle 111 \rangle_{\text{FCC-nanolayers}}$ determined from SAED patterns B) to D).

Even if nanolayers coating is textured, the presence of dotted rings on the corresponding SAED pattern (Figure 68.D)) let suggest that grains have random in-plane orientations relative to rotational axis parallel to the deposition direction [203].

Grain width measurements were completed by the intercept method (Figure 69.A)). Nanolayers are well visible in STEM-HAADF mode and show a regular spatial periodicity. Wavelength measurements were performed on STEM HAADF images and STEM-EDS line profiles. Intensity or concentration profiles were fitted with a sinusoid to extract Λ . Wavelength and grain size magnitude is given as the mean of several measurements while error corresponds to the standard deviation.

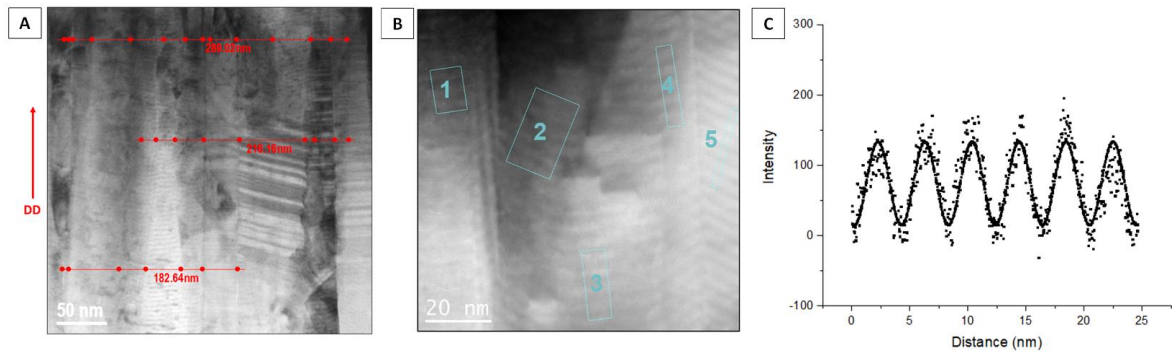


Figure 69 – Measurements done at the as-deposited state. A) Grain size determination via the intercept method. B) and C) Wavelength extraction from an intensity profile drawn in a STEM-HAADF image at different locations.

Numerous defects are observed within the as-deposited nanolayers: grain boundaries (Figure 69), stacking faults, nanotwins and Frank loops (Figure 70). No cavity has been observed. Study of HR-TEM image fast Fourier transform (FFT) and inverse FFT (iFFT), as seen in Figure 70, permitted to identify defect nature and measure their density and size.

Nanotwins are revealed thanks to the mirror symmetry between twins on the FFT image and by selecting $\{111\}$ spots corresponding to individual twins only for the iFFT image (Figure 70. A) & B)). Twin spacing ranges from 0.6 to 6 nm for a mean distance of 1.9 ± 1.3 nm. Twins are parallel to the interfaces between the layers but are not correlated spatially with the composition modulation wavelength. This type of defect is typical in coatings produced by sputtering [187,204].

Stacking faults are revealed by streaks as well as the Frank loops. As they are superimposed, it is not possible to distinguish them directly (Figure 70. A)). However, by selecting G_{111} spots corresponding to the $\{111\}$ planes normal to the deposition direction to construct the iFFT image, they can be discriminated explicitly (Figure 70. C)). On the iFFT image, only SIA type Frank loop is shown but both vacancy and SIA type Frank loops co-exist in as-deposited nanolayers.

Defects arising from aggregation of point defects as faulted dislocation loops, stacking fault tetrahedra, cavities and small gas bubbles (filled with the gas injected to create the plasma) are commonly observed in as-deposited thin films grown by sputtering [187,205–207].

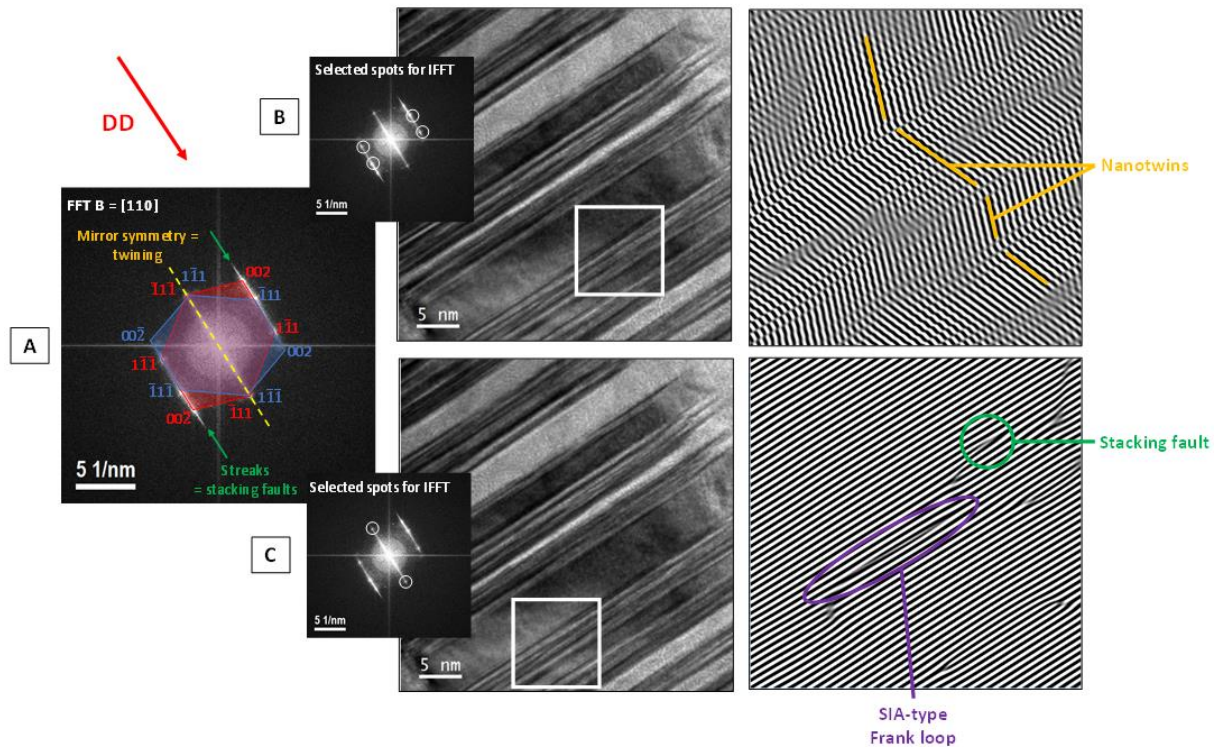


Figure 70 – A) FFT of the HR-TEM grain shown in B) and C) with the $[110]$ zone axis oriented parallel to the electron beam. Mirror symmetry indicates the presence of nanotwins with $\Sigma 3 \{111\}$ twin boundaries revealed in B) and streaks indicate the presence of stacking faults parallel to the deposition direction (DD) revealed in C). Nanotwins, stacking faults and faulted Frank loops coexist in the as-deposited microstructure.

Grain boundaries (GB), nanotwins (NT), stacking faults (SF), Frank loops (FL) and nanolayers interfaces (NL) are all contributing to the overall sink strength k_s^2 during irradiation:

$$k_s^2 = k_{GB}^2 + k_{NT}^2 + k_{SF}^2 + k_{FL}^2 + k_{NL}^2 \quad (141)$$

k_{GB}^2 is calculated from the average width w and the expression from [208]:

$$k_{GB}^2 = \frac{15 \times f(\theta, \gamma)}{R^2} \quad (142)$$

where $f(\theta, \gamma)$ is the sink strength efficiency function of grain boundary energy γ and misorientation angle θ . $f(\theta, \gamma) = 1$ for an ideal high angle grain boundary and $0 \leq f(\theta, \gamma) \leq 1$ for low angle grain boundaries. Because neither θ nor γ are known, $f(\theta, \gamma)$ was taken to be equal to 0.5. R is the grain radius, in our case we assume that $R \sim w$.

Assuming that all nanotwin boundaries are coherent with an average twin spacing, t , k_{NT}^2 is calculated as follows [208]:

$$k_{NT}^2 = \frac{12}{t^2} \quad (143)$$

Indeed, this assumption is rough because, as shown in the iFFT of Figure 70.B), nanotwins boundaries are not flat interfaces. Indirect measurements using void denuded zone widths combined with an atomistic modelling study [209] proved that, in a nanotwinned Cu (twin spacing ~ 10 nm) subjected to high dose He implantation, coherent twins are poor defect sinks. Nevertheless, in a Ag sputtered coating doped with Fe [210], coherent twin boundaries could exhibit stacking faults at their level and the measured average twin spacing (twin spacing ~ 3 nm), approaching the one measured in our nanolayer coatings (twin spacing ~ 2 nm) studied, such high density of nanotwins are efficient defect sinks. Even considering coherent nanotwins, nanotwins are the major contributor of the estimated sink strength.

Stacking faults (SF) plays also a role in defects annihilation [211]. As no expression for stacking fault sink strength could have been found in the literature, k_{SF}^2 is calculated from the number of measured SF per surface unit (Figure 72.A)).

k_{FL}^2 is calculated for both vacancy and interstitial type Frank loops from this equation [212]:

$$k_{FL}^2 = 2 \times \pi \times \frac{d}{2} \times N_d \quad (144)$$

where d is the mean diameter and N_d (m^{-3}) is the number density of loops. Both quantities have been measured (Figure 72.B) and C)), the measured number density have been multiplied by 4 to account for the other variants.

k_{NL}^2 is calculated from layers thickness, h [208] :

$$k_{NL}^2 = \frac{12 \times \eta}{h^2} \quad (145)$$

with h being equal to $\Lambda/2$ and η is the sink efficiency. η approaches 1 for incoherent, immiscible layer interfaces with high interfacial energies and small (but >0) for coherent, miscible layer interfaces. In our case, η is small because layers are miscible and coherent because the nanotwins and stacking faults spacings are not spatially correlated to the composition modulations. Thus, η was taken to be equal to 0.1.

Prepared chunks section is rectangular with a height equal to 1.5 μm and a width equal to 2 μm . Free surface contribution to the sink strength is neglected regarding the other defects type size and density, and the mean free path, δ , a mobile point defect can travel before being captured by a defect sink. Regarding the high density of defects, δ is close to 1 nm. Furthermore, tip extraction is done far from the surfaces $\sim 400 \text{ nm} \gg \delta$.

Thus, the total sink strength k_s^2 is estimated to be equal to 4.10^{18} m^{-2} . Considering numerous sources of errors: measurements for SF and FL were done only on grains oriented in the zone axis $\langle 011 \rangle$, sink efficiencies estimation... Total sink strength should range from 10^{17} to 10^{19} m^{-2} .

Sink efficiency is defined as the ratio of point defect flux to a particular sink to that for a perfect sink and could be estimated directly [213] or indirectly [209] experimentally. As studied coating contain a very high density of numerous type of defects, experimental measurements are complex.

Multilayer wavelength and total sink strength determination were determined from microstructure characterizations at the as-deposited state. As shown in previous section, it was a useful help to select ageing conditions.

After annealing and irradiations, the microstructure was systematically investigated as well.

Integrated diffracted intensity along the reciprocal distance of SAED patterns at the as-deposited state, after annealing and irradiations up to 0.001 and 0.05 dpa are presented Figure 71. Indexation of G_{hkl} with the FCC austenitic phase confirms that the microstructure is mostly austenitic.

Grain size and composition fluctuation wavelength are reported in Table 17. A clear grain growth is observed after 48h of annealing and a slight one after irradiations. Wavelength remain unchanged whatever the state.

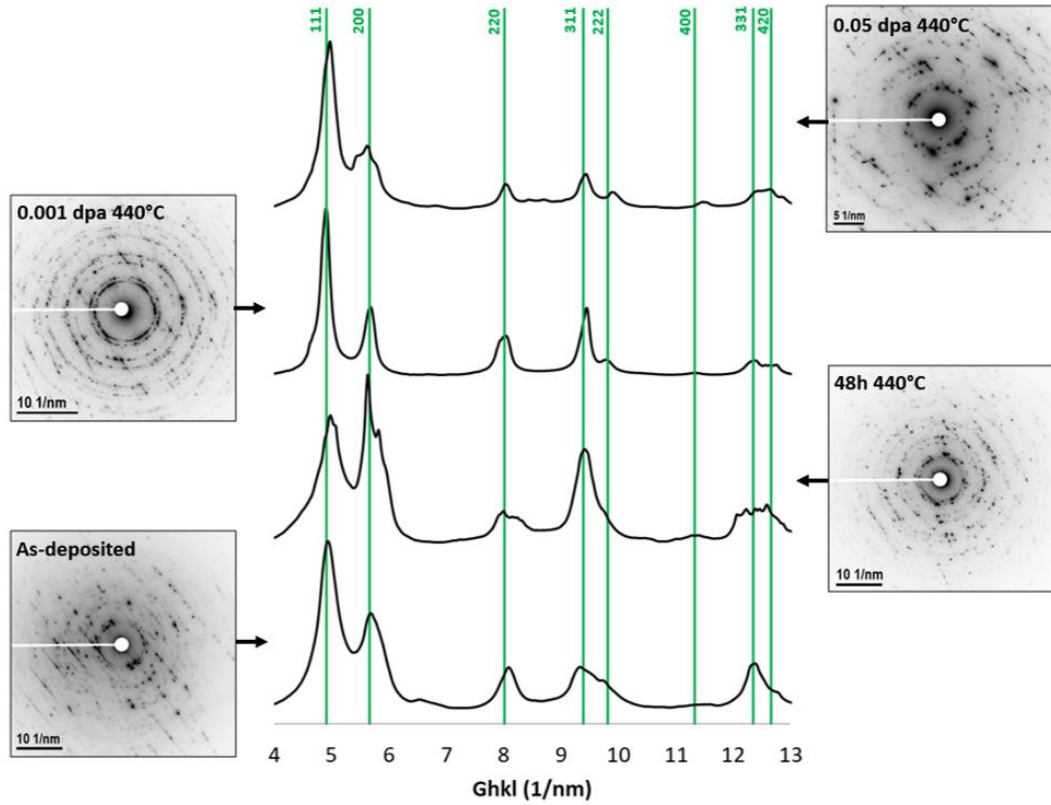


Figure 71 – Integrated diffracted intensity along the reciprocal distance G_{hkl} of SAED patterns in inverted contrast depending on the ageing conditions. FCC austenitic phase is the only one indexed.

Table 17 – Grain width and wavelength evolution after ageing. SD stands for standard deviation.

State	Grain width (nm)		Lambda (nm)	
	Mean	SD	Mean	SD
As-deposited	30	7	4,3	0,3
48h 440°C	50	7	4,4	0,1
0.05 dpa 440°C	35	5	4,3	0,3
0.001 dpa 440°C	39	5,5	4,6	0,1

Stacking faults and frank loops measurements from HR-TEM studies are reported in the graphs A), B) and C) of Figure 72. After 48h of annealing at 440°C, defects density remains roughly unchanged while after irradiation, a slight increase is observed. Concerning defect size, any clear evolution is noticed. Frank loops seems to be surprisingly stable under annealing.

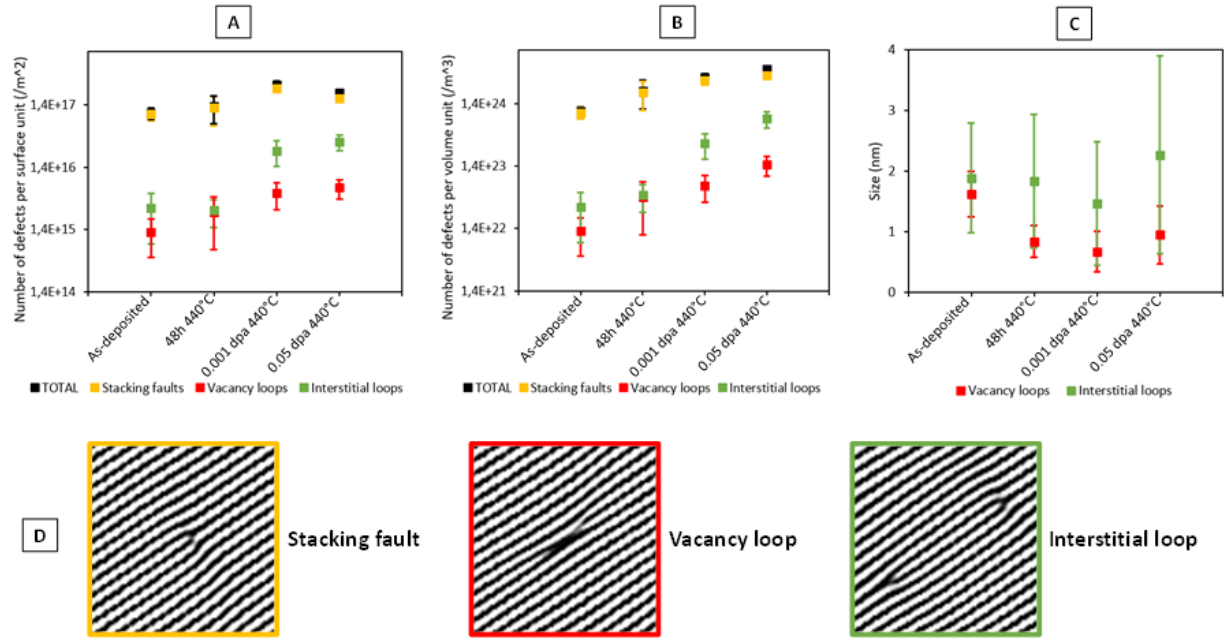


Figure 72 – Evolution of A) the number of defects per surface unit and B) per volume unit. C) Defect size for the different ageing conditions. Defect identification examples are shown in D).

After irradiation to 0.05 dpa, triangular shaped features appeared in the microstructure (Figure 73). The presence of stacking fault tetrahedra is suspected but could not be confirmed from HR-TEM images. SFT formation in Ni-Cr alloys with a composition approaching to Ni-10Cr have been predicted [214,215]. Another way to confirm SFT identification apart from weak beam dark field (WBDF) technique is to combine HR-TEM imaging with a strain analysis [216]. No cavities have been observed after irradiation.

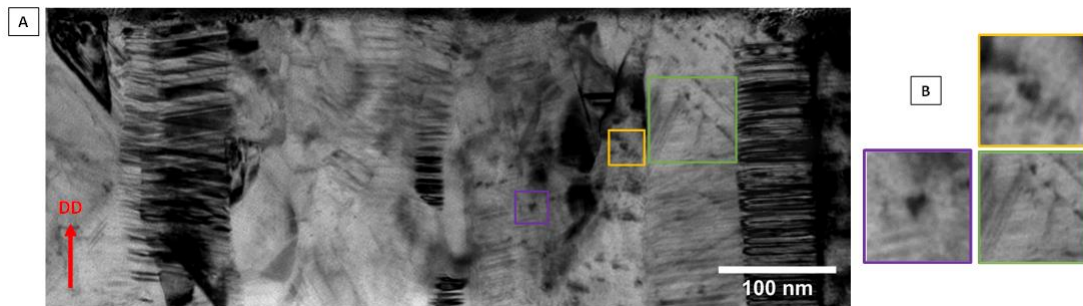


Figure 73 – A) TEM-BF image of the irradiated microstructure damaged up to 0.05 dpa. B) Focus on triangular shaped features observed in A).

While Si-Ti interface flatness is high, Ti-nanolayers interface is rough (Figure 74.A)). This roughness likely induced nanolayers rugosity. Layers are tilted and this tilt is even more pronounced at the vicinity of grain boundaries (Figure 74 B) & C)). As nanolayers rugosity is high, STEM-EDS measurements can underestimate concentrations amplitude if the lamella thickness is not thin enough (<20 nm). If the TEM lamella is prepared by FIB and cleaned with ions, a damaged layer will form at both surfaces where ion beam mixing occurs. As the lamella becomes thinner, the contribution of this layer to the EDS signal becomes non negligible. For this reason, amplitude

concentrations have been quantitatively measured by atom probe tomography (APT) from well oriented sub-volumes. The methodology of amplitude extraction is presented hereafter.

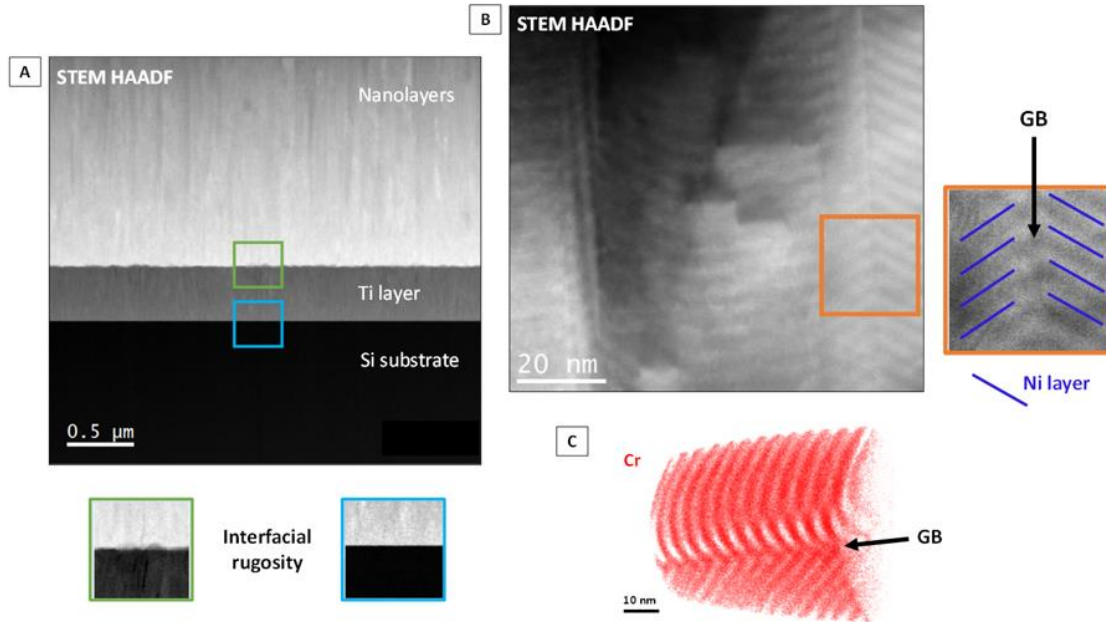


Figure 74 – A) Si-Ti and Ti-nanolayers interfacial rugosity at the as-deposited state. B) STEM HAADF image and C) Cr elemental APT volume show that nanolayers tilt is increased near grain boundaries.

2. Concentration amplitude evolution

Atom probe tomography (APT) experiments were performed with the LEAP 4000HR-X of the GENESIS platform in voltage mode. Acquisition parameters were kept the same for all the volumes and all ageing conditions : base temperature = 63K, pulse frequency = 200kHz, pulse fraction = 20% and a detection rate ranging from 0.05 to 0.2% to keep a constant flux of evaporation and decrease the background level. Volume reconstructions were performed with IVAS commercial software and parameters were tuned to obtain a modulation wavelength equal to the one determined from TEM measurements. When poles were visible, the consistency of the interplanar distance with respect to the indexed pole was checked. Further data treatment was done on the GPM 3Dsoft software.

APT investigations not only permit to extract concentration amplitudes, they brought also extra information about nanolayers microstructure and chemical heterogeneities (other than composition modulations). From Figure 75, it can be seen that Ni-20Cr layers are contaminated with Fe. Layers interfaces are sharp at the as-deposited state and they are not always parallel to the $\{111\}$ planes. It can mean that a small deviation from the strict parallelism of $\{111\}$ planes with the substrate surface exist or the nanolayers are tilted. For both explanations, Ti-nanolayers interfacial roughness is suspected to be the cause.

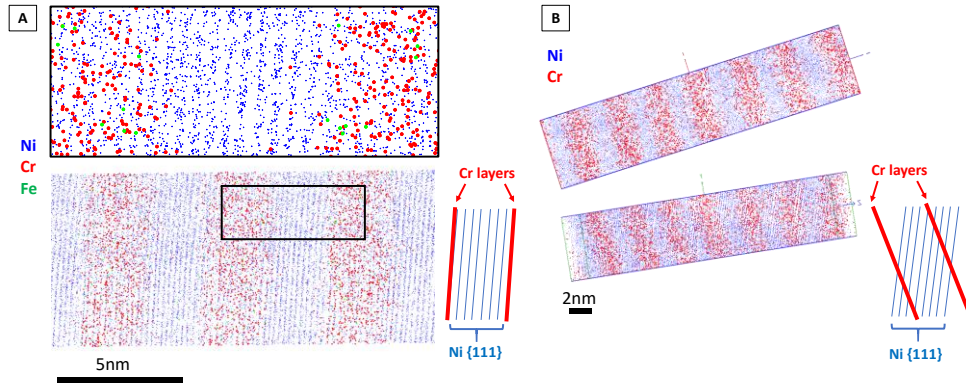


Figure 75 – Nanolayers orientation regarding $\{111\}$ planes from two different APT volumes A) and B) at the as-deposited state. A) Fe contamination is observed in Ni-20Cr layers.

The evolution of elemental distribution within as-deposited and aged nanolayers is summarized in Figure 76. The nanolayers crystallographic texture is confirmed by the observation of 111 pole at the as-deposited state and after 48h of annealing at 440°C on almost all volumes (111 pole was the only one indexed). Grain boundaries were intercepted in all volumes confirming their nanosized width. The modulated structure is well defined at the as-deposited state and is still visible after ageings.

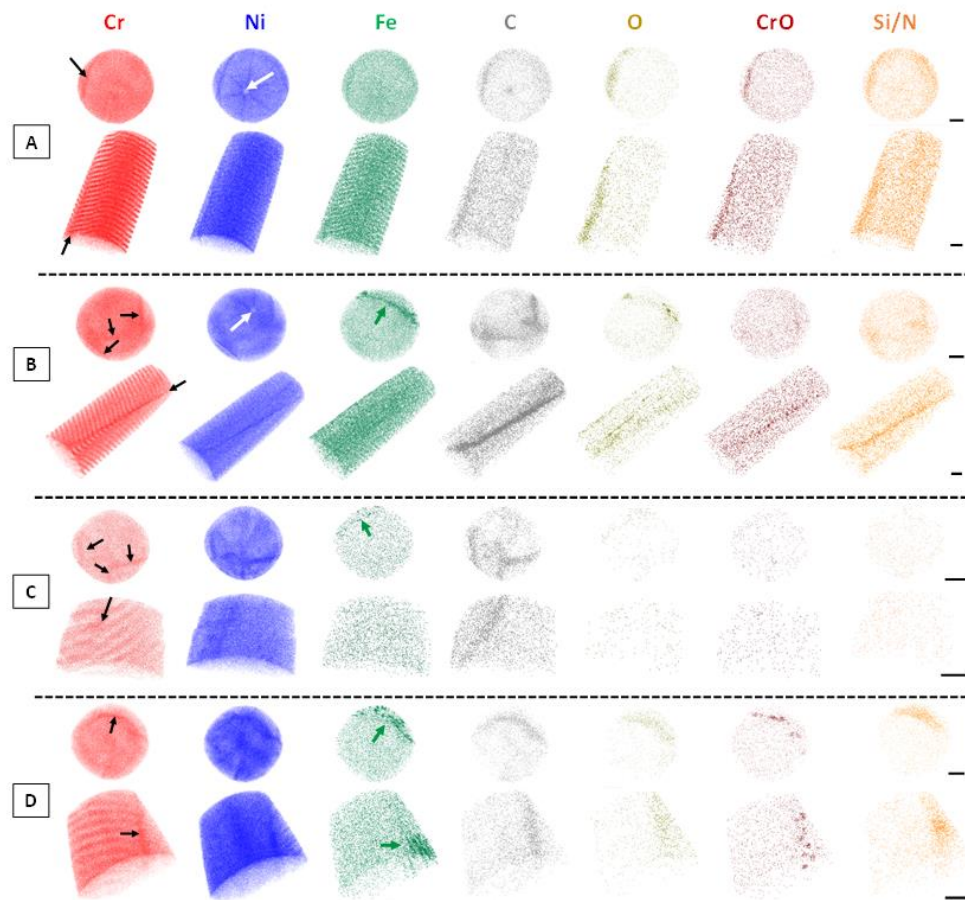


Figure 76 – 3D elemental distributions at the different studied state: A) As-deposited B) 48h 440°C C) 0.001 dpa 440°C D) 0.05 dpa 440°C. Black, white and green arrows indicate grain boundaries, poles and Fe-rich clusters respectively. Scale bar = 10 nm

Minor impurities elements are present such as Fe, C, O and Si/N (for an exhaustive list see Table 18). After ageing, Cr oxides form clusters at grain boundaries. Fe enrichments are also identified after annealing and irradiations. These Fe-rich clusters were not observed within any of the as-deposited state APT volumes.

Despite an increase of C, O and surely N after annealing and irradiations, the global purity remain acceptable for diffusion kinetics investigations. The purity is lower for 0.001 dpa because of an early breakage of all APT needles during analysis for this condition. Therefore, a reduced number of atoms were removed from the first part of the dataset to be able to measure amplitudes accurately.

Table 18 – Evolution of the global composition and nanolayers purity in at.%

	Al	C	Co	Cr	Cu	Fe	Mn	Ni	O	Ti	V	Si/N	Purity
AD	0,020 ± 0,000	0,06 ± 0,00	0,001 ±0,000	10,2 ± 0,4	0,005 ± 0,003	0,38 ± 0,01	0,006 ± 0,001	89,2 ± 0,4	0,05 ± 0,02	0,009 ± 0,003	0,003 ± 0,000	0,07 ± 0,00	99,4 ± 0,0
48h 440°C	0,022 ± 0,001	0,16 ± 0,04	0,001 ± 0,001	10,0 ± 0,3	0,005 ± 0,002	0,44 ± 0,02	0,006 ± 0,002	89,1 ± 0,2	0,08 ± 0,03	0,017 ± 0,004	0,004 ± 0,000	0,20 ± 0,11	99,1 ± 0,1
0.001 dpa 440°C	0,026 ± 0,001	0,56 ± 0,29	0,003 ±0,000	10,3 ± 0,0	0,011 ± 0,002	0,45 ± 0,02	0,017 ± 0,008	88,3 ± 0,3	0,24 ± 0,01	-	0,005 ± 0,001	0,10 ± 0,02	98,6 ± 0,3
0.05 dpa 440°C	0,025 ± 0,000	0,23 ± 0,01	0,002 ± 0,001	10,1 ± 0,2	0,008 ± 0,001	0,46 ± 0,12	0,009 ± 0,000	88,9 ± 0,0	0,14 ± 0,08	-	0,005 ± 0,002	0,10 ± 0,07	99,0 ± 0,3

Concentration profiles have been drawn across grain boundaries (Figure 77). Boxes built to extract the profiles were taken large enough to average the modulations on both sides of the boundary and small enough to ensure that the grain boundary plane is perpendicular to the profile direction. Each box was divided in three sub-boxes. The concentration profiles correspond to the mean concentration while the error bars are calculated from the standard deviation.

At the as-deposited state, grain boundaries are contaminated with O while after ageings, C enrichment is systematically observed. It is associated with an increase of the Cr content after thermal ageing. As was explained in CHAPTER 1, the $M_{23}C_6$, Cr carbide precipitates the fastest in steels and start to nucleate first at grain boundaries. Its precipitation also occurs in Ni-based alloys [217,218]. Segregation of Cr revealed that in-plane grain boundary diffusion happened and aged microstructure is not fully austenitic. The presence of an overdensity of CrO^{2+} molecular ions seen in Figure 76 is not revealed by an increase in oxygen the concentration profiles. Nevertheless, as CrO^{2+} seem to form cluster after ageing, chromium oxides precursors might be present at grain boundaries (GB). GB are surely not homogeneous in composition. Impurities at GB limit grain growth [219].

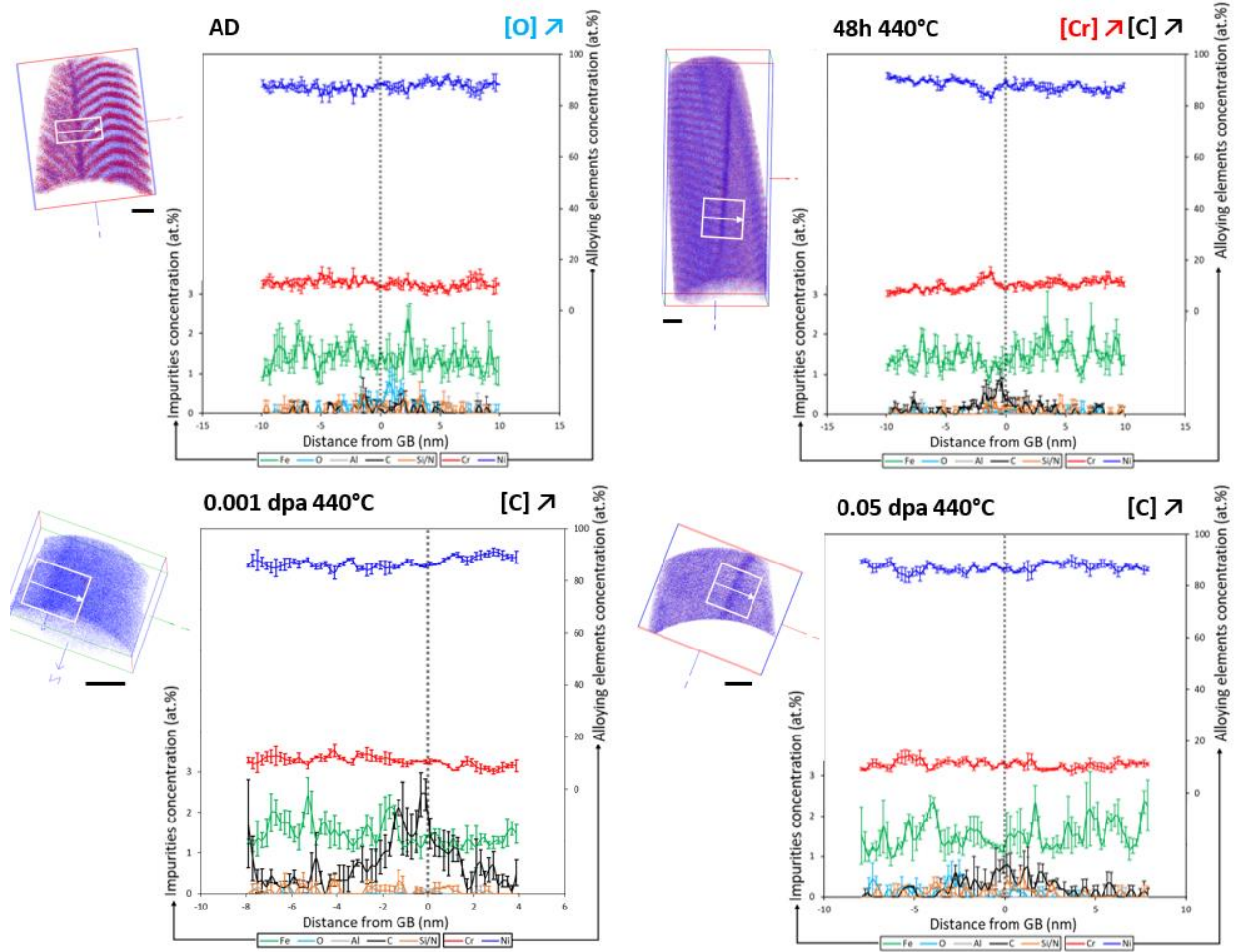


Figure 77 – Evolution of grain boundaries composition after ageings. AD stands for the as-deposited state. APT volumes and line profiles extraction location across grain boundaries are indicated at the left of the corresponding 1D composition profiles. Scale bar = 10 nm.

Fe-rich clusters appear both after annealing and after irradiation (Figure 78). They are suspected to be precursors of the Ni_3Fe ordered phase with L_{12} configuration.

According to Marty et al. [220], the unit cell of this structure is defined as two sublattices : a $\{000\}$ Fe-rich and b $\{\frac{1}{2} \frac{1}{2} 0\}$ Ni-rich. Cr preferentially occupy sublattice a but can occupy b as well, therefore Ni_3Fe stoichiometry is not strict and can contain some limited amount of Cr.

Marwick et al. (1987) [221] studied ordering in $(\text{Ni}_3\text{Fe})_{1-x}\text{Cr}_x$ alloys with x ranging between 0 to 17 at.%. From their study, the critical temperature for ordering is $T_c = 400^\circ\text{C}$ for a Cr content of 10 at.%. No ordering was found in samples with more than 12 at.% of Cr. T_c increases with decreasing Cr content up to 500°C . Cr atoms preferentially occupy Fe sites in Ni_3Fe . This phase is stable under irradiation, at least to the doses explored.

The ordered phase was not identified in SAED patterns (Figure 71).

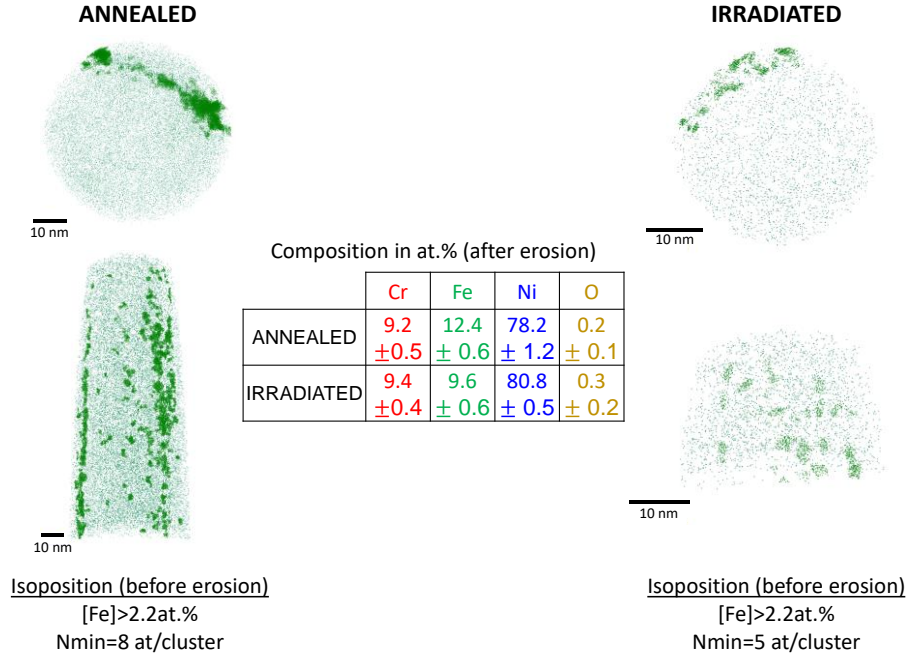


Figure 78 – Fe atom maps in annealed and irradiated binary system. Atoms in Fe rich areas are highlighted. The table gives the average composition of the Fe-rich clusters.

In order to extract concentration amplitude with the highest accuracy, we paid attention to the following points :

- The reconstruction parameters can evolve within the depth of the reconstructed volume [154]. Therefore, the subvolumes should not be too long, we prefer to build several subvolumes of smaller length within an APT volume instead to optimize modulations fit.
- At the as-deposited state, concentration profiles are not pure sine waves but square-like waves because nanolayers interfaces are sharp (Figure 79). This sharpness is more pronounced for the studied binary system. During ageing, concentration profiles are suspected to first smooth into a sinusoid with the same amplitude before amplitude attenuation happens with time. But, in some unusual cases, interface sharpening can be observed initially during annealing as well as interface shifting [222,223]. Transient interfacial sharpening have been shown to occur in systems having a complete mutual solubility as well as in system with phase separation tendency. Initial roughness and wavelength have been demonstrated to play a role in this phenomenon. In-situ x-ray diffraction studies on nanolayers vacuum-annealing of ultra-thin at short annealing times should be performed to investigate experimentally interfacial behaviour at the first stage of annealing because of the associated asymmetry of diffusion coefficients. Fitting the square wave by a sine function gave an as-deposited amplitude concentration higher than Cr average concentration (i.e. for the binary system) which is physically inexact but it is consistent with the larger area below the square wave than a sine wave with the same amplitude.

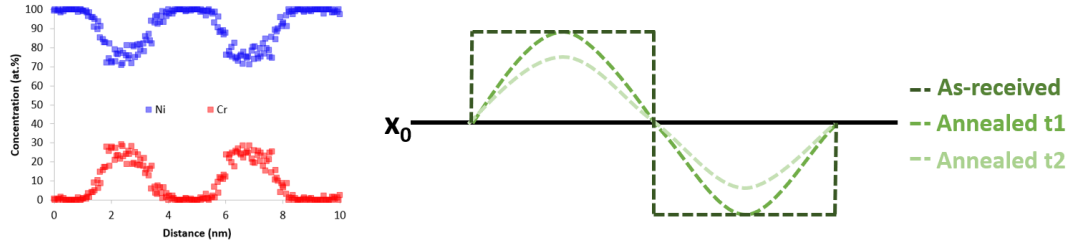


Figure 79 – As-deposited raw concentration modulations (left) and scheme of the concentration profile evolution with ageing time (right).

- Several grain boundaries can be intercepted within an APT volume, subvolumes are extracted inside individual grains.
- If a pole or a precipitate is present in the volume, sub-volumes are extracted out of this region.
- Subvolumes z direction is oriented perpendicular to the layers to draw the concentration profile. In order to avoid any smoothing of the sinusoidal curves due to layers rugosity, as-obtained subvolumes are divided once again. Then, all the individual profiles obtained from this second sub-sampling are superimposed to obtain the final raw curve after a phase shift correction (method #1) or juxtaposed (method #2).
- Concentration profiles are fitted by a sine function described by 4 parameters: the phase shift Φ , the amplitude A , the wavelength Λ and the mean concentration c_0 . For both methods all parameters are variables, the only constrain is that A is positive.

For the method #1 (Figure 80), each sub-volume is sub-divided in four sub-samples. Peak decomposition is performed on each individual profile. The Ni and Cr atomic concentrations are normalized to 100%, a reasonable assumption regarding nanolayers purity. Then, profiles are fitted by a sinusoid to obtain the phase shift, the z values in each concentration profile are corrected by subtracting this phase shift. As-obtained profiles are superimposed before applying a low pass FFT filter with a cut off frequency of 2 nm^{-1} to softly clear noisy raw data. A final fit permitted to obtain the sine function parameters and especially the amplitude A . This method was not kept for interdiffusion coefficients calculation but permitted to illustrate composition modulation evolution after ageing.

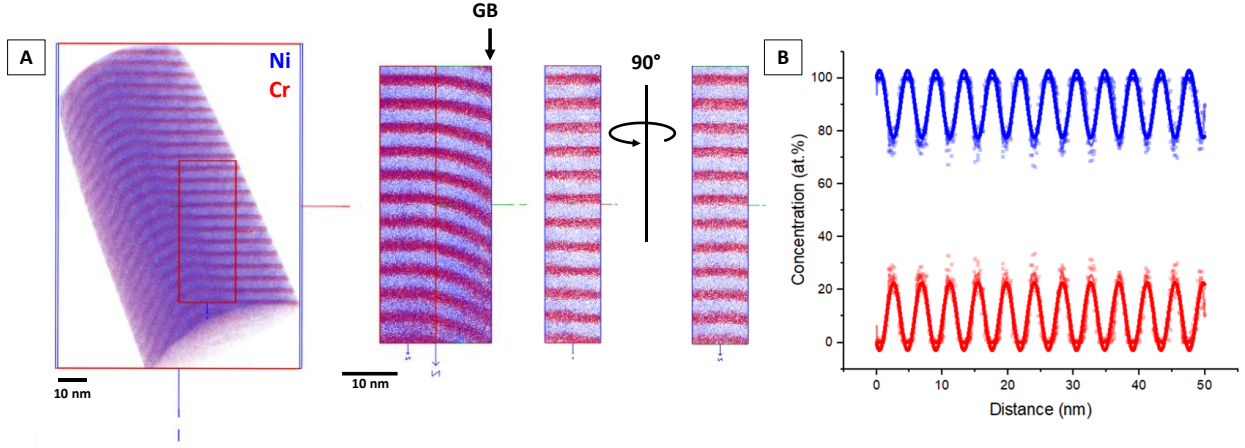


Figure 80 – Method #1. A) Steps of the subvolume extraction. B) Final fit of the concentration profiles for the as-deposited state.

Nanolayers are never perfectly perpendicular to the extracted subvolume. In order to minimize any smoothing effect and to faster data treatment, the method #2 has been used (Figure 81). This time each subvolume is divided in 25 sub-samples (option available in the GPM 3Dsoft software). As no phase shift correction is applied, the number of layers inside the volume should be an integer to minimize the phase shift between profiles. All sub-samples are juxtaposed. Peak decomposition and Ni, Cr concentration normalization is performed on all the dataset. Then, a low pass FFT filter with a cut off frequency of $0.3\text{-}0.4\text{ nm}^{-1}$ is used to denoise raw data. Amplitudes measured from the method #1 were references to set the cut-off frequency of the method #2. Finally, cleared dataset is fitted by a sinusoid to determine A.

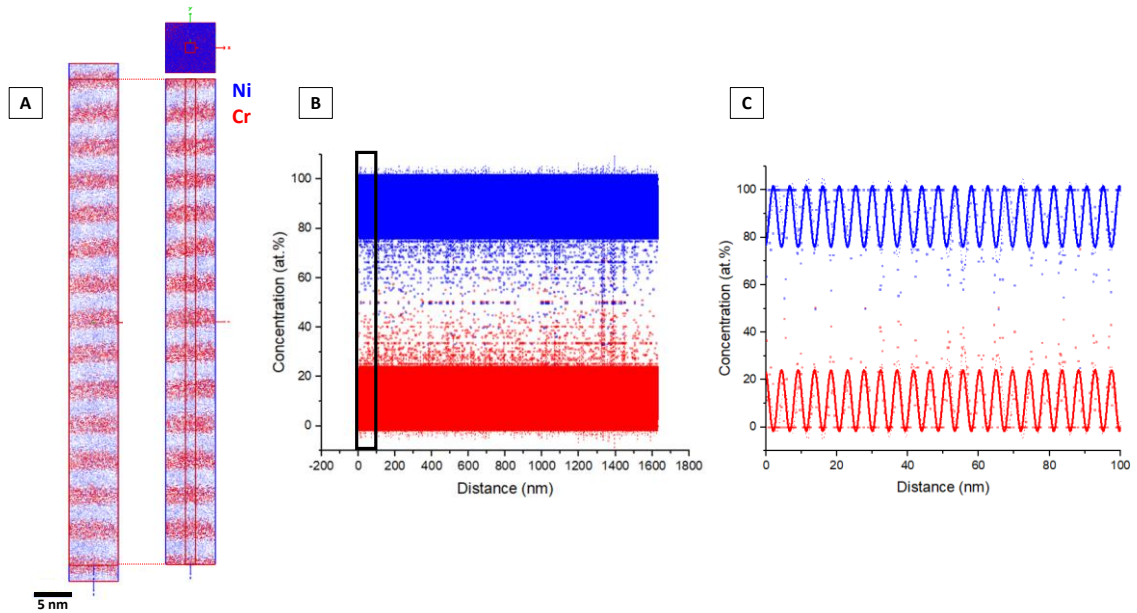


Figure 81 - Method #2. A) Steps of the subvolume and sub-samples extraction. B) Final fit of the concentration profiles for the as-deposited state. C) Close-up on the black square region of the concentration profile.

Examples of concentration profiles treated by the method #1 and the associate mean amplitude for the corresponding state determined by methods #1 and #2 are summarized in Figure 82.

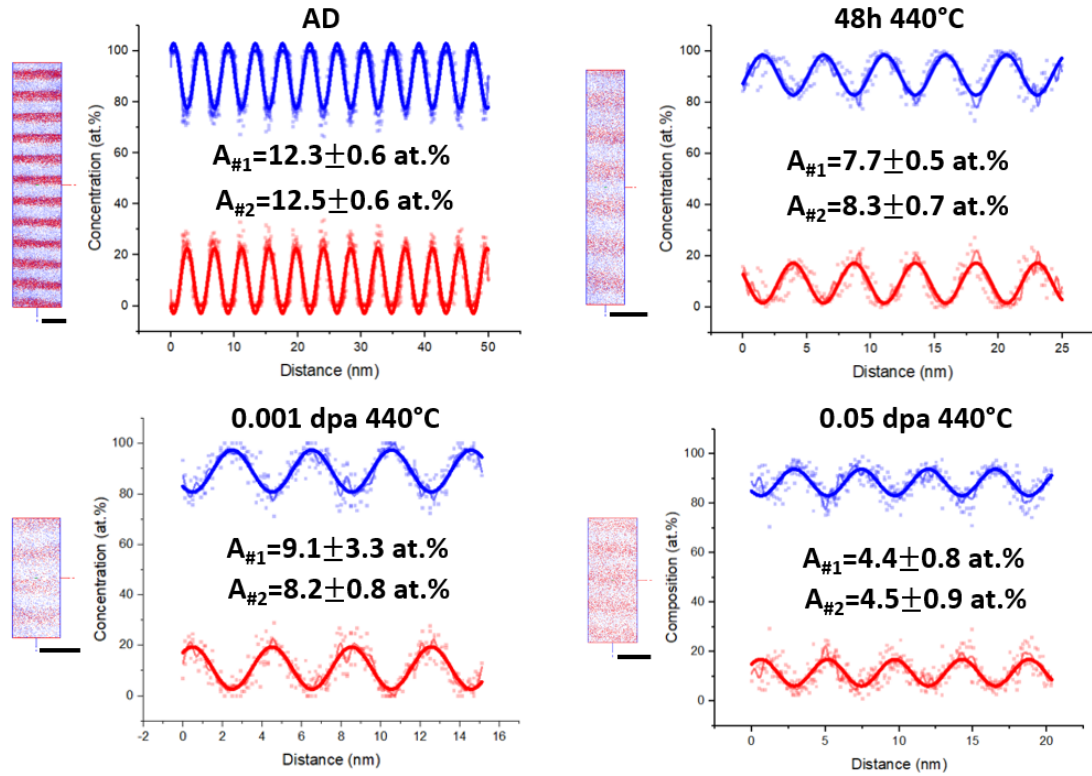


Figure 82 – Concentration profiles (method #1) and mean amplitude evolution (methods #1 and #2) with ageing. Ni and Cr are represented by the blue and the red color respectively. Scale bar = 5nm.

3. Interdiffusion coefficients

In the case of a binary system, only one value is necessary to calculate the interdiffusion coefficient from the amplitude attenuation. Obtained results are summarized in Table 19 and Table 20. Values extracted from the two treatments are presented. As the two methods give approximately the same results and method #2 is much faster, only results of the method #2 are kept for comparison with the bulk theoretical values.

Table 19 – Amplitude attenuation evolution with the ageing conditions. Results are given for both methods.

State	Equivalent time (h)	A_t/A_0			
		Method #1		Method #2	
		Mean	SD	Mean	SD
48h 435°C	48.00	0.6	0.04	0.7	0.1
0.05 dpa 440°C	0.83	0.3	0.1	0.3	0.1
0.001 dpa 440°C	0.02	0.7	0.3	0.7	0.1

Table 20 – Measured effective interdiffusion coefficients after annealing and irradiations. Results are given for both methods.

State	Equivalent time (h)	\tilde{D}_A (m ² .s ⁻¹)			
		Method #1		Method #2	
		Mean	SD	Mean	SD
48h 435°C	48.00	1.2 x10 ⁻²⁴	1.7 x10 ⁻²⁵	1.1 x10 ⁻²⁴	2.3 x10 ⁻²⁵
0.05 dpa 440°C	0.83	1.7 x10 ⁻²²	2.8 x10 ⁻²³	1.7 x10 ⁻²²	3.0 x10 ⁻²³
0.001 dpa 440°C	0.02	2.6 x10 ⁻²¹	2.8 x10 ⁻²¹	3.4 x10 ⁻²¹	7.5 x10 ⁻²²

Theoretical amplitude evolution at 440 ±10°C for bulk thermal interdiffusion is consistent with the amplitude attenuation calculated in this work and the experimental interdiffusion coefficient is close to the theoretical one (Figure 83). It permits to validate the methodology and the assumptions made.

This graph also permits to emphasize interdiffusion enhancement under irradiation. The interdiffusion coefficient under irradiation, based on modelling results and the experimental sink strength determination, ranges between 5x10⁻²⁰ and 1x10⁻²¹ m².s⁻¹. They are higher than the experimental ones. As the damage levels are low, the steady state should not have been reached. The measured coefficients are therefore transient effective interdiffusion coefficients. This point will be discussed in the next section.

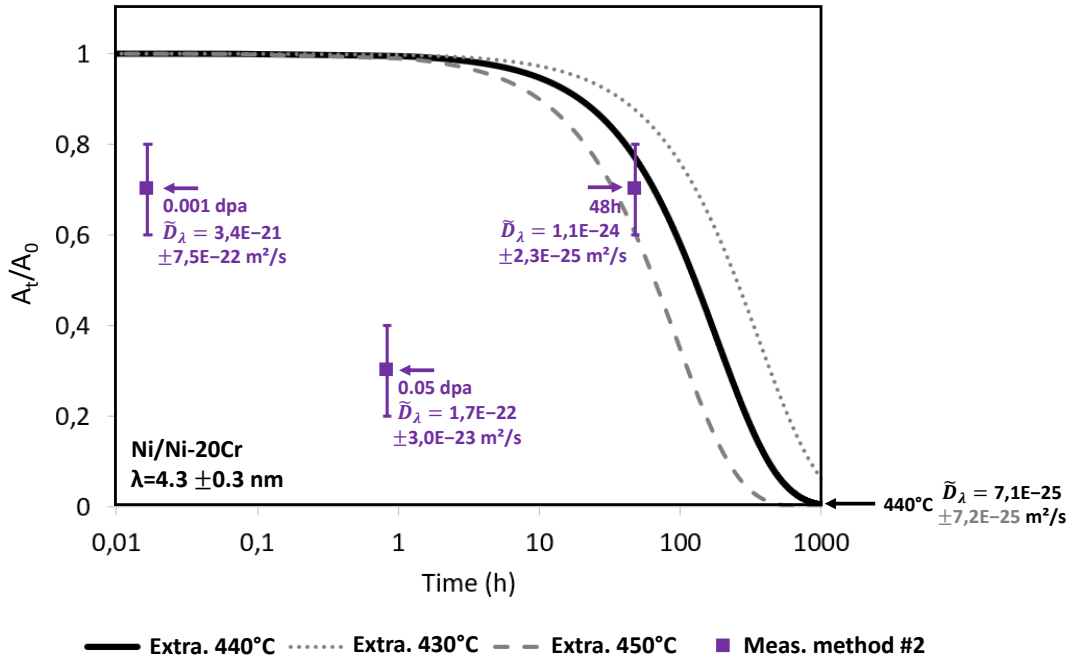


Figure 83 – Interdiffusion kinetics evolution after thermal ageing and under irradiation obtained from the amplitude attenuation of Ni-Ni20Cr nanolayers at 440 ± 10°C.

4. Discussion

The purpose of this discussion is to check the validity of nanolayers method hypotheses, to confront the experimental results to the theory and to suggest recommendations to access to the diffusivity of SIA in a binary alloy.

The main hypothesis of the nanolayers method to be validated is that modulations in composition are small enough to have a constant interdiffusion coefficient. For this binary system, Cr modulations ranges from 0 to 20 at.%. From the calculations made for the interdiffusion coefficient at 440°C in this range of Cr concentrations, \tilde{D} varies from 4×10^{-25} to $7 \times 10^{-25} \text{ m}^2 \cdot \text{s}^{-1}$ (Figure 84 – left axis). This variation is below the uncertainty on the temperature effect on diffusion kinetics as illustrated in Figure 83, therefore \tilde{D} can be considered constant. Results of the calculations are compared to the extrapolations made from the Arrhenius law parameters determined at temperature between 995 and 1300°) for the Ni-10Cr system by Ugaste (1967) from [17] (Figure 84 – right axis). Direct extrapolation of the interdiffusion coefficient from high temperatures induces too large discrepancy for a direct comparison with obtained results. This justified the choice to calculate interdiffusion kinetics from thermodynamics and mobility assessment. Furthermore, the thermodynamic factor at 440°C is equal to 2.6 for concentrated Ni-10Cr alloy and ranges from 1 for pure Ni to 3.16 for Ni-20Cr. Thus, taking the thermodynamic factor equal to 1 in this case would have enlarge error on theoretical interdiffusion coefficient calculations.

\tilde{D} stands for the bulk interdiffusion coefficient but grain boundary diffusion can enhance the kinetics because grain boundaries are high diffusivity paths. The interdiffusion coefficient determined from the nanolayers method should be treated as an effective interdiffusion coefficient because both volume and in-plane grain boundary diffusion (i.e. in a layer plane) can contribute to the measured kinetics. Segregation of Cr after 48h of annealing at 440°C proved that diffusion towards grain boundary occurred.

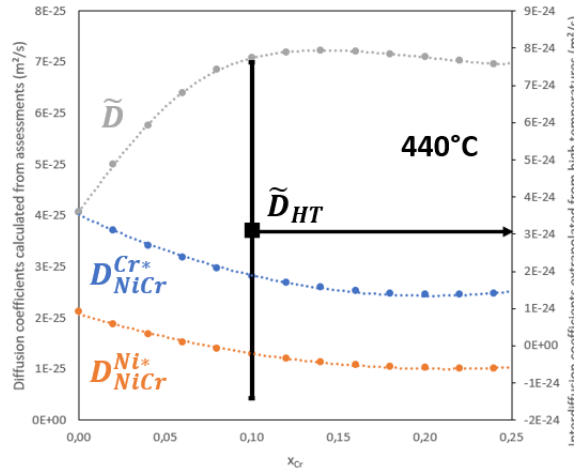


Figure 84 – Left axis. Calculation from mobility assessment of the impurity diffusion coefficients D_{NiCr}^{X*} with $X=Ni, Cr$ and the resulting bulk interdiffusion coefficient \tilde{D} (from Thermo-Calc and mobility assessment) within the composition range 0 to 25 at.% of Cr at 440°C. Right axis. Extrapolation of the interdiffusion coefficient at 440°C from high temperatures for Ni-10Cr and the relative error calculated from uncertainties on Arrhenius law parameters.

From the different existing models (Table 15), we chose the case of thin nanolayers so that the gradient energy coefficient is negligible. To check this hypothesis, the gradient energy coefficient κ and the second derivative of the free energy f_0'' have been calculated thanks to the regular solution model given by Equations (137) & (138) and the equation linking \tilde{D} to \tilde{D}_A in the case of ultrathin nanolayers (continuum model in Table 15) in the absence of elastic stresses. The unknown term is given by the following relationship :

$$\frac{2\kappa}{f_0''} = \frac{4 \times \Omega}{\frac{1}{\bar{c}(1-\bar{c})} - 2 \times Z \times \Omega} \quad (146)$$

The interaction energy factor Ω have been calculated based on the E_{ij} binding energies given in [106]. The binding energies are here considered independent on the temperature. Input values of Equation (146) are given in Table 21.

Table 21 – Input parameters magnitude of Equation (146)

Parameter (unit)	Value
Coordinance number Z	12
Ω interaction energy factor (eV)	-0.005
Ni average atomic fraction \bar{c}	0,9

The effect of the calculated gradient energy term on interdiffusion kinetics is shown in Figure 85. For a wavelength of 4.3 nm, the deviation from the bulk interdiffusion is smaller than the experimental error. Then, effect of the gradient energy on the experimental interdiffusion coefficient can be neglected.

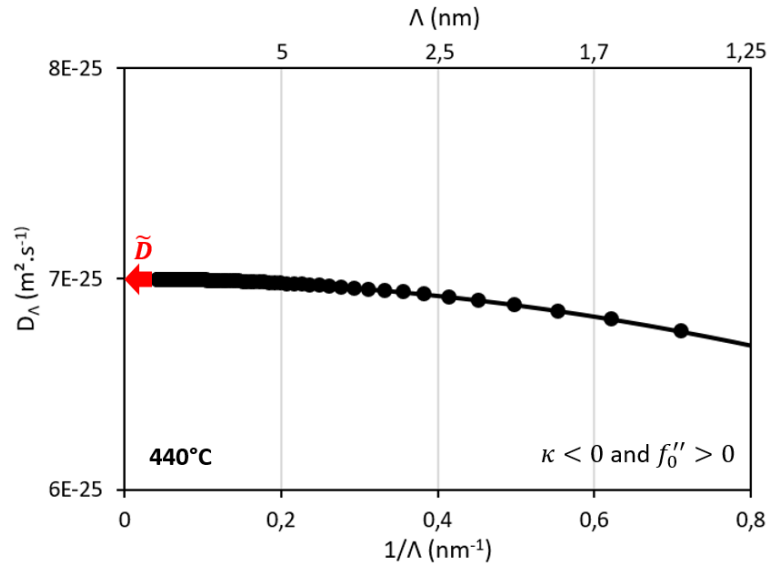


Figure 85 – Effect of the gradient energy on the measured interdiffusion coefficient.

It has been shown on Figure 59 that after thermal annealing the chunk bent. One of the hypotheses stipulated that elastic stresses may have been relaxed during the annealing. A stress gradient is a

driving force for diffusion so it can enhance the kinetics. It could partially explain the higher value obtained for the interdiffusion coefficient compared to the calculated bulk one.

The theoretical value of \tilde{D} was calculated for a pure Ni-10Cr system. However, impurities are present in the system and they can influence diffusion kinetics. Nanolayers coating exhibit a strong $\langle 111 \rangle$ crystallographic texture. Interdiffusion depends also on crystal orientation, therefore measured interdiffusion coefficient differs from the one of a polycrystalline material with random crystallographic orientations.

Measurements of amplitudes were done in different grains (i.e. different grain size, misorientation from $\{111\}$ crystallographic texture, intergranular defects density and size), each grain taken separately should exhibit small variation of the amplitude kinetic attenuation. It can also explain experimental uncertainties. For thermal interdiffusion there is a local variation of the high diffusivity path densities and under irradiation a change in the local sink strength.

Concerning the irradiation experiment, a multi-dose irradiation has been performed. For the chunks irradiated to 0.001 dpa, they have been annealed during 49 min prior irradiation. This annealing should have provoked an amplitude attenuation of 0.995 ± 0.005 from theoretical interdiffusion coefficient and 0.993 ± 0.003 from the one determined experimentally after 48h annealing at 440°C. Thus, this short annealing did not have any detectable effect on amplitude attenuation under irradiation.

After irradiation, the overall sink strength magnitude range is still $10^{17} < 10^{18} < 10^{19} \text{ m}^{-2}$, therefore the interdiffusion coefficient under irradiation evolution should theoretically be modelled without accounting for a sink strength evolution. Nevertheless, the interdiffusion coefficient under irradiation at 0.001 dpa is higher than the one at 0.05 dpa although it should be the same. This could first be explained by an increase in the overall sink strength with dose.

Another explanation could be that, at least for the 0.001 dpa damage level, steady state is not reached. As shown in Figure 60, RIS regime should dominate at steady state. Vacancies and SIA are produced at the same rate. The first point defects to be absorbed by sinks are the SIA because they diffuse the fastest, then the vacancies annihilate as well. At steady state, vacancies and SIA eliminate at the same rate. Even if the overall point defect concentration is smaller at the transient state, SIA contribution to interdiffusion kinetics could be higher than vacancies, thus could faster diffusion if SIA mediated diffusion coefficient is several order higher than vacancy mediated diffusion one.

The experimental interdiffusion coefficient under ion irradiation includes the contributions of the ballistic mixing $\tilde{D}_{ballistic}$ (i.e. dose rate dependent only) and the effective radiation-enhanced diffusion $\tilde{D}_{rad,eff}$ (i.e. dose rate and temperature dependent) [36]:

$$\tilde{D}_{rad,exp} = \tilde{D}_{ballistic} + \tilde{D}_{rad,eff} \quad (147)$$

Recalling Darken approximation for interdiffusion, we have:

$$\tilde{D}_{rad,eff} = X_B D_{A,rad,eff} + X_A D_{B,rad,eff} \quad (148)$$

with $D_{A,rad,eff}$ and $D_{B,rad,eff}$ being the effective radiation-modified intrinsic diffusion coefficients of elements A and B at the temperature T. Assuming, at first approximation, that the thermodynamic factor Φ is equal to unity, they can be expressed as [92]:

$$\begin{cases} D_{A,rad,eff} = d_{AV}X_V + d_{AI}X_{I,rad} \\ D_{B,rad,eff} = d_{BV}X_V + d_{BI}X_{I,rad} \end{cases} \quad (149)$$

where d_{ij} (i=A,B and j=V,I) the partial diffusion coefficients of the species A or B via vacancy or interstitial mechanism. X_j are the remaining atomic fraction of point defects at the non-equilibrium steady-state calculated from the reaction rate theory. Replacing equation (149) in (148), we obtain:

$$\tilde{D}_{rad,eff} = X_B(d_{AV}X_V + d_{AI}X_{I,rad}) + X_A(d_{BV}X_V + d_{BI}X_{I,rad}) \quad (150)$$

Then,

$$\tilde{D}_{rad,eff} = X_V(X_Bd_{AV} + X_Ad_{BV}) + X_{I,rad}(X_Bd_{AI} + X_Ad_{BI}) \quad (151)$$

with $X_V = X_{V,rad} + X_{V,eq}$.

Finally,

$$\tilde{D}_{rad,eff} = X_{V,rad}(X_Bd_{AV} + X_Ad_{BV}) + X_{V,eq}(X_Bd_{AV} + X_Ad_{BV}) + X_{I,rad}(X_Bd_{AI} + X_Ad_{BI}) \quad (152)$$

where

$$\tilde{D}_{th} = X_{V,eq}(X_Bd_{AV} + X_Ad_{BV}) \quad (153)$$

Thus,

$$\tilde{D}_{rad,eff} = \tilde{D}_{th} + X_{V,rad}(X_Bd_{AV} + X_Ad_{BV}) + X_{I,rad}(X_Bd_{AI} + X_Ad_{BI}) \quad (154)$$

and

$$\tilde{D}_{rad} = X_{V,rad}(X_Bd_{AV} + X_Ad_{BV}) + X_{I,rad}(X_Bd_{AI} + X_Ad_{BI}) \quad (155)$$

Finally [224],

$$\tilde{D}_{rad,exp} = \tilde{D}_{ballistic} + \tilde{D}_{rad} + \tilde{D}_{th} \quad (156)$$

$\tilde{D}_{ballistic}$ can be experimentally determined at cryogenic temperature (~ 77 K), it depends on the dose rate but is invariant with the temperature. \tilde{D}_{th} has already been determined at 440°C for the Ni-10Cr system, the SIA concentration at thermal equilibrium is negligible. X_j are obtained at steady state by simulation from the reaction rate theory for defined sink strength and dose rate (see Figure 86). d_{AV} and d_{BV} are determined from thermodynamic, mobility assessments and the equilibrium vacancy concentration. Therefore, the two left unknowns d_{AI} and d_{BI} can be determined by calculating \tilde{D}_{rad} from $\tilde{D}_{rad,exp}$ at steady state for two different dose rates at the same reached dose. These experiments allow to determine experimentally interdiffusion of the species A and B (here Ni and Cr) for one temperature. As ballistic diffusion does not depend on the temperature, \tilde{D}_{rad} and \tilde{D}_{th} should be determined for at least three different temperatures to obtain the magnitude of Arrhenius parameters for d_{AI} and d_{BI} .

The proposed matrix of experiments for a given crystal structure (i.e. in austenite) and average composition \bar{X}_1 (i.e. Ni-10Cr) is then:

$$dpa_1 \cdot \bar{X}_1 \cdot \begin{bmatrix} t_1 \varphi_1 \\ t_2 \varphi_2 \end{bmatrix} \cdot \begin{bmatrix} T_1 \\ T_2 \\ T_3 \end{bmatrix} + dpa_1 \cdot \bar{X}_1 \cdot \begin{bmatrix} t_1 \varphi_1 \\ t_2 \varphi_2 \end{bmatrix} T_{cryo} = 8 \text{ conditions} \quad (157)$$

with dpa the dose, φ the dose rate, T the temperature and t the annealing/irradiation duration. For a given average composition \bar{X}_1 , playing with modulations wavelength is possible taking care of an eventual gradient energy correction term to add in case of ultrathin nanolayers.

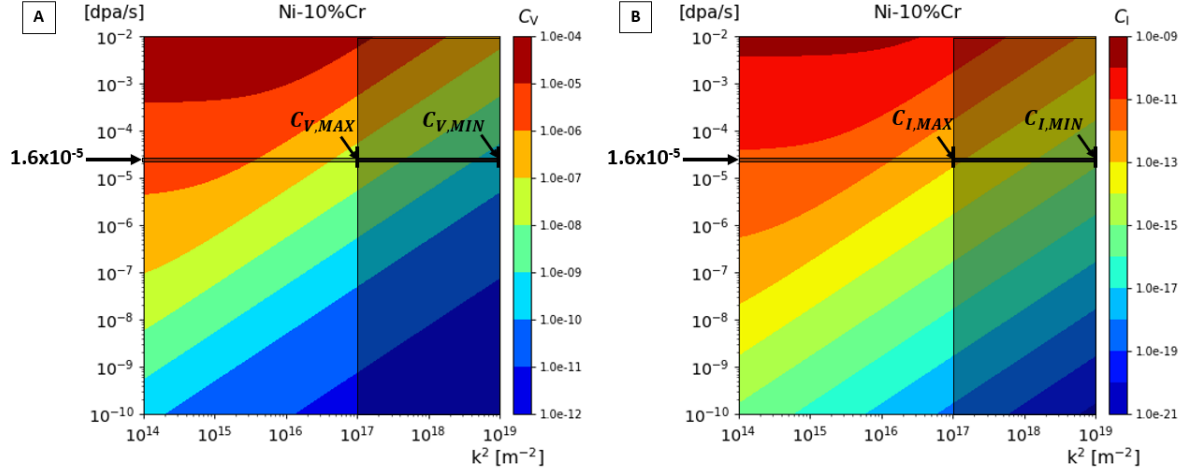


Figure 86 – Concentration of A) vacancies and B) interstitials depending on the dose rate and the sink strength at 440°C steady state (acknowledgements Liangzhao Huang). PD concentration range in our study is indicated by the black windows.

Quan et al. (1992) [224] used a similar method to determine \tilde{D}_{rad} but, contrary to the one proposed, SIA diffusivity was not taken into account and the sink-strength was fitted to the experimental results. These two parameters are believed to play a major role on the radiation-enhanced diffusion and to build a reliable point defect model under irradiation. Sink strength for every sink type (i.e. sink bias) should be determined experimentally with the highest accuracy.

$\tilde{D}_{rad,exp}$ has been determined for very low doses, for which steady state has certainly not been reached. Thus, they can be referred as transient experimental interdiffusion coefficients. To be able to access to interstitial migration energies the minimal necessary dose to reach steady state should be determined. It depends on the dose rate and the sink strength [60,225]. To reach steady state at low dose, the dose rate should be decreased. Heavy ions are limiting in this case because accessible dose rates are high.

To reach higher dose for the nanolayers for the wavelength used in this study (i.e. 4.3 nm) and prevent from a complete homogenization of the nanolayers under irradiation, temperature should be decreased.

This methodology can be applied to other type of particles with lower dose rates (i.e. neutrons, protons or electrons). Cascade mixing also occurs under neutron [226] and protons irradiation. The other possibility is to increase the wavelength to slower the amplitude attenuation rate.

In any case, the wavelength definition regarding the ageing conditions (the reverse is true) for the studied alloy, is a necessary step to reduce the number of experiments/conditions. The methodology

is valid for a binary system. Adding an alloying element to the system complexify the problem at it will be highlighted in the next section.

V. Interdiffusion kinetics in Ni-40Fe-25Cr/Ni-35Fe-20Cr system after thermal ageing and under irradiation

1. Microstructure evolution

Coating architecture and microstructure at the as-deposited state and after ageings have been characterized in the same manner than for the binary system. At the as-deposited state, Ti film was deposited on a $\langle 001 \rangle$ doped Si wafer (Figure 87.A)). Ni-40Fe-25Cr/Ni-35Fe-20Cr nanolayers coating is textured according to $\langle 111 \rangle$ direction, i.e. $\{111\}$ planes are oriented perpendicular to the deposition direction (Figure 87.B)). Columnar grains in the nanolayers coating have a width of tens on nm large while their length corresponds to the thickness of their deposited layer. A large density of defects is observed within the deposited nanolayers: stacking faults, nanotwins, and frank loops (Figure 87.B) and C)). The very thin twin spacing is attributed to a very low stacking fault energy combined with a high sputter deposition rate [204]. No porosity has been revealed by the out-of-focus technique.

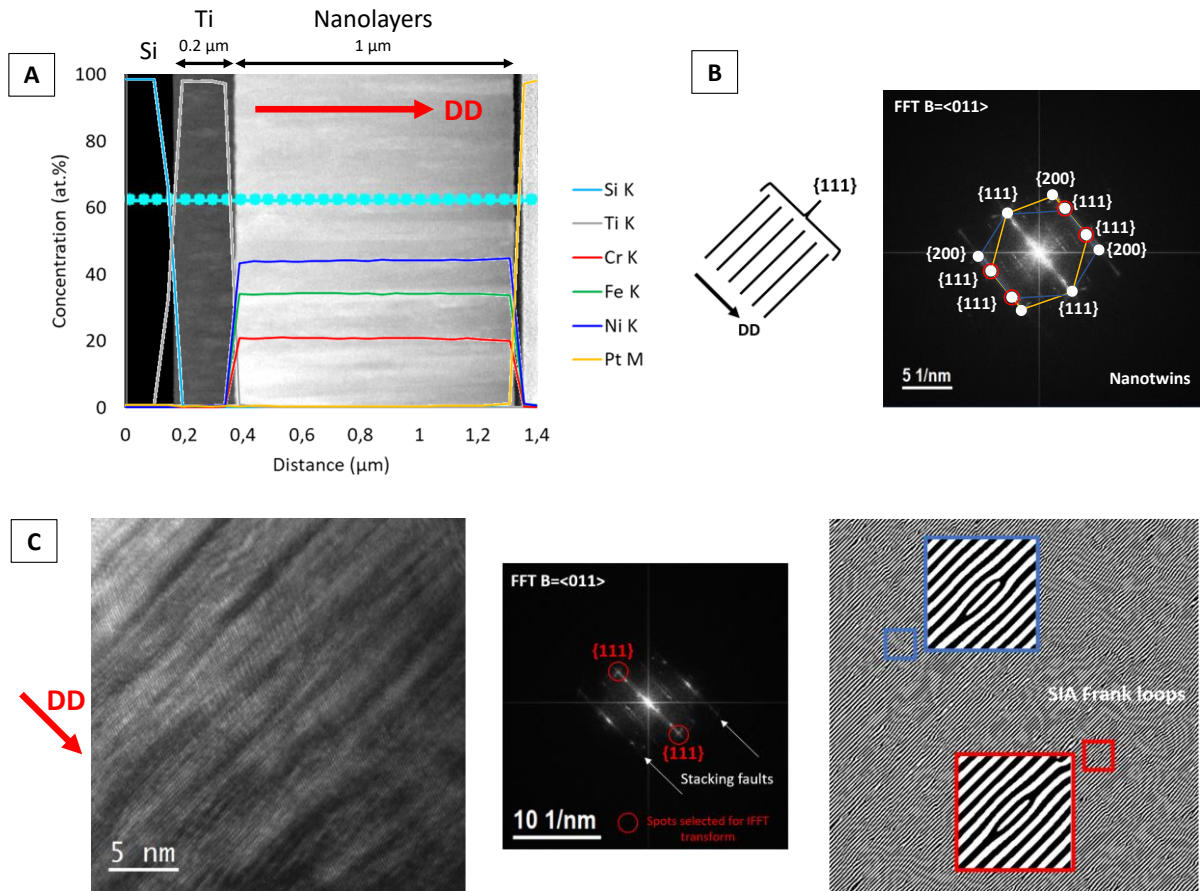


Figure 87 – A) Overview of the coating architecture. STEM-EDS linear profile drawn along the light blue dotted line and the corresponding concentration profiles superimposed to a HAADF image. B) FFT of an HR-TEM image with $\mathbf{B}=\langle 011 \rangle$ confirming the presence of nanotwins. $\{111\}$ planes are normal to the

deposition direction (DD). C) Streaks on the FFT indicate the presence of stacking faults, Frank loops are also observed.

In comparison to the binary system, characteristics of the ternary system are:

- Ti and nanolayers coating are thinner: 200 nm vs. 400 nm and 1000 nm vs. 1500 nm
- Grain size is smaller: 23 ± 1 nm vs. 30 ± 7 nm
- The wavelength is larger: 5.3 ± 0.1 nm vs. 4.3 ± 0.3 nm
- Nanotwins spacing is similar: 2.2 ± 1.4 nm vs. 1.9 ± 1.3 nm
- The number density and size of vacancy Frank loops is similar: $5.0\pm 2.9\times 10^{22}$ m⁻³ vs. $1.3\pm 0.8\times 10^{22}$ m⁻³ and 1.7 ± 0.7 nm vs. 1.6 ± 0.4 nm
- The number density and size of SIA Frank loops is similar: $6.2\pm 4.8\times 10^{22}$ m⁻³ vs. $3.1\pm 2.2\times 10^{22}$ m⁻³ and 1.8 ± 1.2 nm vs. 1.9 ± 0.9 nm
- The number of stacking faults per surface unit is similar: $8.4\pm 1.6\times 10^{16}$ m⁻² vs. $9.8\pm 2.0\times 10^{16}$ m⁻²
- The total sink strength k_s^2 is similar: 3×10^{18} m⁻² vs. 4×10^{18} m⁻²

Considering numerous sources of uncertainties, the total sink strength should range from 10^{17} to 10^{19} m⁻² as it was for the binary system.

Diffraction intensity integration of SAED patterns clearly permitted to index austenite being the major phase even after treatments and it was the only one indexed Figure 88. It is true at the as-deposited state as well as after annealing and irradiations up to 0.001 and 0.01 dpa. In the FeNiCr ternary system, it has been shown [227] that single phase FCC is stabilized at room temperature for a Ni content >36 wt.%, whatever the layers thickness [204].

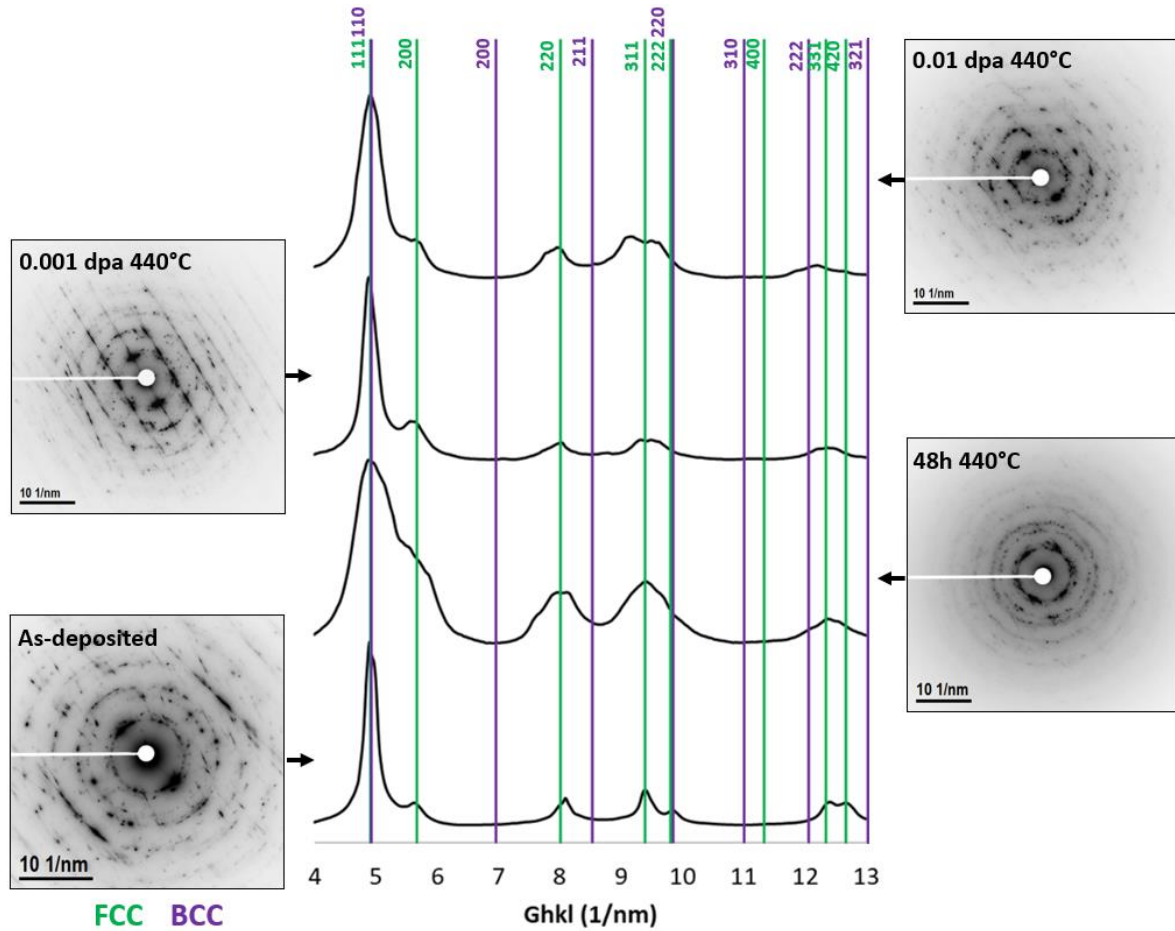


Figure 88 – Integrated diffracted intensity along the reciprocal distance G_{hkl} of SAED patterns in inverted contrast depending on the ageing conditions. FCC austenitic phase is the only one indexed.

Grain growth is not observed in the ternary system (Table 22), probably due to a thinner total thickness of the FeNiCr nanolayers coating than for the binary system [187]. Wavelength remain unchanged whatever the state.

Table 22 - Grain width and wavelength evolution after treatment. SD stands for standard deviation.

State	Grain width (nm)		Lambda (nm)	
	Mean	SD	Mean	SD
As-deposited	23	1	5,3	0,1
48h 440°C	23	1	5,0	0,1
0.01 dpa 440°C	27	4	5,1	0,2
0.001 dpa 440°C	22	5	5,1	0,2

Stacking faults and frank loops measurements from HR-TEM studies are reported in the graphs A), B) and C) of Figure 89. Any clear evolution is noticed whatever the state.

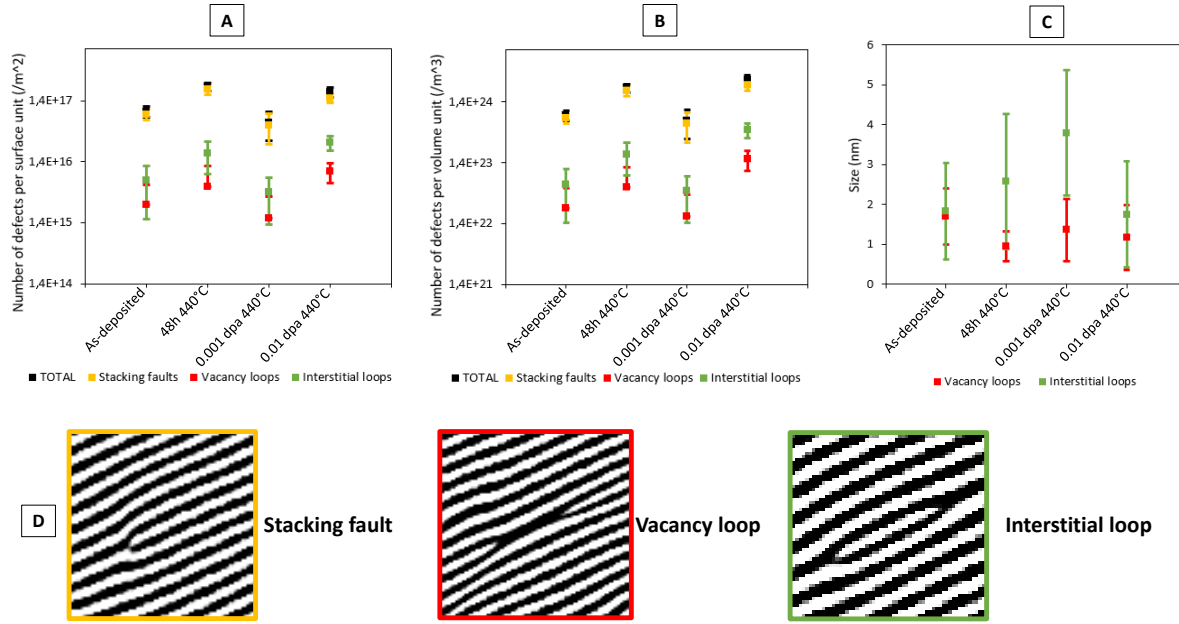


Figure 89 - Evolution of A) the number of defects per surface unit and B) volume unit and C) defect size in terms of ageing conditions. Defect identification examples are shown in D).

Because of nanolayers roughness, concentration amplitude evolution has been determined only from APT analyses.

2. Concentration amplitude evolution

Acquisition parameters were the same as the one chosen to study the binary system. As no pole was visible in any of APT volumes, reconstruction parameters were tuned to obtain a modulation wavelength equal to the one determined from TEM measurements only.

The evolution of elemental distribution within as-deposited and aged nanolayers APT volumes is summarized in Figure 90. Several grain boundaries were intercepted in all volumes confirming their smaller size compared to the one in the binary system. The modulated structure is visible at the as-deposited state and is still visible after ageings, but, because of smaller amplitudes in composition compared to the binary system, they are less easy to observe.

C and O overdensities (i.e. in terms of number of atoms per unit of volume) differ from one grain boundary to another. Some grain boundaries exhibit C, O and CrO overdensities while others only show O and CrO overdensities. Thus, depending on the grain boundary, impurity excess is not the same. After ageings, CrO tends to cluster meaning that the composition of a single grain boundary is heterogeneous.

Other minor impurities elements than C and O are present, for an exhaustive list see Table 23.

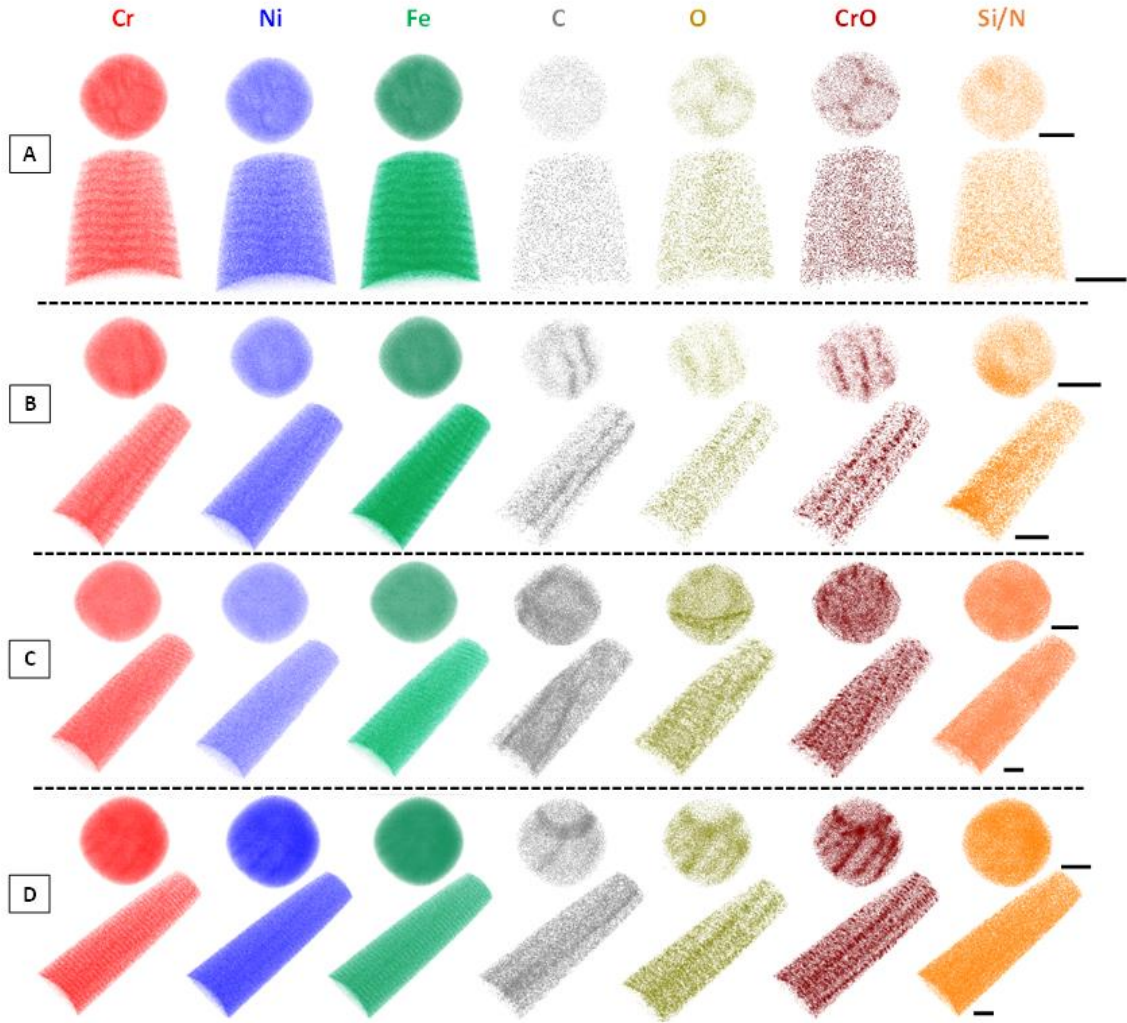


Figure 90 - 3D elemental distribution at the different studied state: A) As-deposited B) 48h 440°C C) 0.001 dpa 440°C D) 0.01 dpa 440°C. Scale bar = 20 nm.

Despite an increase of C after annealing and irradiations (Table 23), the global purity in composition expressed as the sum of the major alloying elements atomic concentration remain acceptable for diffusion kinetics investigations.

Table 23 - Evolution of the global composition and nanolayers purity in at.%

State	Al	C	Co	Cr	Cu	Fe	Mn	Ni	O	V	Si/N	Purity
AD	0,046 ± 0,003	0,12 ± 0,02	0,004 ± 0,002	22,04 ± 0,06	0,013 ± 0,012	35,52 ± 0,13	0,007 ± 0,005	41,66 ± 0,12	0,31 ± 0,03	0,015 ± 0,003	0,27 ± 0,03	99,2 ± 0,0
48h 440°C	0,047 ± 0,000	0,23 ± 0,09	0,003 ± 0,000	22,08 ± 0,03	0,007 ± 0,001	35,31 ± 0,07	0,007 ± 0,001	41,67 ± 0,29	0,28 ± 0,05	0,012 ± 0,000	0,36 ± 0,05	99,1 ± 0,2
0.001 dpa 440°C	0,044 ± 0,002	0,27 ± 0,01	0,003 ± 0,001	22,06 ± 0,12	0,006 ± 0,001	35,28 ± 0,04	0,007 ± 0,002	41,67 ± 0,13	0,32 ± 0,06	0,012 ± 0,001	0,32 ± 0,03	99,0 ± 0,0
0.01 dpa 440°C	0,044 ± 0,003	0,17 ± 0,03	0,008 ± 0,005	22,00 ± 0,11	0,005 ± 0,000	35,64 ± 0,12	0,006 ± 0,001	41,59 ± 0,05	0,24 ± 0,06	0,013 ± 0,000	0,28 ± 0,02	99,2 ± 0,1

Concentration profiles have been drawn across grain boundaries (Figure 91). At the as-deposited state, studied grain boundary is contaminated with O while after ageings, C and O enrichments are observed. Remember that C and O concentration may vary from a grain boundary to another.

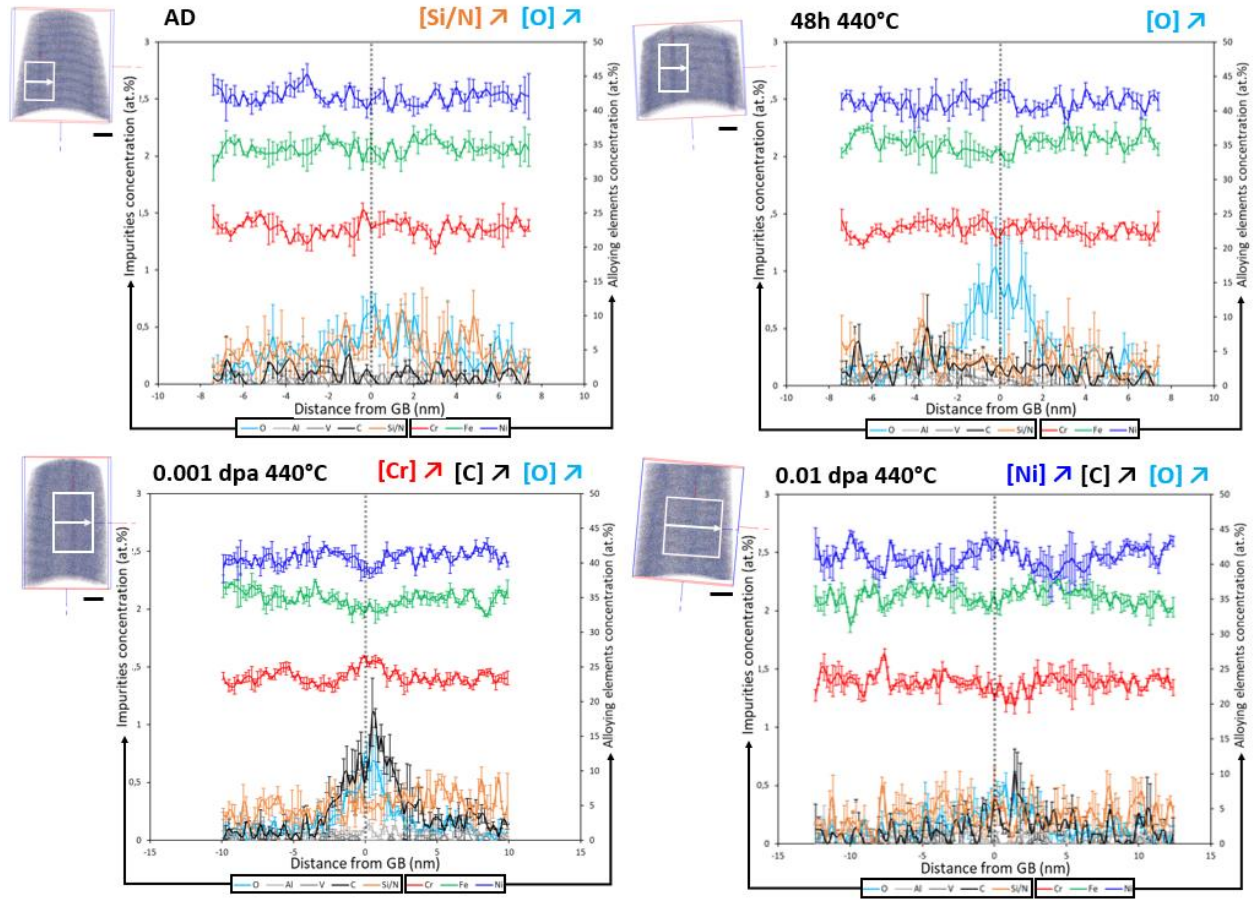


Figure 91 - Evolution of grain boundaries composition after ageings. AD stands for the as-deposited state. APT volumes and line profiles extraction location across grain boundaries are indicated at the left of the corresponding 1D composition profiles. Scale bar = 10 nm.

Nanolayers irradiated to 0.001 dpa show a Cr enrichment associated with C. It is surely the sign of the existence of a precursor of Cr_{23}C_6 carbide. Even if annealing that occurred prior to irradiation for this dose did not provoked any measurable amplitude attenuation, high diffusivity path such as GB could have experience segregation and carbide precipitation. Thus, this phase could have been thermally stabilized during the pre-annealing and/or its precipitation could be enhanced by irradiation, possibly a mix of both. In reaction to Cr enrichment a depletion of Ni and Fe is observed.

After irradiation to 0.01 dpa, while C enrichment is detected, Cr deplete as it is the case for Fe, and Ni slightly segregate at grain boundary. Even if the highest dose studied is smaller than for the binary system, RIS is observed only for the ternary system. An alloy with relatively close composition, Fe-20Cr-24Ni, irradiated to 0.1 dpa at 400°C with protons at $7.10^{-6} \text{ dpa.s}^{-1}$ exhibited RIS while the modified inverse Kirkendall model (MIK) predict RIS at doses even lower than 0.02 dpa [72,106,225,228]. At higher dose rate, for the same dose, to reach an equivalent RIS level,

temperature should be increased. As the temperature is higher in our case, RIS may happen for the selected irradiation conditions.

Examples of concentration profiles treated by the method #1 and the associate mean amplitude for the corresponding state determined by methods #1 and #2 are summarized in Figure 92. Profiles are noisier than for the binary system because interfaces are less sharp and the as-deposited amplitudes are smaller.

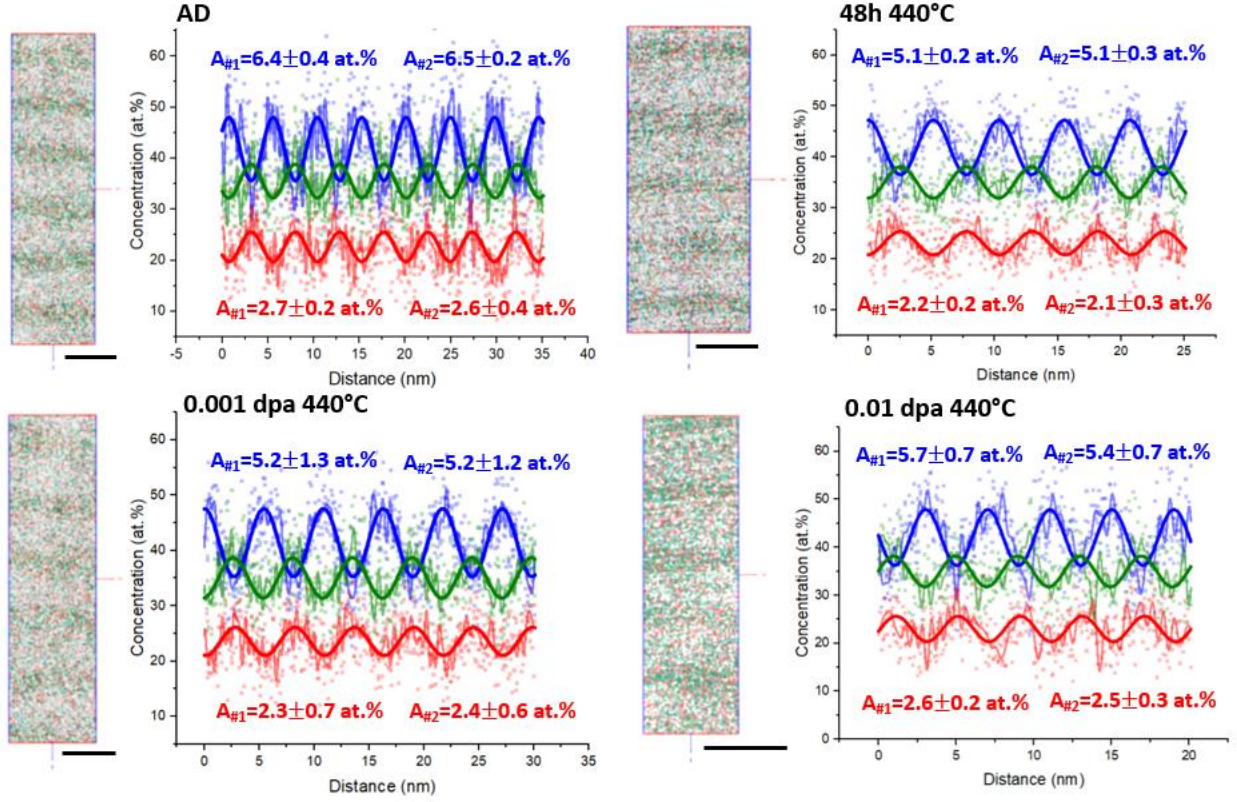


Figure 92 – Concentration profiles (method #1) and mean amplitude evolution (methods #1 and #2) with ageing. Fe, Ni and Cr are represented by the green, the blue and the red color respectively. Scale bar = 5 nm.

3. Interdiffusion coefficients

In the case of a ternary system, several ageing times are necessary to calculate interdiffusion coefficient from the amplitude attenuation. As only one annealing time could have been studied, only amplitude attenuations can be calculated. Obtained results are summarized in Table 24 and Table 25. Values extracted from the two treatments are presented, the two methods gave approximately the same results. As method #2 is much faster, only results of the method #2 are kept for comparison with the bulk theoretical values.

Table 24 - Amplitude attenuation evolution with the ageing conditions. Results are given for both methods (described in section IV-2).

		A_t/A_0 Ni			
		Method #1		Method #2	
State	Equivalent time (h)	Mean	SD	Mean	SD
48h 440°C	48.00	0.8	0.0	0.8	0.01
0.001 dpa 440°C	0.02	0.8	0.2	0.8	0.2
0.01 dpa 440°C	0.17	0.9	0.1	0.8	0.1

Table 25 - Amplitude attenuation evolution with the ageing conditions. Results are given for both methods (described in section IV-2).

		A_t/A_0 Cr			
		Method #1		Method #2	
State	Equivalent time (h)	Mean	SD	Mean	SD
48h 440°C	48.00	0.8	0.1	0.8	0.1
0.001 dpa 440°C	0.02	0.9	0.3	0.9	0.2
0.01 dpa 440°C	0.17	1.0	0.1	1.0	0.1

Theoretical amplitude evolution at $440 \pm 10^\circ\text{C}$ for bulk thermal interdiffusion is consistent with the amplitude attenuation calculated in this work for Cr only (Figure 93). As experimental diffusion data for the ternary system are scarce, and to our knowledge, inexistent at such low temperature, predictions may not fit to the reality. Alternative explanation can be related to in-plane grain boundary (GB) diffusion accelerating amplitude attenuation. Finally, as the amplitudes at the as-deposited state are smaller than for the binary system, experimental uncertainties are larger.

The anomalous amplitude evolution under irradiation can be explained by the latter point. What could be possible also is that RIS observed at 0.01 dpa provoked Cr depletion at GB so enriched the bulk while Ni enriched at GB. It could explain why amplitude attenuation is larger for Ni than for Cr at 0.01 dpa as well as the difference in trend compared to the lower dose. Amplitude attenuation kinetics should be higher for Cr than for Ni and we observe the reverse experimentally at 0.001 dpa. At this dose level, we observed a Cr enrichment at GB while Ni deplete, this could explain this tendency.

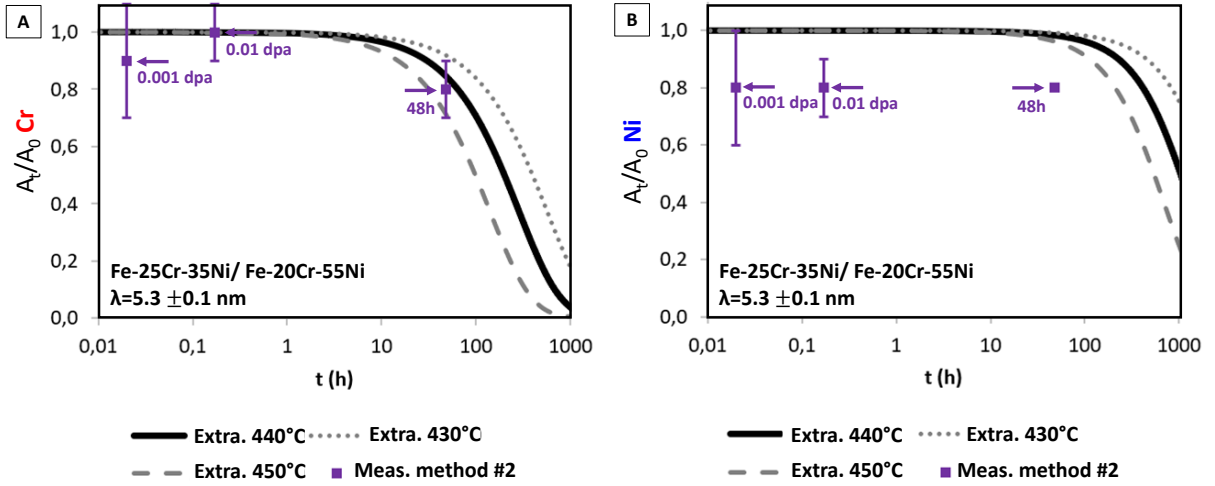


Figure 93 – Evolution of amplitude attenuation of A) Cr and B) Ni after ageings.

Further experimental data are necessary to confirm this hypothesis, but GB are highly suspected to affect a lot amplitude evolution because of the small grain width. Under irradiation, a competition between bulk diffusion and RIS seems to exist. Combined diffusion experiments with RIS modelling in this system is necessary to understand how elements redistribute under irradiation.

4. Discussion

The main hypothesis of the nanolayers method to be valid is the small modulations in composition so the interdiffusion coefficient remain constant. For the ternary system studied, Cr modulations ranges from 25 to 20 at.%, Fe from 40 to 35 at.% while Ni ranges from 35 to 45 at.% (Figure 94.A)). From the calculations made for the interdiffusion coefficient at 440°C between these concentrations, \tilde{D}_{ij} 's are equal to (Figure 94.A)):

- $\tilde{D}_{CrCr} = 6.9 \pm 0.3 \times 10^{-25} \text{ m}^2.\text{s}^{-1}$;
- $\tilde{D}_{CrNi} = -8.6 \pm 8.3 \times 10^{-27} \text{ m}^2.\text{s}^{-1}$;
- $\tilde{D}_{NiCr} = -2.0 \pm 0.2 \times 10^{-25} \text{ m}^2.\text{s}^{-1}$;
- $\tilde{D}_{NiNi} = 1.8 \pm 0.6 \times 10^{-25} \text{ m}^2.\text{s}^{-1}$.

\tilde{D}_{ij} 's variations will provoke a difference in amplitude attenuation below the experimental uncertainty therefore \tilde{D}_{ij} 's can be considered invariants.

As the wavelength is larger for the ternary system than for the binary one, the gradient energy effect on amplitude attenuation evolution is supposed to be negligible but has not been calculated, therefore $\tilde{D}_{ij} \cong \tilde{D}_{ij,\Lambda}$.

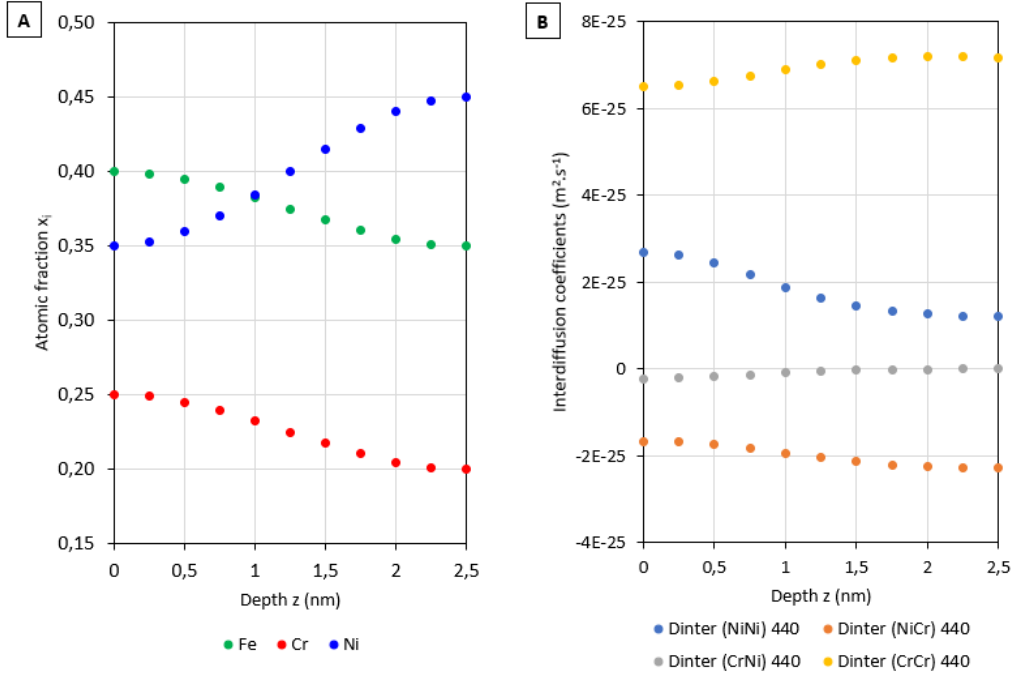


Figure 94 – A) Composition range corresponding to half of Λ . B) Interdiffusion coefficients calculated at 440°C within this composition range.

In order to reduce uncertainties on amplitude attenuation measurements the proposed nanolayers composition for further experiments based on targets availability and to ensure to study a quasi-fully austenitic structure is Ni/Ni-35Fe-20Cr, with a larger wavelength to reach steady state (i.e. higher dose or lower dose rate). The invariability criterion of the interdiffusion coefficients should be checked within this composition range regarding the uncertainty on temperature measurements.

For the ternary system, we assume that the experimental amplitude attenuation under irradiation at intermediate temperature $\left(\frac{A_{A,t_1}}{A_{A,0}}\right)_{rad,exp}$ after a duration t_1 at the dose rate ϕ_1 and a corresponding dose dpa_1 is weighed by amplitude attenuations due to ballistic mixing (ballistic), radiation-enhanced diffusion via vacancy and self-interstitial mechanism (rad) and thermal substitutional diffusion via vacancies with a vacancy concentration at equilibrium (th):

$$\left(\frac{A_{A,t_1}}{A_{A,0}}\right)_{rad,exp} = \left(\frac{A_{A,t_1}}{A_{A,0}}\right)_{ballistic} + \left(\frac{A_{A,t_1}}{A_{A,0}}\right)_{rad} + \left(\frac{A_{A,t_1}}{A_{A,0}}\right)_{th} - 2 \quad (158)$$

In order to extract the four independent interdiffusion coefficients, a minimum of four different values for each regime (i.e. ballistic, radiation-enhanced and thermal) are necessary as illustrated in Figure 95. These values are obtained at four treatment durations $t_{1 \rightarrow 4}$, same durations should be chosen for each regime. The corresponding fluxes $\phi_{1 \rightarrow 4}$ should give the same dose dpa_1 . The non-equilibrium steady-state under irradiation has to be reached, each time-dose rate couple should therefore satisfy this condition. Temperature T_1 is the same for thermal annealing and irradiation at intermediate temperature while, ballistic mixing has to be studied at cryogenic temperature T_{cryo} to prevent migration of point defects.

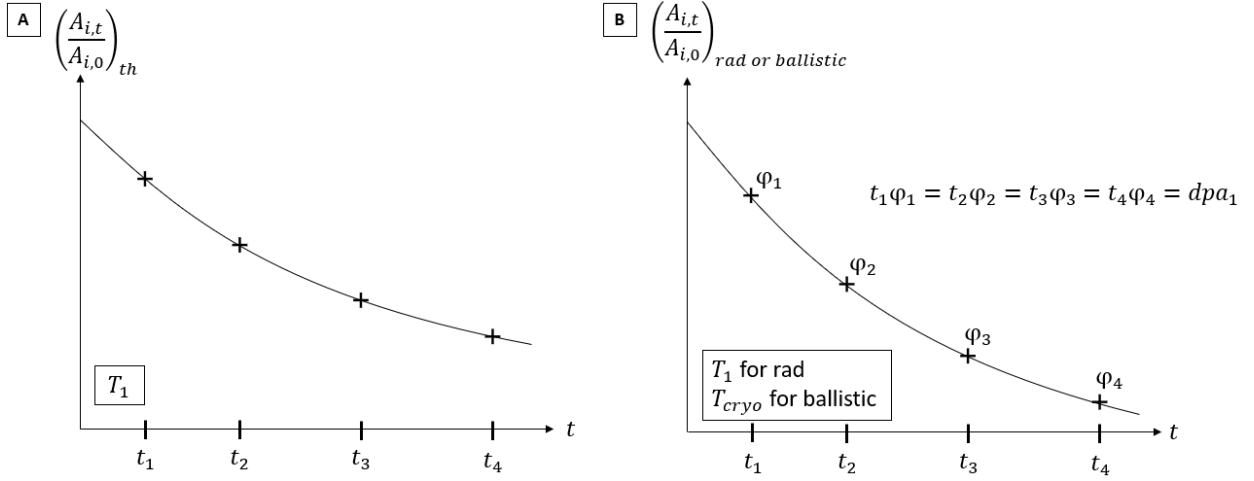


Figure 95 – Schematic evolution of amplitude attenuation for A) thermal, B) radiation-enhanced and ballistic mixing regimes and the corresponding treatment conditions.

$\tilde{D}_{AA,th}^C$, $\tilde{D}_{AB,th}^C$, $\tilde{D}_{BA,th}^C$ and $\tilde{D}_{BB,th}^C$ are determined experimentally from measurement of amplitudes attenuation at several annealing times following the procedure explained in section II-2. If only diagonal terms $D_{AA,th}$, $D_{BB,th}$, $D_{CC,th}$ of the intrinsic coefficients matrix are taken into account (i.e. cross terms neglected), thermal interdiffusion coefficients are linked to intrinsic ones by the following relations [229]:

$$\begin{cases} \tilde{D}_{AA,th}^C = (1 - X_A)D_{AA,th} + X_AD_{CC,th} \\ \tilde{D}_{AB,th}^C = X_A(D_{CC,th} + D_{BB,th}) \\ \tilde{D}_{BA,th}^C = X_B(D_{CC,th} + D_{AA,th}) \\ \tilde{D}_{BB,th}^C = (1 - X_B)D_{BB,th} + X_B D_{CC,th} \end{cases} \quad (159)$$

and,

$$\begin{cases} D_{AA,th} = d_{AV}X_{V,eq} \\ D_{BB,th} = d_{BV}X_{V,eq} \\ D_{CC,th} = d_{CV}X_{V,eq} \end{cases} \quad (160)$$

where d_{iV} (i=A,B,C) are the partial diffusion coefficients via the vacancy mechanism.

Similarly, radiation-enhanced interdiffusion coefficients are given by:

$$\begin{cases} \tilde{D}_{AA,rad}^C = (1 - X_A)D_{AA,rad} + X_AD_{CC,rad} \\ \tilde{D}_{AB,rad}^C = X_A(D_{CC,rad} + D_{BB,rad}) \\ \tilde{D}_{BA,rad}^C = X_B(D_{CC,rad} + D_{AA,rad}) \\ \tilde{D}_{BB,rad}^C = (1 - X_B)D_{BB,rad} + X_B D_{CC,rad} \end{cases} \quad (161)$$

and,

$$\begin{cases} D_{AA,rad} = d_{AV}X_{V,rad} + d_{AI}X_{I,rad} \\ D_{BB,rad} = d_{BV}X_{V,rad} + d_{BI}X_{I,rad} \\ D_{CC,rad} = d_{CV}X_{V,rad} + d_{CI}X_{I,rad} \end{cases} \quad (162)$$

$X_V = X_{V,rad} + X_{V,eq}$ and $X_{I,rad}$ can be determined thanks to the reaction rate theory at steady-state and knowing sink strength magnitude. Replacing Equation (160) in (162), we obtain the following expressions for the partial diffusion coefficients via the SIA mechanism:

$$\begin{cases} d_{AI} = \frac{1}{X_I} \left[D_{AA,rad} - D_{AA,th} \frac{X_{V,rad}}{X_{V,eq}} \right] \\ d_{BI} = \frac{1}{X_I} \left[D_{BB,rad} - D_{BB,th} \frac{X_{V,rad}}{X_{V,eq}} \right] \\ d_{CI} = \frac{1}{X_I} \left[D_{CC,rad} - D_{CC,th} \frac{X_{V,rad}}{X_{V,eq}} \right] \end{cases} \quad (163)$$

Contrary to the binary system, diffusion data in the Fe-Ni-Cr ternary system are scarce and interdiffusion coefficients in the literature have only been measured at high temperatures. Then, it is preferable to determine experimentally interdiffusion coefficients via the nanolayers method at the temperature T_1 . To obtain d_{iI} (i=A,B,C) at T_1 , the resulting matrix of experiments for the average composition of nanolayers \bar{X}_1 is:

$$\bar{X}_1 \cdot \begin{bmatrix} t_1 \\ t_2 \\ t_3 \\ t_4 \end{bmatrix} \cdot T_1 + dpa_1 \cdot \bar{X}_1 \cdot \begin{bmatrix} t_1 \varphi_1 \\ t_2 \varphi_2 \\ t_3 \varphi_3 \\ t_4 \varphi_4 \end{bmatrix} \cdot T_1 + dpa_1 \cdot \bar{X}_1 \cdot \begin{bmatrix} t_1 \varphi_1 \\ t_2 \varphi_2 \\ t_3 \varphi_3 \\ t_4 \varphi_4 \end{bmatrix} \cdot T_{cryo} = 12 \text{ conditions} \quad (164)$$

In order to determine the Arrhenius law parameters for d_{iI} (i=A,B,C), at least three temperatures in total are necessary, enhancing the required number of individual treatment conditions to:

$$\bar{X}_1 \cdot \begin{bmatrix} t_1 \\ t_2 \\ t_3 \\ t_4 \end{bmatrix} \cdot \begin{bmatrix} T_1 \\ T_2 \\ T_3 \end{bmatrix} + dpa_1 \cdot \bar{X}_1 \cdot \begin{bmatrix} t_1 \varphi_1 \\ t_2 \varphi_2 \\ t_3 \varphi_3 \\ t_4 \varphi_4 \end{bmatrix} \cdot \begin{bmatrix} T_1 \\ T_2 \\ T_3 \end{bmatrix} + dpa_1 \cdot \bar{X}_1 \cdot \begin{bmatrix} t_1 \varphi_1 \\ t_2 \varphi_2 \\ t_3 \varphi_3 \\ t_4 \varphi_4 \end{bmatrix} \cdot T_{cryo} = 36 \text{ conditions} \quad (165)$$

Because the proposed model is based on amplitude attenuation, the wavelength should be the same for all conditions. To access to SIA migration kinetics, numerous of ageing conditions are necessary. It demonstrates why saving time in data treatment for amplitudes extraction is crucial without degrading the results (i.e. method #2 is recommended). Further improvements are proposed in the next section.

VI. General discussion

In order to improve the current procedure and give new insights for data interpretation, several points should be discussed:

- Improve specimen fabrication and preparation

Ti layer was added to improve adhesion between the substrate and the coating and to reduce contamination. Over all the improvements done to reduce contamination, Ti layer might not have improved it the most. Indeed, degassing procedure, enhancement of the sputter deposition rate and replacement of the adhesive by silver painting to stick the substrate to the sample holder are believed to have play a larger key role than Ti. Furthermore, Ti layer additions induced nanolayers rugosity making more difficult APT volume extraction and strong reactive diffusion has been observed implying to propose a new procedure for specimen preparation (i.e. chunks attached on a Mo grid by “free welding”). We proved that the proposed method gave reliable results but, a lot of chunks felt during irradiation reducing the available doses per system to two instead of three. This point should clearly be optimized. The new architecture is proposed Figure 96. Find an adapted (i.e. to ensure a good adhesion) and efficient diffusion barrier can be complicated for the studied systems [200]. Remove the substrate (and the Ti layer) appeared to be a relevant way to avoid the formation of a diffusion couple or diffusion of the substrate through grain boundaries. Therefore, the substrate should be removed before ageing. Starting from the proposed preparation of chunks, instead of extracting the coating from a specimen and transfer it to the grid, the coating can be directly deposited on the grid. Substrate flatness is crucial, therefore, the future chunks regions can be flattened and cleaned in a FIB prior to deposition. To avoid redeposition during substrate milling, it is proposed to pre-mill bars in the grid in the shape of the future chunks. After coating, the thin part of the substrate below the coating can be removed. To prevent diffusion from the grid, the chunk is cut on one side and should be sufficiently long ($\sim 50 \mu\text{m}$). If the nanolayers adhere well to the substrate/grid, then the risk that the chunk break is highly decreased. To improve adhesion, it is advised to remove the oxide layer formed by ion etching in-situ in the magnetron sputtering reactor prior to deposition.

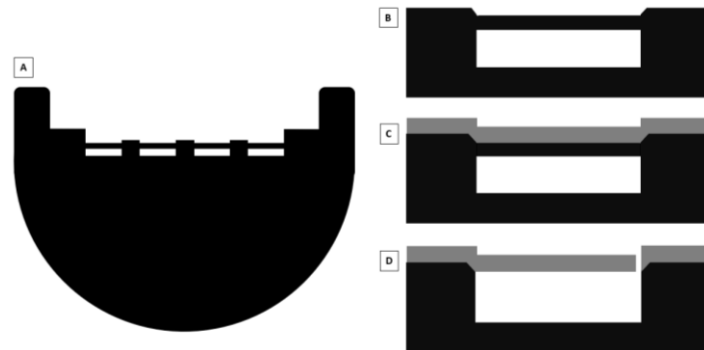


Figure 96 – A) Top view and cross-sectioned B) to D) of the prepared TEM grid before deposition A) and B), after deposition C) and before ageing (annealing or irradiation) D). After ageing, chunk can be transfer on a standard TEM grid or on coupon pretips for further analyses.

Only few chunks can be prepared per grid, but several grids can be coated at the same time by magnetron sputtering if they are located at the same distance from the substrate holder rotation center. Thanks to the proposed specimen architecture, the specimen preparation time is reduced a lot. Moreover, TEM grids have a well-adapted design for specimen-holders dedicated to irradiation because irradiation of TEM lamellas is very common. To ensure that the grid is well held in the specimen-holder for irradiation it can be maintained between two metallic O rings. This design is well-fitted to electron irradiation in HVTEM as well. Neutron irradiations can be also envisaged. The major difficulties in neutrons irradiations (except accessibility and price) is the low dose rate and material activation. Thanks to nanolayers, the time spent inside the reactor is reduced, reducing material activation. With the proposed design, it is possible to weld the chunks on new grids (after irradiation, possible to use a standard Pt welding) in hot cells to reduce the measured radioactivity to the background level. Then, it can be sent to a dedicated facility for further characterizations (to GENESIS platform for example). By studying the effect of different energetic particles on interdiffusion, it will help to determine the temperature shift existing to reach similar RIS levels depending on the particle type [40,193].

By removing the substrate, it permits to relax any stress gradient created at the substrate/nanolayers interface (as is was the case for the Ti layer).

Finally, choice of the material for the grid is crucial. The interdiffusion between the grid and the coating should be modelled (thanks to the diffusion module DICTRA of the Thermo-Calc Software for example) to select the material that diffuses the slowest within the studied nanolayers system. Grid composition should be checked before because TEM grids are not made of pure elements.

- Role of grain boundaries on diffusion kinetics after thermal ageing and under irradiation

Defined as high diffusivity path in case of thermal diffusion or point defect sink in case of diffusion under irradiation, grain boundaries was shown to influence diffusion in nanolayers, especially for the ternary system were the grain width is smaller and the wavelength is larger than for the binary system. Cr segregation at grain boundary after thermal annealing and radiation induced segregation are clear evidence of in-plane grain boundary diffusion. This can explain the anomalous amplitude attenuation evolution for the ternary system. Model the weigh of grain boundary diffusion or RIS on the obtained amplitude attenuation in these systems is a need.

In the case of thermal grain boundary diffusion, models derived from Hart's equation [17] have been proposed [230–232] with attempt to account for the decrease of grain boundary density when grain growth occurs [233].

In any case, concentration profiles across grain boundaries should be systematically drawn after ageing because it can bring quantitative insights to interpret and weigh grain boundary role on the measured diffusion kinetics. APT is well fitted to obtain this information.

Epitaxial growth of single crystal nanolayers [234] can be envisaged to analyse diffusion in a grain boundary free specimen. Study interdiffusion in such materials implies to account for, inter alia,

coherency strains. Two driving forces will therefore get involved in the resulting flux of species (in the case of thermal diffusion): the gradient of chemical potential and the stress gradient.

- Improve sink strength determination

To be able to access accurately to SIA-diffusion coefficient under irradiation, the sink density, size and nature (i.e. bias) should be carefully determined experimentally. Couple different techniques could be a good strategy to achieve this goal, in addition to the characterizations done it could have been possible to perform (non exhaustive list):

- Scanning Precession Electron Diffraction (i.e. ASTAR system from Nanomegas)

The technique automatically record precessed (i.e. beam rotation) nanobeam electron diffraction patterns at each point of a scanned area with a reachable spatial resolution of about 1nm and an angular resolution of about 1° [235]. From the recorded dataset, it is possible to build orientation maps and extract the crystallographic texture of indexed phase, built grain boundary maps to extract the grain size and nanotwin spacing, built phase maps to obtain the phase fraction of the indexed phases and estimate dislocation density [236] (i.e. the geometrically necessary dislocations that induce lattice curvature). This technique has already been successfully employed on magnetron sputtered thin films [237,238].

- Ion beam removal method for the determination of residual stress profiles [239,240]

The residual stress distribution in the thin film is calculated from microcantilever deflection while it is progressively thinned by focused ion beam. The cantilever is cut free on one side while, at the other side over few microns' width, the thickness is gradually reduced by FIB milling. Thus, the curvature changes in the thinned area. The rest of the cantilever stays unaltered and acts as an amplifier for this curvature. Then, the cantilever deflection is measured. Residual stress calculation relies on the Euler-Bernoulli theory for bending beams and they are calculate incrementally based on the cantilever geometry, the elastic properties of the material, and the thickness of the removed layers with the corresponding deflections. Residual stress profiles can be determined with an estimated depth resolution of 50 nm. The novel proposed specimen architecture (Figure 96) is well fitted for this type of experiment.

- APT-TEM correlative microscopy [238,241]

Measurements of amplitudes were done in different grains (i.e. different grain size, misorientation from $\langle 111 \rangle$ crystallographic texture, intergranular defects density and size), each grain taken apart should exhibit small variations of the amplitude kinetic attenuation. TEM-APT correlative microscopy may help to describe the local sink strength within the grain from which amplitude modulations are extracted.

VII. Conclusion

Experimental interdiffusion coefficient for the binary Ni-10Cr system at 440°C have been determined to be equal to $1.1 \pm 0.2 \times 10^{-24} \text{ m}^2 \cdot \text{s}^{-1}$. In order to measure such slow kinetics at the micron scale, as it is usually done via the classic Boltzmann-Matano method [9], it is possible to estimate the annealing time t required for the couples to interdiffuse within a diffusion zone of 1 μm width w thanks to the following formula:

$$w \approx \sqrt{\tilde{D}t} \quad (166)$$

In these conditions, more than 10 000 years would have been necessary to measure so low interdiffusion coefficient ! Diffusion coefficients are generally extrapolated from high temperatures, we can clearly understand why. Thanks to the nanolayers architecture, studied diffusion scale is in the nanometer range. It permits to obtain interdiffusion coefficients at much lower temperature than standard diffusion couple experiments under reasonable time. Furthermore, the amplitude is determined from a stack of bilayers, increasing measurement statistics and accuracy.

Due to vapor quenching, metastable phases can form by magnetron sputtering. It is an important parameter to consider because it can limit the access to certain compositions (as it was the case for the ternary system).

For a given composition, by changing the wavelength, the amplitude attenuation rate change. We showed that it is important to adapt the wavelength to the desired ageing conditions to be able to quantify interdiffusion, a change in amplitude should happen after ageing and in the same time take care that no full homogenization occur (if the system tends to homogenize).

Experimental diffusion kinetics at even lower temperatures are accessible by the nanolayers method after thermal annealing and also at low irradiation doses and dose rates. By adjusting the composition modulation wavelength, interdiffusion kinetics over a large range of irradiation conditions can be investigated. At lower temperature, when interstitial concentration becomes significant in comparison to vacancy concentration it should be possible to access to SIA contribution to the diffusion process and therefore their diffusion kinetics (i.e. related to their migration energy generally calculated from *ab-initio* simulations).

We showed that it is essential to link diffusion kinetics experiments with microstructure characterization (i.e. sink strength) by reducing the number of parameters to fit in order to access to the diffusivity on interstitials. Proposed basic models defined the necessary condition to access to SIA mediated diffusion coefficients. They need to be confirmed by further experiments.

In order to obtain this “gold number”, further improvements need to be done:

- determine sink strength more accurately (i.e. defects density and size quantification regarding their nature, define sink efficiency factors and the sink strength of stacking faults);
- quantify the weigh of in-plane grain boundary diffusion;

- improve nanolayers architecture (i.e. larger as-deposited amplitude for the ternary system and coat directly a prepared TEM grid).

Thanks to the proposed specimen architecture, it is possible to study neutron irradiated materials (as chunks are small the radioactivity level should be low), the grid is well adapted to electron irradiation in high voltage TEM, and fits also to sample-holders used for ion irradiation. In addition, the preparation sample time is drastically reduced, and its geometry is well adapted to stress measurements by FIB removal. Finally, it reduces the risk of chunk fall compared to the “free welding” method.

Based on encouraging results, we were able to formulate recommendations, propose a design and a methodology to obtain reliable data and establish a PD model of diffusion under irradiation. Nanolayers method appear to be a promising one to finally obtain quantitative data about experimental diffusion kinetics of SIA in irradiated materials both in binary and more complex ternary systems.

Experimental results obtained in this work can already be compared to the Atomistic Kinetic Monte Carlo (AKMC) model results developed in task 3.2 of the GEMMA project (see APPENDIX).

CHAPTER 4

INVESTIGATION OF RADIATION INDUCED SEGREGATION ON INTRAGRANULAR DEFECTS IN 316L(N)

I.	Introduction.....	168
II.	As-received material: 316L(N).....	168
1.	At the microscale.....	168
2.	At the nanoscale.....	171
III.	Irradiation conditions.....	177
1.	JANNuS Orsay.....	177
2.	JANNuS Saclay.....	179
IV.	Nanoscale characterizations strategy.....	180
1.	Correlative microscopy on an APT tip.....	180
2.	Correlative microscopy on a tip extracted from a lamella.....	181
V.	Post-irradiations characterizations.....	184
1.	1 dpa 450°C.....	184
1.1.	Cavities and Frank loops.....	184
1.2.	Precipitation and RIS.....	186
2.	2.5 dpa 440°C.....	198
2.1.	Cavities and Frank loops.....	198
2.2.	Precipitation and RIS.....	201
VI.	General discussion.....	205
VII.	Conclusion.....	209

I. Introduction

Austenitic stainless steel nuclear grade nitrogen modified 316L, namely 316L(N), has been optimized and shows the beneficial effect of N addition on mechanical properties, especially on creep strength, for GENIV reactors applications. The studied 316L(N) follows RCC-MRx2012 specification excepted for the nitrogen content which was increased to 0.1 weight percent. Investigations have already been performed by EDF R&D on this alloy at its as-received and thermal aged states but its microstructural response to irradiation has not been studied yet.

As creep, irradiation-assisted corrosion cracking (IASCC) can lead to an unexpected failure of core components made of austenitic stainless steels such as former baffle bolts. Radiation-induced segregation (RIS) has been proven to be one of the various synergetic parameters which are involved in this degradation mechanism [85]. The large majority of experimental RIS studies are done on grain boundaries because IASCC provokes an intergranular fracture. Irradiation hardening is also thought to be conjointly involved with RIS. This increase in yield strength is due to the multiplication of obstacles created during irradiation impeding dislocation motion, e.g. lattice defects. Defect lattice nature, number density, size, RIS levels and tendencies at their vicinity, influence both hardening and segregation at grain boundaries. Intragranular defects can exhibit preferential absorption of a type of point defect [242]. Depending on their respective bias, mechanisms involved in RIS can differ which influences phases stability and precipitate-defect association [104].

The purpose of this work is to compare microstructure evolution under irradiation of this optimized steel with the commercial grades commonly used for GENII reactor internals. Then, investigate RIS on intragranular defects by technique coupling to intend to identify mechanisms involved.

II. As-received material: 316L(N)

A block of matter was supplied by EDF R&D. It was extracted from a sheet of 316L(N). The initial sheet was hot rolled by cross rolling passes to a thickness of 40 mm. Then, the steel was solution annealed at 1085°C during 1h followed by a water quenching. Specimens studied were sampled from the half-thickness of the sheet. Their as-received microstructure at different scales is described in this section.

1. At the microscale

Scanning electron microscopy (SEM) coupled with electron back-scattered diffraction (EBSD) and energy dispersive X-Ray spectroscopy (EDS) was performed on the as-received material to study microstructure heterogeneities at the micron-scale. Measurements were done on the Dual-Beam SEM-FIB (Focused Ga Ion Beam) microscope Zeiss XB-540. On the acquired maps, RD₁ and RD₂ refer to the rolling directions whereas ND denotes the normal direction. RD₁ is the direction of the last cross rolling pass thus RD₂ can also be noted as the transverse direction.

A simultaneous EBSD-EDS map has been collected by TEAM software on the same area of the specimen. EBSD data (Figure 97.A) to D)) were post-treated with OIM analysis software. A phase

map was extracted allowing to calculate the surface fraction of austenite over the residual delta-ferrite which is higher than 0.99. The initial microstructure exhibits equiaxed grains of austenite of approximately 50 μm size with no pronounced preferential crystallographic orientation. More than half of the boundaries are twin boundaries. Delta-ferrite is elongated along the rolling direction RD_1 . Ferrite is shaped as strips in both rolling directions (RD_1 and RD_2) which suggests that it has a ribbon shape (EDF R&D private communication).

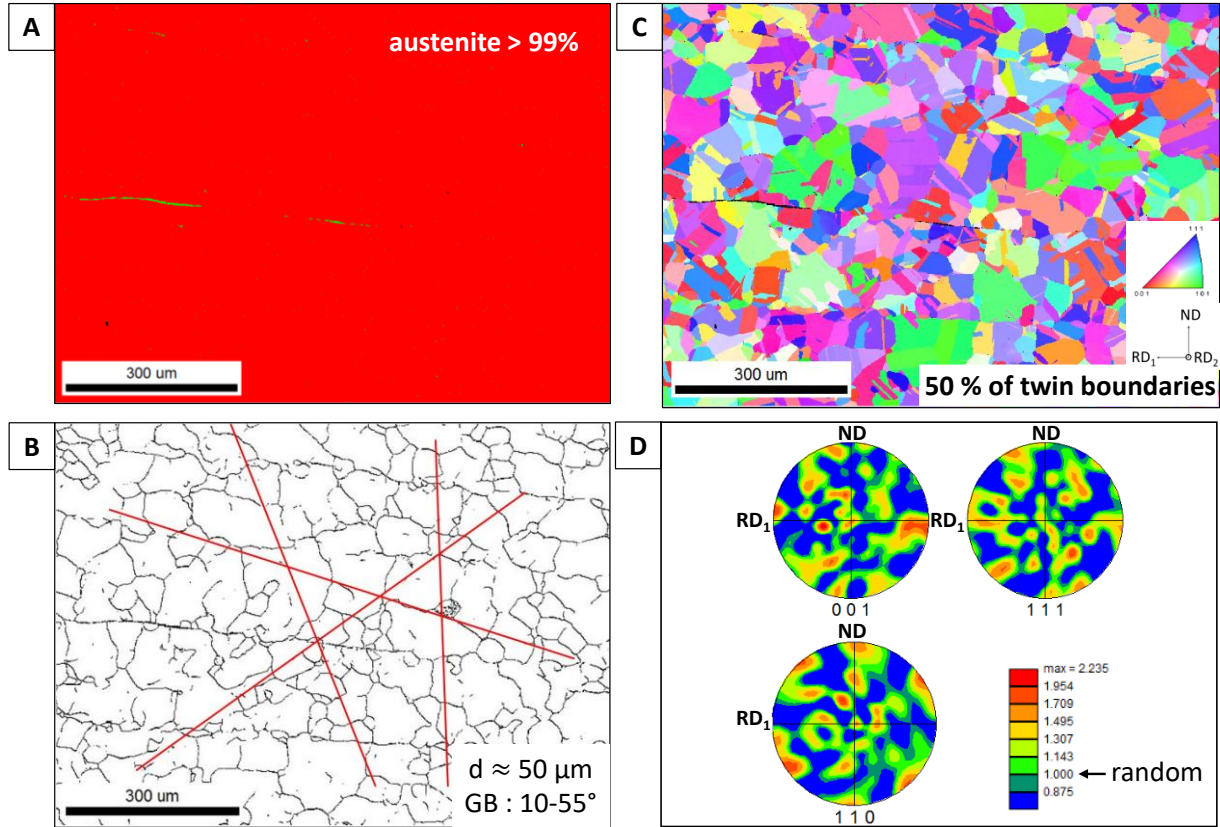


Figure 97 – SEM-EBSD A) Phase map (red: austenite, green: delta ferrite), B) Random high-angle grain boundary map (excluding coincident site lattice boundaries and low-angle boundaries) with red lines drawn for grain size measurement by the intercept method, C) Orientation map (i.e. inverse pole figure map) and D) pole figures along low-index directions: $[001]$, $[111]$ and $[110]$.

In Figure 98.A), SEM-EDS elemental maps reveal alpha-stabilizers (i.e. Cr, Mo, Si) enrichments not only at the ferrite location but at lower levels within the austenitic matrix as well. These chemical heterogeneities are referred as microsegregations, they are also enriched in Mn, an element known as a gamma-stabilizer. These microsegregations are parallel to the rolling directions and spaced of about 50 μm from each other. As shown in Figure 98.B), wavelength-dispersive X-ray spectroscopy measurements have been done by EDF inside and outside microsegregations and at ferrite location. It can be noticed that microsegregations are also enriched in Co, Nb and P with a P amount being more than 2 times greater in ferrite than in austenite.

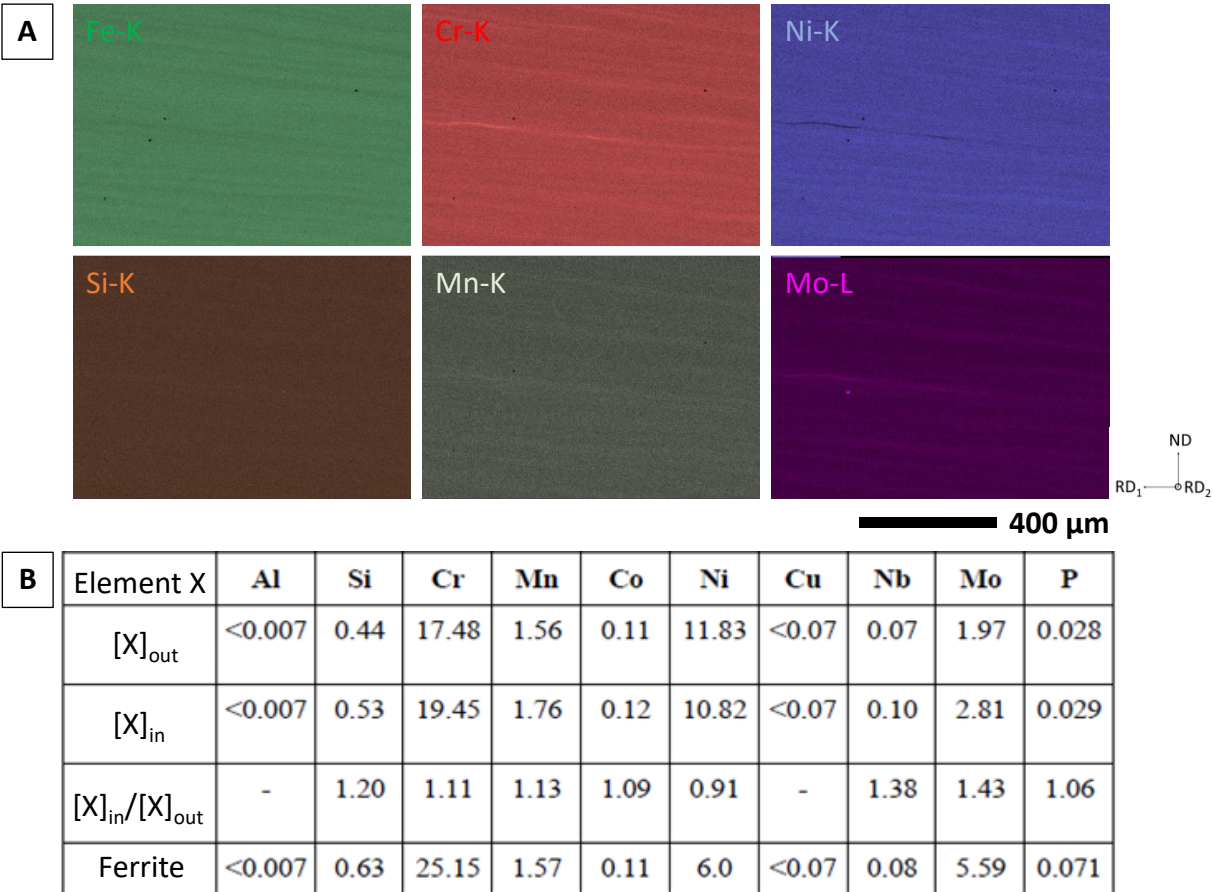


Figure 98 - A) SEM-EDS elemental maps. B) Chemical composition (in wt.%) inside-outside microsegregations and inside ferrite obtained from WDS measurements (EDF R&D private communication).

Coupled EBSD-EDS acquisition also permitted to highlight the presence of micron-sized second phases (i.e. inclusions and precipitates) within the scanned area (Figure 99.A)). The majority of the identified particles are aluminium oxides, one of them being enriched in yttrium. These inclusions are classically observed in 316L grades [243]. Silicon oxide particles, also observed, could be either an inclusion or coming from the last step of polishing with OP-S during specimen preparation. Nb-rich precipitates are observed as well. An EDS spectrum (Figure 99.B)) extracted from one of them shows that this Nb-precipitate is also enriched in N and Cr. Other EDS spectra indicate that Nb-rich precipitates are sometimes enriched in Ti or Mo. At the electron accelerating voltage of 20kV, K rays of Nb and Mo are not detected. L rays of Nb and Mo overlap, but, looking attentively to the corresponding peak shape and the relative intensity of their respective theoretical rays, it is possible to unambiguously determine the presence/absence of these elements from spectrum analysis.

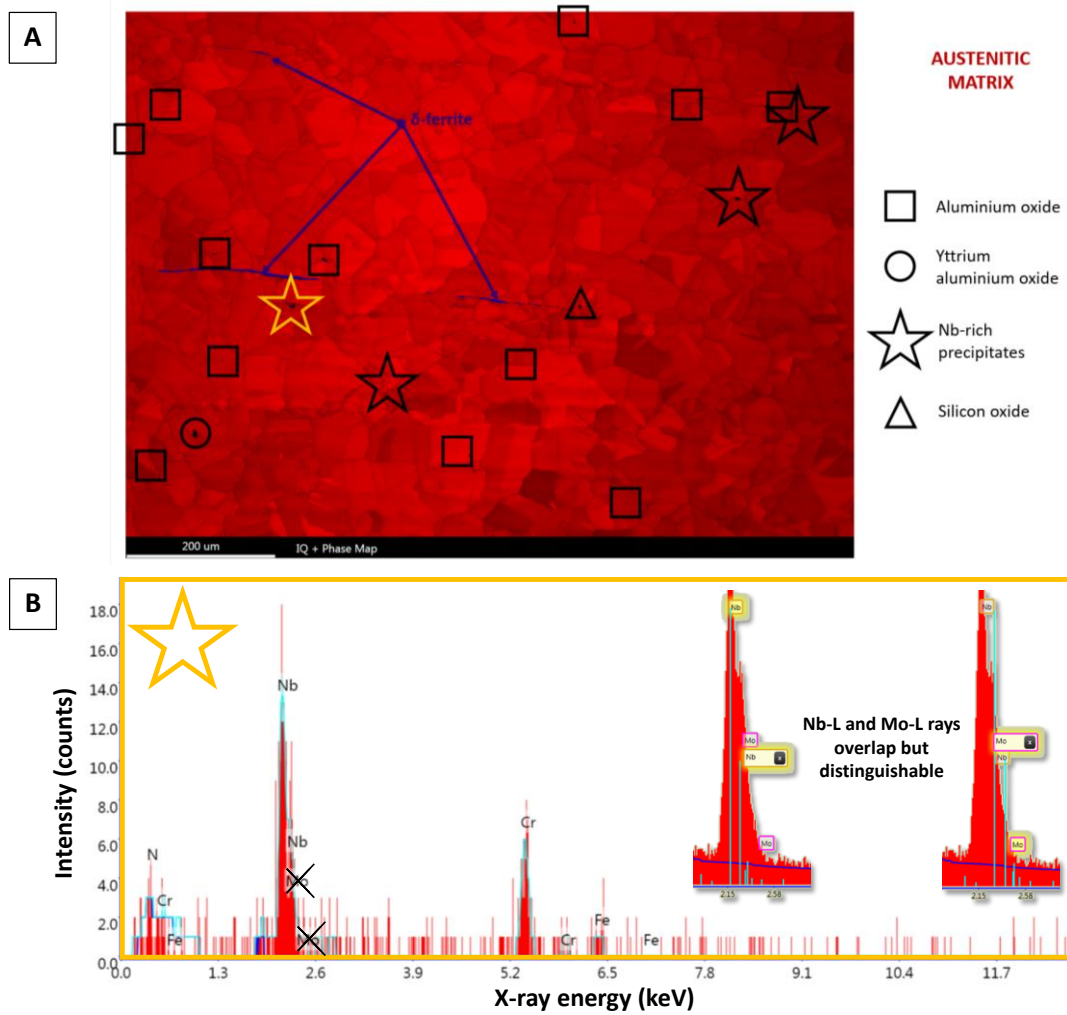


Figure 99 – A) Superimposed index quality map and phase map from EBSD data showing distribution of inclusions and second phases within the austenitic matrix. B) SEM-EDS spectrum of the yellow star labelled precipitate, enriched in N, Nb and Cr. Indexation of the peak at 2.15 keV, discrimination between Nb-L and Mo-L rays.

2. At the nanoscale

The chemical composition of the studied material (Table 26) agrees with nuclear specifications excepted from the nitrogen content which is increased to 0.1 wt.%. Reference measurements were carried out by EDF R&D thanks to the infrared absorption method after combustion for C and S, by the inert gas fusion technique for N and by X-ray Fluorescence Spectrometry. FIB-prepared tips were analysed in a Cameca LEAP 4000X HR in voltage mode, at 63K, a pulse frequency of 200 kHz, and a pulse ratio of 20%. The detection rate was raised during the analyses. These parameters were chosen in order to: maintain a constant flux of evaporated ions, increase signal-to-noise ratio and lower the risk of tip fracture. The collected data were processed with the Cameca IVAS commercial software for 3D reconstruction of APT volumes, thanks to correlative microscopy (i.e. from SEM image) when poles could not be seen or identified. Rest of the data treatment was performed with the GPM 3Dsoft software.

Matrix compositions measured by APT are expressed as mean values and standard deviations from different lift-outs (i.e. different FIB samplings within the specimen, without any preferential

extraction locations inside or outside microsegregations). Comparison of the obtained APT composition with the reference permits to validate the selected acquisition parameters, especially for the temperature.

Table 26 - Chemical composition of the 316L(N) studied grade regarding specifications, as measured by EDF (Ref.) and matrix composition measured by APT (in wt.% and at.%)

	B	C	Co	Cr	Cu	Mn	Mo	N	Nb	Ni	P	Si	S	Al	O	V
RCC-MRx-2012 (wt.%)	≤ 20 ppm	≤ 0.030	<0.20	17.00 - 18.00	≤ 1.00 0	1.60- 2.00	2.30- 2.70	0.06- 0.08	-	12.00 - 12.50	≤ 0.030	≤ 0.50 0	≤ 0.015	-	-	-
Ref. (wt.%)	19 ppm	0.021	0.03	17.7	0.06	1.71	2.46	0.1	0.09	12.6	0.021	0.42	0.002	-	-	-
APT (wt.%)	20 ± 0 ppm	0.019 ± 0.001	0.036 ± 0.004	17.8 ± 0.1	0.051 ± 0.006	1.59 ± 0.07	2.7 ± 0.1	0.087 ± 0.004	0.05 ± 0.01	12.6 ± 0.2	0.015 ± 0.003	0.51 ± 0.02	-	0.10 ± 0.01	25 ± 7 ppm	0.033 ± 0.001
APT (at.%)	0.011 ± 0.002	0.086 ± 0.01	0.034 ± 0.004	19.0 ± 0.1	0.044 ± 0.005	1.61 ± 0.08	1.6 ± 0.1	0.35 ± 0.01	0.031 ± 0.005	12.0 ± 0.2	0.027 ± 0.005	1.00 ± 0.04	-	0.20 ± 0.02	0.008 ± 0.003	0.036 ± 0.001

At this scale, elements distribution is homogeneous (Figure 100).

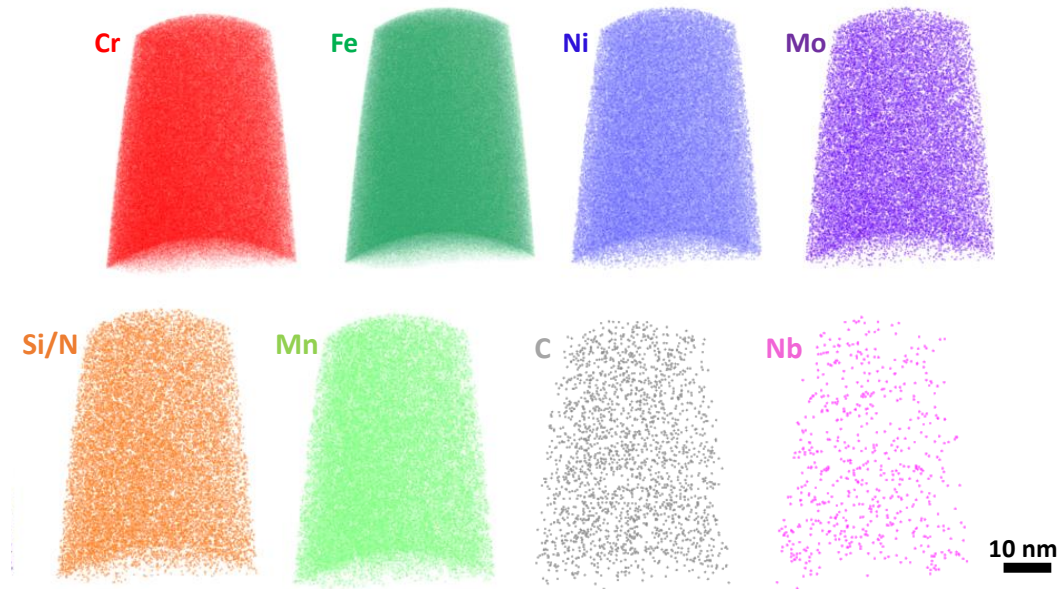


Figure 100 – Homogeneous distribution of elements within an APT 3D-volume

TEM lamellae were cross sectioned by FIB at 30kV in the Dual-Beam Zeiss XB540 and back-polished under a low-voltage Ar⁺ ion beam (0.5 keV) in the Precision Ion Polishing System II from Gatan (acknowledgements L. Legras for polishing conditions). Post-FIB cleaning helps to remove the damaged layer and considerably improve specimen quality [244]. Considering the very low amount of Cu in this steel grade compared to Mo, lamellae were welded on Cu grids post to reduce error in the composition measurements.

S/TEM investigations have been performed with the JEOL-ARM200F at 200kV. Dislocation density have been measured by the line-intercept (Figure 101.A)) and the line-length measurement

methods (Figure 101.B)) with ImageJ on two different lamellae oriented downzone at two different zone axes. The twin boundaries were excluded from the calculation in the case of Figure 101.C). The average dislocation density $\bar{\rho}$ is given as the mean value and the error corresponds to the standard deviation between all these measurements. Correction of the projected length of dislocation lines was done (see CHAPTER 2). At the as-received state, $\bar{\rho} = 1.3 \pm 0.6 \times 10^{14} \text{ m}^{-2}$. This value is high compared to the literature. For solution annealed grades type 316/L, dislocation density is in the range of 10^{10} [245] to 10^{13} m^{-2} [242] (and between 10^{15} and 10^{16} m^{-2} after cold working [3]). In a solution annealed 316LN, with a nitrogen content of 0.06 wt.%, a dislocation density of 1.10^{14} m^{-2} was found [246]. Dislocations can be introduced during sample preparation when they are mechanically polished as it is the case here. Before extracting lamellae by FIB, samples surface have been polished to OP-S using the optimized procedure developed by M. Boisson [61] to avoid this effect.

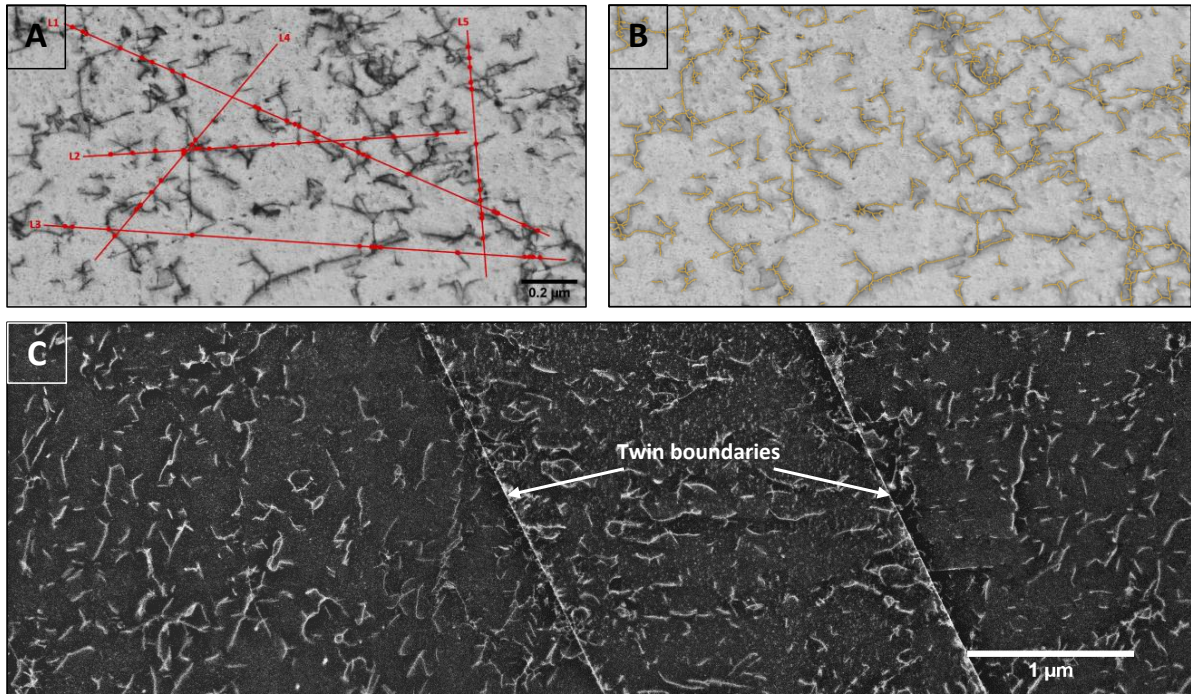


Figure 101 – Dislocation density measurements from BF STEM image with specimen oriented downzone $\mathbf{B}=\langle 111 \rangle$ by A) line-intercept method and B) line-length measurement method. C) STEM LAADF image with $\mathbf{B}=\langle 110 \rangle$ used to calculate dislocation density from another prepared lamella.

The presence of nano-sized precipitates has been detected (Figure 102. A)) thanks to Z-contrast imaging in STEM HAADF mode. Their chemistry has been assessed thanks to EDS mapping (see CHAPTER 2). At 200 kV, K-lines of Nb and Mo are detected. Thus, maps built with the K lines allow to trust their respective local enrichments. Two families of precipitates are discriminated by their composition. The first family is enriched in N, Cr, Nb and Mo with a number density of $4.5 \times 10^{18} \text{ m}^{-3}$, the second one is Ti-rich. These precipitates are less numerous ($1.8 \times 10^{18} \text{ m}^{-3}$). Nb-rich precipitates at the nanoscale have a composition close to the one observed at the microscale letting suggest that they belong to the same family. Ti-rich precipitates are enclosed within Nb-rich ones. This let suggest that Ti-rich precipitates acted as nucleation site for Nb-rich ones during steel elaboration process.

A close-up of the precipitates #1 (Figure 102) is presented Figure 103. On EDS spectra extracted from the matrix, Nb-rich and Ti-rich areas, peak superimpositions can be analysed. It is the case for: N-K and Ti-L, P-K and weak Mo-L, the weakest Cr-K (Cr-K_β) and the strongest Mn-K (Mn-K_α) lines. For Cr and Mn, software deconvolutes well both contributions in their common peak. But for low energy rays (i.e. N-K and Ti-L) uncertainty is higher because background is not well defined in low energy region, but also because of X-ray absorption. This analysis permits to confirm the presence of N in Nb-rich precipitates. Cr and Nb are also present, while Si is absent on the spectrum. Both matrix and Nb-rich area contribute to the Ti-rich area spectrum, as the Nb-rich precipitates is thinner in this region, matrix contribution is higher. It explains why Fe peak is greater in Ti-rich area spectrum than in Nb-rich spectrum. Carbon peak was not clearly detected neither in Ti nor in Nb-rich areas.

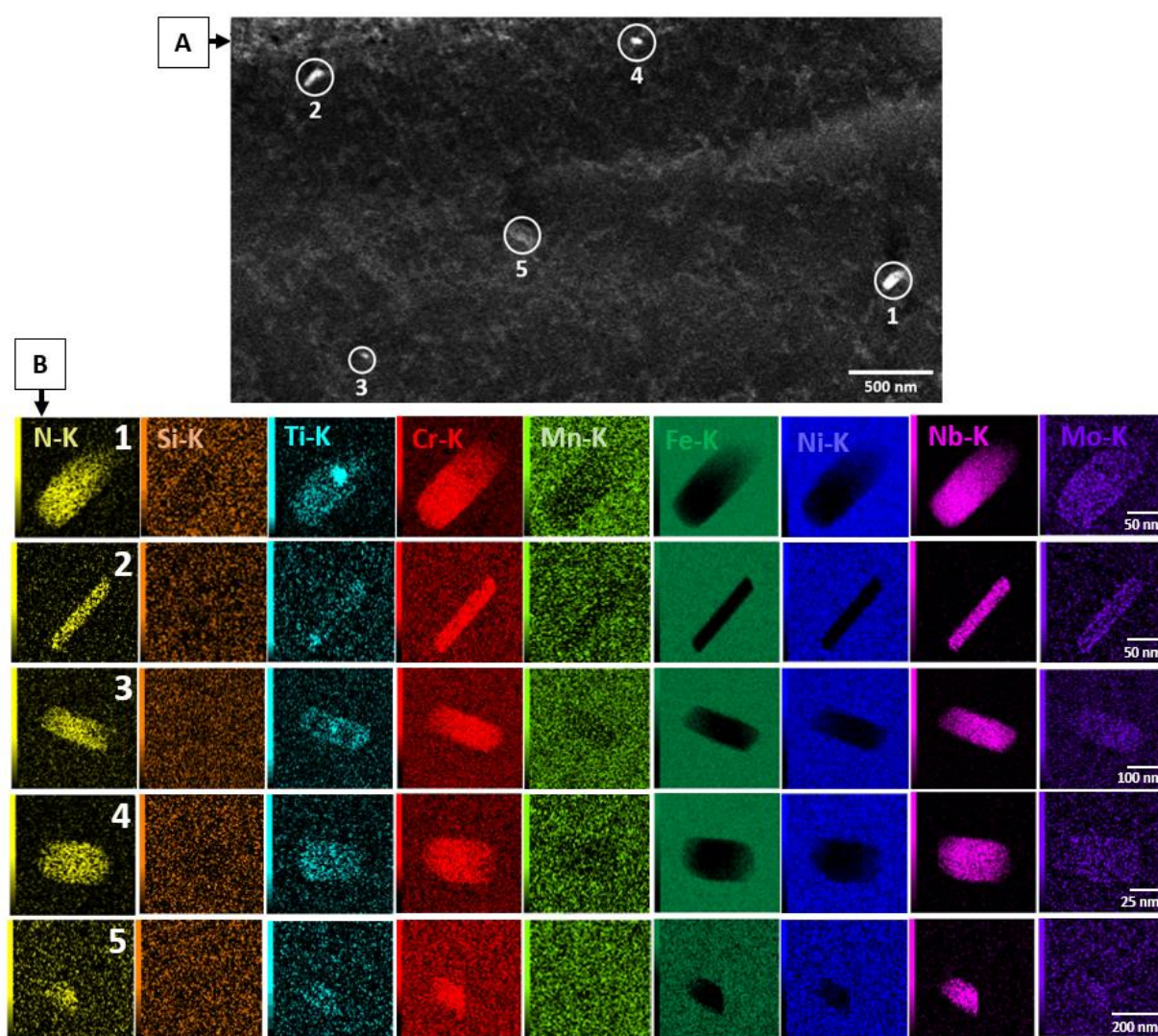


Figure 102 – A) STEM HAADF image revealing the presence of high Z precipitates in bright. B) STEM-EDS maps of the precipitates circled in A).

Two line profiles were drawn at different mapping locations (Figure 103. B)), a curve smoothing was applied by moving average while error bars were calculated from a moving standard error.

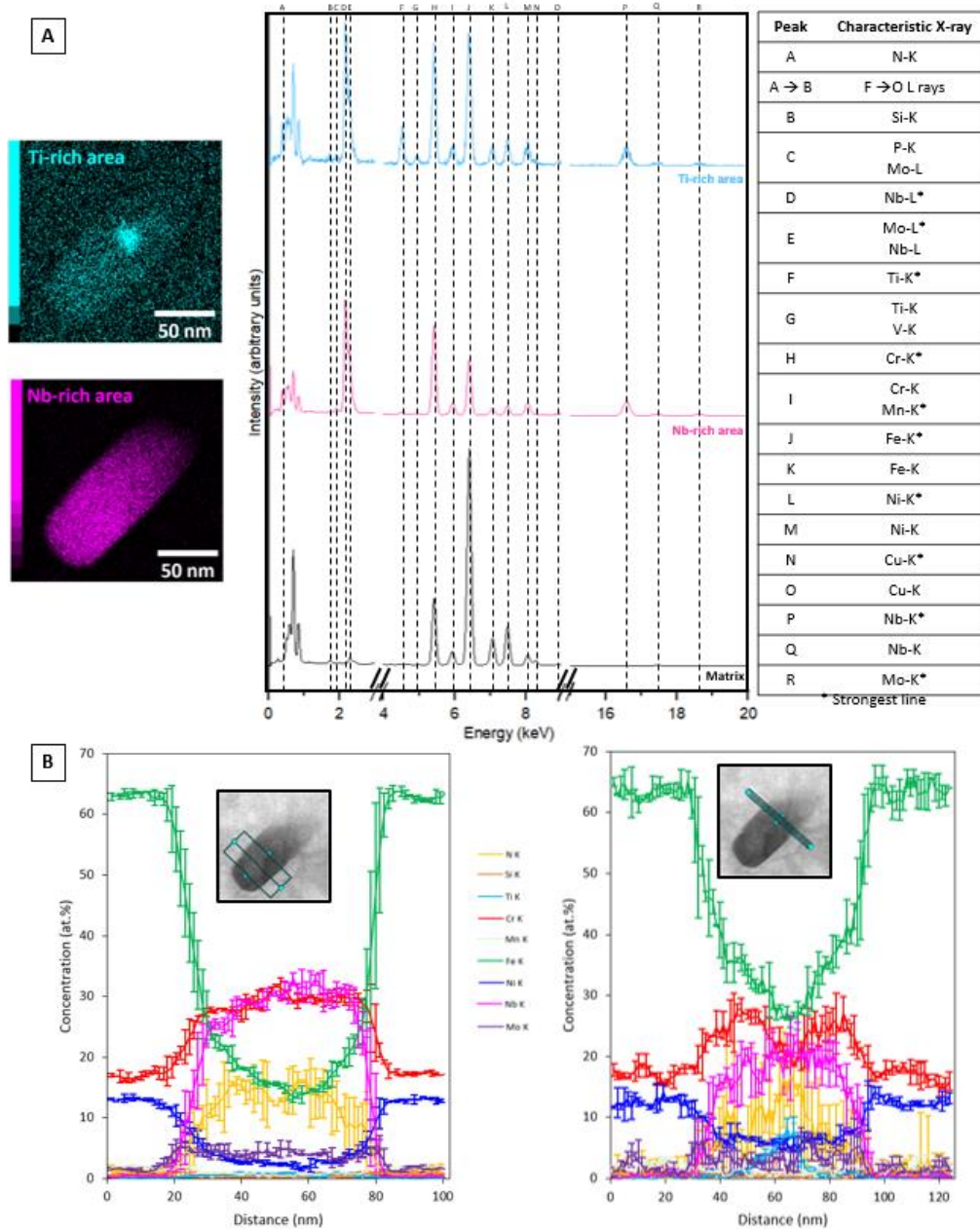


Figure 103 – A) Comparison of EDS spectra extracted from the matrix, Ni-rich and Ti-rich areas and the corresponding peak indexation of the EDS maps #1 (Figure 102). B) Line profiles drawn along the precipitates.

For elements rays chosen for quantification for which uncertainty is higher because of peak superimposition (N-K) or internal fluorescence peak of Si (from the dead layer of the detector even if this effect should be small for SDDs detectors), error bars corresponds to two standard deviations. Concentration profiles were not corrected from absorption. Thus N contents is underestimated in the precipitates. From the analyses of these line profiles, it can be noted that Nb and Cr contents in Nb-rich precipitate are at similar levels. N amount is considerably high as well. Mo level is also noticeable in this precipitate. In the case of Ti-rich precipitate, it seems to be enriched also in N. In order to roughly estimate the composition of each phase, knowing lamella thickness, matrix contribution was removed from the measured composition of the precipitates. As precipitates thickness is not known, mutual weights of the matrix and the Nb-rich precipitate in the measured

composition was determined in order to obtain a Ni content in the precipitate approaching zero. By doing so, obtained matrix fraction over the thickness is equal to 0.16. From the first line profile, Nb-rich precipitate composition was estimated. For the line profile crossing both precipitates, as the mutual weight of the different phases evolves depending on profile location, the ratio between the matrix and Nb-rich precipitate was first determined from the region free of Ti-rich precipitate based on the calculated composition of the Nb-rich precipitate from the first line profile. This ratio was kept constant while calculating Ti-rich precipitate composition (here Ti-rich precipitate is supposed to have a spherical shape). Considering all possible causes of errors (e.g thickness measurement, absorption, poor statistics, hypotheses on precipitates shape), results presented in Figure 104 are given with 50% relative uncertainty for the precipitates and 20% for the matrix.

Regarding the possible candidates for these two nitrides [30], Nb-rich precipitates can be Z-phase (CrNbN) while Ti-rich one can be MX type (TiN).

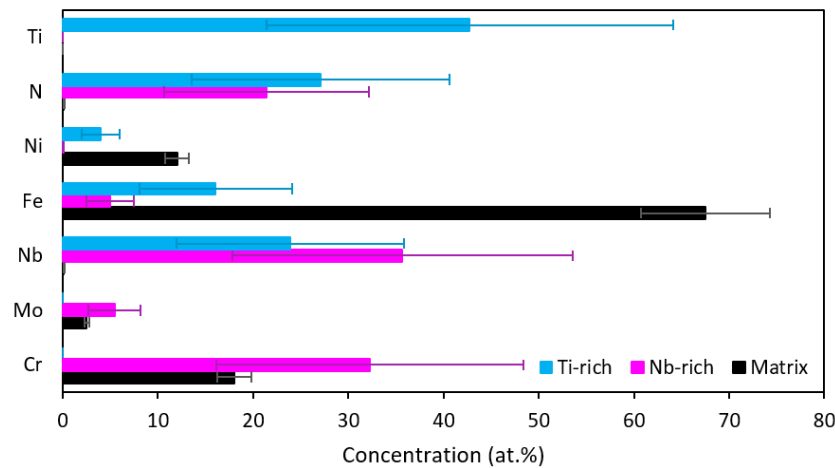


Figure 104 - Deduced composition of Ti-rich and Nb-rich precipitates from matrix composition and thickness measurement

Primary Z-phase, about 100 nm in size, has already been detected in a 316LN+Nb after solution annealing at 1050°C [247]. The investigated steel has the following composition in wt.% (studied 316L(N) one is given for comparison between brackets): C 0.023 (0.021), N 0.161 (0.1), Mn 1.34 (1.71), Si 0.48 (0.42), Cr 18.1 (17.7), Ni 12.5 (12.6), Mo 2.82 (2.46), B 0.0012 (0.0019), Nb 0.106 (0.09) and Fe in balance. Composition of the primary Z-phase has been measured in another 316LN+Nb with [N]=0.161 wt.% and [Nb]=0.106 wt.% [248] and is given as follows in wt.%: [Cr]=26.2±0.6, [Fe]=7.8±0.4, [Nb]=60.9±0.7 and [Mo]=5.1±0.5. These measurements are consistent with our observations. Even though presence of Z-phase is highly suspected (see its characteristics in CHAPTER 1), extra investigations of precipitates crystallography via electron diffraction should be performed to confirm this result.

This section aimed to characterise the as-received state of solution annealed 316L(N) selected for further RIS studies. At the micron scale, an average grain size of 50 μm have been measured and EBSD did not revealed any particular crystallographic texture. Warm rolling produced ribbons of residual δ-ferrite and microsegregations parallel to the rolling direction. These chemical heterogeneities are enriched in ferrite stabilizers elements and Mn. Majority of micron-size particles

are aluminium oxides inclusions, some Nb-rich precipitates were also found at this scale. Nb-rich precipitates of about tenth of nm were also observed at the nanoscale. They are suspected to be Z-phase. They sometimes seem to grow from MX precipitates (TiN) during the steel elaboration process. Dislocation density is in the order of 10^{14} m^{-2} , which is higher than solution annealed 316/L grades but it was found to be close to what was observed in another nitrogen stabilized 316LN. Finally, even if chemical heterogeneities of the matrix were revealed at the micron scale, APT results shown that elements distribution within the matrix is homogeneous at the nanoscale. As-received study is fundamental for further interpretations of microstructural evolution under irradiation.

III. Irradiation conditions

In France, JANNuS-Saclay and JANNuS-Orsay form the multi-ion beam irradiation platform JANNuS (Joint Accelerators for Nanosciences and Nuclear Simulation [249]). Two irradiation campaigns were run at both facilities. All samples analysed consisted in 3 mm diameter disks mechanically polished to OP-S down to a thickness ranging from 120 μm (Saclay) to 250 μm (Orsay) depending on the sample-holder used. Both samples and sample-holders have been plasma-cleaned prior to irradiations to reduce risk of carbon contamination.

1. JANNuS Orsay

First irradiation was run in the implantation beam line connected to the 2 MV Tandem/Van de Graff ARAMIS (Accelerator for Research in Astrophysics, Microanalysis and Implantation in Solids) accelerator [250]. ARAMIS is part of JANNuS-SCALP (Synthesis and Characterization using ion Accelerators for Pluridisciplinary research) platform [251] of the CSNSM lab in Orsay.

Irradiation conditions (Figure 105) have been selected to maximize defect density (i.e. high dose rate and low temperature) and RIS levels (i.e. low dose rate and high temperature) close to SFR GENIV operating temperatures and under the beam time constrain of 6h of irradiation maximum. 1 dpa damaged dose have been fixed for comparison with the work of A. Volgin [55]. The highest achievable beam energy with Fe^{3+} ions was 5 MeV, corresponding to an implantation peak depth at 1.5 μm as calculated using SRIM software. Calculations were made according to Stoller recommendations [252]: Kinchin–Pease model with the selected option ‘Ion Distribution and Quick Calculation of Damage’. A displacement energy of 40 eV was used in pure Fe. 1 dpa at a damage rate of $4.2 \times 10^{-5} \text{ dpa.s}^{-1}$ was reached in the region of interest: between 100 nm and 500 nm under the surface to limit surface effect (i.e. defect sink) and the implantation peak influence. Irradiation was conducted under a vacuum level below 5×10^{-6} mbar. The target temperature was 450°C but a large uncertainty on the irradiation temperature during irradiation experiment was observed. Indeed, almost 200°C difference were measured between the two installed thermocouples as shown in Figure 106. It seems to be likely due to a poor thermal contact between the two parts for the sample-holder.

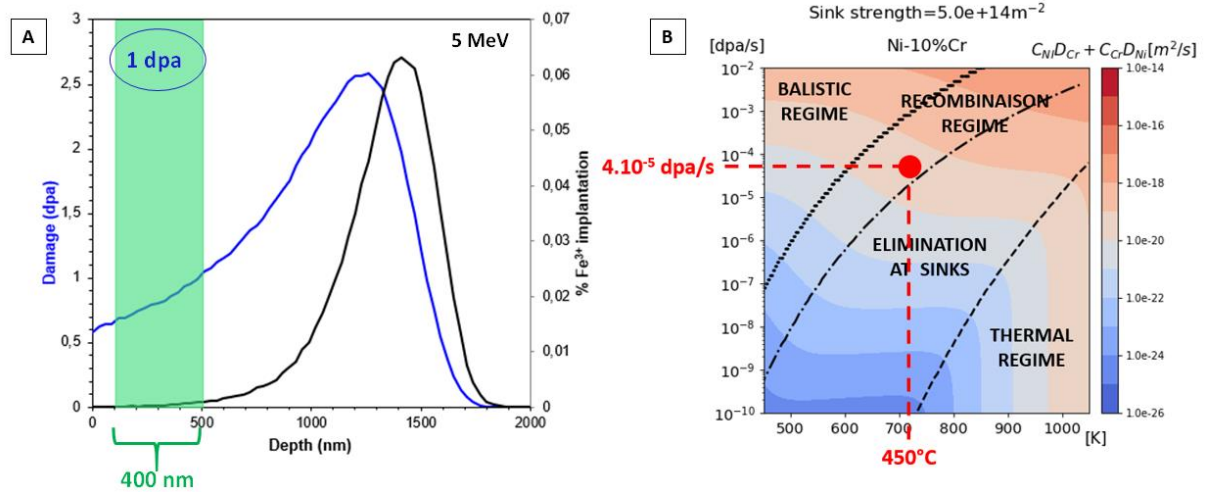


Figure 105 - Irradiation conditions selected for the 1st irradiation campaign with ARAMIS accelerator, A) Region of interest (ROI) depth and B) selected dose rate and temperature regarding the RIS regime (acknowledgements Liangzhao Huang).

As no thermocouple was installed at the vicinity of irradiated samples surface, decision was made to model heat transfers by conduction and radiation in the sample-holder assembly (not convection because the specimen chamber was under vacuum) on COMSOL Multiphysics commercial software in order to estimate the temperature at samples level. A heating block was installed under the angled block. At its bottom surface the temperature was imposed to be the one measured by the thermocouple T_A . Thermal properties (i.e. thermal conductivity, thermal capacity and emissivity coefficient) were defined at 450°C for 316/L grades while mechanical properties were defined at room temperature. A parametric study was done in order to find the coupled parameters (i.e. rugosity and contact pressure) for which temperature at the washer level is equal to 391°C as measured by the thermocouple T_B . When $T_A=593^\circ\text{C}$ is imposed and the set rugosity and contact pressure result in $T_B=391^\circ\text{C}$, the calculated temperature at samples level is equal to 450°C.

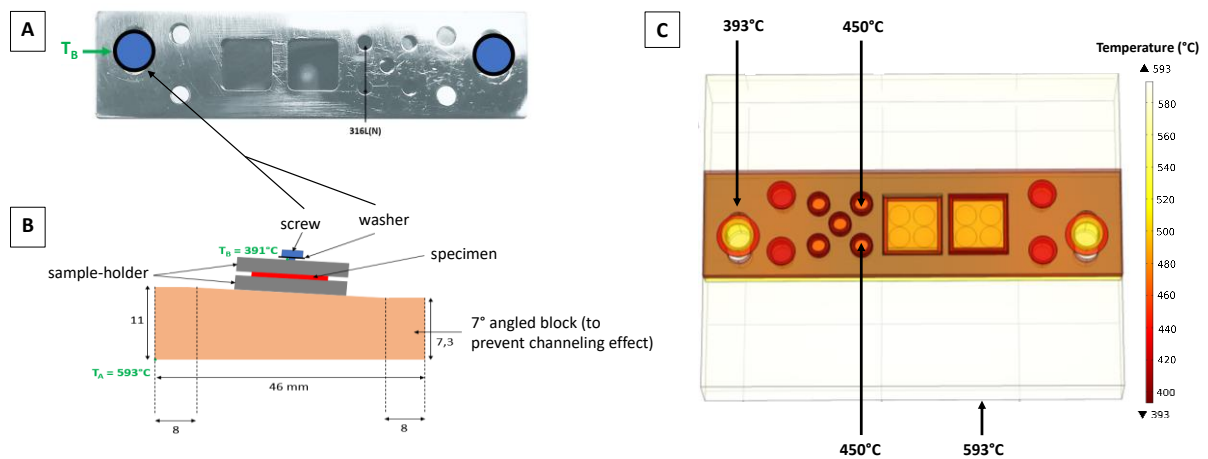


Figure 106 - A) GPM in-house sample holder for irradiation, location of 316L(N) specimens and the closest thermocouple T_B . B) Scheme of the sample holder assembly in the detector chamber and location of the thermocouples, note that all parts of the assembly (including samples) are made from austenitic stainless steels. C) Results from COMSOL heat transfer modelling. (Acknowledgements Brice Armel NJAKOU NGUENDO and Andrey MEDVEDEV)

Ion heating was not taken into account in the model but it can be calculated separately thanks to the following expression [253]:

$$\Delta T = \frac{2J}{k_T} \left(\frac{k_T t}{\rho C_T} \right)^{1/2} \quad (167)$$

Where the thermal conductance k_T is equal to $0.209 \text{ W.cm}^{-1}.\text{K}^{-1}$ [254] and the specific heat C_T is equal to $1.52 \text{ W.s.g}^{-1}.\text{K}^{-1}$ [255] at 450°C , the density ρ was taken to be equal to 7.96 g.cm^{-3} and t is the time in seconds. The beam power density J (in W.cm^{-2}) is given by :

$$J = \Phi \times E \times e \quad (168)$$

Here E is the beam energy in eV, e the elementary charge and Φ is the beam flux. To be able to reach a fluence of $3.2 \times 10^{15} \text{ ions.cm}^{-2}$ during a day session, $\Phi = 1.2 \times 10^{11} \text{ ions/cm}^2.\text{s}^{-1}$. From this calculation, an increase in temperature of 20°C is expected. We postulate that the temperature error is equal to this increase in temperature, therefore the irradiation temperature is estimated to be equal to $450 \pm 20^\circ\text{C}$.

2. JANNuS Saclay

The second irradiation campaign was run in the implantation beam line connected to the 3 MV single-ended electrostatic EPIMÉTHÉE accelerator of JANNuS-Saclay triple beam facility [256].

Irradiation conditions (Figure 107) have been selected to maximize defect density and RIS levels close to SFR GENIV operating temperatures and under the beam time constrain of 5h15min of irradiation maximum to reach 2.5 dpa for comparison with A. Volgin results [55]. The beam energy with Fe^{5+} ions was 10 MeV, corresponding to an implantation peak depth at $2.3 \mu\text{m}$ at a damage rate of $1.3 \times 10^{-4} \text{ dpa/s}$. 2.5 dpa was reached in the region of interest: between 400 nm and 1200 nm under the surface.

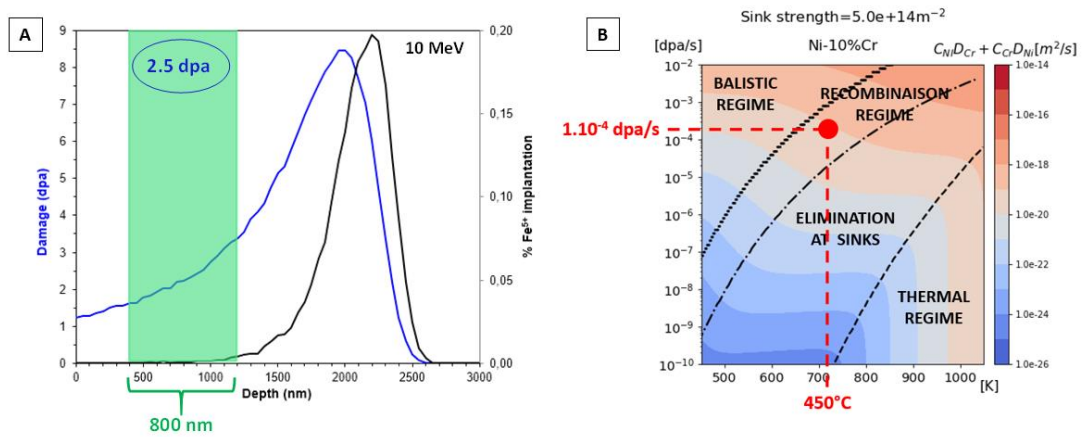


Figure 107 - Irradiation conditions selected for the 2nd irradiation campaign with EPIMÉTHÉE accelerator, A) Region of interest (ROI) depth and B) selected dose rate and temperature regarding the RIS regime (acknowledgements Liangzhao Huang).

Irradiation was conducted under a vacuum level below $1 \times 10^{-6} \text{ mbar}$ and the irradiation chamber was plasma-cleaned prior to run the experiment. The target temperature was 440°C and the

measured one, given as the mean value and the standard deviation calculated from the four installed thermocouples (Figure 108), was 436 ± 12 °C.

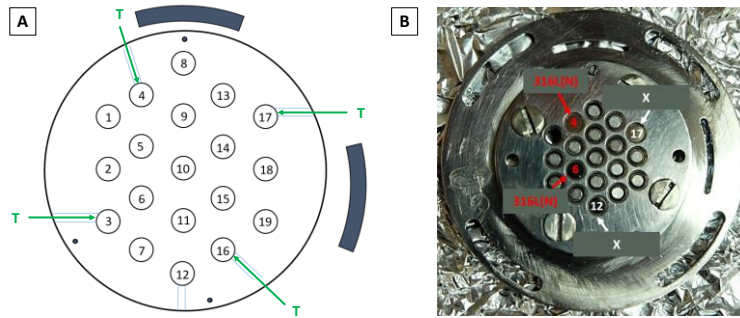


Figure 108 – A) Scheme of Saclay sample-holder with the position of the 4 thermocouples. B) Samples location on the sample-holder.

Solution annealed 316L(N) has been irradiated at 1 and 2.5 dpa at 450 and 440°C respectively. As the ion beam energy and the damage rates differ between irradiations, microstructure evolution under irradiation will be discussed independently for each dose.

IV. Nanoscale characterizations strategy

Two objectives need to be fulfilled. As the studied alloy is a 316L modified in composition, effect of N and Nb additions on microstructural evolution under irradiation should be discussed regarding the literature on standard austenitic stainless steel nuclear grades. To do so, conventional TEM analyses have been performed in order to quantify Frank loops and cavities number densities and sizes. Second, by identifying defects nature and quantifying RIS on each defect type, one should be able to give new keys of understanding about RIS mechanisms involved on different type of biased sinks: cavities are known to be biased for vacancies, interstitial Frank loops for SIA and, because void-precipitate association have been regularly observed under irradiation, it lets suggest that precipitates-matrix interface is also biased [257]. To do so, techniques coupling is a need, three approaches have been defined to this aim:

- 1st – S/TEM imaging associated with analytical STEM-EDS. (see CHAPTER 2)
- 2nd – APT coupled with field evaporation simulation [164,258].
- 3rd – TEM-APT correlative microscopy

Focus is done on the two methods applied for correlative microscopy in the next subsections.

1. Correlative microscopy on an APT tip

In order to access to defect crystallography, the APT tip should be imaged under specific diffraction conditions. To reach them, a double-tilt or a tilt-rotation TEM sample holder need to be used. Therefore, the tip must be mounted on a stand that fits in these TEM sample holders, it implies to prepare them by FIB. W TEM grids with pretips (i.e. pillars) were used because they are easy to manipulate when transferring prepared APT tip from an instrument to another. It also offers the possibility to mount several tips, up to five, on the same grid.

As Frank loops are the most observed defects for the chosen irradiation conditions, choice was made to select cross-section tip orientation close to zone axes $\langle 011 \rangle$ were TEM relrod dark field technique could be used to image the edge-on variants. By selecting the well-suited \mathbf{G} for bright field 2-beam and weak-beam dark field imaging, it is also possible to differentiate between perfect loops and Frank loops close to this zone axis (see CHAPTER 2). Prior to perform standard annular milling procedure to prepare tips with a focused Ga ion beam [156], a relatively large area was mapped by EBSD for grain orientation selection. A final tip cleaning at 2kV is done to reach the 1 and 2.5 regions of interest to reduce the damaged/Ga implanted layer thickness. By preselecting the tip orientation, the tilt angles needed to reach the diffraction conditions of interest are lowered reducing the dimensional bias of the tilted projected tip.

The correlative microscopy holder was fabricated based on the plans shared by M. Herbig from MPIE (Figure 109). It allows an easy-transfer of tips between three instruments: FIB for tip preparation, TEM for defect crystallography characterizations and APT for measurement of chemical heterogeneities at the atomic scale.

APT runs were performed in laser mode at relatively high temperature ($\sim 80\text{K}$) to diminish risk of tip fracture. If the analysis is successful and its end is not the fact of the specimen fracture, the tip is then imaged again by TEM to estimate the evaporated length.

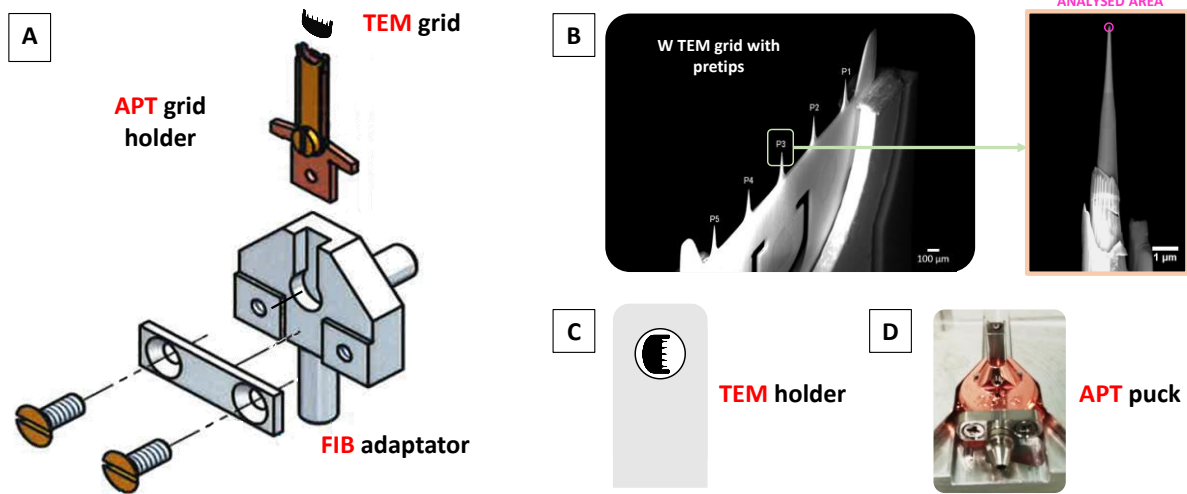


Figure 109 - A) Correlative microscopy holder reproduced from Herbig [108] B) SEM view of the W TEM grid with pretips mounted on the holder presented in A) and zoom on a prepared tip. C) TEM grid fits TEM holders (e.g. double-tilt or tilt-rotation) D) View of the APT grid holder on an APT puck.

2. Correlative microscopy on a tip extracted from a lamella

As it is shown in Figure 110, imaging a tip by TEM can make difficult contrast interpretation compared to images obtained from a lamella. Indeed, FIB damage remains at needle surface after the cleaning step (2kV) whereas a lower voltage ion cleaning with argon (0.5kV) in PIPS II is done on the case of TEM lamella. Also, the conical shape of the tip induces thickness variations along its diameter. An extra contrast due to thickness fringes in WBDF can be seen and HAADF images are more complex to interpret because contrast is not only due to Z but also to sample thickness. To solve these issues, several options can be tried. First, ion cleaning of the tip at a lower voltage

[259] can be performed to remove FIB damage. It has also the advantage to remove the oxide layer and carbon contamination after performing TEM and reduces tip breakage.

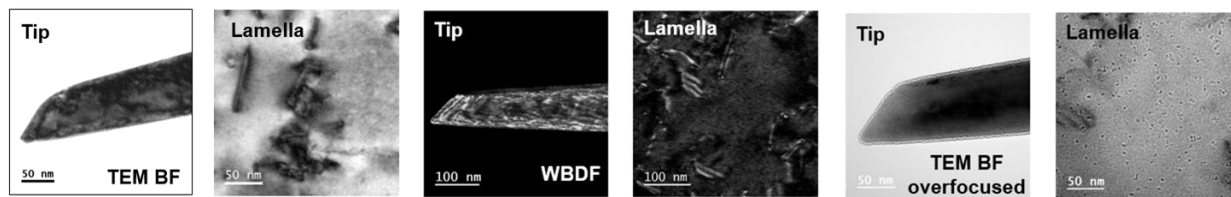


Figure 110 – Comparison of contrast obtained from a tip and a lamella for the same imaging conditions at the same scale for the 1 dpa 450°C irradiated state

Another possibility is to extract a tip from a pre-characterized zone on a TEM lamella. Thus, TEM characterisation benefits from advantages of working on a thin lamella. This was the retained choice. It also allows to extract the tip from a very confined region (e.g. to analyse defects with relatively low number density such as cavities in our case).

Strategies for targeted tip extraction have already been put in practice [260–262] but none of them simultaneously allow to select grain orientation, back-polish samples with the PIPS II and obtain the full irradiated depth within the lamella. A novel method is proposed.

The aim was to perform STEM-EDS on identified crystal defects and target tip apex extraction by FIB at their level. Then, direct comparison of segregation measurements from EDS and APT should be possible to correlate chemical heterogeneities with the defect nature. To be able to see defect contrast at 0° lamella orientation should be close to a low index zone axis, this justifies again the choice of the $\langle 011 \rangle$ zone axes. Then, it will be easier to associate chemical heterogeneities from EDS maps acquired at 0° to defect contrast observable at 0° close to $\langle 011 \rangle$.

First, grain orientation selection by EBSD is done (Figure 111.A), then the lamella is lifted-out and welded on a Mo grid. Because Cu grids can bend easily, this choice was made in the purpose of procedure development, even if peak superimposition of Mo-L and P-K rays worsens EDS analysis. This lamella is designed with three thin windows of the same thickness (Figure 111.B). This design has several benefits: ion polishing at low voltage to remove FIB damage with PIPS II is possible, the reinforced structure prevents from thinnest region bending because of internal stress relaxation and zones to characterize are well delimited. From each window, a tip can be extracted as shown in Figure 111.C), so several tips can be milled from a single lamella.

The needle is prepared by cutting the edges of the window up to obtain a tip with a square section (based on TEM thickness measurement). Then, only one step of annular milling is done with an internal diameter slightly larger than the diagonal of the square section. The ion beam tail will mill the square edges to obtain a circular section. The risk by directly performing annular milling without caring about sample thickness is to obtain a tip with an ellipsoidal section which is not optimum for APT analysis and lead to 3D reconstruction bias. For the last step of preparation, a cleaning is performed to reach approximately the depth of interest (where EDS has been performed). A fast check is done by TEM to determine with precision the amount of material to remove before redoing cleaning step to reach the region of interest.

Even if the lamella was plasma cleaned after EDS analysis, carbon contamination could not be removed. Neither 30s cleaning in the PIPS II at 0.5kV nor FIB cleaning at 2kV was able to remove the carbon cap (Figure 111.D)). Material redeposition during the window edges cutting step is also observed, this redeposition could be removed by a low-voltage cleaning with Ar^+ .

Plasma cleaning should be performed before and after TEM characterizations. PIPS II cleaning was apparently not sufficient to prevent C contamination. In order to reveal enrichments on small defects, where matrix contribution to the signal is high, EDS maps were acquired over long duration under high beam current and high magnification. It promotes the formation of a thick C layer at the specimen surface. Because diffusion of hydrocarbons at lamella's surface is a thermally activated process, cooling the sample down to cryogenic temperature during the experiment stops C contamination. Unfortunately, this sample holder is not well suited for EDS. Beam showering the region of interest of the sample in-situ with electrons is also advised after plasma cleaning [263].

If C contamination is unavoidable and cannot be removed, two other possibilities left: reduce sample thickness to reduce matrix contribution. This option is rejected because tip bends during FIB extraction if the lamella is too thin (<80 nm) in the case of the studied material. The other way is to degrade measurement statistics (lower the beam current and/or acquisition duration) and denoise the dataset thanks to a multivariate statistical analysis (MVSA). Principal component analysis (PCA) is a MVSA techniques that gets more and more popular to process EDS spectrum images. PCA reduces the number of variables of a large dataset necessary to describe it without losing the information of interest [264].

Finally, if only crystallographic information of the defects is sufficient, C contamination placed intentionally hundreds of nm above the target zone can help to track it in the FIB during tip preparation and will be removed during the cleaning step.

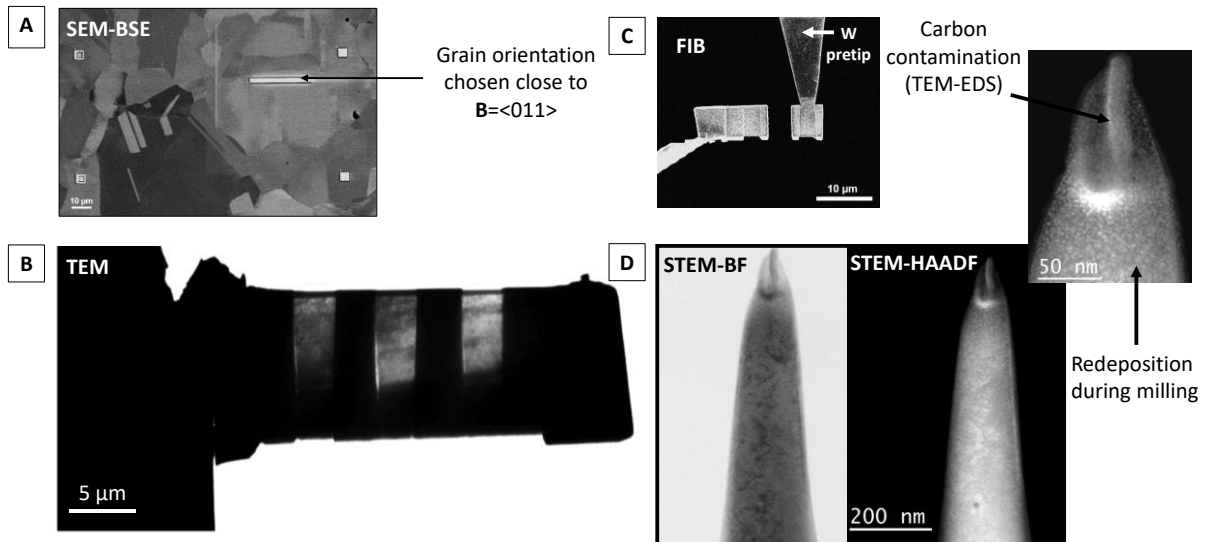


Figure 111 – A) SEM image showing the selected grain for lift-out with a cross-section orientation chosen close to $\mathbf{B}=\langle 011 \rangle$ thanks to EBSD. B) 3-window designed lamella for correlative microscopy. C) Within each window, after being characterized by TEM, a tip is milled by FIB. D) STEM images of the tip after

FIB milling showing material redeposition during preparation. Carbon contamination at the tip apex comes from an EDS map done on the former lamella window.

V. Post-irradiations characterizations

On one hand, cavities and Frank loop populations have been characterized by TEM in the optimized 316L to evaluate microstructure evolution under irradiation at 1 and 2.5 dpa. On the other hand, coupled/correlative techniques, i.e. STEM-EDS, S/TEM-APT and APT-simulation, have been used to link the measured chemical heterogeneities to the observed defects. Each damage state is treated separately in the following sub-sections.

1. 1 dpa 450°C

1.1. Cavities and Frank loops

As it was mentioned before, the first aim of this work was to observe and quantify the microstructure evolution under irradiation of the solution annealed 316L(N). Cavities and Frank loops populations were studied in the region of interest, irradiated to 1 dpa as defined in Figure 112. It is worth to remark that the damaged depth fits with SRIM calculations (Figure 105). As the lamella is oriented near $[01\bar{1}]$ zone axis (defined as **B**) the large majority of defects are visible, even at 0° of tilt (and/or rotation).

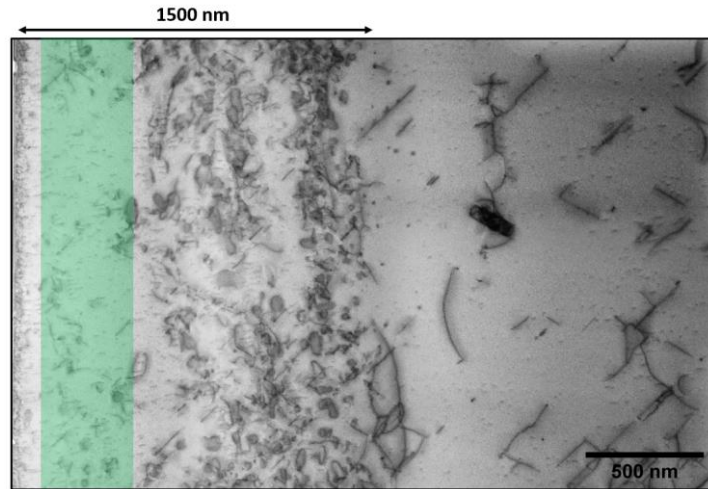


Figure 112 – STEM BF at 0° **B**~ $[01\bar{1}]$ indicating damaged depth, green area corresponds to the 1 dpa ROI

In order to identify cavities, lamella was first tilted away from the zone axis. Then, out-of-focus imaging at $\pm 2 \mu\text{m}$ was performed for identification and counting (Figure 113). Two populations of cavities, distinguished by their size and number densities, coexist. Small cavities are heterogeneously distributed and tend to gather at particular dislocation lines and seem to grow on them. As dislocations are known to be SIA-biased, it yields to a local supersaturation of vacancies at their vicinity and form voids [265].

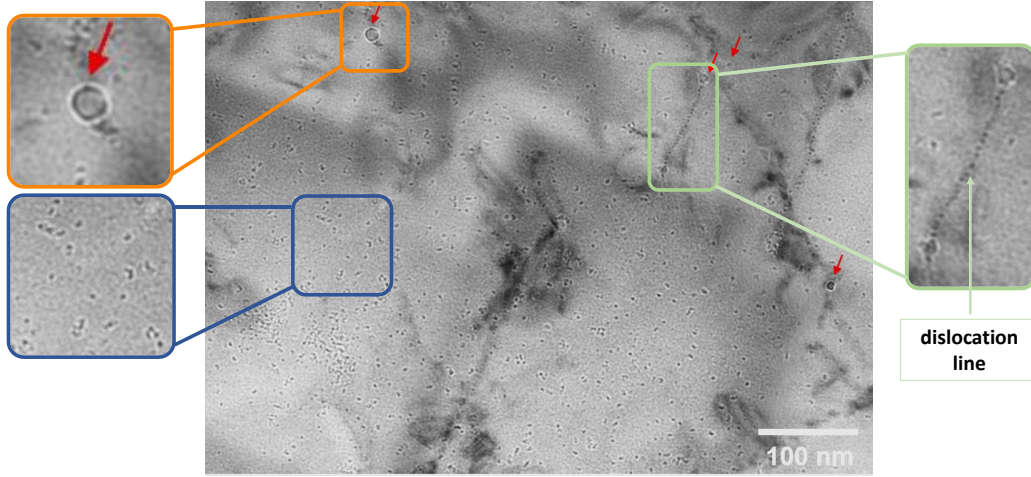


Figure 113 - TEM BF overfocus (+ 2 μm) image showing cavities bimodal distribution in size. Red arrows indicate large cavities as enlarged in the orange box. Small cavities (blue box) sometimes trap dislocations (green box).

As highlighted in CHAPTER 2, large defocus can bias cavities size measurement, especially for the smallest, therefore standard error is multiplied by two for small cavities.

To check error on size measurement for large cavities, comparison was made between grey levels profiles with a focused image of the same cavity (Figure 114.A)). If measurements are done between two minima of intensity, the error is minimized. Therefore, all cavities have been measured this way. Results of the quantification is shown in Figure 114.B). As bias on size measurement is higher for small cavities, they are, at least, in average, three times smaller than the biggest ones and their number density differ by two orders of magnitude.

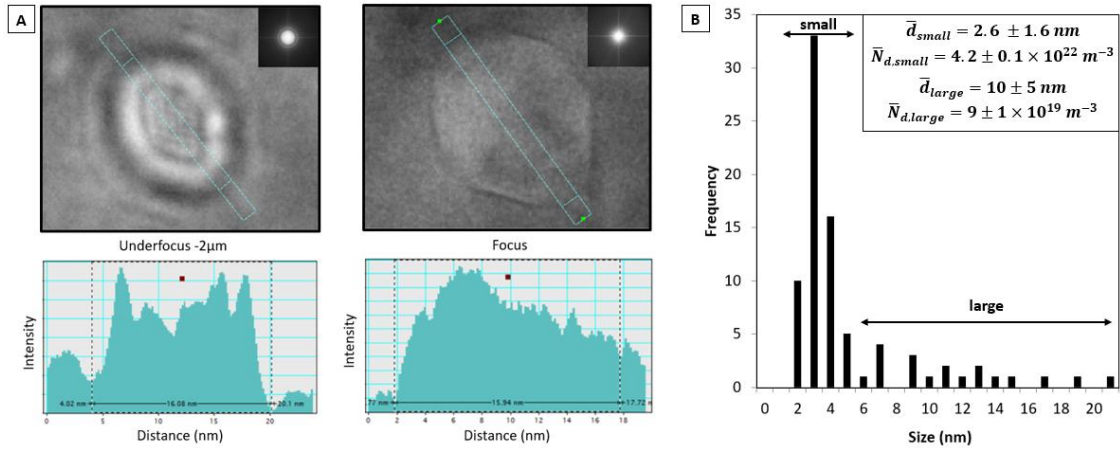


Figure 114 – A) Cavities size measurement definition. B) Cavities size distribution, mean size and mean number density for small and large populations. The frequency corresponds to the number of cavities per size range.

Frank loops were revealed by the relrod dark field (RRDF) technique, two families over the four existing were imaged (Figure 115). Counting was performed thanks to ImageJ software on binarized images. To remove from quantification spurious background noise, Frank loops were analysed as ellipsoids with a circularity factor ranging from 0 to 0.8 (1 being a perfect circular shape), then analysed particles having a tilt angle outside the range of $\pm 15^\circ$ of the measured mean tilt angle

were excluded from the calculation. Frank loop size corresponds to the major axis length of the ellipsoid.

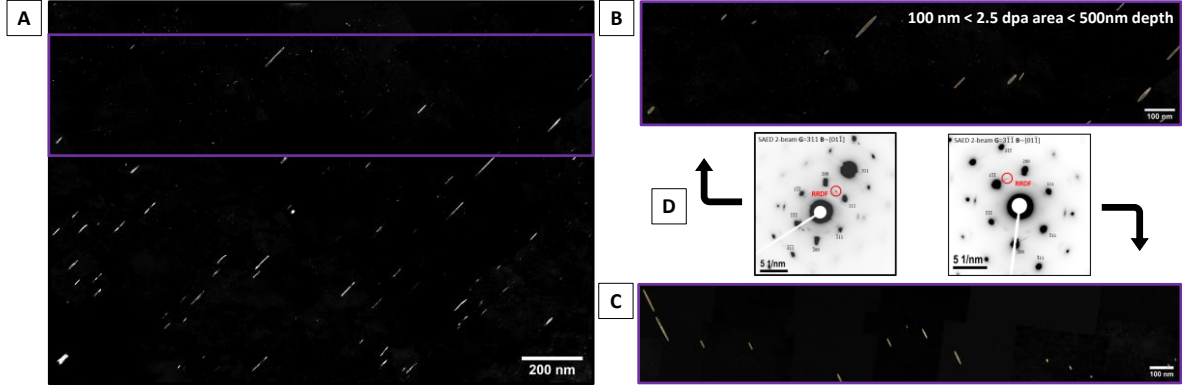


Figure 115 – Frank loops lying on A) and B) $(\bar{1}11)$ and C) $(\bar{1}\bar{1}\bar{1})$ planes imaged thanks to the relrod dark field imaging technique (RRDF), D) corresponding diffraction conditions. Measurement is done within the 1 dpa ROI for the two variants.

Results of the size measurement is summed up in Figure 116. Number density was obtained by multiplying by four the total number of measured Frank loops per area for one family. Calculation was done for both, then averaged.

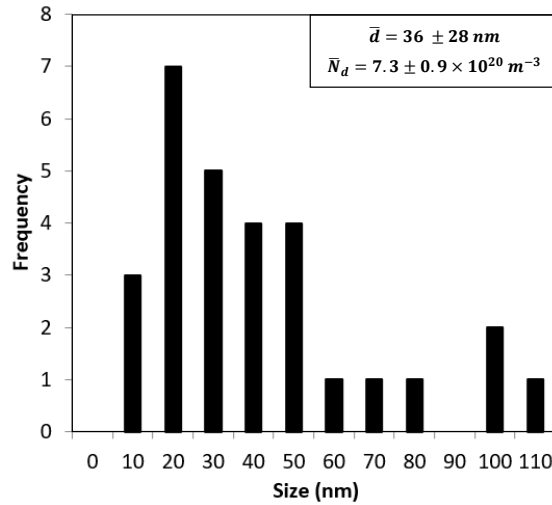


Figure 116 – Frank loops size distribution, mean size and mean number density. The frequency corresponds to the number of cavities per size range.

1.2. Precipitation and RIS

Coupled S/TEM imaging with STEM-EDS mapping was first performed to identify local chemical heterogeneities at the vicinity of identified crystal defects (Figure 117 and Figure 118). Prior to chemical analysis, 1 dpa damaged area was imaged under various techniques and diffraction conditions. Cavities were revealed thanks to out-of-focus TEM imaging, the two edge-on variants of Frank loops at $\mathbf{B}=[01\bar{1}]$ were spotted thanks to the RRDF technique and dislocation analysis was done to distinguish between the two other Frank loop variants and perfect loops. At $\mathbf{G}=\{200\}$ near $\mathbf{B}=\langle 011 \rangle$ in TEM BF 2-beam or $\mathbf{G}/n\mathbf{G}$ weak-beam conditions, oscillatory contrast of stacking faults on Frank loops permit to distinguish between perfect and faulted loops easily and

unambiguously. It is valid for relatively large loops. For smaller loops, invisibility criterion should be preferred for the identification. As it was summed up in Table 14 of CHAPTER 2, near $\mathbf{B}=\langle 011 \rangle$, at $\mathbf{G}=\{200\}$, all faulted loops and 2/3 of perfect loops are visible. On the contrary, near the same zone axis at $\mathbf{G}=\{220\}$, except the ones with their Burgers vector parallel to the electron beam direction (i.e. parallel to the studied zone axis), all perfect loops are visible and at this \mathbf{G} only edge-on Frank loops are visible. In other words, if a loop is visible at $\mathbf{G}=\{200\}$ and invisible at $\mathbf{G}=\{220\}$, this loop is a Frank loop. If a loop is invisible at $\mathbf{G}=\{200\}$ and visible at $\mathbf{G}=\{220\}$, this loop is a perfect loop. If a loop is visible at these two \mathbf{G} , this loop can be either a Frank loop viewed edge-on (can be checked by the complementary RRDF technique) or a perfect loop. Finally, if a loop is invisible at these two \mathbf{G} , this loop is a perfect loop with its Burgers vector parallel to the studied zone axis. Dislocation lines are distinguished from loops by their shape.

The damaged zone was mapped at a magnification sufficiently high to be able to identify the majority of defects inside the studied zone, then images were stitched together, scaled and rotated with the surface at the top of the image (corresponding diffraction patterns were rotated also). Inkscape and ImageJ softwares were used for image post-processing. As reconstructed maps can be compared and any defect can be easily tracked for all imaging conditions. This methodology is particularly useful for highly damaged microstructures.

Figure 117 presents crystal defect identification and associated EDS chemical analysis performed on an area containing a cavity, Frank loops and a perfect loop within the 1 dpa damaged region. From EDS elemental maps, Ni and Si enrichments are observed on all defect types. P enrichment is only observed at the cavity level. As shown in Figure 103, K ray of P is superimposed with one of the Mo L rays. As no Mo enrichment is observed at the cavity level from Mo EDS map reconstructed from Mo K ray, presence of P is confirmed. However, absence of P enrichment at other defects levels cannot be confirmed. Indeed, at the cavity location, the apparent specimen thickness is reduced, lowering at the same time matrix contribution in the detected signal. It is possible that P signal at dislocation levels is drowned in the background noise. Depletion of Cr, Mn and Mo is observed at the level of all defects. Fe exhibits a particular behaviour, i.e. it depletes at defects location and is enriched at its vicinity, resulting in a ‘M-shaped’ concentration profile at Frank loop and cavity location. This phenomenon has already been observed [266] and modelled [267] in Fe-Ni-Cr alloys at grain boundaries. It is explained by the competition of two driving forces: the concentration gradient of defects from bulk to sink first provoke Fe enrichment, then the chemical potential gradient created by segregation of elements at sinks induce a depletion of Fe. N, Ti and Nb maps are displayed because it had been shown from the as-received characterizations that suspected MX TiN type and Z-phase precipitates are present in the material. Their presence is not revealed here.

A moving average smoothing has been applied to the measured concentration profiles, error bars are calculated using a moving standard error. As Mo grid was used, Mo concentration is overestimated, P-K and Mo-L are superimposed and spurious Si signal coming from the detector can be collected. For these reasons, cited elements are given within two standard error. No

absorption correction was used for these profiles, results should be interpreted qualitatively especially for low energy rays selected for quantification (e.g. N-K).

Same procedure was performed on a second region as shown in Figure 118. Concentration profiles crossing a cavity and a Frank loop are reported, same enrichment and depletion tendencies are observed, except for Nb and N that enrich also at the cavity level. Frank loop is not viewed edge-on this time and it can be noted that RIS is only measured on the dislocation line encircling the stacking fault.

Coupling S/TEM imaging with STEM-EDS allows to associate different crystal defects to their respective RIS tendencies. However, two factors limit accurate RIS levels quantification:

- Defects are surrounded by the matrix. The matrix contributes to the signal and the smaller is the defect size to the lamella thickness ratio, the higher is the matrix contribution.
- Several defects can be superimposed within the depth and their respective 3D morphology is not known. Hypotheses (e.g. defect shape, defect position within sample thickness) should be made to extract RIS levels on a defect, increasing measurements uncertainty.

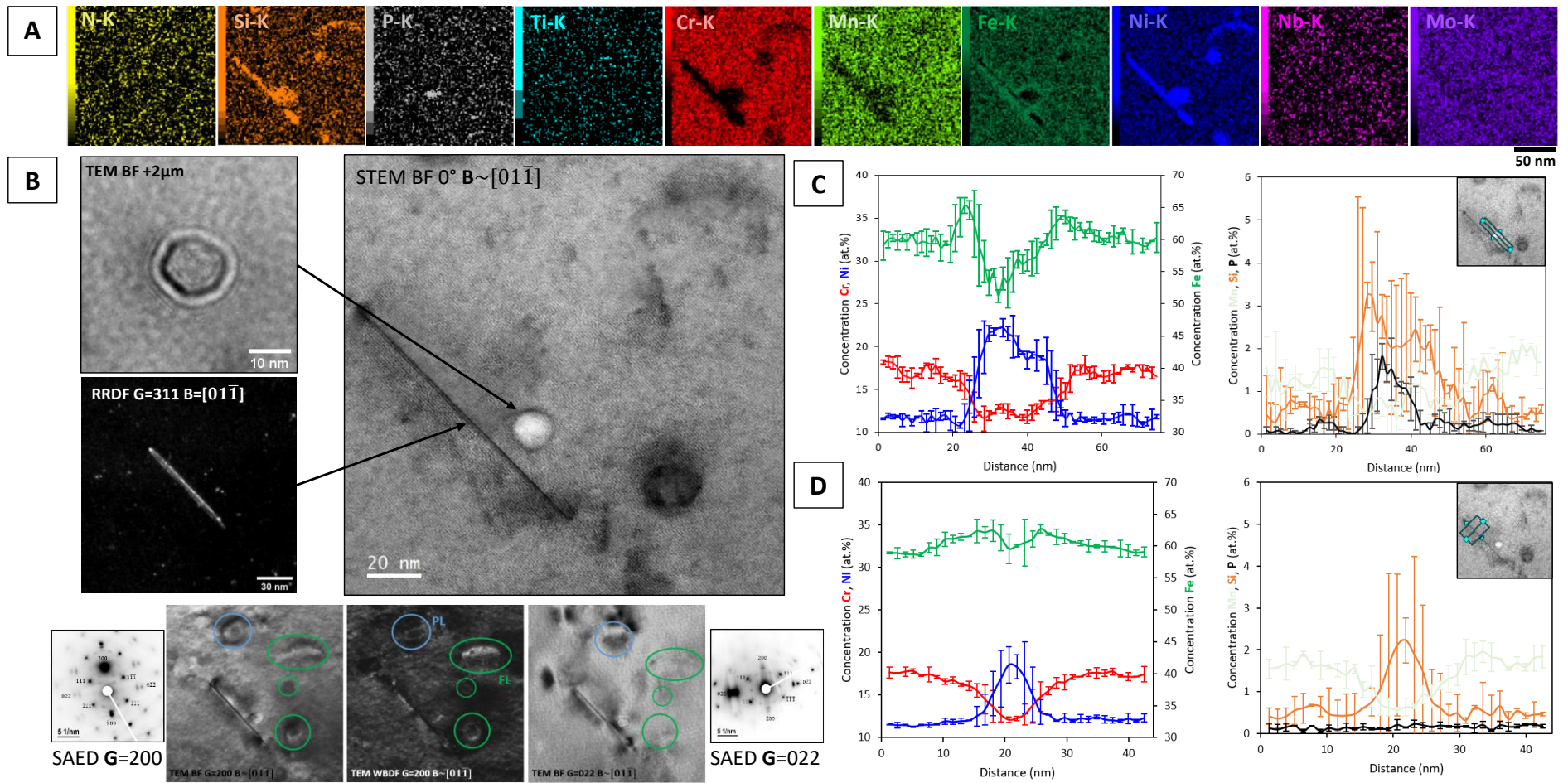


Figure 117 – A) STEM-EDS elemental maps corresponding to the selected region in B). B) also shows the defect nature determination thanks to various imaging techniques (TEM out-of-focus, relrold dark field, 2-beam bright filed and weak-beam dark field and the associated diffraction patterns). Concentration profiles extracted from two different locations of the STEM-EDS map passing through C) a cavity and D) a Frank loop.

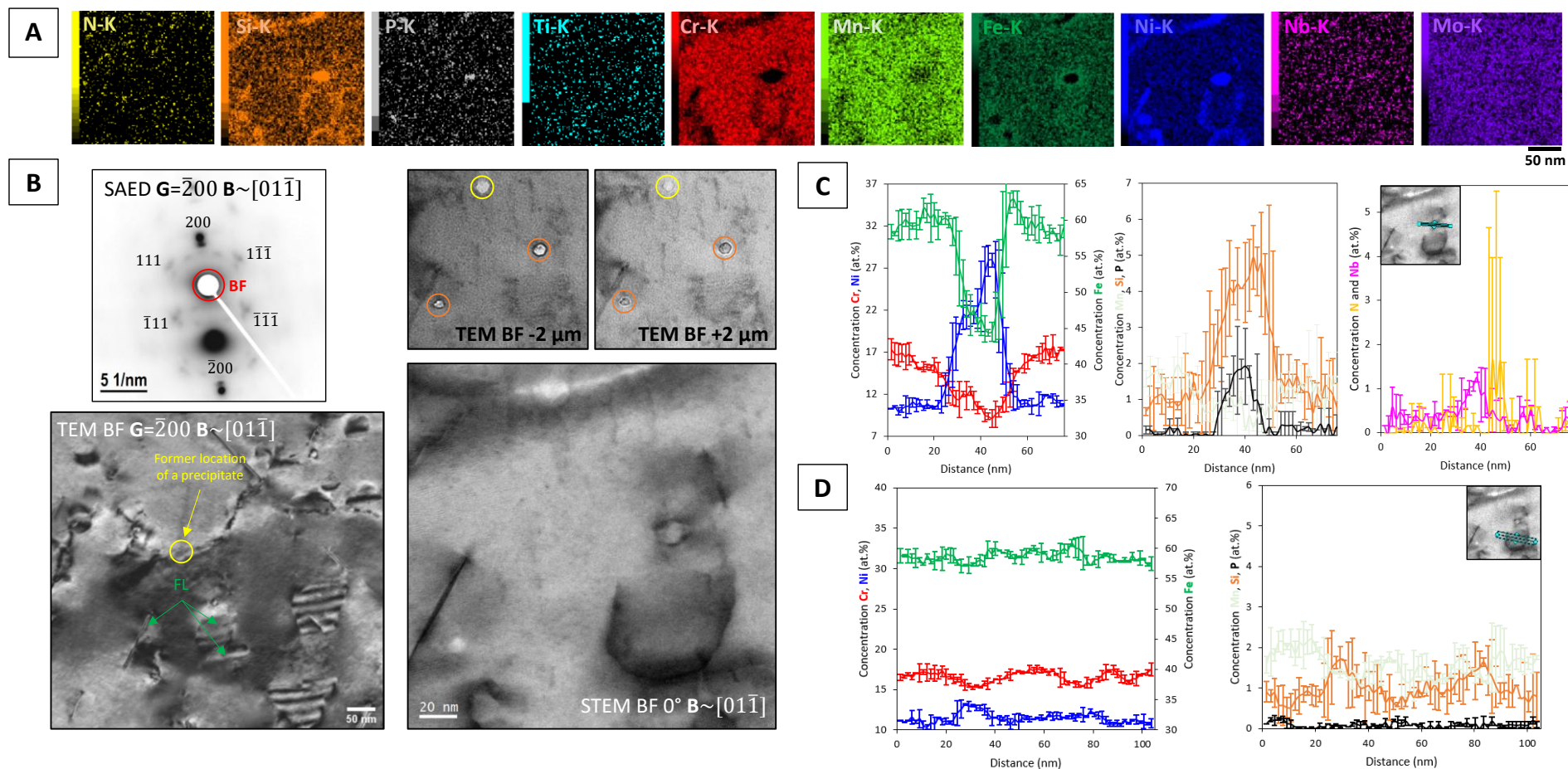


Figure 118 – A) A) STEM-EDS elemental maps corresponding to the selected region in B). B) also shows the defect nature determination thanks to various imaging techniques (TEM out-of-focus, 2-beam bright filed and the associated diffraction patterns). Concentration profiles extracted from two different locations of the STEM-EDS map passing through C) a cavity and D) a Frank loop.

Atom probe tomography gives access to a 3D representation of elemental distribution within the material. RIS levels could be quantitatively determined by this technique. Even if its high depth resolution can permit to see atomic planes at poles levels, lateral resolution is insufficient to identify precisely crystal defects, as it can be done with a TEM. Nevertheless, if poles are present and can be recognised, it is sometimes possible, for example, to associate defect orientation regarding crystallographic directions of identified poles.

APT-TEM correlative microscopy appears as a promising method to take benefit of both techniques to quantify RIS levels on identified defects. Results of the experiment run on a tip are shown in Figure 119, Figure 120 and Figure 122.

As shown in Figure 119, the tip has been characterized before and after APT analysis, permitting to accurately measure the evaporated length for APT reconstruction. An accurate reconstruction allows a reliable size measurement of the defects. Attempts of correlation between defects contained in the APT volume with the one observed on TEM images was done. As already shown in Figure 110, contrast of S/TEM images taken from a tip is difficult to interpret, especially because of FIB damage and tip conical shape. Furthermore, while in the APT volume only four defects are identified, much more are observed in STEM images. Several explanations can be given. First, RIS may not occur on all defects. Second, extra defects are brought because of FIB preparation. Third, APT field of view is limited. Thus defects visible in STEM can be out of the reconstructed volume. On the other hand, one of the features in the APT volume could not be associated with any defect of the tip imaged in STEM. As STEM images were taken at two different zone axes, it could not be explained by the invisibility criterion of dislocations. This point will be discussed in details hereafter.

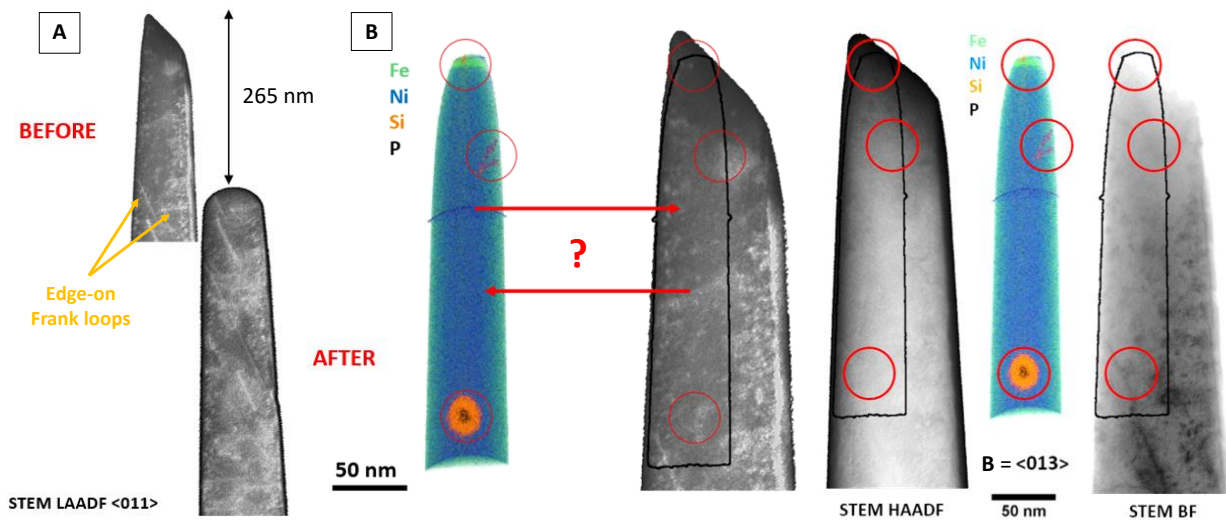


Figure 119 – A) STEM LAADF image of the tip before and after APT analysis taken at $B = \langle 011 \rangle$ B) Correlation between the reconstructed APT volume and the tip imaged in STEM $B = \langle 013 \rangle$ is not straightforward, several defects imaged in TEM are not present within the APT volume and the reverse is also true.

Figure 120 focuses on the two first features observed within the tip. The rod-shaped feature #1 is depleted in nickel. It could be recognised on the corresponding HRTEM image. Unfortunately, study of image fast Fourier transform (FFT) did not permit to identify its crystallographic nature. Feature #2 has the shape of a truncated dislocation loop enriched in Ni and Si, as can also be seen in Figure 119. By knowing edge-on Frank loops orientation it was possible to determine that feature #2 can be either a faulted Frank loop or a perfect loop with a $\{111\}$ habit plane.

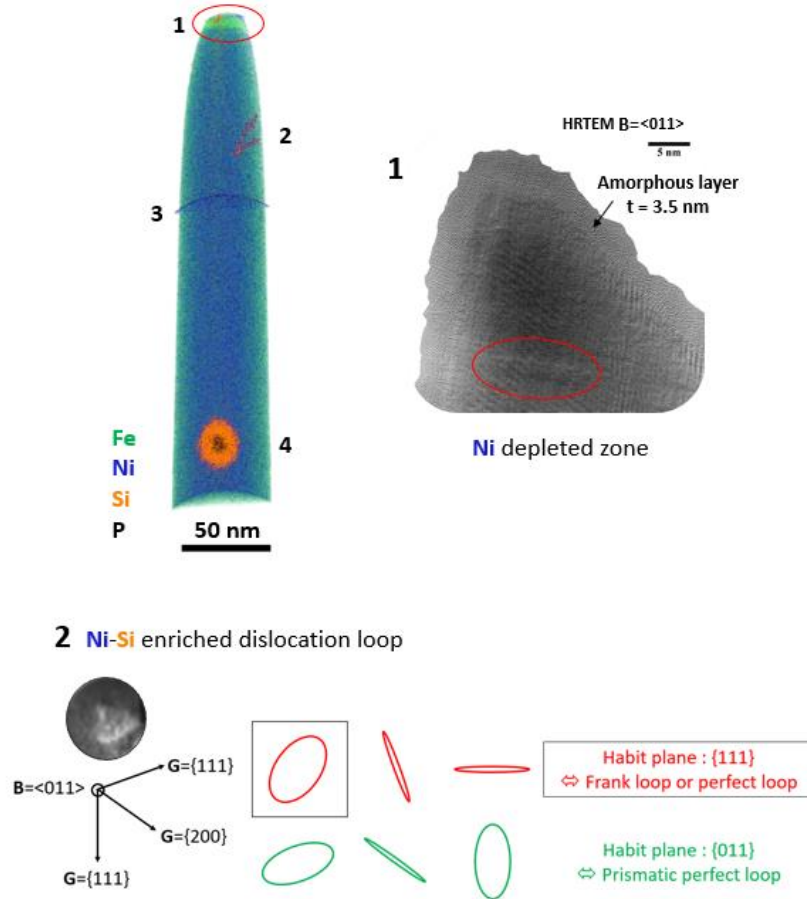


Figure 120 – Investigations on 2 over the 4 observed features. Feature #1: Ni depleted zone and the corresponding defect observed on HRTEM image. Feature #2: a dislocation loop enriched in Ni and Si. Zoom on STEM LAADF image at $\mathbf{B}=\langle 011 \rangle$ from Figure 119. Loop habit plane determination (Figure 32 of CHAPTER 2) for faulted and perfect loops at $\mathbf{B}=\langle 011 \rangle$ assuming that loops are circular. Based on Frank loops viewed edge-on directions and the tilt of the truncated loop, the loop lies on a $\{111\}$ habit plane. Feature #3: increase in voltage observed at the feature level.

Is feature #3 an artefact or a real defect? At its position in the reconstructed volume, an increase in voltage was observed during the experiment (Figure 121). In order to maintain a constant evaporation rate, an abrupt increase in voltage is the result of an increase in the field evaporation. Field evaporation can rise when a microfracture happen. A microfracture is the sudden removal of a relatively large amount of material from the sample surface (i.e. the tip diameter suddenly increases). Usually, after a microfracture, slope of the voltage curve is modified because of the diameter increase. It is not the case here.

An increase in voltage can also happen because the required field to evaporate atoms rises within the specimen at the level of a real defect. As explained in CHAPTER 2, a high-field defect leads to a biased reconstruction. A dilatation of the defect on the XY plane (Z axis being the tip axis) and an atomic underdensity are observed at the defect level. Assuming a constant atomic volume and a constant detector efficiency, reduced density is calculated as the ratio between the measured number of atoms and the mean number of atoms within the matrix. Its evolution close to the defect is plotted in Figure 120. Any reduction of density can be observed, but, the close-up view shows a depletion of Fe over a very small depth of 0.5 nm. As the $\{111\}$ planes are perpendicular to the tip axis (i.e. one variant of Frank loop is perpendicular to the tip axis), the interatomic distance between two planes is equal to 0.201 nm. It means that depletion occurs on 1 to 3 planes maximum. Regarding its shape, we can suppose that this feature may be a planar defect. Planar defects within the studied material could be either a grain boundary or a stacking fault. Frank loops are dislocation loops that encircle a stacking fault lying on a $\{111\}$ plane so it could also be the habit plane of a Frank loop. From STEM LAADF image taken at $\mathbf{B}=\langle 011 \rangle$ (Figure 119), we observe that one variant is perpendicular to the tip axis and it is clearly visible with this imaging condition. If this feature was a planar defect, a contrast could have been seen at its level in STEM images. Thanks to correlative microscopy, it is possible to exclude unambiguously defect hypothesis. While Fe and Cr deplete, all other elements enrich. At feature's level, background noise momentarily rises thus measured composition is not reliable. In laser mode, an abrupt increase in voltage can happen if the laser is not well focused on the tip apex to compensate the lack of thermal energy needed to keep the evaporation rate a constant.

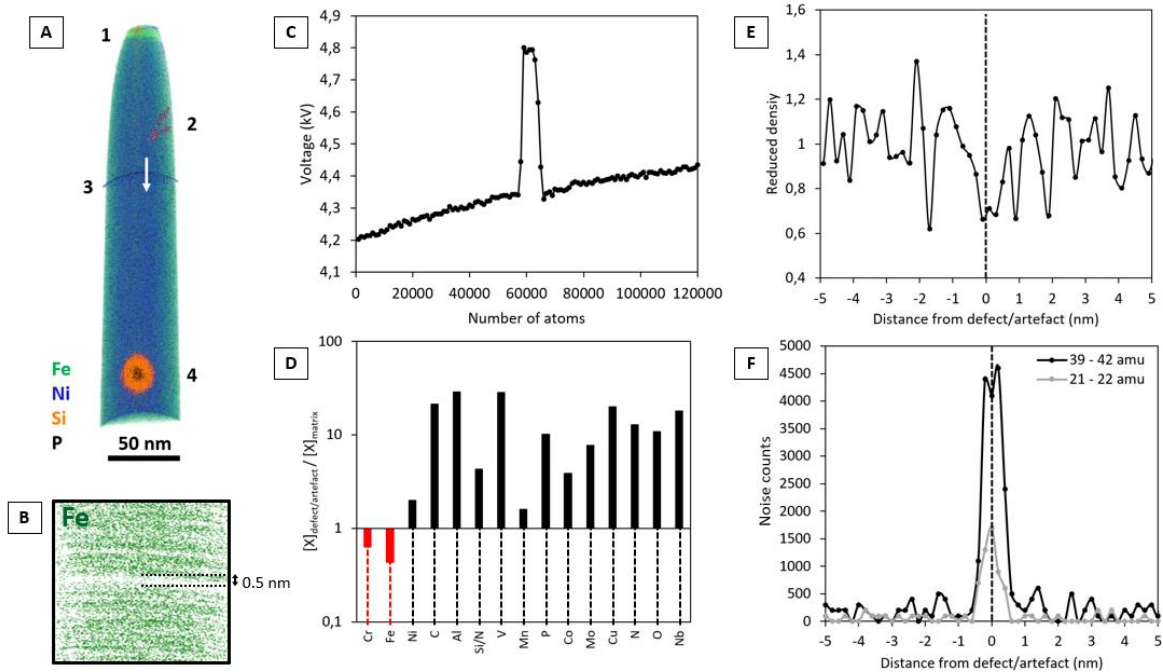


Figure 121 – Determination of feature #3 nature: A) Identified features within the APT volume. B) Close-up on feature #3 showing a Fe depleted zone. C) Increase in voltage at the feature level. D) Atomic concentration ratio between the feature and the matrix. Cr and Fe deplete while other elements artificially enrich. E) Reduced density and F) noise profiles along the tip axis (white arrow in A)). Noise counts have been extracted from two regions of the mass spectrum where no peak is observed at each step of the linear profile.

The feature #4 is presented in Figure 122. This cluster (i.e. local chemical heterogeneities with unidentified crystallographic structure) has a core-shell structure. In comparison to the matrix, its core is depleted in Fe and Cr and enriched in Nb, P, Mo and Si/N. As Ni, Nb and P contribute to the peak at 31 amu, peak was decomposed twice: first for Ni+P, second for Ni+Nb. The resulting two concentration profiles of Nb and P are displayed in Figure 122.C). $^{28}\text{Si}^{2+}$ and $^{14}\text{N}^{+}$ ions are superimposed in the peak at 14 amu. Because the two other isotopes of Si are close to the background level, decomposition of the peak at 14 amu was not performed. In order to reveal Si and/or N contribution at the core level, concentration profiles corresponding to isolated isotopes of Si is compared to the one obtained from the molecular ions $(\text{MoN})^{2+}$ and the peak at 14 amu. At the core level, calculated Si abundance in the peak at 14 amu is close to its natural abundance (89% instead of 92%). It permits to confirm the presence of Si at the core level while N could be absent.

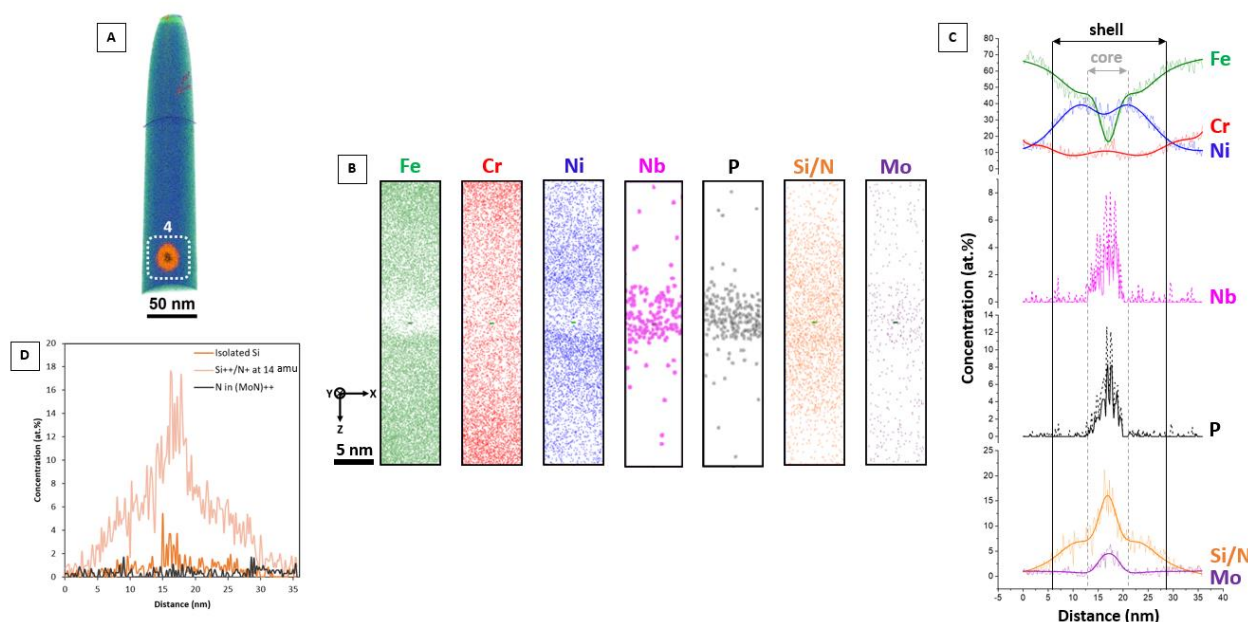


Figure 122 – A) Location of the feature #4 within the APT reconstructed volume. B) Sub-volume extracted from A) passing through the cluster with the z direction parallel to the smallest cluster core length. C) 1D concentration profiles calculated from B) and D) attempt to decorrelate Si and N relative contribution in their common peak at 14 amu.

In comparison to the matrix, the shell is enriched in Ni and Si while it is depleted in Fe, Mo and Cr. Mn concentration profile is very noisy, Mn RIS trend could not be determined and was removed from the graph for clarity. Finally, in comparison to the shell, core is enriched in Cr, Nb, P, Mo and Si. The highest Ni enrichment is observed at the core-shell interface. Cr, Nb and Mo enrichments call to mind the suspected Z-phase observed at the as-received state except for N while P, Ni and Si typically segregate on defects under irradiation in 316/L grades. From the literature, Z-phase stability under irradiation has not been studied yet. Could the cluster core be the primary Z phase modified under irradiation or is it a radiation induced phase?

To better understand how atoms evaporated at the cluster level, a mesoscopic field evaporation simulation was completed. Details about the model can be found in [164] and [258]. Insights about

cluster possible nature and its initial cluster shape are expected. The simulation aims to determine the cluster nature, and if the measured composition at the cluster core is biased. As a reminder, trajectories of evaporated ions can cross and bias composition in case of a low field particle. Based on simulated cluster core reduced density and cluster shape evolutions regarding the reduced field N defined as:

$$N = \frac{F_{core}}{F_{matrix}} \quad (169)$$

with F_{core} and F_{matrix} the field evaporation of the cluster core and the matrix respectively, it should be possible to determine:

- if the cluster core is a low ($N < 1$), equal ($N = 1$) or a high field ($N > 1$) particle \rightarrow composition bias?
- and find out cluster core real density \rightarrow cluster nature?

Model parametrization is based on experimental results. First, the reduced density profile is drawn across the Z_4 direction of the cluster frame (Figure 123.A) & B)). Reduced density of the shell is equal to 0.7 while at the core level it is equal to 0.3. Z-phase atomic density is equal to 88 at.nm⁻³ and the austenitic matrix atomic density is equal to 86 at.nm⁻³. So, the reduced density should approach 1, which is not consistent with the underdensity observed. If the cluster core is a precipitate with an atomic density 0.3 times lower than the matrix, thus the atomic density is equal to 26 at.nm⁻³ resulting in a mass density of 2.1 ± 0.3 g.cm⁻³ (based on the chemical composition measured in the cluster core). This low mass density is far to suit with these following equilibrium phases or phases encountered after irradiation in austenitic stainless steels: Fe₂P (6.9 g.cm⁻³), FeP (6.2 g.cm⁻³), gamma prime Ni₃Si (7.6 g.cm⁻³), G phase Mn₆Ni₁₆Si₇ (7.0 g.cm⁻³), Fe₂Mo (9.5 g.cm⁻³) and NbN (8.3 g.cm⁻³). Such reduced density was found on a cavity exhibiting RIS, but the shape of the reduced density profile does not match with the one obtained [157].

Second, cluster size measurement is performed by isolating cluster shell and core after applying a “concentration filter” (Figure 123.C) & D)). Iso-surfaces permit to represent regions within the APT volume having a minimal threshold concentration. Both shell and core have an ellipsoidal shape with $L_Z = 24.8$ nm and $L_X = L_Y = 21.6$ nm for the shell, $E_Z = 12.8$ nm and $E_X = E_Y = 5.3$ nm for the core. L_Z and E_Z are the longest lengths of the shell and the core respectively, parallel to Z_4 direction of the cluster frame, i.e. by opposition to the tip frame (X,Y,Z). To define cluster shape (i.e. shell and core), a shape factor S is introduced defined as:

$$S_{shell} = \frac{L_X \times L_Y}{L_Z \times L_Z} \quad S_{core} = \frac{E_X \times E_Y}{E_Z \times E_Z} \quad (170)$$

with $S=1$ in case of a spherical shape. Based on experimental results, $S_{shell}=0.8$ (i.e. nearly spherical) and $S_{core}=0.2$.

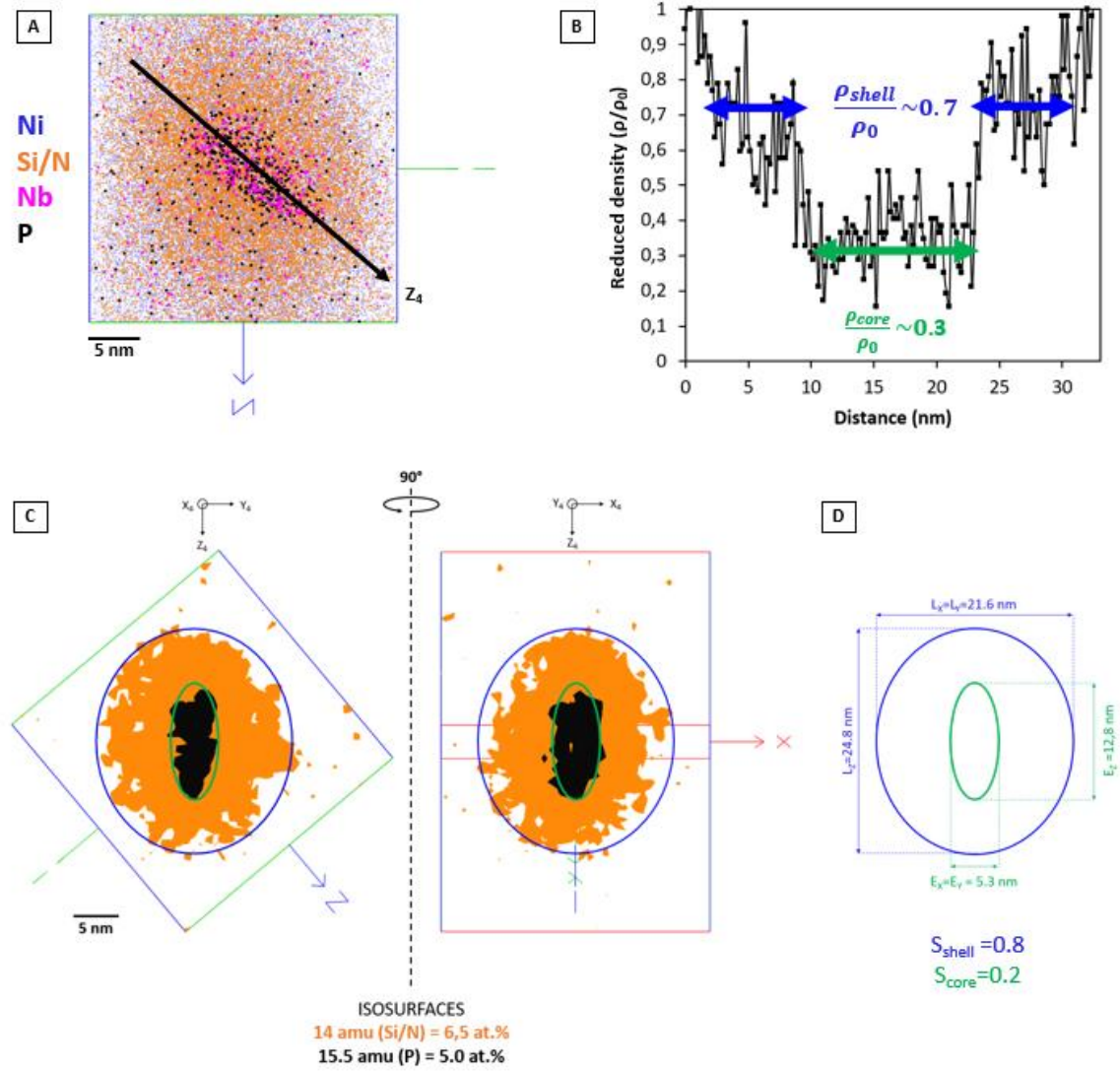


Figure 123 – A) APT subvolume containing the feature #4. B) Linear profile of the reduced density across the cluster drawn along Z_4 direction within the cluster frame (X_4, Y_4, Z_4). 1D profile extraction location is indicated by the black arrow in A). C) Cluster shell and core size measurement from isosurfaces representation. The minimal concentration threshold defined on Si/N (orange) and P (black) isolated peaks at 14 and 15.5 amu of the mass spectrum. Characteristic lengths and shape factors of the cluster shell and core are summarized in D).

Based on previous measurements, input parameters for simulation are defined Figure 124. The tip is defined by its curvature radius R_c , shank angle α and length. The length is not representative of the real tip and was reduced in order to save computation time. The cluster is surrounded by the matrix and cluster core is enclosed in the cluster shell defined as two different features with different evaporation fields, F_{core} and F_{shell} respectively. Before performing the simulation, the cluster shell and core are set to be spherical with a diameter equal to the longest length L_z and E_z as measured experimentally. As the shell density is approximately the same than the matrix, the shell evaporation field was set to be equal to the matrix one. In order to check if a difference in evaporation field between the core and the matrix induced a cluster distortion, the reduced evaporation field of the core is the simulation variable and was set to range between $0.8 < N < 1.2$.

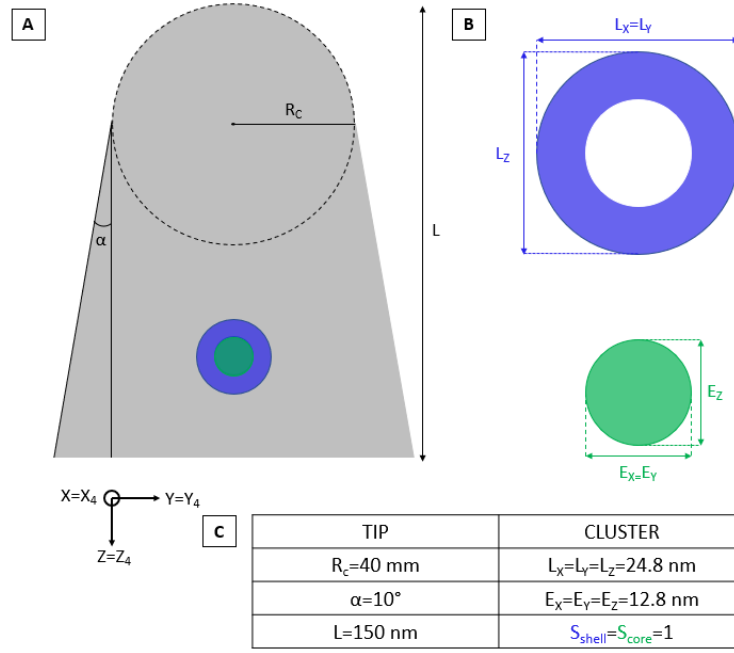


Figure 124 – Schematic representation of A) the simulated tip: in grey the matrix, in blue the cluster shell, in green the core. The tip length L , the curvature radius R_c and the shank angle α are indicated. Cluster characteristic lengths and C) Geometrical input parameters of the model.

At the end of the simulations, the core and shell shape factors S as well as the core reduced density ρ evolution are plotted against the reduced evaporation field of the core N (Figure 125) and compared to experimental ones (dashed arrows in Figure 125). The shell has a shape factor equal to 0.8 for $N=0.91$, while the core has a shape factor of 0.2 for $N=0.89$. These results seem to fit with a low field core (i.e. $N<1$). However, the core reduced density, equal to 0.3 for $N=1.21$, is consistent with a high field core.

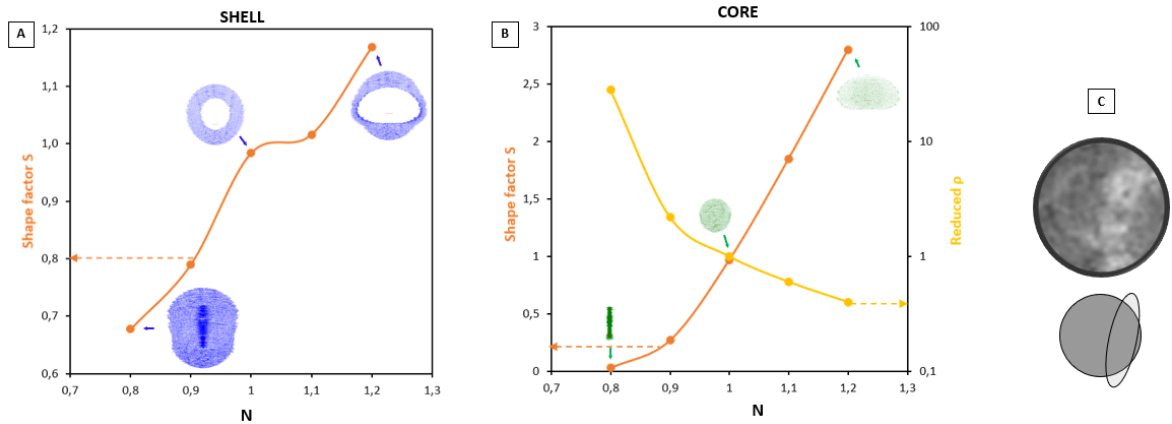


Figure 125 – A) Evolution of the shell morphology as a function of the reduced core evaporation field N . B) Evolution of the core reduced density and shape factor as a function of N . Pictures of the shape evolution of isolated shell and core depending on N (corresponding N is indicated by an arrow). Experimental values are indicated on the graphs by dotted arrows (Acknowledgments C. Hatzoglou). C) Close-up view of the feature #4 in the STEM LAADF image oriented at $\mathbf{B}=\langle 011 \rangle$ (Figure 119) and the scheme of the revealed defects.

The initial shape of the simulated core (i.e. spherical) does not match correctly with any of these three cases: low field, equal field or high field core. If the core has actually an ellipsoidal shape and

an equal evaporation field, it means that it should have an atomic density equal to 26 at.nm^{-3} . This value does not correspond to the ones of known phases precipitating after thermal ageing or under irradiation. It likely means that another feature could be included in this cluster. Figure 125.C) shows a close-up view of the cluster imaged by STEM. From the observed contrast, it is possible to guess that indeed two features seems to form the cluster. One of them is spherical, it could possibly be a cavity, the other one is ellipsoidal, and is assumed to be a precipitate associated with the cavity. Presence of a cavity within the cluster could explain such low value for reduced core density. RIS on the cavity could correspond to the cluster shell while the precipitate having a evaporation field close to the matrix has a ellipsoidal shape, then may have not suffer from any distortion. These assumptions need to be confirmed by extra simulations.

2. 2.5 dpa 440°C

A similar characterization procedure was performed for the 316L(N) irradiated to 2.5 dpa at 440°C. This time, correlative microscopy attempted to extract a tip from a pre-characterized TEM lamella.

2.1. Cavities and Frank loops

Measurements on cavities and Frank loops populations were done in the 2.5 dpa region ranging from 400 to 1200 nm depth (Figure 28). The total damaged depth corresponds to the one calculated with SRIM (Figure 107). Defects number density seems higher than for the previous irradiation conditions.

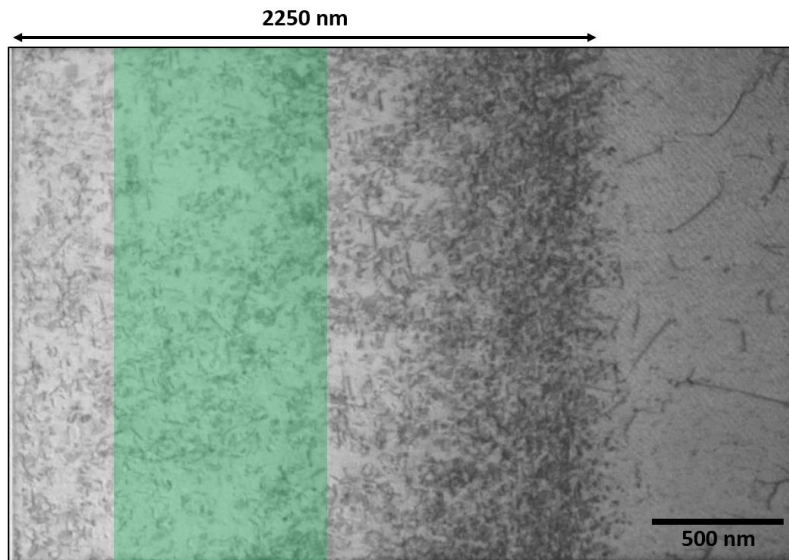


Figure 126 - STEM BF image at $0^\circ \mathbf{B} \sim [011]$. Damaged depth, green area corresponds to the 2.5 dpa ROI

This time, out-of-focus TEM imaging was completed for a defocus of $\pm 1 \mu\text{m}$ to reduce error in size measurement (Figure 127). Measurements were performed on underfocused TEM bright field images.

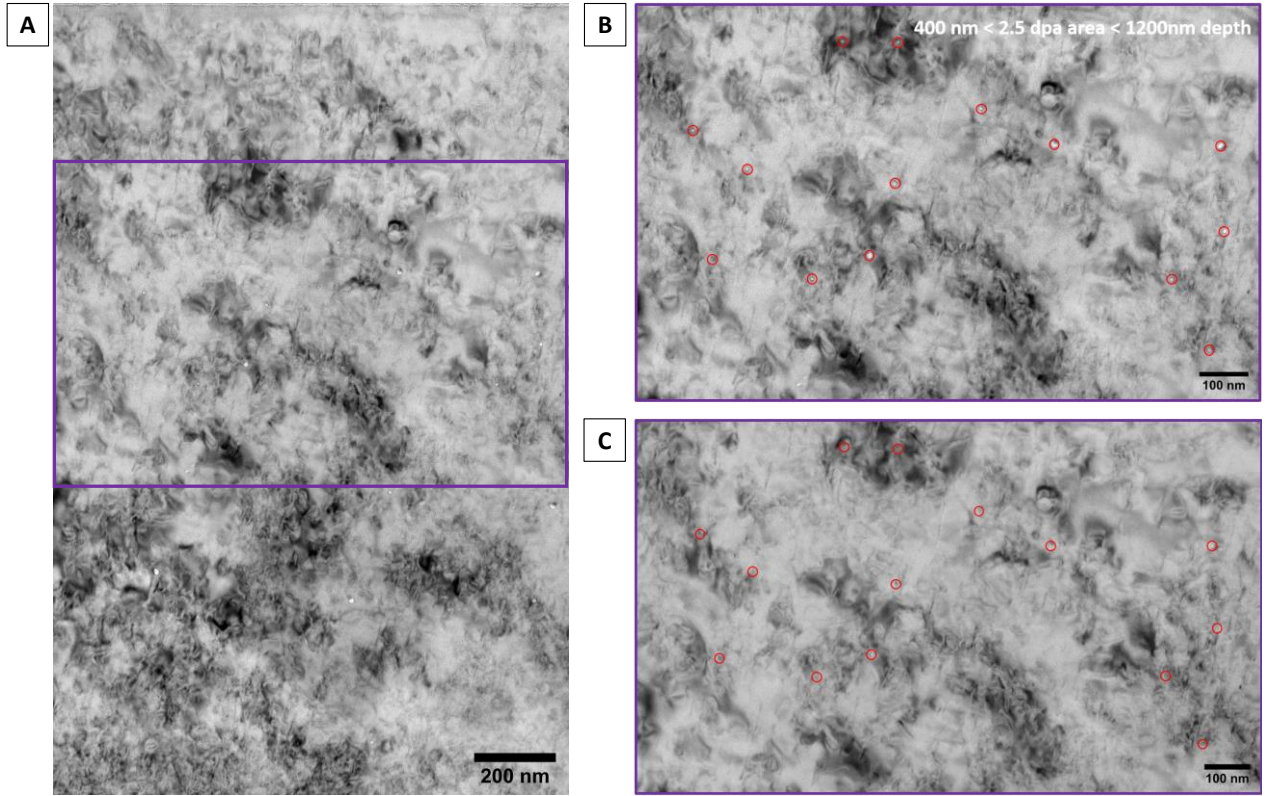


Figure 127 – TEM BF A & B) under- and C) overfocused ($\pm 1 \mu\text{m}$). Measurements are done within the 2.5 dpa ROI (purple box of A)).

Cavity size is defined as the distance between two minima of intensity on grey levels profiles passing through them, on underfocused image (Figure 128.A)). For this irradiation condition, an unimodal size distribution was observed (Figure 128.B)). Since image mapping of the zone was performed at lower magnification, with a lower defocus than previously, smaller size cavities may not have been revealed.

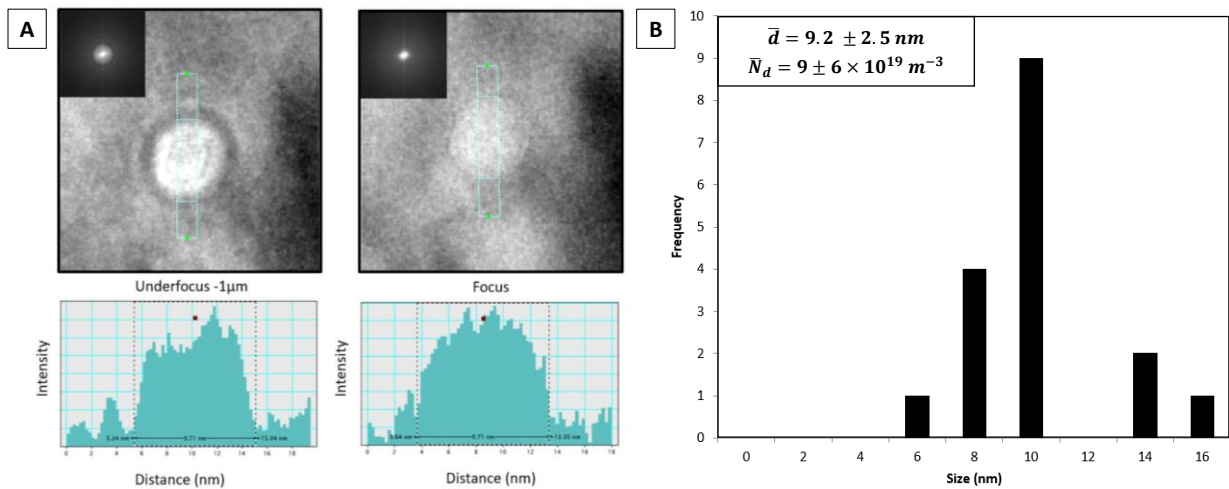


Figure 128 - A) Cavities size measurement definition. B) Cavities size distribution, mean size and mean number density.

The two edge-on Frank loops families were revealed thanks to the relrod dark field technique (Figure 129).

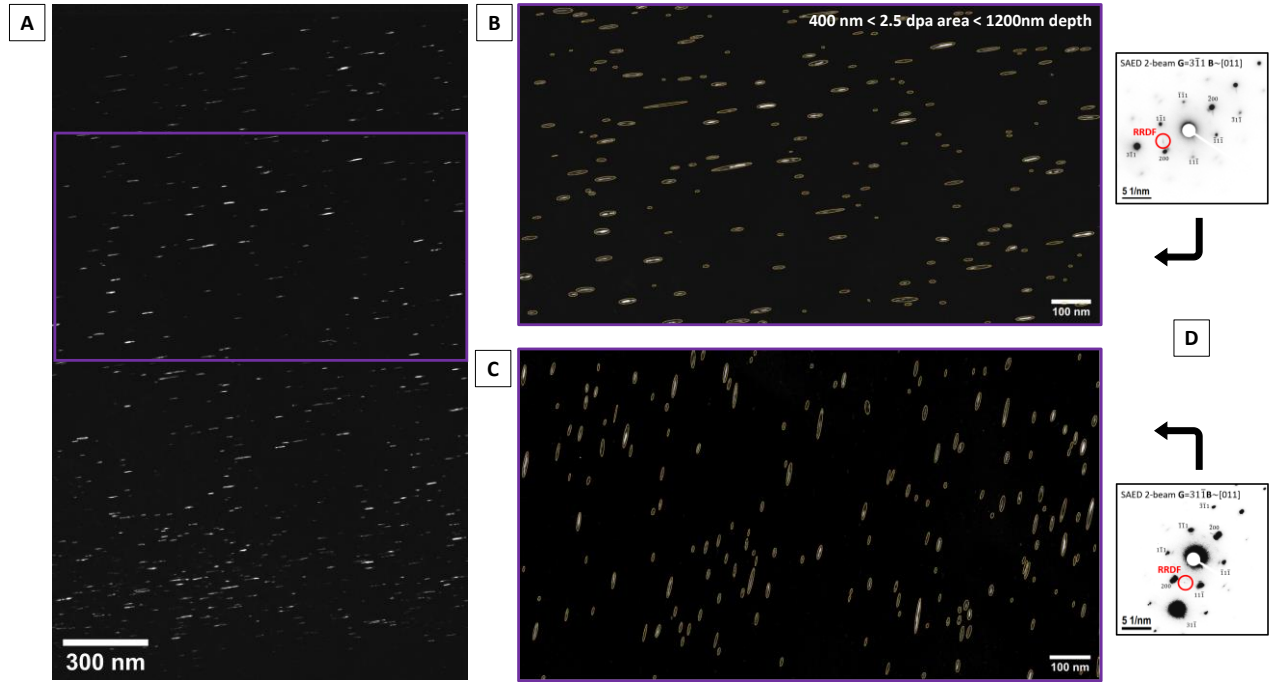


Figure 129 - Frank loops lying on A) and B) $(\bar{1}\bar{1}1)$ and C) $(\bar{1}\bar{1}\bar{1})$ planes imaged thanks to the relrod dark field imaging technique (RRDF), D) corresponding diffraction conditions. Measurement is done within the 2.5 dpa ROI for the two variants.

Same measurement procedure as presented before was performed to calculate Frank loops number density and size (Figure 130).

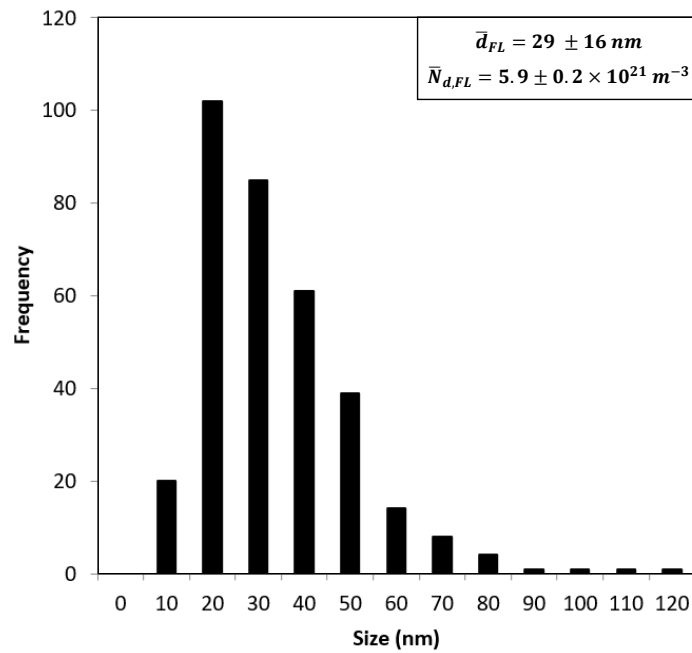


Figure 130 - Frank loops size distribution, mean size and mean number density.

2.2. Precipitation and RIS

As the 2.5 dpa irradiated state exhibits a Frank loops number density ten times higher than for the 1 dpa irradiated state, complementary STEM BF 2-beam and G/3G WBDF, known as diffraction contrast imaging STEM (DCI-STEM), was used in addition to the standard TEM techniques to image and identify defects. Indeed, under proper combination of convergence and collection semi-angles based on the choice of several parameters (i.e. objective and condenser aperture size, camera length, selected annular detector and selected **G**) and adjusting sample tilt, bending contours can be suppressed while **g.b** invisibly criterion remain valid [136].

This technique gain attention because it yields contrast interpretation much easier by removing strain field diffraction contrast. It permits to image thicker zones and, thanks to a smaller convergent semi-angle, increased depth of field compared to conventional STEM.

In Figure 131, studied area shows the presence of Frank loops, a cavity and precipitates. Enrichment of Ni and Si are observed at the vicinity of all defects, while P enrichment is only seen at the common location of the cavity and precipitates. Cr, Fe, Mn and Mo tend to deplete. Nb-rich precipitate seems to embrace a Ti-rich precipitate. At their location, enrichments in Nb, N, Ni, Si, Mo, P and Ti are detected. Removing Ti, these enrichments remind those observed at the cluster core level described in Figure 122.

Could this cluster correspond to a precipitate attached on a cavity exhibiting RIS and explain the low atomic density of the cluster core?

Even if the presented images were taken at various specimen tilt angles, because of TEM projection, it cannot be undoubtedly determined if the precipitates are attached to the cavity or not. HRSTEM images did not permit to determine precipitates crystallography.

Figure 132 shows the chemical distribution in the selected area presenting Frank loops, a cavity and a precipitate. Here also, it cannot be determined if cavity, precipitate and Frank loops are attached together. Same RIS trends were observed. M-shaped Fe concentration profiles are not as clearly defined as it was the case on sample irradiated to 1 dpa at 450°C.

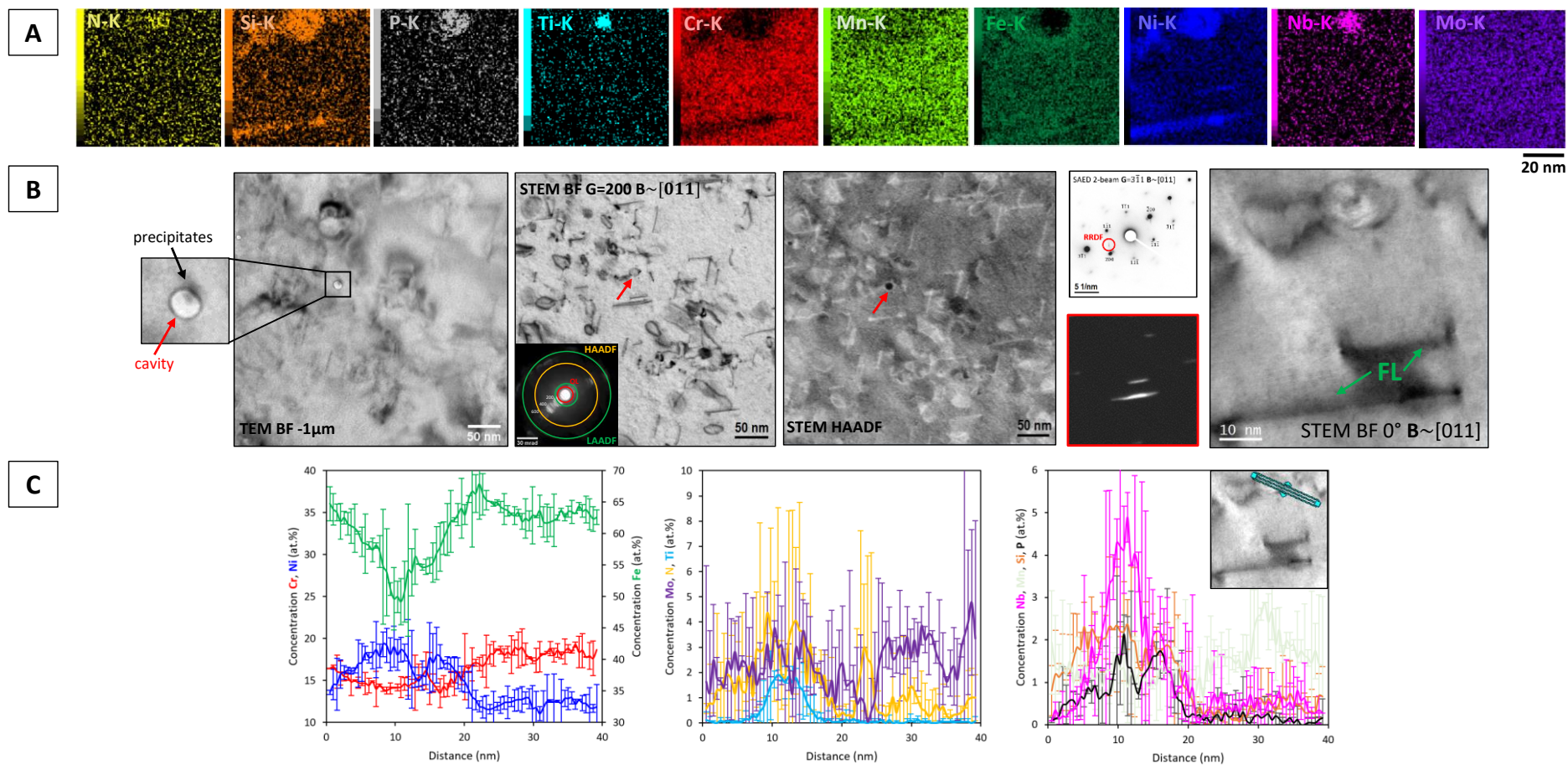


Figure 131 - A) STEM-EDS elemental maps corresponding to the selected region in B) and defect nature determination thanks to various imaging techniques (TEM out-of-focus, conventional BF and HAADF STEM, DCI-STEM BF and the associated CBED pattern with the selected objective aperture (OL), and LAADF/HAADF detector limits). C) Concentration profile extracted from the STEM-EDS map passing through a cavity and precipitates.

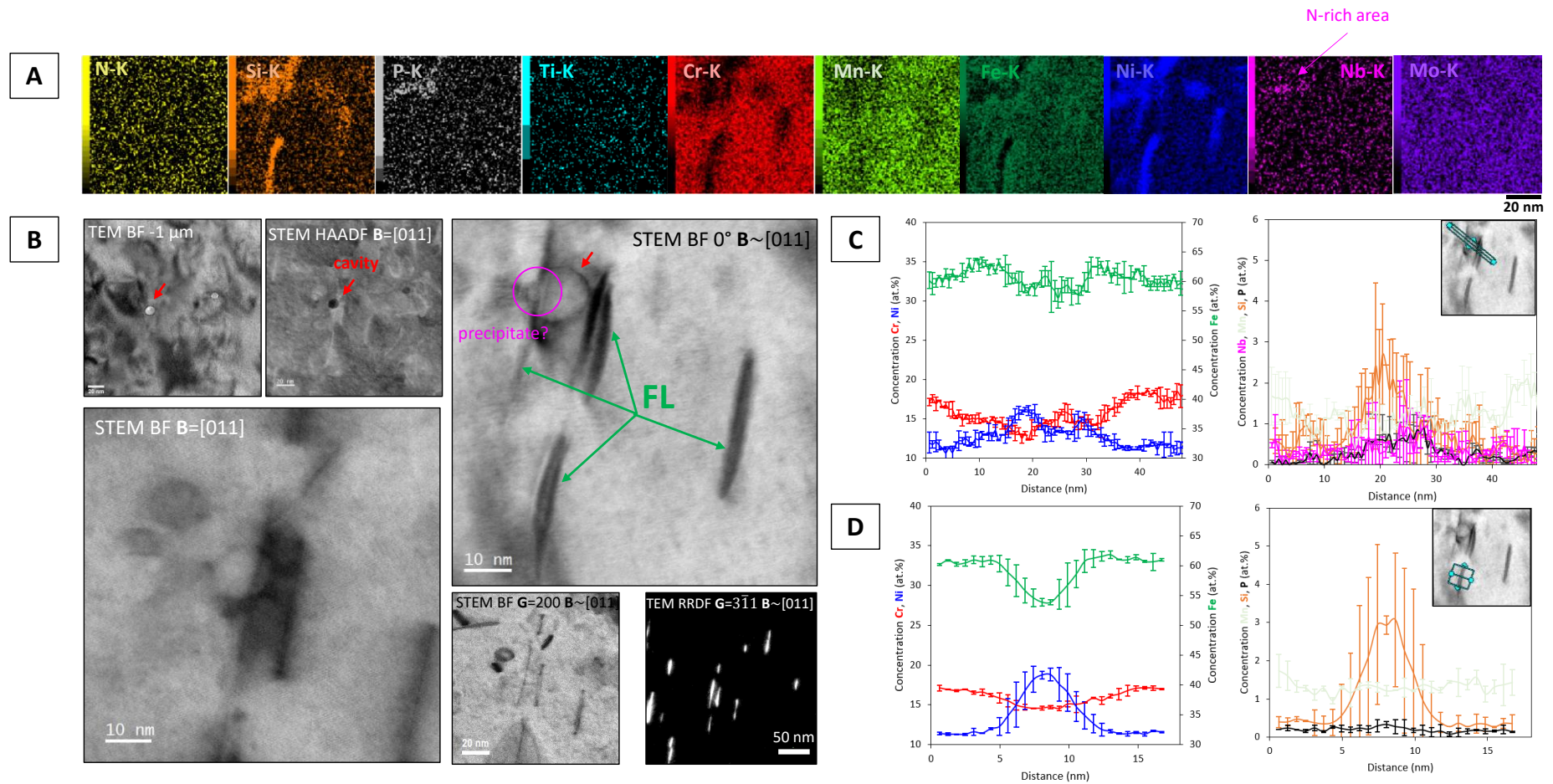


Figure 132 – A) STEM-EDS elemental maps corresponding to the selected region in B) and defect nature determination thanks to various imaging techniques (TEM out-of-focus, TEM RRDF, conventional BF/HAADF STEM and DCI-STEM BF). Concentration profile extracted at two different locations from the STEM-EDS map passing through C) a cavity, a precipitate and Frank loops and D) a single Frank loop viewed edge-on.

Previous characterizations were performed within thinned windows of a lamella designed for correlative microscopy. The region of interest in Figure 131 was well located in the extracted tip apex as shown in Figure 133. A single image of the tip taken with the RRDF technique is enough to find back the tip location in the pre-characterized TEM lamella where the majority of crystal defects were clearly identified. Unfortunately, the C contamination cap formed at the tip apex due to long STEM-EDS elemental mapping resisted to several plasma cleanings, low-voltage ion polishing with PIPS II and ion milling during FIB preparation of the tip. As it was pointed out by Herbig [108], the yield in an APT run is reduced after TEM analysis mainly due to carbon contamination. Indeed, to evaporate this high field C cap, the voltage needs to be increased. The resulting field is therefore superior than the evaporation field of the underlying material increasing significantly tip breakage. Although C cap has been successfully removed at the first stages of the APT analysis, a part of the tip fractured. As starting depth of the analysed volume is not known, a minimum of two defects within the tip would have been necessary for correlation. Nevertheless, regarding clusters shape and orientation observed in the reconstructed 3D volume, it could correspond to the $(\bar{1}1\bar{1})$ habit plane of a Frank loop. Frank loops habit plane is a stacking fault and exhibit here Si and N clear enrichment. It is surprising because strain fields exist at dislocation core while at the level of the habit plane perfect crystal should not act as sink. Enrichments at loop habit plane has already been observed in a BCC Fe-Cr alloy ion irradiated [268]. Cr enrichment was attributed to RIS of Cr as well an impurity effect was suspected based on Cr affinity with C during loop growth. As far as we know, no enrichment have been reported yet on loops habit planes in 304/L or 316/L steels. Even if Si is known to be involved in RIS, N exhibits higher affinity with Al, Cr, V, or Nb than Si.

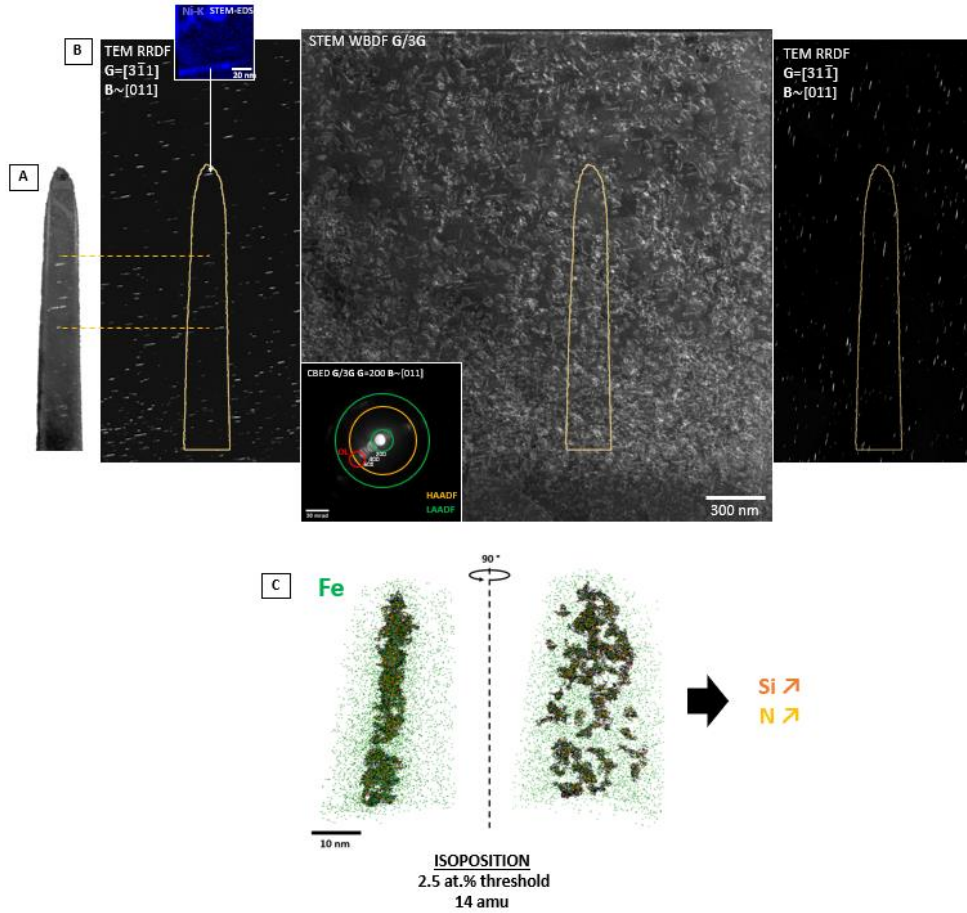


Figure 133 – A) Extracted tip from B) the pre-characterized TEM lamella designed for correlative microscopy. C) The associated APT 3D volume. Cluster formation on a planar defect as revealed by the isoposition method. Comparison of cluster composition with the surrounding matrix shows a noticeable enrichment of Si and N in the clusters.

VI. General discussion

As a reminder, this study has two goals. First, the microstructure evolution under irradiation should be compared to other nuclear grades of austenitic stainless steels. Second, RIS trends and levels on different lattice defects, as well as second phase stability, should be determined by the use of coupled or correlated techniques.

A solution annealed 316L(N) with a noticeable amount of Nb has been investigated. Cavities and Frank loops populations has been investigated at two different irradiation conditions: 1 dpa 450°C

and 2.5 dpa 440°C. As the dose rate and ion beam energies used for irradiation differ, they are not directly compared but are faced to the existing literature as presented in Figure 134.

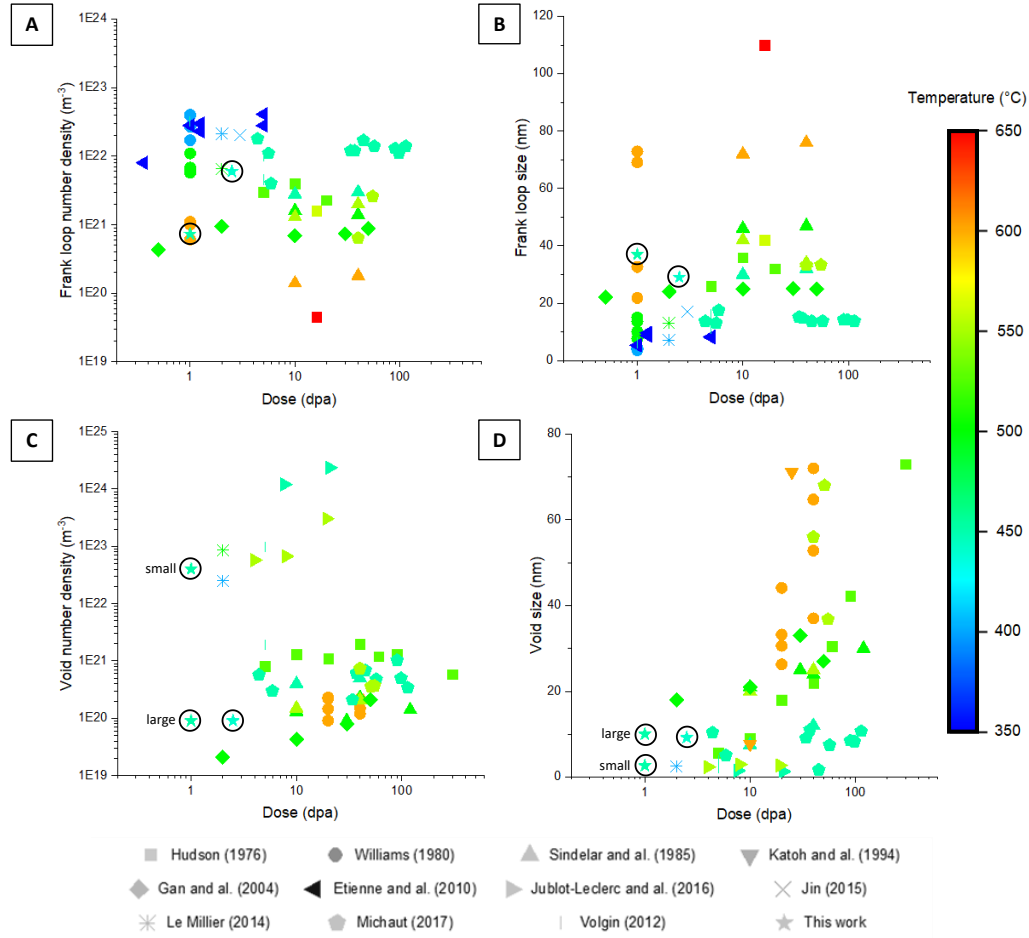


Figure 134 – Microstructure evolution under irradiation in terms of A & B) Frank loops and C & D) cavities number density and size as a function of dose and temperature. Comparison of obtained results with the literature for various 304/L and 316/L austenitic stainless steels ion irradiated ([269], [270], [271], [272], [273], [274], [275], [276], [277], [66], [55]).

Even if it was shown that the dislocation density is higher than in other solution annealed austenitic stainless steels, the corresponding irradiated microstructure of the studied 316L(N) is in accordance with the reviewed literature in terms of defect number density and size ranges. No N or synergetic N+Nb effect is highlighted on the resulting microstructure evolution based solely on Frank loops and cavity evolution under the selected irradiation conditions. Nevertheless, it should be noted that irradiation to 1 dpa fits more with high temperatures for Frank loops. Ion beam heating depends on the thermal contact, heat could have been not well conducted and evacuated within the assembly. From this observation it is reasonable to suppose that the irradiation temperature was underestimated.

In terms of second phase population at the as-received state, it differs from 316/316L grades. Highly suspected complex nitride known as Z-phase that are sometimes linked with MX (TiN) precipitates were observed.

After irradiation, common RIS trends are observed on dislocation loops i.e. Ni and Si enrichments on one hand and Cr, Fe, Mn and Mo depletion. Identified RIS mechanism are the inverse Kirkendall effect (IKE), the vacancy drag and the SIA drag.

Major alloying elements RIS trends can be explained by the IKE mechanism. Cr, the faster diffusing element deplete while slow diffusion of Ni provokes its enrichment at sinks. Fe depletion compensate Ni enrichment [67]. All the listed RIS mechanisms indeed compete. It had been shown [267] that Ni behaviour can balance from a vacancy-dominant to an interstitial-dominant mechanism. Fe exhibit a ‘M-shaped’ profile which could be explained by the competition between point defects concentration gradient and chemical potential gradient due to the segregation of elements at the vicinity of lattice defects. They are supposed to provoke an enrichment then a depletion respectively [266]. Locally, Cr content decreases below 10 at.% (Figure 118 and Figure 122), at these locations the steel could lose its stainless property.

Mn has a faster diffusivity compared to Fe, Ni and Cr and should exhibit a strong depletion at sinks, stronger than Cr [67]. Mn depletion was effectively observed at a similar level than Cr from STEM-EDS maps. Mn-K α and Cr-K β X-ray lines are superimposed in the EDS spectrum, which could bias the Mn measured level if the peak decomposition cannot remove any contribution of Cr in Mn. Nevertheless, similar RIS levels for Cr and Mn has been observed from APT measurements in a 316 [86]. In APT mass spectrum, Mn and Cr peaks do not overlap. From this study [86], Mn segregation levels are shown to differ depending on the sink type. Mn deplete more on dislocation loops than on grain boundaries, IKE mechanism may not be the only one involved to explain Mn RIS behaviour.

Mo deplete as well. Mo has a large size misfit versus the major alloying elements. Due to elastic interactions, oversized solutes are known to deplete and to trap vacancies at temperatures low enough compared to the solute-vacancy binding energy [278]. Nb exhibits also a positive lattice misfit and may behave similarly to Mo. As Nb concentration in solid solution in the studied 316L(N) is very low, it was not possible to confirm this tendency. By trapping vacancies, oversized solutes could increase recombination and decrease RIS levels. This effect can be clearly observed in case of Hf or Zr addition, in the case of Nb addition on RIS is less clear [89,278,279].

SIA drag of undersized elements tend to enrich sinks as it is the case for Si and P [67]. Again, mechanisms compete and it has been shown from ab initio calculation [280] that Si can be affected by both SIA diffusion and vacancy drag. However, this study shown that the vacancy drag mechanism helps to enrich the Si at sinks under irradiation in austenitic systems.

P is often observed to segregate on almost all defect types (see Figure 13 of CHAPTER 1). But, to our knowledge, P segregation on a cavity has not been observed apart in the case of void-precipitate association during neutron irradiation of austenitic stainless steels where two types of phosphides (Fe₂P and Fe₃P) have been observed to be associated with cavities [281]. From the results of the current study, P was clearly segregating on cavities and was not observed to segregate on other defects. Based on presented results, presence of P on other defect types could not be excluded. Indeed, matrix contribution is higher for the measurements done on dislocation loops than for the cavities in the case of STEM-EDS maps. Furthermore, APT data are scarce on dislocation loops.

Anyway, P tendency to preferentially segregate at cavities location is supported. Even if P segregates on other defects, RIS levels are thought to be lower.

Based on concentration profiles drawn across cavities. P enriched over a smaller distance than Si and then Ni. It could be justified by a faster diffusion of P to sinks followed by Si then Ni. Similar trend is observed at dislocation loop for Si and Ni at the 1 dpa irradiated state.

Comparison between RIS levels depending on sink nature and size based on STEM-EDS maps is not done quantitatively because matrix contribution to the signal can skew measurements and consequently result interpretation. Use of MVSA technique to post-treat STEM-EDS data [264] is believed to be a need to answer this question. Nevertheless, APT permits to overcome this issue [86] because matrix contribution can be removed from local chemical heterogeneities. RIS on dislocation loop have been observed at 1 dpa in APT volumes. Si and Ni enrichments are observed on the loop of the 1 dpa APT volume. On the presented volumes, P segregated at the level of a cluster which is suspected to be a precipitate associated with a cavity. These observations let suggest that dislocation loops and precipitate/matrix interfaces could be biased for SIA as P and Si are generally thought to enrich sinks via SIA mediated mechanism. Indeed, SIA trapping by sinks could induce a local vacancy supersaturation at their vicinity responsible for cavities formation. Even if small cavities have been observed to trap a dislocation line in the 1 dpa irradiated state, large cavities are mostly observed being associated with precipitates and not with dislocations. Precipitate interface with the matrix probably exhibits a larger bias for SIA than dislocation loops. Precipitate-cavity association depends on the alloy nominal composition, the phase chemistry and crystallography, its volume misfit, precipitate-matrix interface coherency and precipitate stability under irradiation.

Nb, N and sometimes Ti are also observed at the level of cavities. Their content seems to vary from a precipitate to another. These elements call to mind the suspected Z and TiN phases encountered at the as-received state. On one hand, contrarily to the as-received state, large precipitates (i.e. primary Z-phase) have not been observed within the damaged zone neither at 1 dpa nor at 2.5 dpa. On the other hand, precipitates observed within the irradiated regions showed a high content of elements that usually enrich with RIS: Ni, Si and P. Therefore, primary Z-phases may not be stable under irradiation and seem to shrink. While Nb, N, Mo, Cr and Fe are reinjected in the matrix, P, Si and Ni enrich. Irradiations at higher doses are necessary to know if these precipitates tend to completely disappear or if a phase will finally stabilize at a particular composition. From the literature review, this type of precipitate has never been observed in irradiated austenitic stainless steels grades: 314/L, 316/L, 316LN and 316LN+Nb and Z-phase stability under irradiation has not been studied neither.

Another unusual behaviour has been observed with the APT volume at 2.5 dpa irradiated state. Si and N enrichment are observed at the level of a planar defect. Because this APT volume was extracted from a TEM lamella and we were able to locate the prepared tip within the pre-characterized zone. This planar defect could not be a grain boundary. As the observed feature has the same orientation than a Frank loop variant, it is suggested that this feature is indeed the faulted habit plane of a Frank loop. Such enrichment has never been reported. While Si segregation was observed on other defect type, N enrichment was not.

Coupled and correlated techniques was a grateful help to understand 316L(N) microstructure evolution under irradiation. S/TEM imaging associated with analytical STEM-EDS enable us to

link defects nature to their chemistry but we showed that to obtain reliable quantitative data, data processing (e.g. MVSA) is necessary.

TEM-APT correlative microscopy can overcome this issue because defect crystallographic nature can be first determined by TEM and then analysed APT. The isoposition method applied to APT data permits to remove matrix contribution from observed features. Moreover, APT is more sensitive to impurities and light elements than STEM-EDS. TEM-APT correlative microscopy for RIS studies on intragranular defects helped us to determine the nature and the habit plane of dislocation loops, it gave also insights to determine the nature of a complex cluster and help to understand an APT artefact. Over the two methods put in practice, TEM-APT correlative microscopy on a tip revealed that contrasts in S/TEM images are more difficult to interpret than on a conventional TEM lamella. Two reasons were invoked: FIB damage which can be removed by low voltage ion cleaning thus optimized and the change in thickness along the tip diameter. For this latter reason, it was proposed to extract a tip from a precharacterized lamella. We were able to recognize defect nature within the extracted tip and to extract tip apex from a very confined region. As the investigated zone is larger, it is easier to reach diffraction conditions of interest to image defects than on a tip. Combination of STEM-WBDF imaging also contributed to interpret defect nature and optimize contrast interpretation in regions containing a very high density of defects. But unfortunately, the analysed tip broke rapidly. Carbon contamination was thought to be the main reason of this early breakage. Thus, strategies to avoid or remove carbon contamination should be put in place to optimize the proposed method. TEM-APT correlative microscopy on a tip extracted from a TEM lamella is time consuming. Experimentalist should choose between the time spent to acquire data versus the desired raw data quality (in terms of contrast interpretation). There is no good answer, it is always a question of compromise.

Finally, we shown that APT data interpretation is not straightforward and coupled simulation is sometimes needed and, in complex cases, it is even not sufficient. TEM-APT correlative microscopy coupled with simulation has proven their complementary.

VII. Conclusion

Optimized 316L(N) shown to have a population of Frank loops and cavities equivalent to common nuclear austenitic stainless steels grades. Nevertheless, its behaviour in terms of RIS and precipitation is atypical. Indeed, 0.09 wt % Nb in the nominal composition appears to affect RIS of P, cavities formation location and primary Z-phase stability. To our knowledge, Z-phase stability has never been reported in the literature. N was observed to only enrich at the level of the stacking fault of a Frank loop, new APT volumes are needed to confirm this tendency. N from Z-phase nitride seem to be reinjected in the matrix under irradiation. To postulate on N and Nb addition effect on Cr depletion or impurities enrichment at grain boundaries, trust to be involved in IASCC mechanism, a complementary RIS study at grain boundaries would have brought interesting insights. As RIS levels at grain boundaries are driven by flux coupling, it strongly depends on point defect availability to migrate to grain boundaries. Intragranular sink nature, size, density, bias as well as RIS mechanisms involved strongly affect point defects migration and chemical redistribution under irradiation. Then, RIS levels at grain boundaries cannot be decoupled from RIS behaviour at intragranular sinks.

Correlative microscopy performed on a tip allowed to obtain useful crystallographic information to interpret the local chemical heterogeneities revealed by APT. Limitations were highlighted and, subsequently, a new methodology for TEM-APT correlative microscopy was developed.

Thanks to correlative microscopy, hints about defects nature were obtained. By precisely knowing tip orientation from TEM, it was possible to find out the habit plane of a dislocation loop. A feature was also observed being an APT artefact. Indeed, coupling techniques permits to improve quantitative measurement because it allows to understand sources of artefacts of the coupled techniques which can be responsible of quantification errors. Coupled or correlative techniques, especially for TEM and APT, are under constant development and it is seen to popularize. For this purpose, a method for tip extraction from a confined region of interest of a lamella for RIS investigations on intragranular defects has been proposed. Feasibility of the proposed method was successfully demonstrated, and further developments were proposed to allow correlation between a tip extracted from a confined region of a pre-characterised lamella. Primary results are very encouraging, and ways of optimisations were suggested based on the literature review (e.g. particularly regarding carbon contamination).

Correlative APT-TEM microscopy combined with field evaporation simulations, advanced STEM techniques (e.g. DCI STEM) and data processing (e.g. MVSA) is truly believed to be a complementary toolkit for a highly quantitative description of RIS on small lattice defects and will give new keys of understanding on RIS mechanisms (e.g. precipitate void association). Emerging coupling of EDS-EELS Electron Tomography (ET) [165,282] or even Correlative EDS-ET and APT [283] is also very promising for this purpose.

To understand how N and Nb affect steel susceptibility to IASCC, same study should have been performed on a standard 316L irradiated under the same conditions. RIS measurements at grain boundaries, micro-compression tests on pillars and corrosion tests at as-received and irradiated states would have provided new insights to link nanoscale changes to macroscopic properties evolution under irradiation.

GENERAL CONCLUSION

Austenitic stainless steels (ASS) are widely used as structural materials of actual nuclear reactors core and are candidates for fuel cladding and, in some cases, for the main vessel and the internals of the next generation of reactor prototypes. All along reactors life, irreplaceable or hardly replaceable ASS components are submitted to long term ageing under irradiation and can face diverse degradation mechanisms such as irradiation-assisted stress corrosion cracking.

Radiation-induced segregation (RIS) in ASS encourages Cr depletion at grain boundaries enhancing ASS sensitivity to corrosion and is thought to be one of the factors responsible of IASCC. It is an important concern for the nuclear material community because it reduces components lifetime.

To improve RIS predictive models, it is necessary to extend knowledge on the competing mechanisms involved in RIS and obtain reliable experimental data about diffusion kinetics at the operating temperature range of these reactors.

Diffusion under irradiation is led by point defects, i.e. vacancies and self-interstitials (SIA), exchanges with chemical species. Point defects (PD) availability for long range migration is ruled by the reaction rate theory in which PD concentration is a balance between the production rate and the loss rate by mutual recombination or at sinks. Point defect clusters can create extended defects within the microstructure. As grain boundaries, they are sinks for PD. The sink strength is dependent on the type of sink, its size and density. Particular sinks show to preferentially absorb a type of point defect. Dislocations are for example known to be biased for SIA. The annihilation of PD to sinks become significant within a range of irradiation conditions (i.e. dose rate and temperature) and is closely linked to the damaged level of the microstructure. Flux coupling between chemical species and point defects when they migrate toward sinks lead to enrichment or depletion of elements at the defect vicinity (e.g. grain boundaries, dislocation loops, cavities). Identified mechanisms of RIS are: the inverse Kirkendall effect (IKE), vacancy drag and SIA drag.

On one hand, mutual weight of these competing mechanisms depends on the chemical species and the sink involved. Up to now, this point is still controversial. On the other hand, RIS levels depends on PD-mediated diffusion kinetics, the irradiation conditions and the local sink strength associated to the sink involved and the surrounding ones. A crucial lack of experimental PD-mediated diffusion data under irradiation determined at the operating temperatures of reactors, especially for SIA, are limiting assessment of RIS models' validity.

To build a reliable point defect model of RIS able to predict microstructural evolutions under irradiation in model systems of ASS, nuclear material researchers expressed the need to obtain experimental data about diffusion kinetics within the temperature and dose rate ranges of RIS domain. It is one of the main motivations of the GEneration IV Materials Maturity (GEMMA) H2020 Euratom European project (see APPENDIX). This present work was conducted under the scope of this project.

Thus, first aim consisted to intend to provide experimental diffusion data at the operating temperature range of nuclear reactors and assess effect of irradiation on interdiffusion kinetics.

It has been shown that composition modulated nanolayers enable to measure diffusion kinetics at low temperatures, regarding conventional methods, under a reasonable time. Such nanolayers were synthesized by magnetron cosputtering of metallic targets at Université de technologie de Belfort Montbéliard (UTBM). Interdiffusion coefficients can be extracted from concentration profiles amplitude attenuation obtained by Atom Probe Tomography (APT) and to investigate microstructure evolution thanks to Transmission Electron Microscopy (TEM). The binary Ni/Ni-20Cr and Ni-40Fe-25Cr/Ni-35Fe-20Cr ternary system interdiffusion kinetics have been studied at 440°C.

First set of elaborated samples exhibited high levels of oxygen and carbon contamination as well as a lack of adhesion of the coating on the substrate. Thus, efforts have been firstly focused on fabrication process optimization. A longer degassing process, change of the substrate stacking medium to the substrate holder, increasing the deposition rate and adding a Ti getter layer for trapping oxygen permitted to elaborate samples in line with expectations. However, first performed annealing revealed that Ti diffused through the depth of the nanolayers coating leading to an heterogeneous diffusion. Therefore, specimen preparation has been adapted and both substrate and Ti layer have been systematically removed before performing new annealings and irradiations.

The modulation wavelength was approximately equal to 5 nm for both systems. This value had been selected in order to neglect the effect of a steep concentration gradient on the measured diffusion coefficients and ensure the possibility to access to them after short annealing durations. Annealing and irradiation conditions definition had been assessed thanks to predictions to ensure success of the method.

Experimental thermal interdiffusion coefficient of the binary Ni/Ni-20Cr system has been determined at 440°C as well as under irradiation thanks to the nanolayers method. Measured interdiffusion coefficient after 48h of thermal ageing was equal to $1.1 \pm 0.2 \times 10^{-24} \text{ m}^2 \cdot \text{s}^{-1}$ while the predicted interdiffusion coefficient was equal to $7.1 \pm 0.7 \times 10^{-25} \text{ m}^2 \cdot \text{s}^{-1}$. The discrepancy between measured and predicted results was attributed to in-plane grain boundary Cr diffusion that was revealed to occur. Therefore, measured interdiffusion coefficient are effective ones. After irradiation to 0.001 and 0.05 dpa of damage level at the same dose rate, measured diffusion coefficients were 100 to 1000 times higher than the thermal ones showing diffusion enhancement under irradiation. However, measured interdiffusion coefficients under irradiation differ from each other by one order of magnitude. It had been attributed to the fact that the non-equilibrium steady state has not been reached yet. Then, measured interdiffusion kinetics under irradiation had been defined as effective transient ones. The predictions overestimated interdiffusion kinetics under irradiation. Uncertainties about sink strength experimental determination from TEM measurements, not reached steady state, the lack of experimental data on PD-mediated migration kinetics and model assumptions could explain this difference. Even if the purity level was acceptable to study diffusion, Ni-20Cr layers were contaminated with Fe. After annealing and irradiation, Fe-rich clusters formed and had been attributed to be precursors for the ordered phase Ni_3Fe .

In the case of the ternary system Ni-40Fe-25Cr/Ni-35Fe-20Cr, the limited number of ageing conditions (i.e. annealing and irradiations) did not permit to access to experimental interdiffusion coefficients. Indeed, several ageing durations are required to extract the four independent interdiffusion coefficients of a ternary system. However, predictions of amplitude attenuation after thermal ageing allowed the comparison to the measured ones. Discrepancies with the theoretical predictions had been, here also, attributed to in-plane grain boundaries diffusion because amplitude attenuation were faster than expected. Experimental error cannot be excluded because as-deposited amplitudes for the ternary system were much smaller than for the binary system. After irradiation, amplitude attenuation of Cr was surprisingly higher for the lowest dose. Linear profiles drawn across grain boundaries revealed Cr enrichment at 0.001 dpa and Ni enrichment (i.e. RIS) at 0.01 dpa and could explain the observed tendency. Once again, as experimental error on amplitude measurement was higher for the ternary system. This result needs to be confirmed by further irradiation experiments.

Nanolayers method feasibility to access to interdiffusion kinetics in binary and ternary systems under a reasonable time had been confirmed. However, weight of grain boundary diffusion on measured kinetics should be estimated to extract bulk interdiffusion coefficients. This method is also well fitted to access to interdiffusion kinetics under irradiation. Nevertheless, a careful experimental determination of the sink strength, segregation levels at grain boundaries and ensure to have reached steady state conditions is essential to compare experiment to simulation.

Experimentally determined diffusion kinetics can be compared with atomistic kinetic model results conjointly developed under the scope of the GEMMA project. Nanolayers method is highly flexible and allows access to slow diffusion kinetics, making it particularly adapted to assess effect of irradiation on interdiffusion at low temperature.

In perspectives of this work, improvements have been proposed. Facing numerous breakage associated to the specimen preparation method, a new architecture design is suggested. Complementary techniques to reduce experimental error on measured defect density necessary to estimate the sink strength are advised. Scanning precession electron diffraction allows grain size and nanotwins spacing measurements, and dislocation density estimation whereas ion beam removal method permit to determine residual stress profiles within the coating.

Based on the contribution of ballistic mixing, radiation-enhanced diffusion and thermal diffusion to the measured amplitude attenuation, we proposed a matrix of experiments to access to SIA mediated partial diffusion coefficients both for the binary and the ternary systems. Finally, compare results for different energetic particles (i.e. neutrons, protons and electrons) could bring very interesting insights in emulation of neutron irradiation effects on microstructural evolution.

Second aim of this work aspired to study the competition existing between the different identified mechanisms of RIS in an optimized nuclear steel grade, a 316L(N) provided by EDF R&D, and develop an efficient method of TEM-APT correlative microscopy.

Associated investigations on microstructural and microchemical evolution under ion irradiation of an optimized 316L(N) having a N and Nb content greater than 316L nuclear grade have been done.

Studied material has been hot rolled then solution annealed and water quenched. Less than 0.01 atomic fraction of residual delta ferrite remain within the austenitic structure. Microsegregations enriched in ferrite stabilizers and Mn, aluminium oxide inclusions and Nb-rich precipitates are observed at the micron scale. Thanks to characterizations performed at the nanoscale, a high dislocation density has been measured $\bar{\rho} = 1.3 \pm 0.6 \times 10^{14} \text{ m}^{-2}$. Usually, for solution annealed ASS, dislocation density ranges from 10^{10} to 10^{13} m^{-2} . Due to a higher N and Nb content, tens of nanometers large nitrides TiN and primary Z phase have been recognized from composition measurements. These phases are not commonly observed in 316L steels. APT experiments shown that at the as-received state, elements distribution is homogeneous at thin scale.

In order to link defects crystallography with their chemistry after ion irradiations to 1 and 2.5 dpa between 440 and 450°C respectively, coupled or correlated techniques is a need. Three approaches have been attempted to this aim:

- 1st – S/TEM imaging associated with analytical STEM-EDS
- 2nd – APT coupled with field evaporation simulation
- 3rd – TEM-APT correlative microscopy

First TEM-APT correlative microscopy campaign on the 316L(N) irradiated to 1 dpa at 450°C was performed on an APT tip. With this method, contrasts in S/TEM images were difficult to interpret due to focused ion beam (FIB) damage and thickness evolution over the tip diameter. Even if correlative results could have been extracted with this method, decision was made to extract an APT tip from a pre-characterized lamella to overcome contrast interpretation difficulties.

Despite a higher dislocation density and change in nominal composition, Frank loop and cavities number density and size have a similar magnitude than other ASS nuclear grades.

Same general RIS trends than 316L ASS have been observed, i.e. Ni, Si enrichments and Cr, Fe, Mn and Mo depletion at sinks. Nevertheless, slight changes in the nominal composition appeared to affect RIS of P and N, cavities formation location and primary Z-phase stability. N was suspected to enrich at the level of a Frank loop habit plane. P has been observed to preferentially segregate at the level of large cavities associated with pre-existing nitrides: TiN and Z-phase.

A complex cluster have been observed in an atom probe tomography (APT) volume. Field evaporation simulations permitted to rule out hypotheses about its exact nature but, regarding the high tendency for cavities to associate with precipitates, it is thought to be the case. It could be the first time that Z-phase stability is studied in austenitic stainless steels. A comparison of elements involved in RIS and their identified mechanisms let assume that Z-phase interface with the matrix seems to be more biased for SIA than dislocation loops. Presence of biased sinks for SIA could affect the point defect balance nearby grain boundaries and thus RIS levels or involved mechanisms. RIS investigations at grain boundaries could have brought very complementary insights for this purpose. Performing similar characterisations on a standard 316L would have permit a better comparison of N and Nb addition on RIS.

S/TEM imaging associated with analytical STEM-EDS is very practical but matrix contribution to the signal can make impurities or light elements enrichments hard to detect under a certain

concentration threshold for a given lamella thickness. Use of data processing methods such as multivariate statistical analysis (MVSA) would have permit quantitative measurements. Unfortunately, only qualitative results have been provided from STEM-EDS measurements.

Thanks to correlative microscopy, hints about defects nature were obtained. By precisely knowing tip orientation from TEM, it was possible to find out the habit plane of a dislocation loop and recognized a Frank loop. A feature was also observed being an APT artefact. Indeed, coupling techniques permits to improve quantitative measurement because it allows to understand sources of artefacts of the coupled techniques which can be responsible of quantification errors. From the two methods tested, performing APT-TEM correlative microscopy on an APT tip limited contrast interpretation of small defects such as PD clusters produced by irradiation. The second method enabled to extract a tip from a specific site of a pre-characterized TEM lamella. This method is expected to be really useful to study a particular type of defect if its number density is low. However, it is time consuming and carbon contamination highly increased the risk of tip breakage.

Even if first results are encouraging, they are not satisfying as it is and ask for further improvements. To remove FIB damaged layer on the APT tip surface, ion cleaning of the tip at low voltage with Ar^+ ions can be performed. It has also the advantage to remove the oxide layer and carbon contamination after performing TEM and reduces tip breakage. Beam showering the region of interest of the sample in-situ with electrons is advised after plasma cleaning to prevent from carbon contamination during acquisition of a STEM-EDS map.

Correlative APT-TEM microscopy combined with field evaporation simulations, advanced STEM techniques (e.g. DCI STEM) and data processing (e.g. MVSA) is truly believed to be a complementary toolkit for a highly quantitative description of RIS on small lattice defects.

The two strategies experimented in this present work confirmed the strong complementary and dependency of experiments and simulations as well as coupling/correlating advanced nanoscale techniques to progress on the prediction of RIS. A necessary step to deepen knowledge on the even more complex degradation mechanism of irradiation-assisted stress corrosion cracking limiting austenitic stainless steels components lifetime in the core of nuclear reactors.

REFERENCES

1. Zinkle SJ, Was GS. Materials challenges in nuclear energy. *Acta Mater.* 2013;61:735–758.
2. Şahin S, Übeyli M. A Review on the Potential Use of Austenitic Stainless Steels in Nuclear Fusion Reactors. *J Fusion Energy.* 2008;27:271–277.
3. Garner F. Irradiation Performance of Cladding and Structural Steels in Liquid Metal Reactors. In: Cahn RW, Haasen P, Kramer EJ, editors. *Mater Sci Technol.* Wiley-VCH Verlag GmbH & Co. KGaA; 2006.
4. Villars, Prince, Okamoto. *Handbook of ternary alloy phase diagrams.* ASM international; 1995.
5. Paul A, Divinski SV, editors. *Handbook of solid state diffusion.* Amsterdam, Netherlands: Elsevier; 2017.
6. Mehrer H. *Diffusion in solids: fundamentals, methods, materials, diffusion-controlled processes.* Springer Science & Business Media; 2007.
7. Kizilyalli M, Corish J, Metselaar R. Definitions of terms for diffusion in the solid state. *Pure Appl Chem* 717. 1999;1307–1325.
8. Laskar AL, Bocquet JL, Brebec G, et al., editors. *Diffusion in Materials [Internet].* Dordrecht: Springer Netherlands; 1990
9. Paul A, Laurila T, Vuorinen V, et al. *Thermodynamics, Diffusion and the Kirkendall Effect in Solids.* Springer; 2014.
10. Kirkaldy, Weichert, Haq. Diffusion in multicomponent metallic systems: VI. Some thermodynamic properties of the D matrix and the corresponding solutions of the diffusion equations. *Can J Phys.* 1963;2166–2173.
11. Belova I, Murch G. Expressions for vacancy-wind factors occurring in interdiffusion in ternary and higher-order alloys. *Acta Mater.* 2007;55:627–634.
12. Cserháti C, Ugaste Ü, van Dal MJH, et al. On the Relation between Interdiffusion and Tracer Diffusion Coefficients in Ternary Solid Solutions. *Defect Diffus Forum.* 2001;194–199:189–194.
13. Krishna R, Wesselingh JA. The Maxwell-Stefan approach to mass transfer. *Chem Eng Sci.* 1997;52:861–911.
14. CALPHAD: Calculation of Phase Diagrams - A Comprehensive Guide. Elsevier; 1998
15. Růžicková J, Million B. Self-diffusion of the components in the FCC phase of binary solid solutions of the Fe Ni Cr system. *Mater Sci Eng.* 1981;50:59–64.
16. Moulin, Huntz, Lacombe. Influence du carbone sur la diffusion du chrome et du nickel en volume et dans les joints de grains de l'alliage Ni-Cr 80/20. *Acta Metall.* 1979;1431–1443.
17. Mehrer H. *Diffusion in Solid Metals and Alloys.* Springer; 1990
18. Askill. Tracer diffusion in the chromium–nickel system. *Phys Status Solidi.* 1971;587–596.
19. Rothman SJ, Nowicki LJ, Murch GE. Self-diffusion in austenitic Fe-Cr-Ni alloys. *J Phys F Met Phys.* 1980;10:383.
20. Perkins RA, Padgett, Tunali. Tracer Diffusion of ^{59}Fe and ^{51}Cr in Fe-17 Wt Pct Cr-12 Wt Pct Ni Austenitic Alloy. *Metall Trans.* 1973;4:2535–2540.

REFERENCES

21. Perkins RA. Tracer diffusion of ^{63}Ni in Fe-17 wt pct Cr-12 wt pct Ni. *Metall Trans.* 1973;4:1665–1669.
22. Jung SB, Yamane T, Minamino Y, et al. Interdiffusion and its size effect in nickel solid solutions of Ni-Co, Ni-Cr and Ni-Ti systems. *J Mater Sci Lett.* 1992;11:1333–1337.
23. Duh JG, Dayananda MA. Interdiffusion in Fe-Ni-Cr Alloys at 1100°C. *Defect Diffus Forum.* 1991;39:1–0.
24. Kale, Bhanumurthy, Asundi. Ternary diffusion in FCC phase of Fe-Ni-Cr alloy system at 1223 K. *Mater Trans.* 1991;1034–1041.
25. Belova IV, Murch GE. Interdiffusion Data in Multicomponent Alloys as a Source of Quantitative Fundamental Diffusion Information. *Defect Diffus Forum.* 2007;263:1–10.
26. Belova IV, Murch GE. A new analysis of diffusion in ternary alloys: application to F.C.C. Fe-Ni-Cr alloys. *Acta Mater.* 2002;50:4617–4627.
27. Belova IV, Murch GE, Filipek R, et al. Theoretical analysis of experimental tracer and interdiffusion data in Cu-Ni-Fe alloys. *Acta Mater.* 2005;53:4613–4622.
28. Le Claire ADL. The analysis of grain boundary diffusion measurements. *Br J Appl Phys.* 1963;14:351–356.
29. Padilha, Rios. Decomposition of austenite in austenitic stainless steels. *ISIJ Int.* 2002;325–327.
30. Sourmail. Precipitation in creep resistant austenitic stainless steels. *Mater Sci Technol.* 2001;1–14.
31. Stoter. Thermal ageing effects in AISI type 316 stainless steel. *J Mater Sci.* 1981;1039–1051.
32. Maziasz, Busby. Properties of Austenitic Stainless Steels for Nuclear Reactor Applications. *Compr Nucl Mater.* Elsevier; 2012. page 267–283.
33. Weiss, Stickler. Phase instabilities during high temperature exposure of 316 austenitic stainless steels. *Metall Mater Trans.* 1972;851–866.
34. Lo KH, Shek CH, Lai JKL. Recent developments in stainless steels. *Mater Sci Eng R Rep.* 2009;65:39–104.
35. Lee, Maziasz, Rowcliffe. Structure and composition of phases occurring in austenitic stainless steels in thermal and irradiation environments. Oak Ridge National Lab.; 1980. Report No.: CONF-801072–11.
36. Was GS. Fundamentals of radiation materials science: metals and alloys. Berlin ; New York: Springer; 2007.
37. Malerba L. Multi-scale modelling of irradiation effects in nuclear power plant materials. *Underst Mitigating Ageing Nucl Power Plants.* Elsevier; 2010. page 456–543.
38. Matsukawa Y, Zinkle SJ. One-Dimensional Fast Migration of Vacancy Clusters in Metals. *Science.* 2007;318:959–962.
39. Tucker J, Allen T, Najafabadi R, et al. Determination of solute-interstitial interactions in Ni-Cr by first principle. *Int Conf Adv Math Comput Methods React Phys MC.* 2009;2.
40. Was GS, Busby J, Allen TR. Emulation of neutron irradiation effects with protons: validation of principle. *J Nucl Mater* 3002-3. 2002;198–216.
41. Was GS. Challenges to the use of ion irradiation for emulating reactor irradiation. *J Mater Res.* 2015;30:1158–1182.
42. Kinchin GH, Pease RS. The displacement of atoms in solids by radiation. *Rep Prog Phys* 181. 1955;

-
43. Norgett, Robinson, Torrens. A proposed method of calculating displacement dose rates. *Nucl Eng Des.* 1975;50–54.
 44. Nastasi, Michael, Mayer, et al. *Ion-solid interactions: fundamentals and applications.* Cambridge University Press. 1996.
 45. Nordlund K, Zinkle SJ, Sand AE, et al. Improving atomic displacement and replacement calculations with physically realistic damage models. *Nat Commun.* 2018
 46. Fukuya, Fujii, Nishioka, et al. Evolution of microstructure and microchemistry in cold-worked 316 stainless steels under PWR irradiation. *J Nucl Sci Technol.* 2006;159–173.
 47. Edwards DJ, Simonen EP, Bruemmer SM. Evolution of fine-scale defects in stainless steels neutron-irradiated at 275 °C. *J Nucl Mater.* 2003;317:13–31.
 48. Schibli R, Schäublin R. On the formation of stacking fault tetrahedra in irradiated austenitic stainless steels – A literature review. *J Nucl Mater.* 2013;442:S761–S767.
 49. Silcox J, Hirsch PB. Direct observations of defects in quenched gold. *Philos Mag.* 1959;4:72–89.
 50. Zinkle SJ, Seitzman LE, Wolfer WG. I. Energy calculations for pure metals. *Philos Mag A.* 1987;55:111–125.
 51. Czjzek, Seeger, Mader. Die Stabilität von Stapelfehlertetraedern in abgeschreckten kubisch-flächenzentrierten Metallen und Legierungen. *Phys Stat Sol.* 1962;558–565.
 52. Uberuaga BP, Hoagland RG, Voter AF, et al. Direct Transformation of Vacancy Voids to Stacking Fault Tetrahedra. *Phys Rev Lett [Internet].* 2007 [cited 2020];99.
 53. Yao Z, Caturla MJ, Schäublin R. Study of cascades damage in Ni by MD with different interatomic potentials. *J Nucl Mater.* 2007;367–370:298–304.
 54. Stoenescu R, Schäublin R, Gavillet D, et al. Welding-induced microstructure in austenitic stainless steels before and after neutron irradiation. *J Nucl Mater.* 2007;360:186–195.
 55. Volgin A. Characterization and understanding of ion irradiation effect on the microstructure of austenitic stainless steels. Université de Rouen; 2012.
 56. Satoh Y, Abe S, Matsui H, et al. Void swelling behavior in electron irradiated Fe–Cr–Ni model alloys under temperature variation. *J Nucl Mater.* 2007;367–370:972–976.
 57. Dai, Jia, Chen, et al. Microstructure of both as-irradiated and deformed 304L stainless steel irradiated with 800 MeV protons. *J Nucl Mater.* 2001;174–182.
 58. Kojima S, Sano Y, Yoshiie T, et al. Conversion of stacking fault tetrahedra to voids in electron irradiated Fe–Cr–Ni. *J Nucl Mater.* 1986;141–143:763–766.
 59. Niwase, Phillipp, Sigle, et al. Void formation close to stacking fault tetrahedra in heavily electron irradiated pure Ag and Cu. *J Nucl Mater.* 1999;261–265.
 60. Zinkle, Maziasz, Stoller. Dose dependence of the microstructural evolution in neutron-irradiated austenitic stainless steel. *J Nucl Mater.* 1993;266–286.
 61. Boisson M. Irradiation effects on the oxidation first stages of a 316L austenitic stainless steel. Université de Toulouse; 2018.
 62. Mansur. Correlation of neutron and heavy-ion damage: II. The predicted temperature shift if swelling with changes in radiation dose rate. *J Nucl Mater.* 1978;156–160.
 63. Gelles. A Frank loop unfaulting mechanism in fcc metals during neutron irradiation. *Dislocation Model Phys Syst.* 1981;158–162.
 64. Edwards DJ, Simonen EP, Garner FA, et al. Influence of irradiation temperature and dose gradients on the microstructural evolution in neutron-irradiated 316SS. *J Nucl Mater.* 2003;317:32–45.

-
65. He M-R, Wang S, Shi S, et al. Mechanisms of radiation-induced segregation in CrFeCoNi-based single-phase concentrated solid solution alloys. *Acta Mater.* 2017;126:182–193.
 66. Michaut B. Caractérisation et modélisation de l'évolution de la microstructure et du gonflement d'aciers austénitiques représentatifs des internes inférieurs de Réacteur à Eau Pressurisée sous irradiations aux ions. Paris Saclay; 2017.
 67. Bruemmer SM, Simonen EP, Scott PM, et al. Radiation-induced material changes and susceptibility to intergranular failure of light-water-reactor core internals. *J Nucl Mater.* 1999;274:299–314.
 68. Ayanoglu M, Motta AT. Microstructural evolution of the 21Cr32Ni model alloy under irradiation. *J Nucl Mater.* 2018;510:297–311.
 69. Askill J. Radioactive tracer diffusion data for pure metals. *CRC Handb Chem Phys.* 1989. page F54–F60.
 70. Allen, Busby, Was, et al. On the mechanism of radiation-induced segregation in austenitic Fe–Cr–Ni alloys. *J Nucl Mater.* 1998;44–58.
 71. Perks, Marwick, English. A computer code to calculate radiation-induced segregation in concentrated ternary alloys. United Kingdom: UKAEA Atomic Energy Research Establishment, Harwell. Materials Development Div.; 1986 page 42. Report No.: AERE-R-12121.
 72. Allen TR, Was GS, Kenik EA. The effect of alloy composition on radiation-induced segregation in Fe–Cr–Ni alloys. *J Nucl Mater.* 1997;244:278–294.
 73. Stepanov IA, Pechenkin VA, Konobeev YuV. Modeling of radiation-induced segregation at grain boundaries in Fe–Cr–Ni alloys. *J Nucl Mater.* 2004;329–333:1214–1218.
 74. Etienne A. Etude des effets d'irradiations et de la nanostructuration dans des aciers austénitiques inoxydables. Université de Rouen; 2009.
 75. Jiao Z, Was GS. Novel features of radiation-induced segregation and radiation-induced precipitation in austenitic stainless steels. *Acta Mater.* 2011;59:1220–1238.
 76. Kenik, Busby, Miller, et al. Origin and influence of pre-existing segregation on radiation-induced segregation in austenitic stainless steels. *Mat Res Soc Symp Proc.* 1998;445–450.
 77. Kombariah B, Edmondson PD, Wang Y, et al. Mechanisms of radiation-induced segregation around He bubbles in a Fe–Cr–Ni crystal. *J Nucl Mater.* 2019;514:139–147.
 78. Toyama T, Nozawa Y, Van Renterghem W, et al. Irradiation-induced precipitates in a neutron irradiated 304 stainless steel studied by three-dimensional atom probe. *J Nucl Mater.* 2011;418:62–68.
 79. Van Renterghem W, Al Mazouzi A, Van Dyck S. Influence of post irradiation annealing on the mechanical properties and defect structure of AISI 304 steel. *J Nucl Mater.* 2011;413:95–102.
 80. Fujii K, Fukuya K. Irradiation-induced microchemical changes in highly irradiated 316 stainless steel. *J Nucl Mater.* 2016;469:82–88.
 81. Jiao Z, Was GS. Precipitate behavior in self-ion irradiated stainless steels at high doses. *J Nucl Mater.* 2014;449:200–206.
 82. Etienne A, Radiguet B, Pareige P, et al. Tomographic atom probe characterization of the microstructure of a cold worked 316 austenitic stainless steel after neutron irradiation. *J Nucl Mater.* 2008;382:64–69.
 83. Chen Y, Chou PH, Marquis EA. Quantitative atom probe tomography characterization of microstructures in a proton irradiated 304 stainless steel. *J Nucl Mater.* 2014;451:130–136.

-
84. Boisson M, Legras L, Andrieu E, et al. Role of irradiation and irradiation defects on the oxidation first stages of a 316L austenitic stainless steel. *Corros Sci.* 2019;161:108194.
 85. Busby, Was, Kenik. Isolating the effect of radiation-induced segregation in irradiation-assisted stress corrosion cracking of austenitic stainless steels. *J Nucl Mater.* 2002;20–40.
 86. Etienne A, Radiguet B, Cunningham NJ, et al. Atomic scale investigation of radiation-induced segregation in austenitic stainless steels. *J Nucl Mater.* 2010;406:244–250.
 87. Liu X, He L, Yan H, et al. A transmission electron microscopy study of EBR-II neutron-irradiated austenitic stainless steel 304 and nickel-base alloy X-750. *J Nucl Mater.* 2020;528:151851.
 88. Ardell AJ. Radiation-Induced Solute Segregation in Alloys. In: Ghetta V, Gorse D, Mazière D, et al., editors. *Mater Issues Gener IV Syst.* Dordrecht: Springer Netherlands; 2008
 89. Nastar, Soisson. Radiation-induced segregation. *Compr Nucl Mater.* Elsevier; 2012. page 471–496.
 90. Was GS, Wharry JP, Frisbie B, et al. Assessment of radiation-induced segregation mechanisms in austenitic and ferritic–martensitic alloys. *J Nucl Mater.* 2011;411:41–50.
 91. Fukuya K. Current understanding of radiation-induced degradation in light water reactor structural materials. *J Nucl Sci Technol.* 2013;50:213–254.
 92. Wiedersich, Okamoto, Lam. A theory of radiation-induced segregation in concentrated alloys. *J Nucl Mater.* 1979;98–108.
 93. Lam, Kumar, Wiedersich. Kinetics of radiation-induced segregation in ternary alloys. 1982. page 985.
 94. Dimitrov C, Huguenin, Moser, et al. Electron-irradiation induced defects in an Fe9Cr16Ni75 austenitic alloy. *J Nucl Mater.* 1990;22–34.
 95. Dimitrov O, Dimitrov C. Defect recovery in irradiated high-purity austenitic Fe-Cr-Ni alloys: activation energies and dependence on initial defect concentration. *J Nucl Mater.* 1982;39–47.
 96. Dimitrov C, Dimitrov O. Composition dependence of defect properties in electron-irradiated Fe-Cr-Ni solid solutions. *J Phys F Met Phys.* 1984;793–811.
 97. Dimitrov C, Dimitrov O. Influence of nickel concentration on point defect migration in high-nickel Fe-Cr-Ni alloys. *J Nucl Mater.* 1988;21–29.
 98. Benkaddour, Dimitrov C, Dimitrov O. Influence of chromium concentration on point defect properties in austenitic Fe-Cr-Ni alloys. *J Nucl Mater.* 1994;118–126.
 99. Watanabe, Sakaguchi, Kurome, et al. On the mechanism of radiation-induced segregation. *J Nucl Mater.* 1997;251–253.
 100. Liu, Tsai, Kai. Proton irradiation induced phase transformation in AISI 304L stainless steel. *Scr Metall Mater.* 1994;547–552.
 101. Michalička J, Jiao Z, Was G. Radiation-Induced Precipitates in a Self-ion Irradiated Cold-Worked 316 Austenitic Stainless Steel Used for PWR Baffle-Bolts. In: Jackson JH, Paraventi D, Wright M, editors. *Proc 18th Int Conf Environ Degrad Mater Nucl Power Syst – Water React.* Cham: Springer International Publishing; 2018
 102. Maziasz. Effects of helium content of microstructural development in Type 316 stainless steel under neutron irradiation. Oak Ridge National Lab; 1985. Report No.: ORNL-6121.
 103. Suk, Yoon, Hong, et al. Formation of phosphides in P-doped 304L stainless steel. *Mater Lett.* 1992;161–165.

-
104. Maziasz. Formation and stability of radiation-induced phases in neutron-irradiated austenitic and ferritic steels. *J Nucl Mater.* 1989;95–115.
 105. Renault Laborne A, Gavaille P, Malaplate J, et al. Correlation of radiation-induced changes in microstructure/microchemistry, density and thermo-electric power of type 304L and 316 stainless steels irradiated in the Phénix reactor. *J Nucl Mater.* 2015;460:72–81.
 106. Allen TR, Was GS. Modeling radiation-induced segregation in austenitic Fe–Cr–Ni alloys. *Acta Mater.* 1998;46:3679–3691.
 107. Chang LL, Giessen BC, editors. *Synthetic modulated structures.* Orlando: Academic Press; 1985.
 108. Herbig M, Choi P, Raabe D. Combining structural and chemical information at the nanometer scale by correlative transmission electron microscopy and atom probe tomography. *Ultramicroscopy.* 2015;153:32–39.
 109. Barr CM, Felfer PJ, Cole JJ, et al. Observation of oscillatory radiation induced segregation profiles at grain boundaries in neutron irradiated 316 stainless steel using atom probe tomography. *J Nucl Mater.* 2018;504:181–190.
 110. Harte A, Babu RP, Hirst CA, et al. Understanding irradiation-induced nanoprecipitation in zirconium alloys using parallel TEM and APT. *J Nucl Mater.* 2018;510:460–471.
 111. Mazumder B, Parish CM, Miller MK. Correlative TEM and APT of Helium Bubbles in Ion-Irradiated RAFM Steel. *Microsc Microanal.* 2015;21:587–588.
 112. Reyes-Gasga J, García-García R. Analysis of the electron-beam radiation damage of TEM samples in the acceleration energy range from 0.1 to 2MeV using the standard theory for fast electrons. *Radiat Phys Chem.* 2002;64:359–367.
 113. Krumeich F. *Properties of Electrons, their Interactions with Matter and Applications in Electron Microscopy.* 2011;
 114. Ul-Hamid A. *A Beginners' Guide to Scanning Electron Microscopy.* Cham: Springer International Publishing; 2018
 115. Williams DB, Carter CB. *Transmission electron microscopy: a textbook for materials science.* 2nd ed. New York: Springer; 2008.
 116. Rafailović LD, Gammer C, Ebner C, et al. High density of genuine growth twins in electrodeposited aluminum. *Sci Adv.* 2019
 117. Laplanche G, Kostka A, Reinhart C, et al. Reasons for the superior mechanical properties of medium-entropy CrCoNi compared to high-entropy CrMnFeCoNi. *Acta Mater.* 2017;128:292–303.
 118. Hren JJ, Goldstein JI, Joy DC, editors. *Introduction to Analytical Electron Microscopy.* Boston, MA: Springer US; 1979
 119. Egerton RF. *Electron Energy-Loss Spectroscopy in the Electron Microscope.* Boston, MA: Springer US; 2011
 120. Jublot-Leclerc S, Lescoat M-L, Fortuna F, et al. TEM study of the nucleation of bubbles induced by He implantation in 316L industrial austenitic stainless steel. *J Nucl Mater.* 2015;466:646–652.
 121. Schäublin R, Meng X, Stobbs WM. Weak beam under convergent beam illumination. *Ultramicroscopy.* 2000;83:145–157.
 122. Ulmer CJ, Motta AT. Characterization of faulted dislocation loops and cavities in ion irradiated alloy 800H. *J Nucl Mater.* 2018;498:458–467.

-
123. Yao B, Edwards DJ, Kurtz RJ, et al. Multislice simulation of transmission electron microscopy imaging of helium bubbles in Fe. *J Electron Microsc (Tokyo)*. 2012;61:393–400.
 124. Krumeich F, Müller E, Wepf RA. Phase-contrast imaging in aberration-corrected scanning transmission electron microscopy. *Micron*. 2013;49:1–14.
 125. Parish CM, Miller MK. Aberration-Corrected X-Ray Spectrum Imaging and Fresnel Contrast to Differentiate Nanoclusters and Cavities in Helium-Irradiated Alloy 14YWT. *Microsc Microanal*. 2014;20:613–626.
 126. Jenkins ML, Cockayne DJH, Whelan MJ. The determination of the geometry and nature of small Frank loops using the weak-beam method. *J Microsc*. 1973;98:155–164.
 127. Schäublin * R, Yao Z, Baluc N, et al. Irradiation-induced stacking fault tetrahedra in fcc metals. *Philos Mag*. 2005;85:769–777.
 128. Lu C, Jin K, Béland LK, et al. Direct Observation of Defect Range and Evolution in Ion-Irradiated Single Crystalline Ni and Ni Binary Alloys. *Sci Rep*. 2016;6:19994.
 129. Jenkins ML. Characterisation of radiation-damage microstructures by TEM. *J Nucl Mater*. 1994;216:124–156.
 130. Fultz, Howe. *Transmission electron microscopy and diffractometry of materials*. Springer Science & Business Media; 2012.
 131. Schäublin R. Chapter 11 TEM imaging of crystal defects. CIME-EPFL
 132. Stubbins, Heuser, Hosemann, et al. *Fundamental Studies of Irradiation-Induced Modifications in Microstructural Evolution and Mechanical Properties of Advanced Alloys*. Univ. of Illinois at Urbana-Champaign; 2018. Report No.: 14-6762.
 133. Idrissi H, Turner S, Mitsuhashi M, et al. Point Defect Clusters and Dislocations in FIB Irradiated Nanocrystalline Aluminum Films: An Electron Tomography and Aberration-Corrected High-Resolution ADF-STEM Study. *Microsc Microanal*. 2011;17:983–990.
 134. Garnier J, Bréchet Y, Delnondedieu M, et al. Irradiation creep of SA 304L and CW 316 stainless steels: Mechanical behaviour and microstructural aspects. Part I: Experimental results. *J Nucl Mater*. 2011;413:63–69.
 135. Bailey JE, Hirsch PB. The dislocation distribution, flow stress, and stored energy in cold-worked polycrystalline silver. *Philos Mag*. 1960;5:485–497.
 136. Zhu Y, Ophus C, Toloczko MB, et al. Towards bend-contour-free dislocation imaging via diffraction contrast STEM. *Ultramicroscopy*. 2018;193:12–23.
 137. Phillips PJ, Mills MJ, De Graef M. Systematic row and zone axis STEM defect image simulations. *Philos Mag*. 2011;91:2081–2101.
 138. Parish CM, Field KG, Certain AG, et al. Application of STEM characterization for investigating radiation effects in BCC Fe-based alloys. *J Mater Res*. 2015;30:1275–1289.
 139. Edmondson PD, Parish CM, Nanstad RK. Using complimentary microscopy methods to examine Ni-Mn-Si-precipitates in highly-irradiated reactor pressure vessel steels. *Acta Mater*. 2017;134:31–39.
 140. van Dalen ME, Dunand DC, Seidman DN. Effects of Ti additions on the nanostructure and creep properties of precipitation-strengthened Al-Sc alloys. *Acta Mater*. 2005;53:4225–4235.
 141. Heczko M, Esser BD, Smith TM, et al. On the origin of extraordinary cyclic strengthening of the austenitic stainless steel Sanicro 25 during fatigue at 700 °C. *J Mater Res*. 2017;32:4342–4353.
 142. Gault B, Moody MP, Cairney JM, et al. Atom probe crystallography. *Mater Today*. 2012;15:378–386.

-
143. Kingham. The post-ionization of field evaporated ions: A theoretical explanation of multiple charge states. *Surf Sci.* 1982;273–301.
 144. Da Costa G, Vurpillot F, Bostel A, et al. Design of a delay-line position-sensitive detector with improved performance. *Rev Sci Instrum.* 2005;76:013304.
 145. Bémont E, Bostel A, Bouet M, et al. Effects of incidence angles of ions on the mass resolution of an energy compensated 3D atom probe. *Ultramicroscopy.* 2003;95:231–238.
 146. Kelly TF, Camus PP, Larson DJ, et al. On the many advantages of local-electrode atom probes. *Ultramicroscopy.* 1996;62:29–42.
 147. Gault B, Vurpillot F, Vella A, et al. Design of a femtosecond laser assisted tomographic atom probe. *Rev Sci Instrum.* 2006;77:043705.
 148. Gault B, Moody MP, Cairney JM, et al. *Atom Probe Microscopy*. New York, NY: Springer New York; 2012 [cited 2019].
 149. De Geuser F, Gault B, Bostel A, et al. Correlated field evaporation as seen by atom probe tomography. *Surf Sci.* 2007;601:536–543.
 150. Saxey DW. Correlated ion analysis and the interpretation of atom probe mass spectra. *Ultramicroscopy.* 2011;111:473–479.
 151. Pareige P. Etude à la sonde atomique de l'évolution microstructurale sous irradiation d'alliages ferritiques FeCu et d'aciers de cuve de réacteurs nucléaires. Université de Rouen; 1994.
 152. Meisenkothen F, Steel EB, Prosa TJ, et al. Effects of detector dead-time on quantitative analyses involving boron and multi-hit detection events in atom probe tomography. *Ultramicroscopy.* 2015;159:101–111.
 153. Bas P, Bostel A, Deconihout B, et al. A general protocol for the reconstruction of 3D atom probe data. *Appl Surf Sci.* 1995;87–88:298–304.
 154. Hatzoglou C, Da Costa G, Vurpillot F. Enhanced dynamic reconstruction for atom probe tomography. *Ultramicroscopy.* 2019;197:72–82.
 155. Vurpillot F, Bostel A, Blavette D. Trajectory overlaps and local magnification in three-dimensional atom probe. *Appl Phys Lett.* 2000;76:3127–3129.
 156. Lefebvre-Ulrikson W, editor. *Atom probe tomography: put theory into practice*. London: Academic Press; 2016.
 157. Wang X, Hatzoglou C, Sneed B, et al. Interpreting nanovoids in atom probe tomography data for accurate local compositional measurements. *Nat Commun.* 2020;11:1022.
 158. Takahashi J, Kawakami K, Raabe D. Comparison of the quantitative analysis performance between pulsed voltage atom probe and pulsed laser atom probe. *Ultramicroscopy.* 2017;175:105–110.
 159. Larson DJ, Prosa TJ, Ulfing RM, et al. *Local Electrode Atom Probe Tomography*. New York, NY: Springer New York; 2013.
 160. Hatzoglou C, Rouland S, Radiguet B, et al. Preferential Evaporation in Atom Probe Tomography: An Analytical Approach. *Microsc Microanal.* 2020;26:689–698.
 161. Philippe T, De Geuser F, Duguay S, et al. Clustering and nearest neighbour distances in atom-probe tomography. *Ultramicroscopy.* 2009;109:1304–1309.
 162. Lindgren K, Stiller K, Efsing P, et al. On the Analysis of Clustering in an Irradiated Low Alloy Reactor Pressure Vessel Steel Weld. *Microsc Microanal.* 2017;23:376–384.

-
163. Hyde JM, DaCosta G, Hatzoglou C, et al. Analysis of Radiation Damage in Light Water Reactors: Comparison of Cluster Analysis Methods for the Analysis of Atom Probe Data. *Microsc Microanal.* 2017;23:366–375.
 164. Hatzoglou C, Radiguet B, Vurpillot F, et al. A chemical composition correction model for nanoclusters observed by APT - Application to ODS steel nanoparticles. *J Nucl Mater.* 2018;505:240–248.
 165. Haberfehlner G, Orthacker A, Albu M, et al. Nanoscale voxel spectroscopy by simultaneous EELS and EDS tomography. *Nanoscale.* 2014;6:14563–14569.
 166. Piecuch M. Diffusion in multilayers. *Rev Phys Appliquée.* 1988;23:1727–1732.
 167. Greer AL. Measurements of atomic diffusion using metallic multilayers. *Curr Opin Solid State Mater Sci.* 1997;2:300–304.
 168. Murakami M, Segmüller A, Tu K-N. X-Ray Diffraction Analysis of Diffusion in Thin Films. *Treatise Mater Sci Technol.* Elsevier; 1988. page 201–248.
 169. Tsakalakos T. Composition-modulated films: New materials for studying stability and critical phenomena in solid solutions. *Thin Solid Films.* 1981;86:79–90.
 170. Cahn JW, Hilliard JE. Free Energy of a Nonuniform System. I. Interfacial Free Energy. *J Chem Phys.* 1958;28:258–267.
 171. Cook H_ E, De Fontaine D, Hilliard JE. A model for diffusion on cubic lattices and its application to the early stages of ordering. *Acta Metall.* 1969;17:765–773.
 172. Paulson WM, Hilliard JE. Interdiffusion in composition-modulated copper-gold thin films. *J Appl Phys.* 1977;48:2117–2123.
 173. DuMond J, Youtz JP. An X-Ray Method of Determining Rates of Diffusion in the Solid State. *J Appl Phys.* 1940;11:357–365.
 174. Cook HE, Hilliard JE. Effect of Gradient Energy on Diffusion in Gold-Silver Alloys. *J Appl Phys.* 1969;40:2191–2198.
 175. Hillert M. A solid-solution model for inhomogeneous systems. *Acta Metall.* 1961;9:525–535.
 176. Cahn JW. On spinodal decomposition in cubic crystals. *Acta Metall.* 1962;10:179–183.
 177. Cook HE, De Fontaine D. On the elastic free energy of solid solutions—II. Influence of the effective modulus on precipitation from solution and the order-disorder reaction. *Acta Metall.* 1971;19:607–616.
 178. Nastar M. Atomic diffusion theory challenging the Cahn-Hilliard method. *Phys Rev B.* 2014
 179. Murakami M, de Fontaine D, Sanchez JM, et al. Diffusion in AgAuPd thin film microcouples. *Acta Metall.* 1974;22:709–719.
 180. Murakami M, De Fontaine D, Sanchez JM, et al. Ternary diffusion in multilayer Ag-Au-Cu thin films. *Thin Solid Films.* 1975;25:465–482.
 181. Chaudhuri J, Tsakalakos T. Measurements of interdiffusivities in Cu/NiFe ternary alloy thin films. *Acta Metall.* 1985;33:1939–1943.
 182. Morral JE, Cahn JW. Spinodal decomposition in ternary systems. *Acta Metall.* 1971;19:1037–1045.
 183. Bhattacharyya S, Abinandanan TA. A study of phase separation in ternary alloys. *Bull Mater Sci.* 2003;26:193–197.
 184. Honjo M, Saito Y. Numerical simulation of phase separation in Fe–Cr binary and Fe–Cr–Mo ternary alloys with use of the Cahn–Hilliard equation. *ISIJ Int* 409. 2000;914–919.
 185. Svedberg EB, Howard KJ, Bønsager MC, et al. Diffusion in Co₉₀Fe₁₀/Ru multilayers. *J Appl Phys.* 2003;94:993–1000.

-
186. Morral JE, Cahn JW. Spinodal decomposition in ternary systems. *Acta Metall.* 1971;19:1037–1045.
 187. Chopra KL, Kaur I, editors. *Thin Film Device Applications*. Boston: Springer US; 1983.
 188. Billard A, Perry F. Pulvérisation cathodique magnétron. *Tech L'Ingénieur*. 2005;M1654 V1:1–17.
 189. Martin PM, editor. *Handbook of deposition technologies for films and coatings: science, applications and technology*. 3. ed. Amsterdam: Elsevier; 2010.
 190. Wasa K, Kanno I, Kotera H, editors. *Handbook of sputter deposition technology: fundamentals and applications for functional thin films, nanomaterials and MEMS*. 2nd ed. Waltham, MA: William Andrew; 2012.
 191. Campbell CE, Boettinger WJ, Kattner UR. Development of a diffusion mobility database for Ni-base superalloys. *Acta Mater.* 2002;50:775–792.
 192. Gheno T, Jomard F, Desgranges C, et al. Tracer diffusion of Cr in Ni and Ni-22Cr studied by SIMS. *Materialia*. 2018;3:145–152.
 193. Huang L, Nastar M, Schuler T, et al. Multi-scale modeling of the effects of temperature, radiation flux and sink strength on point-defect and solute redistribution in dilute Fe-based alloys. *arXiv:200902971*. 2020;
 194. Nastar M. Segregation at grain boundaries: from equilibrium to irradiation induced steady states. *Philos Mag.* 2005;85:641–647.
 195. Billard A. Magnetron sputtering deposition of Ni/Ni20Cr, Cr/Ni20Cr and Fe35Ni25Cr/Fe25Ni20Cr nanometric scale multilayer coatings. 2018 page 1–15.
 196. Cantor B, Cahn RW. Metastable alloy phases by co-sputtering. *Acta Metall.* 1976;24:845–852.
 197. Malavasi S, Oueldennaoua A, Foos M, et al. Metastable amorphous and crystalline (α, σ) phase in physical vapor deposited Fe-(Cr)-Ni-(C) deposits. *J Vac Sci Technol Vac Surf Films*. 1987;5:1888–1891.
 198. Rar A, Frafjord JJ, Fowlkes JD, et al. PVD synthesis and high-throughput property characterization of Ni-Fe-Cr alloy libraries. *Meas Sci Technol.* 2005;16:46–53.
 199. Colignon Y. Étude par sonde atomique tomographique de la décomposition spinodale dans le système Fe-Cr en couches minces. Aix-Marseille Université; 2015.
 200. Nicolet M-A. Diffusion barriers in thin films. *Thin Solid Films*. 1978;52:415–443.
 201. Liu J, Niu R, Gu J, et al. Effect of Ion Irradiation Introduced by Focused Ion-Beam Milling on the Mechanical Behaviour of Sub-Micron-Sized Samples. *Sci Rep.* 2020;10:10324.
 202. Muraishi S, Aizawa T, Kuwahara H. Fabrication of nanostructured titanium thin films via N ion implantation and postannealing treatment. *Surf Coat Technol.* 2004;188–189:260–264.
 203. Thompson CV. Structure Evolution During Processing of Polycrystalline Films. *Annu Rev Mater Sci.* 2000;30:159–190.
 204. Zhang X, Misra A, Wang H, et al. Enhanced hardening in Cu/330 stainless steel multilayers by nanoscale twinning. *Acta Mater.* 2004;52:995–1002.
 205. Hultman L, Petrov I, Adibi F, et al. Transmission electron microscopy studies of microstructural evolution, defect structure, and phase transitions in polycrystalline and epitaxial Ti(1-x)AlxN and TiN films grown by reactive magnetron sputter deposition. *Thin Solid Films*. 1991;205:153–164.

-
206. Hultman L, Barnett SA, Sundgren JE, et al. Growth of epitaxial TiN films deposited on MgO (100) by reactive magnetron sputtering: The role of low-energy ion irradiation during deposition. *J Cryst Growth*. 1988;92:639–656.
 207. Herzog L, Egger U, Breitenstein O, et al. Defects in GaAs after Si indiffusion and annealing: A TEM and CL study. *Mater Sci Eng B*. 1995;30:43–53.
 208. Zhang X, Hattar K, Chen Y, et al. Radiation damage in nanostructured materials. *Prog Mater Sci*. 2018;96:217–321.
 209. Demkowicz MJ, Anderoglu O, Zhang X, et al. The influence of $\Sigma 3$ twin boundaries on the formation of radiation-induced defect clusters in nanotwinned Cu. *J Mater Res*. 2011;26:1666–1675.
 210. Li J, Xie DY, Xue S, et al. Superior twin stability and radiation resistance of nanotwinned Ag solid solution alloy. *Acta Mater*. 2018;151:395–405.
 211. Zhang Y, Ishimaru M, Varga T, et al. Nanoscale engineering of radiation tolerant silicon carbide. *Phys Chem Chem Phys*. 2012;14:13429.
 212. Kondo S, Katoh Y, Snead LL. Analysis of grain boundary sinks and interstitial diffusion in neutron-irradiated SiC. *Phys Rev B*. 2011;83:075202.
 213. Mao S, Shu S, Zhou J, et al. Quantitative comparison of sink efficiency of Cu–Nb, Cu–V and Cu–Ni interfaces for point defects. *Acta Mater*. 2015;82:328–335.
 214. Chakraborty D, Aidhy DS. Cr-induced fast vacancy cluster formation and high Ni diffusion in concentrated Ni–Fe–Cr alloys. *J Alloys Compd*. 2017;725:449–460.
 215. Aidhy DS, Lu C, Jin K, et al. Point defect evolution in Ni, NiFe and NiCr alloys from atomistic simulations and irradiation experiments. *Acta Mater*. 2015;99:69–76.
 216. Schouteden K, Amin-Ahmadi B, Li Z, et al. Electronically decoupled stacking fault tetrahedra embedded in Au(111) films. *Nat Commun*. 2016;7:14001.
 217. Garosshen TJ, McCarthy GP. Low temperature carbide precipitation in a nickel base superalloy. *Metall Trans A*. 1985;16:1213–1223.
 218. Lee T-H, Suh H-Y, Lee J-H. Precipitation behavior of $M_{23}C_6$ carbides and its effect on mechanical properties of Ni-based Alloy 690. *J Nucl Sci Technol*. 2020;1–6.
 219. Drolet JP, Galibois A. The impurity-drag effect on grain growth. *Acta Metall*. 1968;16:1387–1399.
 220. Marty A, Bessiere M, Bley F, et al. Determination of long range order in Ni-Base ternary alloys by X-ray anomalous diffraction using synchrotron radiation. *Acta Metall Mater*. 1990;38:345–350.
 221. Marwick AD, Piller RC, Cranshaw TE. The influence of Cr additions on the ordering of Fe–Cr–Ni alloys near the Ni_3Fe composition. *J Phys F Met Phys*. 1987;17:37–45.
 222. Erdélyi Z, Szabó IA, Beke DL. Interface Sharpening instead of Broadening by Diffusion in Ideal Binary Alloys. *Phys Rev Lett*. 2002;89:165901.
 223. Roussel J-M, Bellon P. Interface sharpening and broadening during annealing of Cu / Ni multilayers: A kinetic Monte Carlo study. *Phys Rev B*. 2006;73:085403.
 224. Quan Z, Naundorf V, Wollenberger H. Diffusion and phase stability in ion irradiated Cu/Pd thin films. *J Nucl Mater*. 1992;199:12–21.
 225. Damcott, Allen, Was. Dependence of radiation-induced segregation on dose, temperature and alloy composition in austenitic alloys. *J Nucl Mater*. 1995;97–107.
 226. Alexander DE, Fullerton EE, Baldo PM, et al. Neutron-induced collision cascade mixing in Nb/V superlattices. *Nucl Instrum Methods Phys Res*. 1994;344–348.

-
227. Zhang X, Misra A, Schulze RK, et al. Critical factors that determine face-centered cubic to body-centered cubic phase transformation in sputter-deposited austenitic stainless steel films. *J Mater Res.* 2004;19:1696–1702.
 228. Busby JT, Allen TR, Carter RD, et al. Dose Dependence of Radiation Induced Segregation in Proton Irradiated Austenitic Alloys. *MRS Proc.* 1996;439:563.
 229. Shevchuk YuA. Phenomenological description of the stability of a ternary alloy under irradiation. *At Energy.* 1994;76:96–100.
 230. Zotov N, Ludwig A. Atomic mechanisms of interdiffusion in metallic multilayers. *Mater Sci Eng C.* 2007;27:1470–1474.
 231. Venos R, Pamler W, Hoffmann H. Grain boundary diffusion in Ni-Cu multilayer films. *Thin Solid Films.* 1988;162:155–160.
 232. Belova IV, Murch GE. Diffusion in nanocrystalline materials. *J Phys Chem Solids.* 2003;6.
 233. Hashim I, Atwater HA, Kung KTY, et al. Evolution of structural and magnetic properties in Ta/Ni₈₁Fe₁₉ multilayer thin films. *J Appl Phys.* 1993;74:458–464.
 234. McIntyre PC, Wu DT, Nastasi M. Interdiffusion in epitaxial Co/Pt multilayers. *J Appl Phys.* 1997;81:637–645.
 235. Viladot D, Véron M, Gemmi M, et al. Orientation and phase mapping in the transmission electron microscope using precession-assisted diffraction spot recognition: state-of-the-art results. *J Microsc.* 2013;252:23–34.
 236. Leff AC, Weinberger CR, Taheri ML. Estimation of dislocation density from precession electron diffraction data using the Nye tensor. *Ultramicroscopy.* 2015;153:9–21.
 237. Ortel E, Häusler I, Österle W, et al. In-depth structural and chemical characterization of engineered TiO₂ films: Characterization of engineered TiO₂ films. *Surf Interface Anal.* 2016;48:664–669.
 238. Zhou X, Thompson GB. The influence of alloying interactions on thin film growth stresses. *Appl Surf Sci.* 2019;463:545–555.
 239. Schöngrundner R, Tremel R, Antretter T, et al. Critical assessment of the determination of residual stress profiles in thin films by means of the ion beam layer removal method. *Thin Solid Films.* 2014;564:321–330.
 240. Tremel R, Kozic D, Zechner J, et al. High resolution determination of local residual stress gradients in single- and multilayer thin film systems. *Acta Mater.* 2016;103:616–623.
 241. Herbig M. Spatially correlated electron microscopy and atom probe tomography: Current possibilities and future perspectives. *Scr Mater.* 2018;148:98–105.
 242. Stoller RE. Modeling dislocation evolution in irradiated alloys. *Metall Trans A.* 1990;21:1829–1837.
 243. Yin X, Sun YH, Yang YD, et al. Inclusion evolution during refining and continuous casting of 316L stainless steel. *Ironmak Steelmak.* 2016;43:533–540.
 244. Legras L, Lescoat M-L, Jublot-Leclerc S, et al. Optimisation of TEM preparation in metallic materials using low voltage ions. 2016.
 245. Pokor C, Brechet Y, Dubuisson P, et al. Irradiation damage in 304 and 316 stainless steels: experimental investigation and modeling. Part II: Irradiation induced hardening. *J Nucl Mater.* 2004;326:30–37.
 246. Hashimoto N, Wakai E, Robertson JP. Relationship between hardening and damage structure in austenitic stainless steel 316LN irradiated at low temperature in the HFIR. *J Nucl Mater.* 1999;273:95–101.

-
247. Vodárek V. Stability of Z-phase and M₆X in creep-resistant steels. *Scr Mater.* 2012;66:678–681.
 248. Vodarek V. Z phase stability in AISI 316LN + Nb austenitic steels during creep at 650°C. *Mater Adv Power Eng.* 2010;10.
 249. Gentils A, Cabet C. Investigating radiation damage in nuclear energy materials using JANNuS multiple ion beams. *Nucl Instrum Methods Phys Res Sect B Beam Interact Mater At.* 2019;447:107–112.
 250. Cottureau E, Camplan J, Chaumont J, et al. ARAMIS: An ambidextrous 2 MV accelerator for IBA and MeV implantation. *Nucl Instrum Methods Phys Res Sect B Beam Interact Mater At.* 1990;45:293–295.
 251. Bacri C-O, Bachelet C, Baumier C, et al. SCALP, a platform dedicated to material modifications and characterization under ion beam. *Nucl Instrum Methods Phys Res Sect B Beam Interact Mater At.* 2017;406:48–52.
 252. Stoller RE, Toloczko MB, Was GS, et al. On the use of SRIM for computing radiation damage exposure. *Nucl Instrum Methods Phys Res Sect B Beam Interact Mater At.* 2013;310:75–80.
 253. Fu EG, Misra A, Wang H, et al. Interface enabled defects reduction in helium ion irradiated Cu/V nanolayers. *J Nucl Mater.* 2010;407:178–188.
 254. Hogan CL, Sawyer RB. The Thermal Conductivity of Metals at High Temperature. *J Appl Phys.* 1952;23:177–180.
 255. Redmond RF, Lones J. Enthalpies and heat capacities of stainless steel (316). zirconium. and lithium at elevated temperatures. Oak Ridge National Lab.; 1952. Report No.: 1342.
 256. Beck L, Serruys Y, Miro S, et al. Ion irradiation and radiation effect characterization at the JANNUS-Saclay triple beam facility. *J Mater Res.* 2015;30:1183–1194.
 257. Brailsford AD, Mansur LK. The effect of precipitate-matrix interface sinks on the growth of voids in the matrix. *J Nucl Mater.* 1981;104:1403–1408.
 258. Hatzoglou C, Vurpillot F. A Mesoscopic Field Evaporation Model. *Microsc Microanal.* 2019;25:286–287.
 259. Herbig M, Kumar A. Removal of hydrocarbon contamination and oxide films from atom probe specimens. *Microsc Res Tech.* 2020;jemt.23587.
 260. Makineni SK, Lenz M, Kontis P, et al. Correlative Microscopy—Novel Methods and Their Applications to Explore 3D Chemistry and Structure of Nanoscale Lattice Defects: A Case Study in Superalloys. *JOM.* 2018;70:1736–1743.
 261. Baik S-I, Isheim D, Seidman DN. Systematic approaches for targeting an atom-probe tomography sample fabricated in a thin TEM specimen: Correlative structural, chemical and 3-D reconstruction analyses. *Ultramicroscopy.* 2018;184:284–292.
 262. Zschiesche H, Campos APC, Dominici C, et al. Correlated TKD/EDS - TEM - APT analysis on selected interfaces of CoSi₂ thin films. *Ultramicroscopy.* 2019;206:112807.
 263. Mitchell DRG. Contamination mitigation strategies for scanning transmission electron microscopy. *Micron.* 2015;73:36–46.
 264. Burke MG, Watanabe M, Williams DB, et al. Quantitative characterization of nanoprecipitates in irradiated low-alloy steels: advances in the application of FEG-STEM quantitative microanalysis to real materials. *J Mater Sci.* 2006;41:4512–4522.

-
265. Barcellini C, Harrison RW, Dumbill S, et al. Evolution of radiation-induced lattice defects in 20/25 Nb-stabilised austenitic stainless steel during in-situ proton irradiation. *J Nucl Mater.* 2019;514:90–100.
 266. Edwards D, Garner FA, Simonen EP, et al. Characterization of Neutron-Irradiated 300-Series Stainless Steels to Assess Mechanisms of Irradiation-Assisted Stress Corrosion Cracking: Volume 2: Core Components. EPRI; 2001.
 267. Yang Y, Field KG, Allen TR, et al. Roles of vacancy/interstitial diffusion and segregation in the microchemistry at grain boundaries of irradiated Fe–Cr–Ni alloys. *J Nucl Mater.* 2016;473:35–53.
 268. Bhattacharya A, Meslin E, Henry J, et al. Chromium enrichment on the habit plane of dislocation loops in ion-irradiated high-purity Fe–Cr alloys. *Acta Mater.* 2014;78:394–403.
 269. Hudson. Void formation in solution-treated AISI 316 and 321 stainless steels under 46.5 MeV Ni⁶⁺ irradiation. *J Nucl Mater.* 1976;89–106.
 270. Williams. The effect of soluble carbon on void swelling and low dose dislocation structures in type 316 austenitic stainless steel irradiated with 46.5 MeV Ni⁶⁺ ions. *J Nucl Mater.* 1980;217–225.
 271. Sindelar, Kulcinski, Dodd. Heterogeneous void formation in 14 MeV nickel-ion irradiated 316 SS. *J Nucl Mater.* 1985;544–548.
 272. Katoh, Stoller, Kohno, et al. The influence of He/dpa ratio and displacement rate on microstructural evolution: a comparison of theory and experiment. *J Nucl Mater.* 1994;290–302.
 273. Gan J, Simonen EP, Bruemmer SM, et al. The effect of oversized solute additions on the microstructure of 316SS irradiated with 5 MeV Ni⁺⁺ ions or 3.2 MeV protons. *J Nucl Mater.* 2004;325:94–106.
 274. Etienne A, Hernández-Mayoral M, Genevois C, et al. Dislocation loop evolution under ion irradiation in austenitic stainless steels. *J Nucl Mater.* 2010;400:56–63.
 275. Jublot-Leclerc S, Li X, Legras L, et al. Microstructure of Au-ion irradiated 316L and FeNiCr austenitic stainless steels. *J Nucl Mater.* 2016;480:436–446.
 276. Jin H-H, Ko E, Lim S, et al. Effects of helium and hydrogen on radiation-induced microstructural changes in austenitic stainless steel. *Nucl Instrum Methods Phys Res Sect B Beam Interact Mater At.* 2015;359:69–74.
 277. Le Millier. Fragilisation des aciers inoxydables austénitiques sous irradiation: évolution de la microstructure et amorçage de la corrosion sous contrainte assistée par l’irradiation en milieu REP. Ecole Nationale Supérieure des Mines de Paris; 2014.
 278. Kato T, Takahashi H, Izumiya M. Grain boundary segregation under electron irradiation in austenitic stainless steels modified with oversized elements. *J Nucl Mater.* 1992;189:167–174.
 279. Ardell AJ, Bellon P. Radiation-induced solute segregation in metallic alloys. *Curr Opin Solid State Mater Sci.* 2016;20:115–139.
 280. Tan L, Stoller RE, Field KG, et al. Microstructural Evolution of Type 304 and 316 Stainless Steels Under Neutron Irradiation at LWR Relevant Conditions. *JOM.* 2016;68:517–529.
 281. Pedraza, Maziasz. Void-precipitate association during neutron irradiation of austenitic stainless steel. Oak Ridge National Laboratory; 1987. Report No.: CONF-860605-33.
 282. Ercius P, Alaidi O, Rames MJ, et al. Electron Tomography: A Three-Dimensional Analytic Tool for Hard and Soft Materials Research. *Adv Mater.* 2015;27:5638–5663.

-
283. Guo W, Sneed BT, Zhou L, et al. Correlative Energy-Dispersive X-Ray Spectroscopic Tomography and Atom Probe Tomography of the Phase Separation in an Alnico 8 Alloy. *Microsc Microanal.* 2016;22:1251–1260.



APPENDIX



Generation IV Materials Maturity – The GEMMA project

In 2015, Paris Agreement dealt to contain global warming below 2°C while keeping the objective to limit it to 1.5°C. Through the Net-Zero 2050 initiative of the European Climate Foundation³, a clean energy transition is engaged in Europe to achieve a net-zero greenhouse gas emissions by 2050. Nuclear fission is a low-carbon energy source involved in the decarbonisation energy mix in Europe. Ageing of current nuclear reactors implies to propose in the next decades a new generation of industrial reactors with the highest performance in terms of safety, sustainability and economy.

Launched in 2000 by the United States Department of Energy (DOE), the Generation IV International Forum⁴ (GIF) ambitioned to coordinate research and development to deploy next generation of nuclear reactors. Among more than a hundred submitted projects, GIF selected in 2002 the six more promising systems based on several criteria:

- Economic and environmental sustainability, by upcycling used fuel to new fuel, reducing nuclear wastes lifetime and toxicity;
- Competitiveness, by reducing energy production costs and being able to provide other type of energy products (e.g. hydrogen, heating);
- Safety and reliability, by improving accident management and minimization of consequences;
- Proliferation resistance and physical protection, by reducing the produced amount of plutonium and increasing facilities robustness against terrorism.

The six systems selected were:

- Sodium-cooled Fast Reactors (SFR);
- Very High Temperature Reactors (VHTR);
- Gas-cooled Fast Reactors (GFR);
- Lead-cooled or Lead-Bismuth Eutectic (LBE) cooled Fast Reactors (LFR);
- Molten Salt Reactors (MSR);
- SuperCritical Water Reactors (SCWR).

In 2010, the Sustainable Nuclear Energy Technology Platform (SNETP) created the European Sustainable Nuclear Industrial Initiative⁵ (ESNII) to mature the GEN-IV Fast Neutron Reactor technologies in Europe. SNETP has prioritised the different GEN-IV systems:

³ <https://europeanclimate.org/>

⁴ <https://www.gen-4.org/>

⁵ <https://snetp.eu/esnii/>

- the SFR ASTRID (host in France) as the most advanced technology;
- the LFR ALFRED (host in Romania) supported by a lead-bismuth irradiation facility project MYRRHA (host in Belgium) as a first alternative;
- the GFR ALLEGRO (host by Czech Republic) as a second alternative.

Despite ASTRID project abortion for political and economic reasons in 2019, the need to keep and expand the expertise built over decades on SFR (e.g. SUPERPHENIX in France, BN-600 in Russia) motivates ongoing research on this technology for a longer-term deployment.

All GEN-IV reactor core materials in contact with corrosive fluids will experience higher operating temperatures and radiation doses. Therefore, design rules for nuclear reactors must be adapted.

The European Energy Research Alliance⁶ (EERA) is working on the improvement of safety and sustainability of nuclear energy by focusing on materials issues. One of the main objectives is to develop the AFCEN's⁷ (Association Française pour les règles de Conception de construction et de surveillance en Exploitation des matériels des chaudières électroNucléaires) RCC-MRx Design Code into a joint European code for all future reactors. The EERA Joint Programme on Nuclear Materials⁸ (JPNM) coordinates European activities on qualification, modelling and development of structural and fuel materials for this purpose.

Started in 2017, the European Generation IV Materials Maturity⁹ project (GEMMA) is supervised by EERA JPNM and is financed by the European Commission as part of its Horizon 2020¹⁰ (H2020), the biggest EU research and innovation programme.

The GEMMA project aims is to qualify and codify the selected GEN-IV reactor core materials to support the development of design rules for RCC-MRx code. Among all the material candidates, the GEMMA project focuses on austenitic stainless steels (ASS) because almost all four system prototypes plan to use ASS both for the fuel cladding (i.e. cold worked Ti-stabilised AIM1) and for reactor core structural components (i.e. AISI 316L(N)). While structure materials will be exposed to low irradiation flux and dose in the intermediate temperature range 400-550°C during decades, the core components and the fuel cladding tubes will receive very high irradiation dose within the temperature range 300 to 700°C. ASS microstructural evolution under these extrem operating conditions is poorly reviewed. Swelling, corrosion and mechanical issues limiting components and reactor lifetime are the degradation mechanisms envisaged.

Through a complementary use of modelling and experiments, the project intends to characterize and predict microstructural evolution under irradiation of ASS and weldings joints as well as optimized/advanced ASS to ensure components integrity under such harsh and corrosive environment.

To reach these objectives, the project organized research themes within four work packages:

⁶ <https://www.eera-set.eu/>

⁷ <https://www.afcen.com/en/>

⁸ <http://www.eera-jpnm.eu/>

⁹ <http://www.eera-jpnm.eu/gemma/>

¹⁰ <https://ec.europa.eu/programmes/horizon2020/>

-
- WP1 – Advanced corrosion mitigation strategies
Aims to investigate and optimise surface engineering techniques applied to ASS and develop of advanced (alumina-forming) ASS.
 - WP2 – Welding development and characterization
Aims to provide recommendations for welding assessment procedures and design rules for welded components in liquid metal cooled nuclear reactors.
 - WP3 – Irradiation effects: modelling and experiments
Aims to get a better understanding of the thermodynamics (phase diagram, point defect formation free energies) and kinetics (diffusion properties, ordering and radiation induced segregation in the vicinity of structural defects) under irradiation in Fe-Ni-Cr model alloys.
 - WP4 – Compatibility with heavy liquid metal and helium coolants
Aims to study welded joints and optimized ASS corrosion resistance (i.e. microstructural and mechanical properties evolution) by means of experimental and modelling investigations to understand liquid metal corrosion phenomena.
 - WP5 and WP6 are dedicated to management and dissemination respectively.

The WP3 is subdivided in four tasks:

- Task 3.1: Atomistic calculations in Ni-Cr-(Fe) / Thermodynamic and kinetic models
Aims to develop thermodynamic and diffusion models of austenitic steels by considering Ni-Cr as a model alloy of austenitic steels and treat Fe as a ternary dilute species as a first step.
- Task 3.2: Modelling of nanoscale diffusion in Fe-Ni-Cr under irradiation
Aims to investigate the role of magnetism on the thermodynamic properties of Fe-Ni-Cr solid solutions. Vacancy and self-interstitial diffusion models in Fe-Ni-Cr solid solutions are being developed and implemented into Atomistic Kinetic Monte Carlo (AKMC) simulations in order to investigate the thermodynamic and kinetic properties of the ternary alloy under irradiation.
- Task 3.3: Nanoscale Interdiffusion experiments in ion irradiated Fe-Ni-Cr multilayers
Aims to determine experimentally diffusion kinetics in (Fe)-Ni-Cr model alloys under thermal ageing and ion irradiations at temperatures representative of operating temperatures of Gen IV reactors.
- Task 3.4: Ion irradiation of alumina forming alloys, modified surface layers and protective coatings
Aims to quantify and understand the effects of radiation damage on the optimized ASS.

This present work was founded by the GEMMA European project and involved in the WP3 task 3.3 dedicated to the “Experimental determination of diffusion kinetics after thermal and irradiation ageing in the FeCrNi system”.

Experimental study of diffusion kinetics under irradiation and radiation-induced segregation of austenitic model and industrial alloys.

Radiation induced segregation (RIS) is a process identified to be involved in most of the degradation mechanisms of austenitic stainless steels core components of nuclear reactors. During irradiation within the operating temperature range of present and possible prototypes of future reactors, chemical elements of reactor internal metallic components redistribute heterogeneously and segregate on the pre-existent and newly created defects. Local enrichments or depletions levels depend, inter alia, on the element and nature of the defect affected. While mechanisms involved in RIS have already been identified, their kinetics and mutual weigh are still poorly known. Indeed, current theoretical models of RIS suffer from a lack of experimental data. These two aspects motivated this study. First, by the determination of interdiffusion kinetics after thermal ageing and under irradiation on model alloys in the Fe-Ni-Cr system. Irradiation effect on diffusion have been studied at 440°C. At this temperature, conventional methods to study diffusion fail to give access to such slow kinetics under reasonable time. Experimental implementation of the nanolayers method on binary and ternary alloys gave, in this case, encouraging results. However, discrepancies between experiments and predictions revealed the need of optimizations on both sides. In the framework of this study, recommendations have been established to account for the effect of the microstructure and the selected ageing conditions on measured effective kinetics. Experiments on model alloys have the great interest to be directly confronted to simulation. Nevertheless, nuclear steels contain a large variety of minor alloying elements and impurities which have shown to play a key role on RIS behaviour. Thus, in a second part, RIS study on various bulk defects of an optimized nuclear austenitic stainless steel, a 316L(N) has been performed. Consequently, nanoscale coupled and correlated techniques (Atom Probe Tomography and Transmission Electron Microscopy) have been implemented. Techniques complementarity offered the possibility to associate enrichments to defect crystallography and revealed singular tendencies of RIS depending on the element and the defect involved. Furthermore, a higher nitrogen and niobium content in the steel nominal composition formed primary Z-phase, its stability under irradiation had also been for the first time studied in austenitic stainless steels.

Key words : radiation-induced segregation, austenitic stainless steels, diffusion (metallurgy) microstructural characterization, transmission electron microscopy, atom probe tomography, correlative microscopy, ionic irradiation, magnetron sputtering, multilayers, thin films, chromium-nickel alloys, chromium-iron-nickel alloys, thermodynamics, point defects.

Etude expérimentale des cinétiques de diffusion et de la ségrégation induite sous irradiation d'alliages modèles et industriels austénitiques.

L'implication de la ségrégation induite par l'irradiation (SIR) dans la majorité des mécanismes de dégradation des composants du cœur des réacteurs nucléaires en aciers inoxydables austénitiques est avérée. Aux températures de fonctionnement des réacteurs actuels et possibles prototypes du futur, les éléments chimiques des pièces métalliques des structures internes se redistribuent de manière hétérogène en ségrégeant sur les défauts préexistants et nouvellement créés par l'irradiation. L'intensité des enrichissements ou des appauvrissements locaux dépendent, entre autres, de la nature de l'élément et du défaut concerné. Si les différents mécanismes de ségrégation sont aujourd'hui bien identifiés, leur cinétique et leur degré d'implication respectifs sont encore peu renseignés. En effet, les modèles théoriques actuels de la SIR souffrent d'un manque de données expérimentales. Ces deux aspects sont le moteur de cette étude. Dans un premier temps, les cinétiques d'interdiffusion après vieillissement thermique et sous irradiation ont été déterminées dans des alliages modèles du système Fe-Ni-Cr. L'effet de l'irradiation sur la diffusion a été étudié à 440°C. A cette température les coefficients de diffusion sont faibles et les méthodes classiques d'étude de la diffusion ne permettent pas d'y accéder dans un délai raisonnable. La mise en œuvre expérimentale de la méthode des multicouches à période nanométrique dans des alliages binaires et ternaires a montré, dans ce cas, des résultats encourageants. Toutefois, des divergences entre les résultats expérimentaux et les prévisions théoriques ont révélé la nécessité d'optimiser ces deux approches. Dans le cadre de cette étude, des recommandations ont été formulées pour tenir compte de l'impact de la microstructure et du choix des conditions de vieillissement sur les cinétiques effectives mesurées. Les expériences réalisées sur des alliages modèles offrent l'intérêt de pouvoir être directement confrontées à la simulation. Néanmoins, les aciers de l'industrie nucléaire contiennent une grande variété d'éléments d'alliage minoritaires et d'impuretés qui jouent un rôle clé sur le comportement des éléments impliqués dans la SIR. Ainsi, dans un second temps, une étude de la SIR sur différents défauts intragranulaires d'un acier inoxydable austénitique optimisé, un 316L(N) a été réalisée. Pour cela, des techniques couplées et corrélées à l'échelle nanométrique (Sonde Atomique Tomographique et Microscopie Electronique en Transmission) ont été mises en place. La complémentarité des techniques a rendu possible l'association des enrichissements locaux observés à la cristallographie des défauts concernés. Des tendances singulières de SIR ont été observées selon l'élément et la nature du défaut impliqués. Une teneur plus élevée en azote et en niobium dans la composition nominale de l'acier a entraîné la précipitation de phase Z primaire. La stabilité de cette phase sous irradiation dans les aciers inoxydables austénitiques a pour la première fois pu être étudiée.

Mots-clés : ségrégation induite par l'irradiation, aciers inoxydables austénitiques, diffusion (métallurgie), caractérisations microstructurales, microscopie électronique en transmission, sonde atomique tomographique, microscopie corrélative, irradiation ionique, pulvérisation magnétron, multicouches, couches minces, alliages chrome-nickel, alliages chrome-fer-nickel, thermodynamique, défauts ponctuels.